DTU Physics
Department of Physics

Chemically tunable antiferromagnets as a conceptual pathway to quaternary memory systems

Adheena Painganoor
Ph.D. thesis

Supervisor: Niels Bech Christensen
Co-supervisors: Navid Qureshi, Paul Steffens

30th November 2025

This thesis was prepared by
Adheena Painganoor

Supervisors
Niels Bech Christensen
Navid Qureshi, Paul Steffens

Due date: 30th of November 2025
Comments: This thesis is part of the requirements to achieve the Doctorate of Philosophy (PhD) from the Technical University of Denmark.
Citation (APA):
Department of Physics, Technical University of Denmark.

Department of Physics
Technical University of Denmark

Fysikvej, Buildings 307-309-311-312
DK-2800 Kongens Lyngby
Denmark

Tel: (+45) 45 25 33 44
E-mail: info@fysik.dtu.dk
www.fysik.dtu.dk

Acknowledgements

First and foremost, I would like to thank my supervisors, Niels Bech Christensen and Navid Qureshi, for introducing me to the world of neutron scattering and for their constant guidance, patience and scientific insights without which the PhD thesis would not have been possible. I am also grateful to Paul Steffens at ILL and Rasmus Toft-Petersen at DTU for their valuable discussions and guidance throughout this work.

I am thankful to the various instrument teams at the ILL for their assistance during the many beam times I participated in during this thesis. Especially, Inés Puente Orench, María Teresa Fernández Díaz, Óscar Fabelo Rosa and José Alberto Rodriguez Velamazán, whose help during demanding beam times and willingness to teach me the practical aspects of each instrument were invaluable. I would like to thank Ketty Beauvois at ILL for her support during the D3 beam time.

This thesis would not have been possible without the collaboration with Professor Efrain E. Rodriguez and his research group at the University of Maryland, who provided the single crystals and powder samples for the $\mathrm{LiNi}_{1-x}\mathrm{Fe}_x\mathrm{PO}_4$ series. I am especially grateful to the PhD students Hector Cein Mandujano and Cecilia Machiko Wheeler for growing the crystals and participating in the beam time.

I would like to thank the research group of Kasper Steen Pedersen at DTU Chemistry for providing access to laboratory facility for synthesis of the powder samples for the $\mathrm{LiCo}_{1-x}\mathrm{Ni}_x\mathrm{PO}_4$ series and for allowing the use of PPMS and X-ray diffraction instruments. In particular, I thank Maja A. Dunstan and Carl Emil Andersen for their help and valuable discussions during the synthesis and characterization of $\mathrm{LiCo}_{1-x}\mathrm{Ni}_x\mathrm{PO}_4$. I am also grateful to the Bachelor students at DTU Physics Mikkel C. Larsen and Mikkel Ravn-Feld for their Monte-Carlo simulations of the $\mathrm{LiCo}_{1-x}\mathrm{Ni}_x\mathrm{PO}_4$ series. I am thankful to Dr. Sandip Guchhait at DTU Physics for carrying out the magnetization measurements of $\mathrm{LiNi}_{1-x}\mathrm{Fe}_x\mathrm{PO}_4$ and for participating in the beam times. I would also like to thank all my colleagues at DTU Physics and at the ILL for the support, camaraderie and the many enjoyable moments that made the PhD journey evenmore memorable.

A special thanks to all my malayali friends in Denmark who made me feel at home far away from Kerala. I am sincerely grateful to Anand Raj Palanisamy and R. Baby Dhanalakshmi for all their help from the day I moved to Denmark. My PhD journey would not have been the same without the friends in Grenoble who filled this period with warmth, laughter and unforgettable memories. I would like to thank Sreelakshmi, Firoz and Farhan for the travels, food and conversations that made my time in Grenoble truly colourful.

Finally I express my deepest gratitude to my parents. Your unconditional love and strength have always guided me throughout my life. Your belief in me and the many sacrifices you made are the foundation on which this work rests. To Sooraj, thank you for always being there, despite the distance and timezones. Thank you for your trust even when I doubted myself. Your presence has meant more than words can express.

Abstract

Engineering materials with tailored physical properties is central to advancing technology. Multi-state logic memory concepts remain the most promising route to surpass the storage limits of conventional binary memory devices. However, realizing such a multi-domain configuration in a single phase material remains challenging. This thesis explores chemically substituted lithium orthophosphates, ($LiMPO_4$, M = Mn, Fe, Co, Ni), where the frustration introduced by the substitution of ions with mismatched anisotropy modifies the antiferromagnetic ground state of the mixed compounds. The resulting symmetry lowering due to the rotation of spins away from the easy axes of the parent compounds and stabilization of an oblique antiferromagnetic ground state, generates multiple domains for intermediate composition ranges. By utilizing the ferrotoroidal nature of the domains, this thesis demonstrates the selective poling of these domains, paving the way to development of multi-state memeory concepts using single phase antiferromagnetic materials.

Using neutron powder diffraction experiments the complete composition-temperature phase diagram for the mixed anisotropy series $LiCo_{1-x}Ni_xPO_4$ and $LiNi_{1-x}Fe_xPO_4$ were established. These studies confirm the existence of oblique antiferromagnetic phases with distinct symmetry in both series, consistent with the theoretical predictions for mixed-anisotropy antiferromagnets. The powder diffraction work identifies the composition range where symmetry lowering generates four antiferromagnetic domains. In the present work, the particular composition $LiNi_{0.8}Fe_{0.2}PO_4$ for which the symmetry lowering driven by anisotropy-competition generates four antiferromagnetic domains, was investigated using spherical neutron polarimetry. This technique allows to differentiate each domain. The study successfully demonstrates the selective population of four different domains using appropriate combinations of applied magnetic and electric fields exploiting the ferrotoroidal ordering of the system, thereby establishing non-volatile, controllable four domain states in a single-phase antiferromagnetic system. Finally, contradicting reports concerning the existence and symmetry of minor magnetic structure components in the end compounds $LiCoPO_4$ and $LiFePO_4$ were revisited using a combination of spherical neutron polarimetry and single crystal neutron diffraction. Overall, the thesis establishes chemically tunable mixed-anisotropy antiferromagnets as a highly promising route to design controllable multi-domain states, offering a path towards antiferromagnetic quaternary memory concepts.

Resumé

Evnen til at udvikle materialer med skræddersyede fysiske egenskaber er central for teknologiske fremskridt. Med henblik på at opnå højere datalagringstætheder er hukommelses-koncepter, der baserer sig på N-bit tilstande snarere end de konventionelle binære ($N = 2$) løsninger iblandt de mest lovende. Det er dog fortsat udfordrende at realisere de nødvendige multi-domæne konfigurationer i et enkelt-fase materiale. I denne afhandling udforskes kemisk substituerede lithium-orthofosfater ($LiMPO_4$, M = Mn, Fe, Co, Ni), hvori den magnetiske frustration, der introduceres når ioner med forskellige enkelt-ion anisotropier blandes, fører til ændringer af den antiferromagnetiske grundtilstand. Den symmetri-sænkning, der resulterer ved rotation af de magnetiske momenter bort fra de foretrukne akser i moder-forbindelserne, fører til eksistensen af fler-domæne tilstande i mellemliggende kemiske kompositioner.

Ved hjælp af neutron pulverdiffraktions blev komposition-temperatur fasediagrammerne for de blandede anisotropi-serier $LiCo_{1-x}Ni_xPO_4$ og $LiNi_{1-x}Fe_xPO_4$ bestemt. For begge serier bekræftede disse undersøgelser eksistensen af antiferromagnetiske faser med symmetrier, der er distinkte fra dem, der observeres i moder-forbindelserne $LiFePO_4$, $LiCOPO_4$ og $LiNiPO_4$. Disse observationer stemmer overens med teoretiske forudsigelser for antiferromagneter bestående af ioner med distinkte anisotropi-energier. Pulverdiffraktions-eksperimenterne tillod identifikation af de kompositioner, hvor symmetri-sænkning genererer fire antiferromagnetiske domæner. Den specifikke komposition, $LiNi_{0.8}Fe_{0.2}PO_4$, hvori fire antiferromagnetiske domæner eksisterer, blev undersøgt ved hjælp af sfærisk neutronpolarimetri. Denne teknik gør det muligt at differentiere hvert enkelt domæne. Undersøgelsen demonstrerede at det er muligt selektivt at populere de fire forskellige domæner ved hjælp af en passende kombinationer af påtrykte magnetiske og elektriske felter, hvorved der etableres stabile, kontrollérbare domæne-tilstande i et enkeltfaset antiferromagnetisk materiale. Endelig blev eksistensen og symmetrien af sub-dominante komponenter af den magnetiske struktur i moder-forbindelserne $LiCoPO_4$ og $LiFePO_4$ undersøgt ved hjælp af en kombination af sfærisk neutronpolarimetri og én-krystal neutrondiffraktion. Samlet set etablerer denne afhandling kemisk justérbare antiferromagnetiske materialer indeholdende ioner med forskellige enkelt-ion anisotropier som en yderst lovende rute imod design af kontrollérbare multidomæne-tilstande, hvorved N-bit hukommelses-koncepter gøres mulige.

Contents

List of Figures

List of Tables

Introduction

Magnetism has been known to humankind for millennia, with accounts dating back to ancient Greek civilizations. Over time, magnetic phenomena have played a central role in technological progress, from enabling navigation with the compass in historical times to contributing to ultrafast spintronic devices that have revolutionized modern information technology. Although the practical aspects of magnetism have been familiar since antiquity, the quantum mechanical origins of the magnetic ordering remain an area of active research. For centuries, technological applications of magnetism were almost entirely realized using ferromagnetic materials, whose macroscopic magnetization provide an easy handle for detection and manipulation. In contrast, antiferromagnetic materials were not detected until the twentieth century. At the time of discovery, although its importance as a scientifically intriguing class of materials was recognized, they were deemed to be technologically irrelevant. This perspective has changed dramatically, now antiferromagnetic materials are at the forefront of emerging technologies especially in data storage applications owing to the additional advantages of ultra fast spin dynamics, robustness against external magnetic fields and absence of stray fields.

The ever increasing demand for data storage has driven the search for novel concepts to increase data storage density such as spintronic devices. Magnetoelectric materials are a particularly interesting class of materials in this context, as the coupling between magnetic and electric degrees of freedom enables more energy-efficient data storage devices. Moreover, magnetoelectric materials have been utilized in devices that exploit multi-state logic, where more than two stable states can be manipulated by appropriate external fields in contrast to the conventional memory devices that use binary logic states and as a result increase data storage density.

Within this context, the family of isostructural antiferromagnetic compounds lithium orthophosphates ($LiMPO_4$, M = Mn, Fe, Co, Ni) has attracted scientific interest due to their ferroic and magnetoelectric properties. In particular, $LiCoPO_4$ is one of the few materials that hosts the fourth ferroic order, known as ferrotoroidal order. Generally in the discovered magnetoelectric and ferrotoroidic compounds one of the factors hindering their practical usage is the small magnitude and the low operating temperatures. Therefore a method to engineer the materials in order to tune these properties hold significant technological implications. In the $LiMPO_4$ family of compounds, the dominant magnetic structure is identical, except for different transition metal ions possessing distinct easy axes of the spin alignment, therefore presenting a controlled system for studying the effect of competing single-ion anisotropies.

This thesis explores the possibility of tuning the antiferromagnetic ground states of the compounds in the $LiMPO_4$ family through chemical substitution on the transition metal site. Introducing ions with mismatched single-ion anisotropies modifies the balance between single-ion anisotropy energies and exchange interactions altering the stabilized magnetic ground state and spin direction. Demonstrating and characterizing these effects of competing anisotropies in the family $LiMPO_4$ provides a way to engineer technologically relevant physical properties.

This thesis progresses from chemically tuning the antiferromagnetic ground state to demonstrating controllable multi-domain states in the mixed-anisotropy compound of the $LiMPO_4$ family and ends by utilizing the domain selection procedure developed in the present work to resolve the long debated magnetic structure components in the stoichiometric compounds. It establishes that chemical substitution of the transition metal sites with ions of mismatched easy axis direction reshapes antiferromagnetic ground states by lowering the magnetic structure symmetry and generates non-volatile controllable multidomain states in the mixed anisotropy compounds of $LiMPO_4$. This provides a rare account of multi domain state in a single phase antiferromagnetic material in the literature which has significant implications for next generation spintronic devices that rely on multi-state memory. Therefore, this thesis establishes chemically tuning antiferromagnetic ground states by utilizing the competing anisotropies as a route to realize the quaternary memory concepts. The thesis explores the mixed anisotropy systems $LiCo_{1-x}Ni_xPO_4$ and $LiNi_{1-x}Fe_xPO_4$ series, investigating the magnetic structure across the entire composition phase diagram using neutron powder diffraction. These experimental phase diagrams are compared with theoretical predictions for the mixed-anisotropy antiferromagnets. The work on the $LiNi_{1-x}Fe_xPO_4$ series provides the experimental verification of the previously published phase diagram from Monte-Carlo simulations [1]. The detailed phase diagram reveals the composition ranges where the anisotropy-driven spin rotation stabilizes multiple domains. One such mixed compound $LiNi_{0.8}Fe_{0.2}PO_4$ is investigated where domain resolved studies were carried out using spherical neutron polarimetry. This work demonstrates the existence of four antiferromagnetic domains and more importantly demonstrates successful selective stabilization of these domains using appropriate combinations of external electric and magnetic fields. Finally, the domain selection mechanism developed in this work was exploited in combination with single crystal neutron diffraction to revisit the contradicting reports of the minor magnetic moment components in $LiCoPO_4$ and $LiFePO_4$ which govern the toroidal moment direction and magnitude as well as the non-zero magnetoelectric tensor elements in these compounds.

Chapter 1 of the thesis presents the theoretical concepts of magnetism that is used in this thesis. It briefly reviews key concepts such as crystal field effect and magnetic interactions, before shortly discussing the magnetic and crystallographic symmetry considerations that are used throughout the later chapters. The chapter also introduces the ferroic orders relevant to this thesis.

Chapter 2 provides an overview of the lithium orthophosphates, describing the crystal structure, magnetic structure and known physical properties of the stoichiometric end compounds. The chapter further discusses the experimental and theoretical work on mixed anisotropy antiferromagnets which present a framework for understanding the behaviour of the chemically substituted systems explored in the later chapters.

Chapter 3 briefly discusses the basic concepts of neutron scattering which builds the foundation for the analysis and interpretation of the experimental results presented in this thesis.

Chapter 4 outlines the experimental techniques employed in this thesis. It includes a short review of the solid-state synthesis procedures reported in the literature for the $LiMPO_4$ family, along with bulk characterization methods. Further, the chapter describes the X-ray and neutron diffraction techniques used to determine the crystal and magnetic structures of the systems studied in this thesis and provides a brief introduction to the spherical neutron polarimetry technique which was utilized to characterize domain distributions in the result chapters.

Chapter 5, describes the synthesis routes attempted to produce phase-pure samples of the $LiCo_{1-x}Ni_xPO_4$ and $LiNi_{1-x}Fe_xPO_4$ series, motivated by previous literature reports. It details the synthesis procedure for obtaining phase pure $LiCo_{1-x}Ni_xPO_4$ and discusses the challenges faced in the synthesis of $LiNi_{1-x}Fe_xPO_4$ series within the scope of this thesis.

Chapter 6 and Chapter 7 present the detailed investigation of $LiCo_{1-x}Ni_xPO_4$ and

$LiNi_{1-x}Fe_xPO_4$ respectively using neutron powder diffraction. Chapter 8 discusses the controllable domain distribution and confirmation of toroidal order in $LiNi_{0.8}Fe_{0.2}PO_4$. Chapter 9 details the attempts made at resolving the minor magnetic structure components in $LiCoPO_4$ and $LiFePO_4$.
Finally, chapter 9 includes a brief discussion and conclusion of the results presented in this thesis along with an outlook mentioning the possible avenues for future studies.

1

Theoretical Concepts

This chapter provides an overview of the theoretical concepts essential in the context of the results presented in this work. The discussion builds upon the treatment of magnetism, magnetic interactions and symmetry presented in references [2–8], which serve as general sources and are used without further citation throughout this chapter.

1.1 Magnetism

Magnetism is a quantum mechanical phenomenon whose fundamental entity is the magnetic moment. In an atom, both the electrons and the nucleus possess magnetic moments. However, since the electronic and nuclear magnetic moments are expressed in the units of Bohr magnetons (μ_B) and nuclear magnetons (μ_N), respectively, which differ by the ratio of mass of electron to proton, the electron magnetic moment is orders of magnitude higher than the nuclear contribution. Therefore the electron magnetic moment constitutes the primary source of magnetism in solids. The magnetic moment of the electron has two contributions. The intrinsic spin angular momentum, characterized by the quantum numbers $s = \frac{1}{2}$ and $m_s = \pm\frac{1}{2}$, is associated with a magnetic moment of $\boldsymbol{\mu_S} = -g_S\mu_B\mathbf{S}$, where g_S is the electron spin g-factor (≈ 2 for a free electron) . The orbital angular momentum associated with the motion of an electron around the nucleus, characterized by the quantum numbers l and m_l (where $m_l = -l, \cdots, +l$), gives rise to a magnetic moment $\boldsymbol{\mu_L} = -\mu_B g_L\mathbf{L}$ ($g_L \approx 1$). These two contributions combine ($\boldsymbol{\mu} = -\mu_B(g_L\mathbf{L} + g_S\mathbf{S})$ to give the magnetic moment of an electron in general.

A typical atom consists of many electrons, which adopt a configuration that minimizes the total energy of the system. For a many-electron atom, the atomic Hamiltonian contains contributions from the kinetic energy of the electrons, the Coulomb interaction between the nucleus and electrons and the electron-electron repulsion. In the central field approximation, each electron is assumed to move in an average spherically symmetric potential generated by the nucleus and the screening effect of all other electrons. From these considerations, we get energy states characterized by principal and orbital quantum numbers n and l.

For a realistic many-electron atom, at least two additional perturbations to the Hamiltonian must be considered. (i) Electron-electron interaction beyond the central field approximation that are not spherically symmetric and (ii) relativistic spin–orbit interaction, which causes the weak coupling of electron spin and orbital angular momenta. In the rest frame of the electron, the positively charged nucleus appears to move around it, producing a magnetic field at the position of the electron. The interaction between this effective magnetic field and the magnetic moment associated with the spin of the electron gives rise to an additional energy term, proportional to the scalar product of $\mathbf{L} \cdot \mathbf{S}$. This coupling is known as the spin-orbit coupling. When electrostatic interactions of the electrons dominate over the spin-orbit effect, LS (Russell–Saunders) coupling is followed. The angular momenta of unpaired electrons are combined to give the total orbital angular momentum $\mathbf{L}$ and total spin $\mathbf{S}$. The electrons from the completely filled shells do not contribute to the total angular momentum. Because by Pauli's principle, only electrons with opposite spin can occupy an orbital, giving $S = 0$. In a filled subshell, all m_l states are occupied symmetrically, giving $L = 0$.

When the weak perturbation of spin-orbit coupling—which scales as Z^4 (Z = atomic number)—is taken into account, L and S are no longer conserved individually; instead, the total angular momentum $\mathbf{J} = \mathbf{L}+\mathbf{S}$ is conserved. The LS multiplets (degenerate states with same $\mathbf{L}$ and $\mathbf{S}$) are hence split into states characterized with different J values ranging from $|L - S|$ to $L + S$. Each J state has a degeneracy of $2J + 1$, which can be lifted in the presence of a magnetic field (Zeeman splitting). Since different combinations of angular momenta lead to different energies, to find the ground state of an atom, Hund's rules can be applied.

1. For a given electronic configuration, that is, for a given number of electrons in a partially filled subshell characterized by the quantum numbers n and l, maximize the total spin S.

2. For the states of maximum S identified by Hunds first rule, maximize the total

orbital angular momentum L.

3. For a given value of S and L, the lowest-energy multiplet has $J = |L - S|$ if the shell is less than half-filled, and $J = L + S$ if it is more than half-filled.

The first two rules work by lowering the energy by minimizing the Couloumb repulsion, in accordance with Pauli's exclusion principle, while the third rule lowers the energy from spin-orbit interaction.

For example, consider the Fe^{2+} ion, which has six electrons in the 3d subshell ($3d^6$). According to Hund's first rule, S must be maximized. To achieve this, the five degenerate $3d$ orbitals are singly occupied with parallel spins and the remaining one electron is filled in one of the $3d$ orbitals. This results in 4 unpaired electrons, corresponding to S=2. According to Hund's second rule, for this maximum S configuration, L should also be maximized. The possible m_l values of the $3d$ orbitals are -2,-1,0,+1,+2. The electrons are distributed in these orbitals so as to maximize the sum of m_l,resulting in L=2. Finally, since the subshell is more than half-filled according to Hund's third rule the total angular momentum quantum number of the ground state is $J = L+S=4$. Similarly the ground states for Co^{2+} and Ni^{2+} determined using the Hund's rules are summarized in table1.1.

Ion	Electronic configuration	S	L	J
Fe^{2+}	$3d^6$	2	2	4
Co^{2+}	$3d^7$	3/2	3	9/2
Ni^{2+}	$3d^8$	1	3	4

Table 1.1: Ground-state quantum numbers of relevant transition-metal ions determined from Hund's rules.

1.1.1 Crystal field effect

In a crystal lattice, each magnetic ion occupies a well defined position, where it is surrounded by neighbouring ions. The electrostatic field created by this local environment, known as the crystal field, acts as a perturbation to the atomic Hamiltonian, lifting the degeneracy of the multiplets and thereby modifying the ground state. Among the atomic orbitals only the s orbital is spherically symmetric while the p, d and f orbitals have electron charge density distributions with an angular dependence. Consequently, the effect of crystal field is dependent on the symmetry

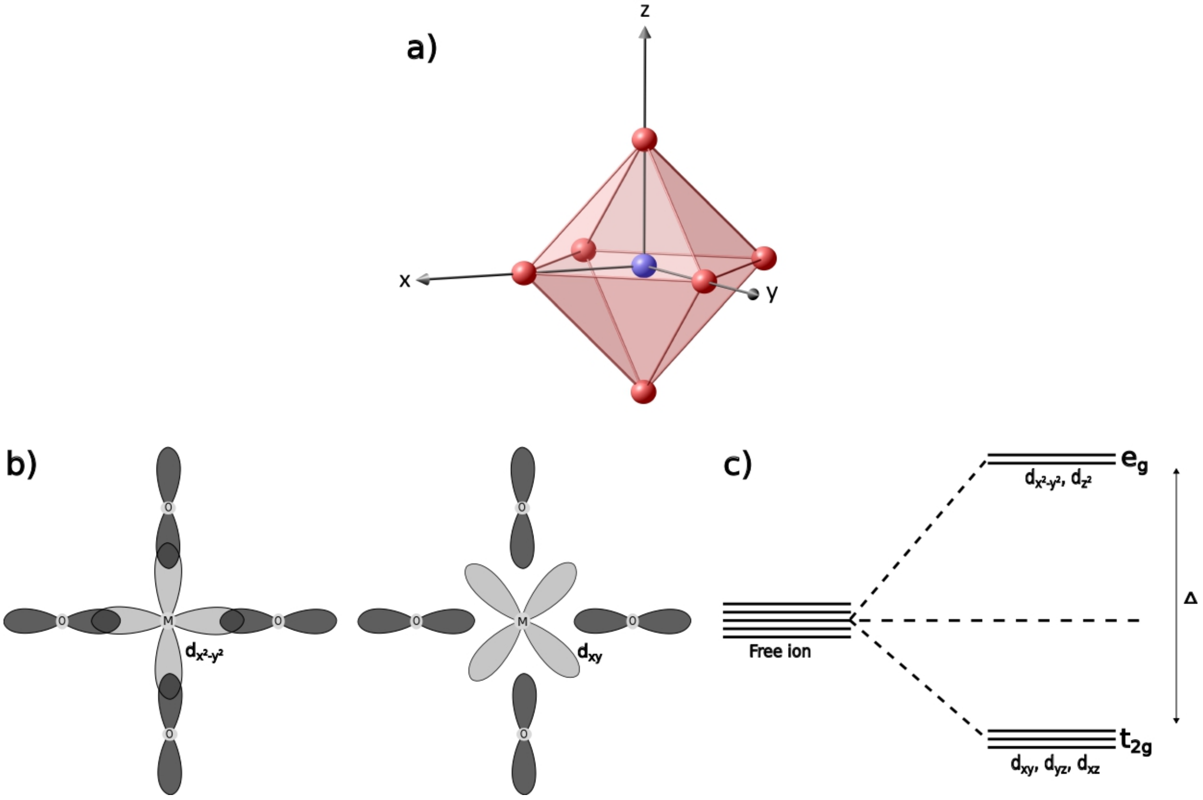

Figure 1.1: Schematic representation of crystal field splitting in an octahedral environment. a) The figure represents an ideal octahedron formed by oxygen anions shown in red and a metal ion shown in blue. b) Illustration of the spatial orientation of the $d_{x^2-y^2}$ and d_{xy} orbitals on the metal site with respect to surrounding oxygen p orbitals. c) The crystal field splitting of the five degenerate d orbitals of the free ion into a lower-energy t_{2g} triplet and a higher-energy e_g doublet, seperated by the crystal field energy Δ.

of the local environment.

In lithium orthophosphates ($LiMPO_4$), the magnetic ion M^{2+} (M= Mn, Fe, Co, Ni) is surrounded by six oxygen anions arranged in a distorted octahedral coordination. The five-fold degeneracy of the $3d$ valence electrons of the metal ion can be lifted by the crystal field effect depending on the interaction of $3d$ orbitals with the $2p$ orbitals of the surrounding oxygen atom. To lower the Coulomb energy, the orbitals that minimize d-p overlap are favoured. In an ideal octahedral environment, this results in the splitting of $3d$ shell into a lower energy triplet t_{2g} (d_{xy}, d_{xz}, d_{yz}) and a higher energy doublet e_g (d_{z^2}, $d_{x^2-y^2}$), as illustrated in the figure 1.2. The balance between the crystal-field splitting energy Δ and the electron pairing energy

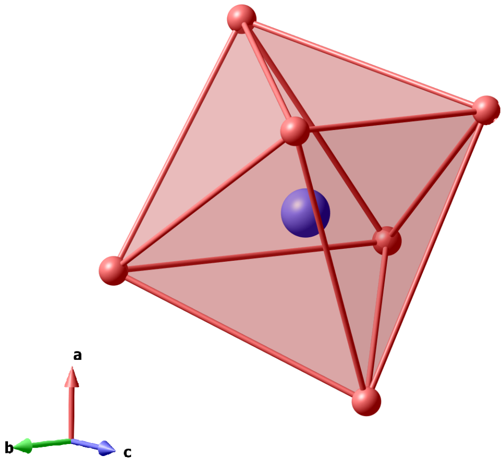

Figure 1.2: Distorted MO_6 octahedron in LiMPO$_4$.The distortion plays an important role in lifting the degeneracy of the d orbitals in LiMPO$_4$.

P, i.e. the energy cost of double-occupancy of an orbital determines the orbital occupation. If $\Delta \lesssim P$, it is energetically favorable to maximize the spin multiplicity by occupying the higher-energy e_g orbitals, leading to a high-spin state. Conversely, if $\Delta > P$, it is favorable for electrons to fully occupy the lower-energy t_{2g} levels before the e_g orbitals, resulting in a low-spin state. In LiMPO$_4$, the oxygen octahedra are distorted, which further lifts the degeneracy and results in non-degenerate singlets as reported for LiCoPO$_4$ by Kornev et al. [9]. Table 1.2 summarizes the octahedra distortion reported for the LiMPO$_4$ compounds.

Compound	M–O range (Å)	$\langle d \rangle$ (Å)	δ ($\times 10^{-3}$)
LiMnPO$_4$	2.160 – 2.246	2.202	0.347
LiFePO$_4$	2.061 – 2.253	2.157	1.447
LiCoPO$_4$	2.056 – 2.192	2.123	0.743
LiNiPO$_4$	2.042 – 2.140	2.0897	0.339

Table 1.2: M-O bond length ranges, average bond length ($\langle d \rangle$) and the calculated distortion of the MO$_6$ octahedra. The distortion is defined as $\delta = \frac{1}{6}\sum_{i=1}^{6}\left(\frac{d_i - \langle d \rangle}{\langle d \rangle}\right)^2$, where d is the individual M-O bond lengths. The values are taken from references [10–13].

Because $3d$ orbitals are more spatially extended compared to $4f$ orbitals, the crystal field effects in transition metal ions are much stronger than the spin-orbit coupling. Consequently, Hund's third rule, which considers spin-orbit coupling as the dominant perturbation, does not generally apply in these systems. A major consequence of the dominance of the crystal field effect over the spin-orbit coupling is orbital quenching: in the non-degenerate orbital ground state resulting from crystal field splitting, the expectation value of the orbital angular momentum operator vanishes. Hence in transition metal compounds, the magnetic moment is predominantly spin derived. Nonetheless, quenching is not always complete. The spin-orbit coupling mixes excited crystal field levels into the ground state, partially restoring the orbital contribution. This transfers the local symmetry of the environment onto the spin degree of freedom, giving rise to single-ion anisotropy—an energetic preference for spins to align along specific crystallographic directions. In the effective spin Hamiltonian this contribution is written as,

$$H_{\text{ani}} = \sum_i \sum_{\mu,\nu} D_{\mu\nu} S_{i,\mu} S_{i,\nu} \tag{1.1}$$

Where μ and ν represent cartesian coordinates. In most cases this can be diagonalized to give $D_{\mu\nu} \approx \text{diag}(D_a, D_b, D_c)$, i.e.

$$H_{\text{ani}} = \sum_i \left(D_a S_{i,a}^2 + D_b S_{i,b}^2 + D_c S_{i,c}^2 \right) . \tag{1.2}$$

The signs and magnitudes of D_a, D_b, and D_c determine the easy and hard directions of spin alignment. Since the total spin magnitude is fixed and can be written as $S^2 = S_x^2 + S_y^2 + S_z^2$, one of the diagonal component of the anisotropy parameters can be absorbed into an energy shift. This leaves only two independent parameters without altering the physical description of the system. Hence, the anisotropy hamiltonian can be expressed as

$$H_{\text{ani}} = D S_c^2 + E \left(S_a^2 - S_b^2 \right)$$

where D represents an axial anisotropy and E represents the orthorhombic in-plane anisotropy.

1.1.2 Magnetic interactions

In this section, the interactions between the magnetic moments across the lattice that may give rise to long-range order and determine the type of ordering are explored. Even though dipole-dipole interactions between the localized magnetic moments exist, they are too weak to account for the long-range order observed at the characteristic temperatures of many magneic systems. Therefore, to explain long-range ordering in these systems, it is necessary to consider exchange interactions of quantum mechanical origin.

Classically, the Coulomb interaction depends only on the electronic charge and spatial separation and is independent of the spin. However due to Pauli's exclusion principle, total wavefunctions should be anti-symmetric under particle exchange. This couples the spin part of the total wave function to the spatial part. If the spin wave function is symmetric corresponding to a triplet state (parallel spin), then the spatial part must be anti-symmetric. Conversely, when the spin part is anti-symmetric corresponding to a singlet state (antiparallel spins), then the spatial part must be symmetric.

These two possibilities differ in energy due to the competition between potential and kinetic energies (i) In the anti-symmetric spatial state, the Coulomb repulsion is minimized by reducing the probability of two electrons being close together, favouring the parallel-spin state. (ii) In the symmetric spatial state, the overlap between the orbitals is maximized, which lowers the kinetic energy by increasing electron delocalization. This spatial state is compatible with the antiparallel spin state. The balance between these two contributions determine whether the parallel or antiparallel alignment is preferred. The energy difference between these two states is encoded in the exchange integral J, which is defined as the difference between the energy of the singlet state and triplet state. If $J > 0$, parallel alignement of spins are prefered while $J < 0$, favours antiparallel alignment of spins. In many electron atom, this can be expressed as an effective Heisenberg Hamiltonian:

$$H_{\text{ex}} = -\sum_{\langle i,j\rangle} J_{ij}\, \mathbf{S}_i \cdot \mathbf{S}_j. \tag{1.3}$$

Here J_{ij} is the exchange constant between i^{th} and j^{th} spin.

The simplest exchange interaction in solids is the direct exchange, where the electronic wavefunctions of the neighbouring magnetic ions overlap directly. However in magnetic solids with localized electrons, the direct overlap between the orbitals of the neighbouring magnetic ions is insufficient for direct exchange to produce the long-range ordering observed at typical ordering temperatures for these systems. Hence indirect exchange interactions also known as superexchange must be considered.

In superexchange, the interaction between two magnetic ions are mediated by non-

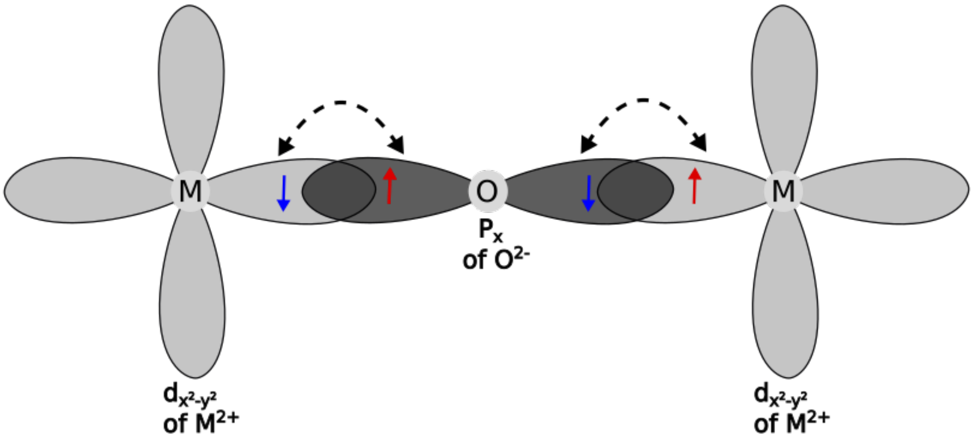

Figure 1.3: Schematic illustration of superexchange interaction between two metal cations (represented by M^{2+}) , mediated by oxygen anion (O^{2-}). The virtual hopping of electrons (dashed arrows) between metal and oxygen orbitals enable delocalization over the entire $M-O-M$ unit. The coupling illustrated here results in a AFM coupling characteristic of 180° superexchange pathway.

magnetic ions such as oxygen. Here the electron is allowed to virtually hop from one cation to intermediate anion orbital, and then to the neighbouring cation (figure 1.3). This delocalizes the electron over the entire M-O-M unit and lowers the kinetic energy of the system. When the half filled cation orbitals overlap with the same oxygen orbital, superexchange stabilizes antiparallel alignment of spins giving rise to a strong antiferromagnetic coupling. However, superexchange can also give rise to a ferromagnetic coupling depending on the symmetry of the orbitals. If the cation orbitals couple via orthogonal oxygen orbitals, superexchange stabilizes parallel arrangement of spins, resulting in a ferromagnetic coupling, even though this is less common. The strength and sign of the superexchange interaction are therefore highly sensitive to the M–O–M bond geometry and orbital orientations as described by the Goodenough Kanamori rules.

The anisotropic exchange interaction that arises when the excited state of one ion mixes with the ground state of another ion via spin orbit coupling is known as Dzyaloshinskii-Moriya (DM) interaction. The DM interaction can be expressed as

$$H_{\mathrm{DM}} = \sum_{\langle i,j \rangle} \mathbf{D}_{ij} \cdot (\mathbf{S}_i \times \mathbf{S}_j) \tag{1.4}$$

Here D_{ij} is the DM vector. The allowed direction of the DM vector is determined by the space group symmetry of the crystal. All the symmetry operations that leave the bond between the sites i and j, must transform the DM vector into itself. In particular, if there is an inversion center at the midpoint of the bond between S_1 and S_2 then D_{12}=0. The magnitude of the DM vector is dependent on the strength of spin-orbit coupling. Unlike the Heisenberg interaction discussed above, which favours collinear spin arrangements, the DM interaction stabilizes spins that align perpendicular to each other in the plane normal to the DM vector. In most cases this manifests as a small canting of otherwise collinear antiferromagnetic structures, producing a weak ferromagnetic moment [14, 15].

The combination of direct exchange, indirect exchange and DM interactions defines the microscopic mechanisms that couple localized moments in solids. Their combined action is responsible for stabilizing long-range magnetic order and determining its character. The next sections address the role of symmetry in constraining these ordered states and subsequently ferroic orders.

1.2 Crystallographic and magnetic symmetry

Symmetry plays an essential role in condensed matter physics, as it defines how the atoms are arranged in the space and constrains the physical properties of the material. An ideal crystal is defined as an infinite periodic arrangement of a group of atoms which can be generated by a basic structural unit called the unit cell, through translations along three independent directions spanned by lattice vectors in three dimensions.

A symmetry operation of a crystal is a geometric operation that leaves the crystal invariant. The complete set of symmetry operations that leave the crystal invariant is called a space group. For a set of symmetry elements to constitute a group, the following conditions should be fulfilled.

(i) There must be an identity element present for all the elements in the group

(ii) There must be an inverse present for all elements in the group

(iii)The product of two elements in the group must also be contained within the group.

(iv) Associativity of the elements in the group

In a crystal all symmetry operations can be generated from three fundamental operations: rotation about a specific axis, reflection about a mirror in a plane, and translation with a specified translation vector. A crystallographic point group is the set of symmetry elements of a crystal that leaves at least one point fixed. They include rotation, reflection and inversion but exclude translations. A space group

combines the symmetry operations described by the point group with the translational symmetries and include symmetry elements such as screw axes (rotation followed by fractional translation along the rotation axis) and glide planes (Reflection followed by fractional translation). There are 230 unique space groups that allow the complete classification of all possible 3D crystals with different symmetries.
The $LiMPO_4$ compounds belong to the space group Pnma (62). The allowed symmetry operations in this group are:

- 1: Identity : $(x, y, z) \rightarrow (x, y, z)$
- $2'_x$: 2-fold screw axis at $(x, 0.25, 0.25)$: $(x, y, z) \rightarrow (x + 0.5,\ 0.5 - y,\ 0.5 - z)$
- $2'_y$: 2-fold screw axis at $(0, y, 0)$: $(x, y, z) \rightarrow (-x,\ 0.5 + y,\ -z)$
- $2'_z$: 2-fold screw axis at $(0.25, 0, z)$: $(x, y, z) \rightarrow (0.5 - x,\ -y,\ 0.5 + z)$
- I: Inversion in $(0, 0, 0)$: $(x, y, z) \rightarrow (-x,\ -y,\ -z)$
- m_{xz}: Mirror plane at $y = 0.25$: $(x, y, z) \rightarrow (x,\ 0.5 - y,\ z)$
- m'_{xy}: Glide plane at $z = 0.25$ with glide vector $(0.5, 0, 0)$:
  $(x, y, z) \rightarrow (x + 0.5,\ y,\ 0.5 - z)$
- m'_{yz}: Glide plane at $x = 0.25$ with glide vector $(0, 0.5, 0.5)$:
  $(x, y, z) \rightarrow (0.5 - x,\ y + 0.5,\ z + 0.5)$

$LiMPO_4$ belongs to the point group $D_{2h} = \{1,\ 2_x,\ 2_y,\ 2_z,\ \mathrm{I},\ m_{xy},\ m_{yz},\ m_{xz}\ \}$, from which the symmetry operations discussed above can be generated.
Understanding the crystallographic symmetry of the compounds $LiMPO_4$ is fundamental in order to describe the magnetic ordering of the system. The introduction of magnetic moments, introduces a new degree of freedom into the crystal symmetry and requires the extension of crystallographic symmetry to account for time reversal effects, making the concept of magnetic space groups relevant, which are discussed in the following section.

1.2.1 Magnetic symmetry and irreducible representations

As explained in the section above, crystallographic symmetry describes how the atomic positions are arranged. The magnetic symmetry determines how the spins transform under the spatial operation combined with time reversal. Therefore, 3D magnetic space groups are built by combining 230 crystallographic space groups with time-reversal symmetry, resulting in 1651 unique magnetic space groups (Shubnikov groups) [16]. Analogous to the crystallographic case, magnetic point group is obtained by retaining only the rotational, reflection and time reversal operations of magnetic space groups, while removing the translational elements.

To describe the arrangement of spins, it is convinient to express the spin configuration in reciprocal space. The Fourier transform of the spin operator can be expressed as

$$\mathbf{S}_{ij}(\mathbf{k}) = \frac{1}{N}\sum_{n} \mathbf{S}_{ij}(\mathbf{R}_n) e^{i\mathbf{k}\cdot\mathbf{R}_n}$$

where $\mathbf{S}_{ij}(\mathbf{R}_n)$ is the j^{th} cartesion component $(j = x, y, z)$ of the spin of the i^{th} atom in the n^{th} unit cell. $\mathbf{k}$ is the propagation vector which describes the periodicity of the magnetic structure.

In LiMPO$_4$, the propagation vector is reported to be $\mathbf{k} = (0, 0, 0)$, meaning that the crystallographic unit cell and magnetic unit cell are identical. There are 4 magnetic ions at the 4c Wyckoff positions in the unit cell [17, 18], with position vectors.

$$\begin{aligned} \mathbf{r}_1 &= (\tfrac{1}{4} + \epsilon,\ \tfrac{1}{4},\ 1 - \delta), & \mathbf{r}_2 &= (\tfrac{3}{4} + \epsilon,\ \tfrac{1}{4},\ \tfrac{1}{2} + \delta) \\ \mathbf{r}_3 &= (\tfrac{3}{4} - \epsilon,\ \tfrac{3}{4},\ \delta), & \mathbf{r}_4 &= (\tfrac{1}{4} - \epsilon,\ \tfrac{3}{4},\ \tfrac{1}{2} - \delta) \end{aligned} \tag{1.5}$$

where ϵ and δ are the displacements of the magnetic ions from the face-centered position. Each ion here has 3 independent spin components. The system therefore posses $4 \times 3 = 12$ degrees of freedom, corresponding to 12 components of $\mathbf{S}_{ij}(\mathbf{k})$ that spans the 12 dimensional vector space Σ. To describe how these spin components transform under symmetry operations in the magnetic space group G, the concept of a representation is introduced. All symmetry operations g in the group G, act as a linear operation on the magnetic vector space Σ. The set of all such linear operations on Σ forms a group denoted by $L(\Sigma)$. Here the representation of the group G is defined as a map Γ between the group G and $L(\Sigma)$;

$$\Gamma : G_{\mathbf{k}} \rightarrow L(\Sigma)$$

if Γ is a group homomorphism: i.e. for all $g_1, g_2 \in G_{\mathbf{k}}$,

$$\Gamma(g_1 g_2) = \Gamma(g_1)\Gamma(g_2).$$

Irreducible representations	Basis vectors	Magnetic space group
Γ_1	G_y	$Pnma$
Γ_2	C_x, A_z	$Pn'm'a'$
Γ_3	G_x, F_z	$Pn'm'a$
Γ_4	C_y	$Pnma'$
Γ_5	F_y	$Pn'ma'$
Γ_6	A_x, C_z	$Pnm'a$
Γ_7	F_x, G_z	$Pnm'a'$
Γ_8	A_y	$Pn'ma$

Table 1.3: Irreducible representations, corresponding basis vectors and magnetic space groups for $LiMPO_4$ with crystallographic space group $Pnma$.

Since the representation space Σ is 12-dimensional, each symmetry operation g is represented by a 12×12 matrix $\Gamma(g)$. The symmetry operations of the group G mix the spin components on different atomic sites. By forming suitable linear combination of such components, the representation can be reduced to independent parts, each acting on a subspace of Σ Thus a representaion Γ can be reduced by dividing the representation space Σ into subspaces spanned by new set of basis vectors. If the representation cannot be decomposed further into smaller invariant subspaces, it is called irreducible representaion (irrep). Physically, each irreducible representaion corresponds to a distinct symmetry allowed magnetic mode. Hence experimentally determined magnetic structures corresponds to one of these irreps or a linear combination of the irreps.

Irreducible representations in $LiMPO_4$ The detailed representaion analysis for $LiMPO_4$ is presented in [19]. The results relevant for this work are summarized below.

In $LiMPO_4$, the parent group Pnma with $k = 0$, gives rise to eight one-dimensional irreps. The representation subspace of these irreps are spanned by the basis vectors A, G , C and F :

$$\begin{aligned}
A_j &= S_{1j} - S_{2j} - S_{3j} + S_{4j}, \\
C_j &= S_{1j} + S_{2j} - S_{3j} - S_{4j}, \\
G_j &= S_{1j} - S_{2j} + S_{3j} - S_{4j}, \\
F_j &= S_{1j} + S_{2j} + S_{3j} + S_{4j}.
\end{aligned}$$

The basis vectors corresponding to each irreps are given in table 1.3. Here the basis vectors A,G and C corresponds to a antiferromagnetic arrangement of spins along the j axis where as F corresponds to a ferromagnetic arrangement of spins.

Together they describe all 12 possible arrangements of the spins within the unit cell.

1.3 Ferroic orders

Landau theory provides a description for a phase transition, where a spontaneous long range order occurs below a critical temperature (T_c). The free energy of the system can be expanded in even powers of the order parameter η as

$$F = F_0 + a(T)\eta^2 + b\eta^4 + c\eta^6 + \dots \tag{1.6}$$

Where $a(T) = \alpha(T - T_c)$. Above T_c, the free energy is minimized when $\eta = 0$, corresponding to disordered high-symmetry phase. Below T_c, the free energy minimum is attained with a finite η, corresponding to a lower symmetry ordered phase. The phase transition is said to be ferroic if it involves loss of one or more point-symmetry operations of the high symmetry phase. Such transitions are generally second order, indicating that the order parameter grows continuously below T_c. There are four primary ferroic orders: Ferromagnetism, ferroelasticity, ferroelectricity and ferrotoroidicity. Each of these involves the spontaneous appearance of a distinct order parameter below T_c, namely magnetization, spontaneous strain, electric polarization and torroidization respectively. They can be classified according to their symmetry behaviours under spatial inversion and time reversal as shown in table 1.4.

Ferroic order	**Order parameter**	**Spatial inversion**	**Time reversal**	**Conjugate field**
Ferromagnetism	Magnetization ($\mathbf{M}$)	Even	Odd	Magnetic field ($\mathbf{H}$)
Ferroelectricity	Polarization ($\mathbf{P}$)	Odd	Even	Electric field($\mathbf{E}$)
Ferroelasticity	Strain (ε)	Even	Even	Mechanical stress (σ)
Ferrotoroidicity	Toroidization ($\mathbf{T}$)	Odd	Odd	Curl of magnetic field ($\nabla \times \mathbf{H}$)

Table 1.4: Classification of primary ferroic orders based on their symmetry behaviour under spatial inversion and time reversal, and their corresponding conjugate fields.

A characteristic feature of ferroic materials is domain formation. Domains are energetically degenerate regions that have different orientation of order parameter and are separated by domain walls. These domains can be switched by the application of an appropriate vector or tensor field that transforms in the same way as the order parameter under spatial inversion and time reversal. For a ferroic order characterized by the order parameter η, in the presence of an appropriate external field $\mathbf{A}$, there is a contribution to free energy of the form $-\eta \cdot \mathbf{A}$. Therefore under the external field,the domain with the order parameter parallel to the field is energetically preferred. Microscopically, the domain switching under the application of external field occurs through the motion of domain walls rather than by a collective rotation of entire domain. However, this motion of domain walls can be hindered due to the pinning effects caused by the presence of defects or impurities. Any ferroic order that only needs a single conjugate field is called primary ferroic order. Ferroic material that require two fields to manipulate the direction of the order parameter is called secondary ferroic where the contribution to free energy is $-\eta_{\mathbf{12}} \cdot \mathbf{A_1 A_2}$. Where $\mathbf{A_1}$ and $\mathbf{A_2}$ represent two fields. Similar extension can be applied to define ferroics of higher order. [20, 21].

Multiferroic materials posses more than one ferroic order – most commonly ferromagnetic and ferroelectric – coexisting in a single phase as illustrated in figure 1.4 . In multiferroics, different ferroic orders may arise from independent mechanisms, often resulting in separate transition temperatures and weak coupling between them. Electric and magnetic orders in $BiFeO_3$ and $YMnO_3$ are examples for this type of ferroic materials [22, 23]. Conversely, if they are caused by the same microscopic mechanism they are strongly coupled and often have a single transition temperature as observed in $TbMnO_3$ and $Ni_3V_2O_8$ for example [24–26].

Magnetoelectric materials constitutes a class in which magnetic and electric degrees of freedoms are coupled. Here an applied magnetic field can produce a electric polarization ($\mathbf{P}$) and an applied electric field can produce a magnetization ($\mathbf{M}$). The free energy of such materials contains coupling terms of the form

$$F = F_0 - P_i E_i - M_i H_i - \alpha_{ij} E_i H_j + \dots \tag{1.7}$$

Where the Einstein summation over repeated indices i and j are implied. Minimizing free energy with respect to the fields E_i and H_i yields linear constitutive relations of the form

$$P_i = -\left(\frac{\partial F}{\partial E_i}\right)_H = \varepsilon_{ij} E_j + \alpha_{ij} H_j + \cdots ,$$

$$M_i = -\left(\frac{\partial F}{\partial H_i}\right)_E = \mu_{ij} H_j + \alpha_{ji} E_j + \cdots .$$

where the first term of the both equation $\varepsilon_{ij} E_j$ and $\mu_{ij} H_j$ represent the induced

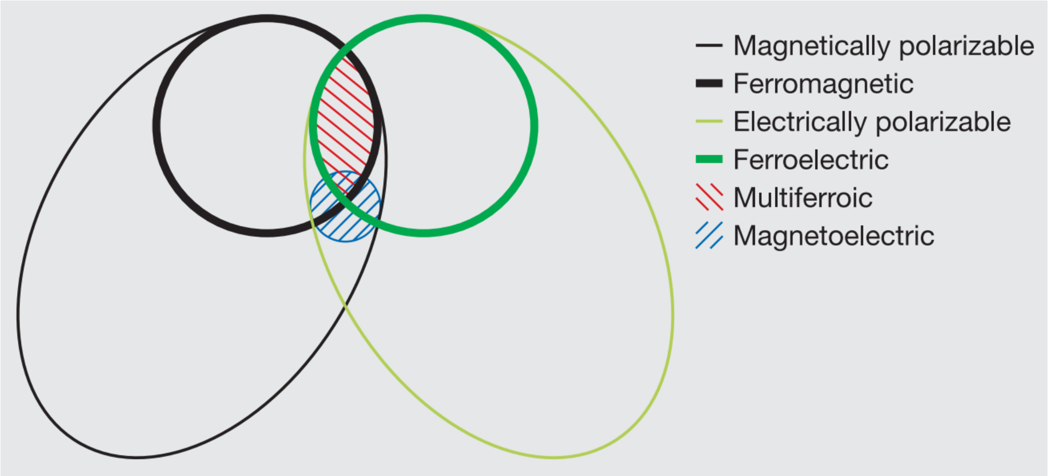

Figure 1.4: Schematic illustration of the relation between different categories of materials. The large black circle represents magnetically polarizable materials, and the thick black circle corresponds to ferromagnetic materials. Similarly thick green circle represents ferroelectric materials, while the light green ellipse encloses all electrically polarizable materials. The overlapped region shaded in red colour indicates multiferroic materials and the blue shaded area represents magnetoelectric matetials. As shown in the figure, magnetoelectric materials do not necessarily need to be ferromagnetic or ferroelectric. The figure taken from [27]

electric polarization due to applied electric field and induced magnetization due to the applied magnetic field respectively. The second term represents the linear magnetoelectric coupling [28].Where α_{ij} is the linear magnetoelectric tensor that couples ($\mathbf{P}$) and ($\mathbf{M}$). The magnetoelectric effect is only allowed in systems that break both time and space reversal symmetry. The symmetric part of α_{ij} satisfying $\alpha_{ij} = \alpha_{ji}$ represents the magnetoelectric response where applied magnetic field produces $\mathbf{P}$ and applied electric field produce $\mathbf{M}$. The presence of an antisymmetric part of α_{ij} satisfying the condition $\alpha_{ij} = -\alpha_{ji}$, indicates the toroidal contribution to magnetoelectric tensor. However the presence of antisymmetric component of α_{ij}, does not necessarily indicate the presence of a ferrotoroidal order [29, 30].

1.3.1 Ferrotoroidicity

Ferrotoroidal order, which is relevant to the present work, is discussed in this section following the framework presented in references [21, 28, 31].

Ferrotoroidicity is the fourth ferroic order which is expected from the categorization of the three well-established primary ferroic orders based on their symmetry

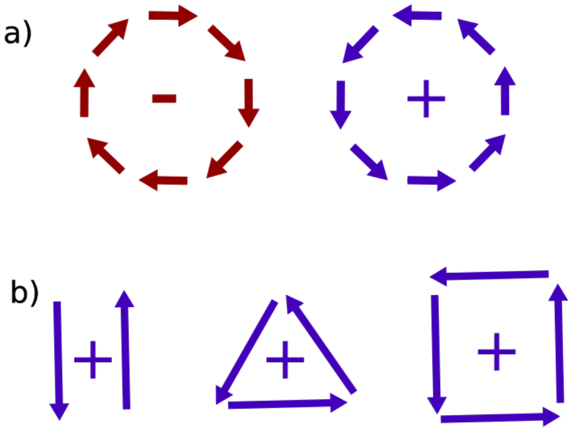

Figure 1.5: Schematic representation of spin arrangements giving rise to toroidal moments. a) Clockwise (red) and anti clockwise (blue) head-to-tail arrangement of spins produce toroidal moments of opposite directions. The minus sign indicate the toroidal moment pointing into the plane, while the plus sign indicate the toroidal moment pointing out of the plane. b) Examples of opposing arrangement of spins that can give rise to toroidal moment in realistic magnetic systems.Figure adapted from reference [28]

behaviours. As illustrated in table 1.4, ferrotoroidicity breaks both time reversal and space inversion. It is defined as a spontaneous long-range order of toroidal moment. A toroidal moment can arise from head-to-tail arrangement of spins or from orbital currents. If we consider the spin-only contribution to the toroidal order, a head-to-tail arrangement of spins is often realized in real systems by two or more spins opposing each other as illustrated in figure 1.5. Consequently, ferrorotoroidal systems are often realized by antiferromagnetic materials sometimes exhibiting weak ferromagnetic component due to slight spin canting. From this, ferrotoroidic order can be visualized as an array of spin vortices of the size of one unit cell. The detailed derivation of toroidal moment $\mathbf{t}$ from the multipole expansion of a vector field is presented in [21, 31]. It can be expressed as

$$\mathbf{t} = \frac{1}{2}\sum_i \mathbf{r}_i \times \mathbf{m}_i, \tag{1.8}$$

where $\mathbf{r}_i$ is defined as the position vector of individual magnetic moments $\mathbf{m}_i$. In analogy with magnetization, which is defined as the density of magnetic moments, the toroidization $\mathbf{T}$ is defined as the toroidal moment per unit cell volume $\mathbf{T} = \mathbf{t}/\Omega$.

For systems with non-zero net magnetization such as canted antiferromagnetic strucutres in which the deviation from perfect antiparallel alignment may give rise to an uncompensated component, the magnetic moment distribution can be seperated into a fully compensated part, with zero net magnetization, and an uncompensated part corresponding to the total magnetization of the system. The contribution to the toroidal moment from the compensated part is origin independent, whereas that from the uncompensated part is not. This follows from the fact that toroidal moment is defined as a cross product of r_i and m_i. The shift of origin by a vector a produces a change in position vectors by $r_i \rightarrow r_i + a$. For an uncompensated structure with a net magnetization $\Sigma_i m_i = m$, this change produces an additional term in toroidal moment proportional to the magnetization $\frac{1}{2} a \times m$ making it origin dependent. The uncompensated part can contribute to the toroidal moment only when the magnetic moments are positioned in a non-centrosymmetric manner, since the time reversal is automatically broken due to the presence of a non-zero net magnetization $\mathbf{m}$. As will be discussed later, only changes in toroidization are physically meaningful. Therefore, in the case of an origin dependent toroidal moment arising from the uncompensated part of the magnetic distribution, the change in toroidal moment is well-defined, provided that the choice of origin remains fixed between the two configurations considered.

In a bulk periodic system with infinite periodic arrangement of spins, translation of a magnetic moment $\mathbf{m_i}$ by a lattice vector $\mathbf{R_n}$ leaves the system invariant, but changes the toroidization by a discrete increment,

$$\Delta \mathbf{T}_{n,i} = \frac{1}{2\Omega} \mathbf{R}_n \times \mathbf{m}_i, \tag{1.9}$$

here Ω is the unit cell volume. This leads to a multivaluedness of toroidization analogous to multivaluedness of polarization in ferroelectric materials. Hence the absolute value of toroidization is not physically meaningful. In analogy to the treatment of polarization, the difference in toroidization between different domain states of ferrotoroidic phase or between a ferrotoroidic state and its non-ferrotoroidic counterpart where both spatial and/or time reversal symmetries are conserved, is uniquely defined and represents a physically observable quantity.

Since ferrotoroidic order is a primary ferroic order, it also exhibits the characteristics common to all ferroic states, such as domain formation and domain switching. Hence a ferrotoroidic system has a term in the free energy $F = -\mathbf{T} \cdot \mathbf{G}$ where G is the conjugate field that couples to the order parameter **T** and facilitates domain switching. Because free energy must remain invariant under all symmetry operations of the system, the conjugate filed **G** must transform in the same way as **T**, and break both time reversal and space inversion symmetry. A magnetic field with non-zero curl, $\nabla \times \mathbf{H}$, satisfies these symmetry requirements. The most practical way to create such a conjugate field is the application of perpendicular electric and magnetic field ($\mathbf{E} \times \mathbf{H}$) where the order parameter couples to the cross product of these two fields.

Toroidal order is one of the most intriguing ferroic states, offering numerous opportunities to explore its functionalities in next generation spintronics devices. It provides a unique possibility for selective domain population, since a toroidal field only affects toroidal domains and the non-toroidal domain structures remain invariant. Hence there is an intersting possibility to manipulate domains with different space-time symmetry behaviours independently, in ferrotoroidic materials. In addition to this, due to the inherent magnetoelectric effect associated with the ferrotoroidic order, it is possible to electrically control magnetic degree of freedom, making it more appealing for applications such as data storage [21,31].

2

Overview on lithium orthophosphates

This chapter summarizes the established facts about the family of compounds lithium orthophosphates, $LiMPO_4$, where M denotes the transition metals Fe, Co, Ni and Mn. The crystal structures , magnetic structures and the relevant magnetoelectric and ferrotoroidic properties already reported in the literature for these compounds are described briefly with emphasis on aspects relavant for this work. In addition, the theoretical and experimental studies on mixed-anisotropy antiferromagnets are discussed.

2.0.1 Crystal structure and magnetic structure of $LiMPO_4$

The compounds $LiMPO_4$ are isostructural and crystallize in the olivine type orthorhombic crystal structure with the space group Pnma (space group no. 62). The unit cell contains four transition metal ions occupying the 4c Wyckoff positions with position vectors $\mathbf{r_1}, \mathbf{r_2}, \mathbf{r_3}, \mathbf{r_4}$, as defined in section 1.2.1. Each transition metal ion is surrounded by six oxygen atoms forming a distorted MO_6 octahedron. These octahedra shares corners to form a network interconnected through LiO_6 octahedra and PO_4 tetrahedra as illustrated in figure 2.1. The lattice paramters at room temperature reported for all stoichiometric compounds are summarized in table 2.1.
The four magnetic ions in the unit cell give rise to three possible AFM and one FM spin arrangement as described in chapter1. The three AFM arrangements are denoted by A, G and C , while the FM spin arrangement is denoted by F with subscripts denoting the spin direction (x, y, z). The magnetic interaction between the ions is governed predominantly by super-exchange pathways. The nearest neighbour couplings occur through Metal-Oxygen-Metal (MOM) pathways, while longer range interactions are mediated by Metal-Oxygen-Phosphorous-Oxygen-Metal (MOPOM)

M	a (Å)	b (Å)	c (Å)	T_N (K)	**Easy axis**
$LiMnPO_4$	10.4367(3)	6.0959(2)	4.7417(1)	34.9	$\mathbf{S} \parallel \mathbf{a}$
$LiFePO_4$	10.3273(1)	6.0071(3)	4.6917(2)	50.0	$\mathbf{S} \parallel \mathbf{b}$
$LiCoPO_4$	10.2001(6)	5.9199(4)	4.6899(2)	21.6	$\mathbf{S} \parallel \mathbf{b}$
$LiNiPO_4$	10.0317(1)	5.8539(1)	4.6768(1)	20.7	$\mathbf{S} \parallel \mathbf{c}$

Table 2.1: Reported lattice parameters, Néel temperatures, and magnetic easy-axis directions for $LiMPO_4$ (M = Mn, Fe, Co, Ni), where the lattice parameters are taken from references [32–35]. The ordering temperatures are taken from the references [17, 18, 36]

pathways through PO_4 tetrahedra as illustrated in figure 2.2. The interplay between these interactions and single ion anisotropy determines the magnetic structure and magnetic phase diagram for each compound in the $LiMPO_4$ series.

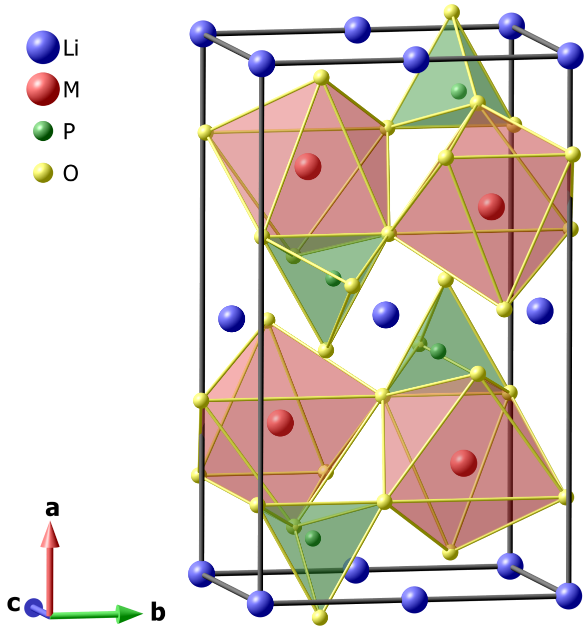

Figure 2.1: Crystallographic unit cell of LiMPO$_4$. MO_6 octahedra and PO_4 tetrahedra are shaded in red and green, respectively. For clarity, LiO_6 octahedra are not shown.

The following section provides a brief overview of the experimentally determined magnetic structures and properties of individual stoichiometric compounds in the series $LiMPO_4$, that are discussed in this work.

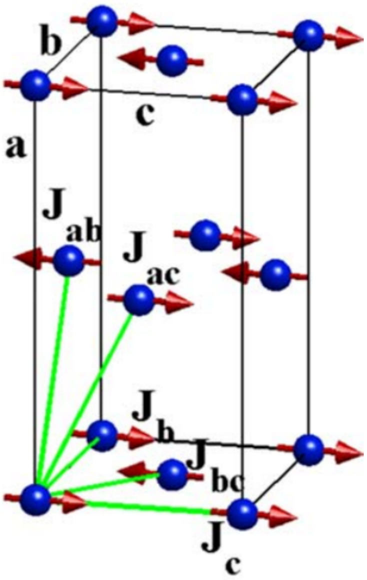

Figure 2.2: Superexchange interactions in LiNiPO$_4$. Within the *bc*-plane Ni spins are coupled by nearest neighbour interaction J_{bc} and two next nearest neighbour interactions J_b and J_c. The coupling between the *bc*-plane is given by the nearest neighbour interactions J_{ab} and J_{ac}.Figure taken from [37].

2.0.2 LiFePO$_4$

LiFePO$_4$ orders magnetically at $T_N \approx$50 K, with a commensurate antiferromagnetic structure predominantly described by C_y basis vector (Γ_4 irreducible representation) corresponding to an AFM state with moments along the b axis [18]. In addition to the major magnetic moment component along the b-axis, small finite components are observed along both a and c axes ($mu_a = 0.067\mu_B$, $\mu_c = 0.063\mu_B$). These correspond to a rotation towards a axis described by C_x and a spin canting along c axis described by A_z. The total deviation of the magnetic moment from the b axis of 1.3° is observed [38]. The magnetic moment of $\mu \approx 4.2\mu_B$ is reported which is slightly higher than the spin-only moment expected for high-spin Fe^{2+} ($3d^6, S = 2$), indicating a small orbital contribution [10]. The magnetic structure can therefore be represented by a combination of irreducible representations $\Gamma_2 + \Gamma_4$ which is not allowed under the symmetry constraints of *Pnma* group and suggests lowering of the magnetic symmetry .

LiFePO$_4$ exhibits a linear magnetoelectric effect with non-zero α_{xy} and α_{yx} tensor elements, consistent with the magnetic symmetry described by Γ_4 irrep and magnetic point group mmm'. Recent studies report the existence of an additional diagonal tensor element α_{xx} , consistent with the lowering of symmetry in the mixed-irreps magnetic state. The corresponding magnetic point group is proposed to be $2_z/m'_z$ [39].

The inelastic neutron scattering studies on this compound, reports the b axis as the easy axis and c axis as the hard axis. This follows from fitting the magnon dispersion curves to a spin-wave model and determining the single-ion anisotropy parameters. The extracted anisotropy parameters are consistent with the energy minimum for spins along b-axis. The reported parameters are summarized in table 2.2. The spin dimensionality lies between the ising and XY-type limits, with comparitively small single-ion anisotropy compared to other members in the LiMPO$_4$ series.

Inelastic studies reports strong exchange interactions and mild frustration due to competing interaction in the bc-plane [38] where all interactions in the bc-plane (figure 2.2) favour antiferromagnetic alignment. A spin-flop transition is observed at $H \approx 31T$, for magnetic field along b-axis. Above this field, the spins reorient towards a-axis, while remaining commensurate with C_y and A_z as minor magnetic moment components. In this phase, the magnetoelectric tensor α_{xy} is suppressed and α_{yy} is activated [40] which is expected for $Pnma$ structures.

	LiMnPO$_4$	**LiFePO$_4$**	**LiCoPO$_4$**	**LiNiPO$_4$**
J_{bc}	0.48(5)	0.77(7)	–	1.04(6)
J_b	0.200(4)	0.30(6)	–	0.670(9)
J_c	0.076(4)	0.14(4)	–	-0.05(6)
J_{ac}	0.062(3)	0.05(2)	–	-0.11(3)
J_{ab}	0.036(2)	0.14(2)	–	0.30(6)
D_a	0	0.62(12)	–	0.339(2)
D_b	0.009(1)	0	–	1.82(3)
D_c	0.007(1)	1.56(3)	–	0

Table 2.2: Exchange constants and single-ion anisotropy parameters for LiMPO$_4$ (M = Mn, Fe, Co, Ni), compiled from inelastic neutron scattering studies [36–38],Values are reported with the precision given in the source literature. Reliable inelastic studies on LiCoPO$_4$ is unavailable.

2.0.3 LiCoPO$_4$

LiCoPO$_4$ orders magnetically below $T_N \approx 21.6K$ with a commensurate antiferromagnetic structure described by C_y with spins predominantly along b-axis [17]. The ordered magnetic moment of $3.6\mu_B$ is reported for $LiCoPO_4$, which indicate a partially unquenched orbital angular momentum contribution to the magnetic moment (high-spin configuration of Co^{2+} ,$3d^7, S = 3/2$) [41]. In addition to the major component along b-axis represented by Γ_4, a rotation of magnetic moment away from b-axis of 4.6° was observed by Vaknin et al. lowering the symmetry and resulting in a magnetic point group of $2'_x/m_x$ [42]. Other than that a weak ferromagnetic component was observed further lowering the magnetic point group to $2'_x$ [43]. However, a recent study reports a spin canting of 7° described by A_z which suggest the that magnetic point group is $2'_z/m_z$, which combined with the ferromagnetic component results in a m'_z magnetic point group [44].

The magnetic phase diagram of $LiCoPO_4$ has been mapped for magnetic fields along the b-axis and along the a-axis. For $H \parallel b$, the saturation field at 1.7 K was determined to be 28.3 T. Two distinct phase transitions at $\sim$ 12 T and $\sim$ 22 T were first reported by Kharchenko et al. based on the magnetization measurements [45]. Subsequent neutron diffraction studies by Fogh *et al.* established a detailed magnetic phase diagram for magnetic fields up to 25.9 T along the b-axis. A series of transitions at 11.9, 20.5 and 21.0 T were reported.

Above 11.9 T, phase transition to an incommensurate phase with propagation vector $\mathbf{Q} = (0, \frac{1}{3}, 0)$ is reported, corresponding to a magnetized elliptic cycloid with spins in the bc-plane and major axis aligned along b axis. In the field interval 20.5 - 21.0 T, the propagation vector remains the same $\mathbf{Q} = (0, \frac{1}{3}, 0)$ but the spin orientation changes. Above 21 T, $LiCoPO_4$ becomes commensurate again, exhibiting a ferromagnetic component along b-axis and an antiferromagnetic component along c-axis [46].

$LiCoPO_4$ exhibits the strongest magnetoelectric effect among the $LiMPO_4$ series. In $LiCoPO_4$, the non-zero components of the magnetoelectric tensor observed are α_{xy} and α_{yx} which is the same non-zero elements allowed in $LiFePO_4$. This is expected because the form of magnetoelectric tensor is determined by the symmetry of magnetic structure and both compounds exhibit magnetic structure with spins along b-axis. However the magnetoelectric effect disappears in the incommensurate phase above 11.9T and re-emerges above 21 T, in the commensurate phase, where the tensor elements α_{xy} and α_{yx} are active but their magnitudes are 5 times smaller than in the low-field phase below 12 T [47, 48]. However from the symmetry considerations for a predominantly C_z type magnetic structure, the expected non-zero

elements are α_{xz} and α_{zx} .
For $H \parallel a$, the DM interaction couples the induced ferromagnetic component along a to an additional spin canting component of G_z [44]. An upper limit of DM interaction strength was estimated to be comparable to the single-ion anisotropy constant along the c-axis.

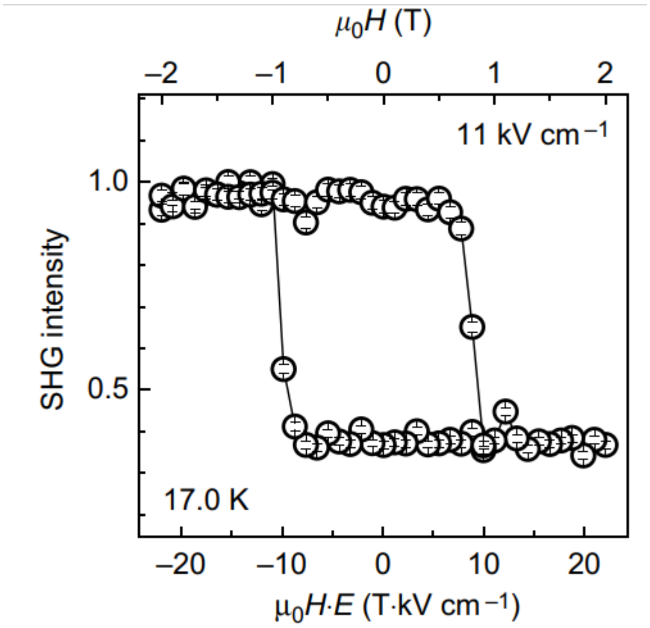

Figure 2.3: Hysteretic poling of toroidal moment in LiCoPO$_4$ achieved by the application of conjugate field. Figure taken from reference [49]

From symmetry considerations, LiCoPO$_4$ is a potential host of the ferrotoroidic order. In the space group $Pnma'$ (corresponding to the magnetic moment aligned along b-axis), the symmetry operation include combined space and time inversion but not the pure time and space inversion individually. The symmetry group also constrains the allowed ferrotoroidal moment to be oriented along the c-axis. However, the rotation of magnetic moment within the bc-plane lowers the symmetry to $2'/m$, allowing an additional toroidal moment component to exist along b-axis. For a compensated antiferromagnetic structure of LiCoPO$_4$ (ignoring the suggested ferromagnetic component), the toroidal moment takes the form

$$\mathbf{t} = 2\mu\epsilon a \left(\cos\theta\,\hat{\mathbf{z}} + \sin\theta\,\hat{\mathbf{y}}\right) \tag{2.1}$$

where μ is the ordered magnetic moment, ϵ is the small displacement of the magnetic ions from high-symmetry positions along the crystallographic a axis as indicated in equation 1.5, and θ is the angle between the magnetic moment and the b-axis [31]. The existence of ferrotoroidic domains in $LiCoPO_4$ was confirmed by Van Aken et al. using optical second harmonic generation. They directly observed ferrotoroidal domains that are independent of the antiferromagnetic domains, thereby demonstrating $LiCoPO_4$ to be a ferrotoroidic material [50]. In a followup study by Zimmermann et al [49], hysteretic poling of toroidal moment was demonstrated as indicated in the figure 2.3. This confirms the switchability of toroidal domains- one of the characteristic behaviour of ferroic orders-and verifies the status of ferrotoroidal order as the fourth ferroic order.

2.0.4 $LiNiPO_4$

Unlike $LiCoPO_4$ and LiFePO4, LiNiPO4 exhibits an incommensurate magnetic phase in a narrow temperature range below $T_{\mathrm{IC}} = 21.7$ K. This incommensurate magnetic structure is characterized by a propagation vector $\mathbf{q} = (0, q, 0)$ with $0.07 < q < 0.155$. Below $T_N = 20.8K$, $LiNiPO_4$ transitions from the incommensurate magnetic structure to a commensurate antiferromagnetic structure. The commensurate phase is described by the C_z basis vector with spins primarily aligned along c-axis [51, 52]. A minor magnetic component of A_x symmetry has also been reported in the zero-field structure, corresponding to a non-collinear spin rotation of about $\sim 8°$ towards a-axis.
The magnetic phase diagram of $LiNiPO_4$, has been mapped for magnetic fields applied along the a,b and c axes. No phase transitions were observed for magnetic fields along a and $b$axes. However, for the magnetic field along c-axis the compound undergoes a series of field-induced phase transitions as illustrated in fig 2.4 [53]. For magnetic field below 12 T, $LiNiPO_4$ remains in the commensurate antiferromagnetic phase, which exhibit linear magnetolectric effect with active tensor components α_{xz} and α_{zx} [54].

For magnetic fields above 12 T, the system undergoes a phase transition into a an incommensurate spiral phase with propagation vector along b and spins within the ac-plane [51]. Upon further increasing the magnetic field, the modulation gradually locks into a spiral structure with $q = \frac{1}{5}$. In the field interval between 19 - 21 T , $LiNiPO_4$ becomes commensurate again, with the spins rotating away from c axis towards the a-axis. This phase exhibits a magnetoelectric effect, whereas the

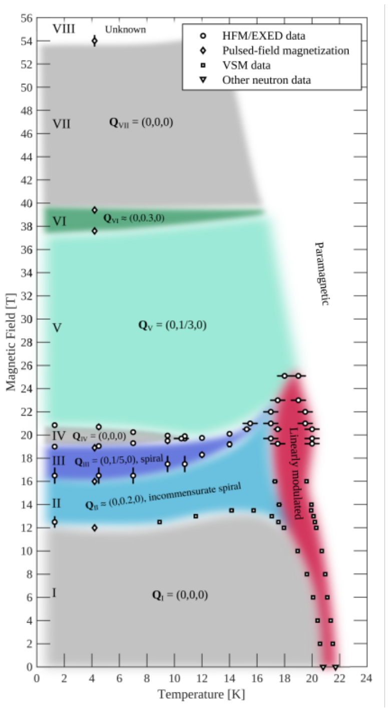

Figure 2.4: Magnetic field vs. temperature phase diagram for $LiNiPO_4$ reported by Fogh *et al* [53], illustrating the field induced phase transitions for applied magnetic field along *c*-axis.

incommensurate phases are non-magnetoelectric [55]. Above 21 T, a new incommensurate phase with propagation vector $(0, \frac{1}{3}, 0)$ develops which persists upto 37.6 T. In the narrow field interval of 37.6- 39.4 T, a similar incommensurate structure with a longer magnetic period is observed. Beyond 39.4 T, another commensurate phase is established which exhibits quadratic magnetoelectric response [53] .
Inelastic neutron scattering studies on $LiNiPO_4$, revealed a strong antiferromagnetic next-nearest-neighbour interaction along *b*-direction which competes with the nearest-neighbour antiferromagnetic coupling, leading to mild frustration in the system. The competetion between these exchange interactions places $LiNiPO_4$ on the verge of instability between commensurate and incommensurate structures, thereby explaining the emergence of the incommensurate phase below T_{IC}. The additional single-ion anisotropy energy gained in the commensurate phase at slightly lower temperature below T_N, stabilizes the commensurate ground state against the frustrated incommensurate structure [37]. The high temperature incommensurate phase is a spin density wave where the magnitude of the spins modulated.

2.0.5 Mixed anisotropy magnets

The stoichiometric compounds of the family $\mathrm{LiMPO_4}$ described in the preceeding subsections exhibit different single-ion anisotropy energies and corresponding magnetic easy-axis directions. When ions with different anisotropies are combined in solid solutions such as $\mathrm{LiNi_{1-x}Fe_xPO_4}$ or $\mathrm{LiCo_{1-x}Ni_xPO_4}$, the competition between their single-ion anisotropies give rise to complex magnetic phase behaviours characteristic of mixed-anisotropy magnets.

The theoretical framework for mixed-anisotropy magnets with orthogonal easy axes was developed from the renormalization-group methods. In this approach, the quartic coupling term that quantifies the coupling between the two order parameters determines the nature of the multicritical point. Depending on the sign and magnitude of this coupling, the two order parameters may either exclude each other, producing a bicritical point with a first-order transition seperating the two ordered phases, or coexist to form a mixed phase where second order transitions seperates the three possible phases producing a tetracritical point [56, 57]. The same physics can be captured through Landau free energy expansion for two order parameters ϕ_1 and ϕ_2,

$$G = G_0 + \frac{1}{2}\left(a_1\phi_1^2 + a_2\phi_2^2\right) + \frac{1}{4}\left(b_{11}\phi_1^4 + 2b_{12}\phi_1^2\phi_2^2 + b_{22}\phi_2^4\right),$$

For the phase transitions determined by this free enrgy to be stable, the following conditions must be satisfied.

$$b_{11} > 0, \qquad b_{22} > 0 \quad \text{and}$$

$$b_{12} > -(b_{11}b_{22})^{1/2}.$$

Taking into account these constraints and minimizing G with respect to ϕ_1 and ϕ_2, yields three solutions in addition to the trivial solution $\phi_1 = \phi_2 = 0$, indicating disordered state,

(I) Pure ϕ_1 phase: stable when $a_1 < 0$

$$\phi_1^2 = -\frac{a_1}{b_{11}}, \qquad \phi_2 = 0.$$

(II) Pure ϕ_2 phase: stable when $a_2 < 0$

$$\phi_2^2 = -\frac{a_2}{b_{22}}, \qquad \phi_1 = 0.$$

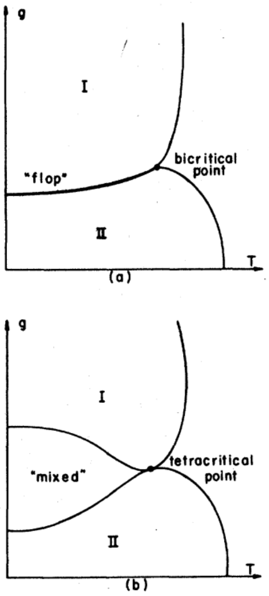

Figure 2.5: Phase diagram of a mixed anisotropy antiferromagnet showing the case where a mixed phase called oblique antiferromagnetic phase is present and the case where a mixed phase is absent. Figure taken from [57]

(III) Mixed phase:

$$\phi_1^2 = \frac{-b_{22}a_1 + b_{12}a_2}{b_{11}b_{22} - b_{12}^2}, \qquad \phi_2^2 = \frac{-b_{11}a_2 + b_{12}a_1}{b_{11}b_{22} - b_{12}^2}.$$

A mixed phase exists and is stable only if $b_{11}b_{22} > b_{12}^2$. Therefore, a tetracritical point is present in the phase diagram if this condition is satisfied [58]. However, if the condition is not satisfied, then the phase diagram exhibits a bicritical point as indicated in figure 2.5.

When the critical fluctuation of the order parameter become strong near multicritical region, the mean-field predicted fixed point is destabilized and the second order transition becomes fluctuation induced first order. In the case of a real mixed system, where local exchange and anisotropy parameters vary from site to site, this first-order transition is further broadened into a smeared crossover between the different phases [59].
Matsubara *et al.* developed a mean-field model for a mixture of antiferromagnets with different orthogonal uniaxial anisotropy, which predicted the existence of an oblique antiferromagnetic phase arising from the competition between anisotropy and exchange energies. In the oblique phase the magnetization is rotated away from

the easy axes of both parent compounds, forming a finite angle within the plane defined by the two orthogonal easy directions. This oblique phase is bounded by two second-order transitions to the two collinear phases, which meet at a tetracritical point in the temperature-composition phase diagram [60]. This framework was later extended to include the orthorhombic antiferromagnetic systems. This lead to the prediction that depending on the relative anisotropy strengths, the shared intermediate anisotropy axis of the parent compounds can become the effective easy axis of the system within the oblique antiferromagnetic phase [61]. For example for the mixture of two ions, A with x, y,z axes as easy, intermediate and hard axes respectively and B with z, y,x axes as easy, intermediate and hard axes , an oblique antiferromagnetic phase with spins along y-axis can be stabilized based on the relative anisotropy strengths.

The predicted appearance of an oblique phase and multicritical behaviour seperating regions of distinct spin orientation has been experimentally verified in a wide range of magnets where ions with orthogonal anisotropies are randomly mixed.

The quasi-two dimensional compound $K_2Mn_{1-x}Fe_xF_4$ provides a clear experimental realization of the theoretical $x - T$ phase diagram. Mn^{2+} ions are nearly isotropic Heisenberg like spin systems, where as Fe^{2+} ions possess strong planar (XY-type) anisotropy. The competition between these anisotropies gives rise to two successive transitions corresponding to Mn-type and Fe-type ordering, seperated by an oblique antiferromagnetic phase and a tetracritical point where the four second-order transition lines meet [62, 63].

The hydrated chloride $Fe_{1-x}Co_xCl_2.2H_2O$ also exhibits a phase-diagram consistent with theoretical predictions. Here both parent compounds are uniaxial ising antiferromagnets but with orthogonal easy directions. Two distinct second-order transitions and a well defined mixed phase and a tetracritical point is observed in this series of compounds [64]. In contrast, the anhydrous $Fe_{1-x}Co_xCl_2$ exhibits significant deviations from the theoretically proposed phase-diagrams. In this system, the Fe^{2+} moments exhibit ising-like behaviour and align along c-axis and Co^{2+} moments show XY-type anisotropy in the ab plane. Although a mixed phase and a tetracritical points are observed, the transition lines do not cross each other smoothly. There is a change in the slopes of the transition lines near the tetracritial point and the lower transitions are broadened instead of the predicted sharp second-order transitions. These deviations are attributed to the off-diagonal coupling terms in the Hamiltonian excluded in theory. These terms may have different origins, such as anisotropic exchange, dipolar interactions and magnetostriction effects. While such

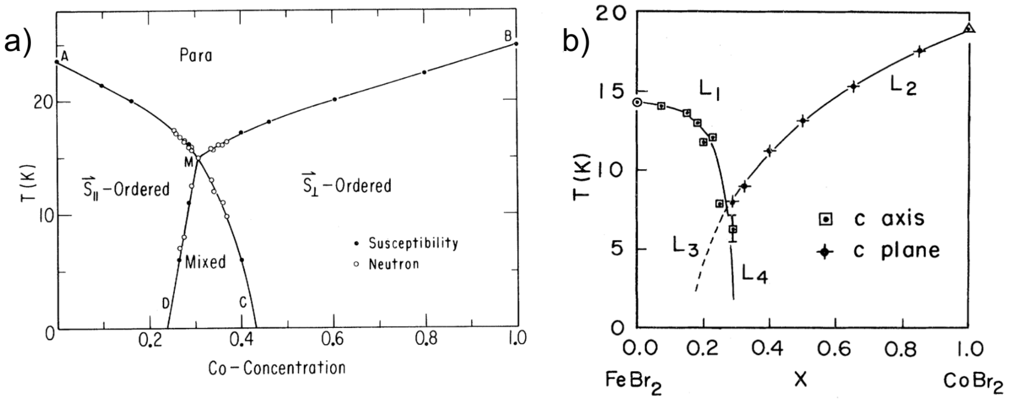

Figure 2.6: a) Phase diagram of $Fe_{1-x}Co_xCl_2$ [66]. b) Phase diagram for $Fe_{1-x}Co_xBr_2$ [67].

terms average to zero macroscopically, the local variations give rise to a site random magnetic field, which smear the phase boundaries [65, 66].

The bromide analogue $Fe_{1-x}Co_xBr_2$ exhibits even stronger suppression of the lower transition. Here Fe^{2+} ions have an ising type anisotropy along *c* axis and Co^{2+} ions have a XY-type anisotropy in the *ab*-plane. However, only one lower transition corresponding to the ising-like order is observed while the lower transition corresponding to XY-type order disappears entirely. The mixed phase region is either extremely narrow or replaced by a continous rotation of the spins [67] .
These experimental observations of rich and tunable magnetic phase diagrams of mixed-anisotropy magnets provide an essential framework for this thesis as it explores multiple such systems.

3

Neutron scattering theory

This thesis relies on X-ray and neutron scattering to probe the nuclear and magnetic structure of the studied compounds with a focus on elastic (diffraction) measurements. The theoretical concepts used in this work is briefly presented here detailed account of which can be found in references [3, 68–71] and is used without further reference through out the chapter.

3.1 Basic properties of neutrons

Neutrons are electrically neutral particles that carry a finite magnetic moment with their de Broglie wavelength in the angstrom range.

Unlike X-rays that interact with the electron cloud of an atom, because of their electrical neutrality neutrons interact only weakly with matter providing large penetration depth making it suitable for bulk measurements. The neutrons interact directly with the nuclei of the matter through strong nuclear interaction therefore providing excellent sensitivity to the isotopes and atoms with close atomic numbers. Since their de Broglie wavelength is comparable to the inter atomic distances in typical experimental conditions, neutrons provide ideal tool to probe crystal lattices.

More importantly for this thesis, the intrinsic spin of the neutorn give rise to a magnetic moment which can interact directly with the magnetic moment of the unpaired electrons in a magnetic material through dipole interaction. This makes neutrons an ideal direct probe to determine the magnetic structure.

For the scattering experiments neutrons are produced in two ways

- **Nuclear reactors:** Neutrons are produced through the fission of a heavy

mass, m_n	1.675×10^{-27} kg
charge	0
spin, s_n	$\frac{1}{2}$
magnetic moment, μ_n	$-1.913\,\mu_N = -0.0010\,\mu_B$
mean lifetime, τ_n	880 s

Table 3.1: Basic properties of the neutron. Table adapted from reference [68]

nuclei such as $^{235}_{92}$U in a self sustaining chain reaction. The heavy nuclei splits into lighter nuclei with the release of, on average 2.5 neutrons per fission event. The energy of a neutron produced through such a fission reaction is $\approx$ 2MeV which is then cooled down to the desired wavelength for scattering experiments by using moderators of different temperatures.

- **Spallation sources:** In spallation sources, heavy nuclei (tungsten, mercury, lead) are bombarded with high energy protons. The excited heavy nuclei decays by emitting $\approx$ 30 neutrons per incident proton. Similar to the nuclear reactors, moderators are used to tailor the neutron energies for scattering experiments

All the work presented in this thesis was carried out at the nuclaer reactor facility Institut Laue Langevin at Grenoble.

3.2 Scattering cross section

In a typical scattering geometry the incident neutron beam is characterized by the wave vector $\mathbf{k_i}$ and energy E_i. After interacting with the sample, neutron is scattered to a final state with wave vector $\mathbf{k_f}$ and final energy E_f. The momentum transfer during the scattering process is defined as

$$\mathbf{Q} = \mathbf{k_i} - \mathbf{k_f}$$

where the $\mathbf{Q}$ is known as scattering vector and is respresented by the scattering triangle presented in figure 3.1. The angle 2θ represents the scattering angle which is two times the Bragg reflection angle defined in section 3.3 . The energy transfer during the scattering process is defiend as

$$\hbar\omega = E_i - E_f$$

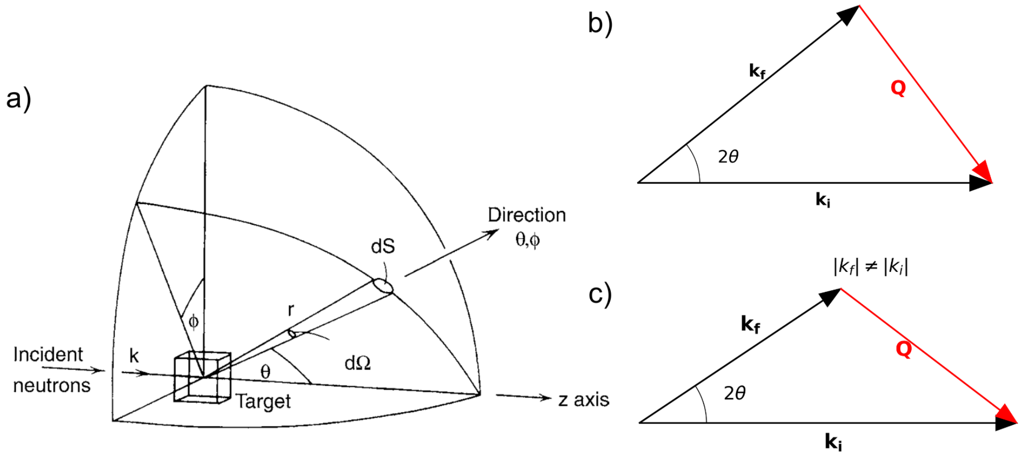

Figure 3.1: a) Geometry of a neutron scattering experiment. Figure taken from [72] b) Scattering triangle for elastic scattering where $|k_i| = |k_f|$ c) Scattering triangle for inelastic scattering where $|k_i| \neq |k_f|$

Elastic scattering corresponds to the case where no energy exchange takes place between the sample and neutron ($\hbar\omega = 0$) where $|k_f| = |k_i|$. Elastic scattering (diffraction) allows the structural study of materials. All works presented in this thesis utilizes neutron diffraction. In inelastic scattering a non-zero energy transfer takes place between the sample and the neutrons and such inelastic scattering experiments allows to determine the dynamic properties of the material.

In a typical scattering geometry defined above, the concept of scattering cross sections allows to connect the underlying arrangement of atoms and magnetic moments to the absolute intensity which is the number of counts per second recorded at the detector. The total scattering cross section is defined as the total number of scattered neutrons per unit time divided by the incident neutron flux (Φ_0). This measures the probability of neutrons being scattered from the target irrespective of direction and energy. Usually in an experiment, the interest is to measure scattered neutrons in a particular direction and within a particular energy interval. For this we define a partial differential cross section which is defined as

$$\frac{\mathrm{d}^2\sigma}{\mathrm{d}\Omega\,\mathrm{d}E_f} = \frac{\begin{array}{c}\text{number of neutrons scattered per second}\\ \text{into solid angle } \mathrm{d}\Omega \text{ about a given direction}\\ \text{with final energy between } E_f \text{ and } E_f + \mathrm{d}E_f\end{array}}{\Phi_0\,\mathrm{d}\Omega\,\mathrm{d}E_f}$$

Under the Born approximation, where the neutron only interact weakly with the sample and the neutron is assumed to scatter only once from the sample, the partial differential cross section can be written in its general form as

$$\frac{\mathrm{d}^2\sigma}{\mathrm{d}\Omega\,\mathrm{d}E_f} = \frac{k_f}{k_i}\left(\frac{m_n}{2\pi\hbar^2}\right)^2 \sum_{\lambda_i} p_{\lambda_i} \sum_{\lambda_f} \left|\langle \sigma_f \lambda_f \,|\, V(\mathbf{Q}) \,|\, \sigma_i \lambda_i \rangle\right|^2 \delta\big(E_{\lambda_f} - E_{\lambda_i} - \hbar\omega\big)$$

Here the interaction matrix element $\left|\langle \sigma_f \lambda_f \,|\, V(\mathbf{Q}) \,|\, \sigma_i \lambda_i \rangle\right|^2$ denotes the coupling of neutron to the sample through the interaction potential $V(\mathbf{Q})$, which contains a nuclear part arising from the scattering from atomic nuclei and a magnetic part arising from the scattering from the interaction between neutron magnetic moment and the magnetic moment of the unpaired electrons. The dirac delta function $\delta\big(E_{\lambda_f} - E_{\lambda_i} - \hbar\omega\big)$ ensures the conservation of energy. In the elastic scattering process considered in this thesis $E_{\lambda_f} = E_{\lambda_i}$, with $\hbar\omega = 0$. The summation over λ_f represents the summation over all final states of the sample, while the summation over all initial states λ_i is performed by taking a thermal average weighted by the Boltzmann population.

3.3 Nuclear scattering

The interaction between neutron and atomic nuclei arises from strong nuclear interaction and is extremely short ranged. Therefore nuclei can be treated as point scatterers and the interaction potential corresponding to the nuclear part can be replaced with Fermi pseudo potential given by

$$V_N(\mathbf{r}) = \frac{2\pi\hbar^2}{m_n} \sum_j b_j\, \delta(\mathbf{r} - \mathbf{r}_j)\,,$$

where b_j is the scattering length of the nucleus and the $\mathbf{r}_j$ is the position of the nucleus inside the unit cell.

In the crystalline solids, neutrons are scattered from a periodic array of atomic nuclei giving rise to a distinct diffraction pattern. Inserting the Fermi pseudopotential into the equation for scattering cross section and taking into account the translational symmetry of the crystal lattice, the coherent elastic nuclear cross section can be written as,

$$\frac{d\sigma}{d\Omega} = N\,\frac{(2\pi)^3}{V}\, e^{-2W}\, |F_N(\mathbf{Q})|^2 \sum_G \delta(\mathbf{Q} - \mathbf{G})\,,$$

Here N is the number of unit cells and V is the unit cell volume. The e^{-2W} denotes the Debye-Waller factor which accounts for the thermal vibrations of atoms. In this equation $F_N(\mathbf{Q})$ is defined as the nuclear structure factor given by

$$F_N(\mathbf{Q}) = \sum_j b_j \, e^{i\,\mathbf{Q}\cdot\mathbf{r}_j}.$$

3.3.1 Diffraction condition

The delta function in the equation indicates the fact that the diffraction intensity is non-zero only when the momentum transfer is equal to the reciprocal lattice vector

$$\mathbf{Q} = \mathbf{G}$$

This is known as Laue condition. where the reciprocal lattice vector is defined as

$$\mathbf{G} = h\,\mathbf{a}^* + k\,\mathbf{b}^* + l\,\mathbf{c}^*.$$

Therefore Laue condition states that the non-zero intensity is achieved only for a discrete set of momentum transfer $\mathbf{Q}$.

While Laue condition describes diffraction in the reciprocal space, Bragg's law offers an equivalent description in real space. Considering a set of lattice planes seperated by a distance d_{hkl}, the Bragg's law states that constructive interference takes place only when the path difference between the two waves reflected from the two adjacent planes is equal to the integer multiple of the wavelength of the neutron wavelength expressed as

$$2d_{hkl} sin\theta = n\lambda$$

where n is an integer, λ is the wavelength of the neutron and θ is the Bragg angle, double of this angle represents scattering angle. This equivalence follows from the identity $\mathbf{G} = \frac{2\pi}{d_{hkl}}$ together with the elastic scattering constraint $\mathbf{Q} = 2ksin\theta$.

Ewald sphere construction

Ewald sphere is a geometrical construction that helps visualize and analyse the diffraction condition and is particularly useful for single-crystal experiments. In elastic scattering, $|k_i| = |k_f| = k = \frac{2\pi}{\lambda}$. Here Ewald sphere represent a sphere in the reciprocal space as represented in the figure 3.2. The point O represents the origin of the reciprocal space. The incident wave vector k_i is drawn starting at point A

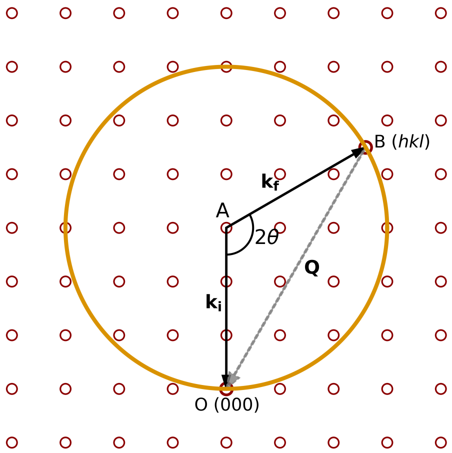

Figure 3.2: Ewald sphere represented in 2D as a circle. The points represents the reciprocal lattice points and the point O represent the origin. $\mathbf{k_i}$ and $\mathbf{k_f}$ represent incident and final wave vector respectively. $\mathbf{Q}$ is the scattering vector.

and terminating at the point O. The Ewald sphere is drawn with a radius of k with the centre on the point A. With this geometry, all the reciprocal lattice points that intersect the Ewald sphere satisfies the Laue condition and a Bragg peak can be observed if the detector is aligned in the direction of $\mathbf{k_f}$ as indicated in the figure for the case of point B. To access different reflections with a fixed neutron wavelength, the crystal can be rotated which represents the rotation of Ewald sphere with respect to the origin O.

Debye-Scherrer cone

Powder samples contain a large number of crystallites that are randomly oriented. Therefore, there is always a fraction of crystallites oriented at the correct angle to satisfy the Bragg's law for any set of lattice planes (hkl). As aresult the diffracted beam is produced along the surface of a cone with opening angle 2θ as illustrated in figure 3.3, instead of being produced in a single direction as in the case of a single crystal. This is known as the Debye-Scherrer cone. When these cones are intercepted by a 2D detector, each cone gives rise to a Debye-Scherrer ring, where each ring corresponds to a particular (hkl) reflection . The intensity of each ring is governed by the corresponding nuclear or magnetic structure factors. The powder diffraction, therefore represents a orientational average of the Ewald sphere condition, because the random orientation of crystallites is equivalent to rotating the crystal to access different reflections corresponding to different orientations.

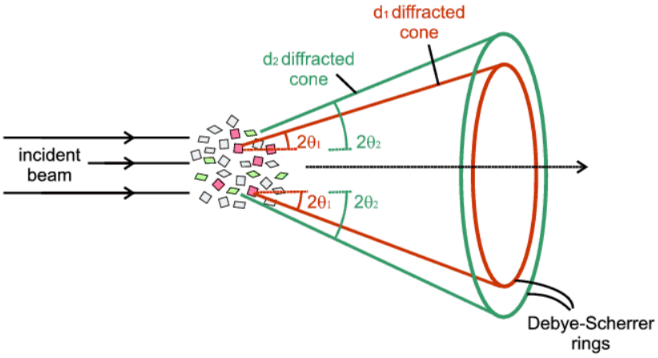

Figure 3.3: Neutrons are scattered from a set of crystallites that satisfy Bragg's law for a particular set of lattice planes is represented in colour red giving rise to a Debye-scherrer cone corresponding to scattering angle $2\theta_1$ and the crystallites that satisfy Bragg's law for a different set of lattice planes is represented in colour green giving rise to a Debye-scherrer cone corresponding to scattering angle $2\theta_2$. The figure is taken from the reference [73].

3.4 Magnetic scattering

The neutron magnetic interaction potential can be written as

$$\hat{V}_M(\mathbf{r}) = -\,\hat{\boldsymbol{\mu}}_n \cdot \hat{\mathbf{B}}(\mathbf{r}),$$

where the neutron magnetic moment $\hat{\boldsymbol{\mu}}_n$ couples to the magnetic field produced by the unpaired electrons including both spin and orbital contributions. Analogous to the considerations in nuclear scattering section 3.3, the elastic magnetic scattering cross section can be written as

$$\frac{d\sigma}{d\Omega} = \left[\gamma r_0 \frac{g}{2} f(\mathbf{Q})\right]^2 N_m \frac{(2\pi)^3}{v_m} e^{-2W} \sum_{G_m} |F_M(G_m)|^2 \delta(\mathbf{Q} - G_m),$$

Where N_m is the number of magnetic unit cells and the v_m is the volume of the magnetic unit cell which can be different from the nuclear unit cell depending on the propagation vector. Magnetic scattering occurs as a result of interaction with the electron cloud, which is an extended object. Therefore the magnetic form factor $f(\mathbf{Q})$ representing the spatial distribution of the magnetic electron density is included in the scattring cross section. The γ, r_o and g represents the neutron gyromagnetic ratio, electron radius and Lande g-factor respectively. The magnetic structure factor appearing in the cross section is given by

$$F_M(\mathbf{Q}) = \sum_j \hat{\mathbf{Q}} \times (\mathbf{s}_j \times \hat{\mathbf{Q}})\, e^{i\,\mathbf{Q}\cdot\mathbf{r}_j}$$

where s_j is the spin magnetic moment on the site j and r_j is the corresponding position. the $\hat{\mathbf{Q}}$ represents the unit vector along the scattering vector.

The vector $\hat{\mathbf{Q}} \times (\mathbf{s}_j \times \hat{\mathbf{Q}})$ is known as Halpern-Johnson vector and as consequence of this term, only the spin components perpendicular to the scattering vector contributes to the magnetic scattering and thereby allows the determination of direction of ordered moments presented in the result section of the thesis from the recorded diffraction pattern.

For a commensurate magnetic structure that can be represented as a linear combination of basis vectors R corresponding to an irreducible representation of a magnetic space group, the magnetic scattering intensity can be written as

$$I_M(\mathbf{Q}) \propto \langle S\rangle^2 f(\mathbf{Q})^2 \sum_R |F_R(\mathbf{Q})|^2 \sum_i |P_i(\mathbf{Q})|^2,$$

where $\langle S\rangle$ represent the thermal average of ordered magnetic moment for structure R. The observed intensity also depends on the polarization factor $P_i(\mathbf{Q})$ along crystallographic directions $i = x, y, z$. Therefore the factor $|P_i(\mathbf{Q})|^2$ determines how strongly a given spin component along i contribute to the observed intensity.

3.5 Polarized neutron scattering

So far, only unpolarized neutron scattering has been discussed, where the incident beam has no preferred direction for neutron spin and the only the total scattered intensity is measured. Such measurements do not allow the seperation of nuclear and magnetic contributions and are sensitive only to the magnitude of the magnetic structure factor.

Polarized neutron techniques overcome these limitations by producing an incident neutron beam with a well defined neutron spin state along any chosen direction and analysing the spin state of the scattered neutron. This allows to seperate the scattering cross section into spin-flip (SF) and non-spin flip (NSF) channels. Since the nuclear scattering does not couple to the neutron spin, nuclear scattering produces NSF scattering.

On considering the the magnetic scattering, only the magnetic moment components perpendicular to the neutron spin produce SF scattering while the components parallel to the incident neutron spin give rise to NSF scattering. By controlling both incident and outgoing neutron polarizations and analyzing them along all three spatial directions, the different scattering cross sections can be detected seperately thereby providing full directional information of the magnetic structure. This is achieved by spherical neutron polarimetry which is discussed in detail in section 8.3.

4

Experimental methods

In this chapter, the experimental techniques utilized in this work are discussed. The solid state synthesis methods, magnetization measurements and neutron diffraction techniques employed in the result section are discussed briefly.

4.1 Sample preparation and characterization

The following section details the reported solid-state synthesis procedures in literature which served as a foundations for the optimization attempts discussed in the chapter 5. Then the bulk characterization techniques used in this thesis are discussed.

4.1.1 Synthesis

Numerous synthesis methods have been reported in the literature for lithium orthophosphates, largely due to their established use as cathode materials in lithium-ion batteries. Among these approaches, solid state synthesis remains the widely used method to obtain polycrystalline samples due to its simplicity and cost effectiveness.

In this project, optimization of solid state synthesis methods is explored to produce pure samples of $LiMPO_4$(M= Fe, Ni, Co) as well as solid solutions $LiNi_{1-x}Fe_xPO_4$ and $LiCo_{1-x}Ni_xPO_4$. A wide range of precursors are used in the reported synthesis procedures. Li_2CO_3, LiH_2PO_4, Li_3PO_4 and $LiOH.2H_2O$ are the most commonly used precursors for Li, whereas carbonates(eg.$CoCO_3$), acetates(eg.$Fe(CH_3CO_2)$), oxalates(eg.$FeC_2O_4.2H_2O$) and oxides(eg.NiO) are used as transition metal sources. $NH_4H_2PO_4$ and $(NH_4)_2HPO4$ are the widely used precursors for phosphates [41, 74–77]. For example, the total reaction of the olivine synthesis for $LiFePO_4$ using oxalate precursors for Fe is given by

$$\begin{aligned} Li_2CO_3 + 2\,NH_4H_2PO_4 + 2\,FeC_2O_4 \longrightarrow{}& 2\,LiFePO_4 + 3\,CO_2 \\ &+ 2\,NH_3 + 2\,CO + 3\,H_2O \end{aligned} \tag{4.1}$$

The first step in all reported synthesis procedures involves the mixing of precursors. The two reported approaches are ball milling and manual grinding in an agate mortar with or without dispersing the precursors into a solvent. Ball milling in particular is reported to enable mechanochemical activation and intimate mixing of the starting materials. Additionally, dispersing the reagents into a solvent enables thorough mixing and improves the homogeneity of the reaction mixture, which ensures the phase purity of the sample since the homogeneity of the reaction mixture has been emphasized to be crucial to obtain a pure phase sample and to lower the reaction temperature [76, 78–80].

Most reported solid-state synthesis procedures employ multiple heat treatment steps to produce pure-phase samples. Typically, the initial step involves evaporation of the solvent after mixing, performed at temperatures 70-100°C depending on the solvent used. This is followed by the first heat treatment in the temperature range 250- 400 °C. During this step, the precursors are decomposed and the gases according to the precursors, and reaction pathways are expelled. The second heat treatment is reported to be in the temperature range 600- 850°C, which facilitates the complete progression of the solid state reactions. In some procedures, the powder is pressed into pellets before the high-temperature heat treatment to shorten the diffusion path and ensure the completion of the reaction [75, 80–82]. While multiple heat treatment steps are the most commonly employed approach, single-step heat treatments in the temperature range 700- 800°C are also reported to produce phase-pure samples [83–85].

The atmosphere in which the heat treatments are carried out has been widely recognized as a critical factor influencing the phase purity of the final product. Inert(Ar) or reductive (N_2, 3%H_2+Ar) environments are reported for $LiFePO_4$ to prevent the formation of Fe^{3+} impurities. In contrast, studies report that pure samples of $LiCoPO_4$ and $LiNiPO_4$ can be obtained under both air and inert atmospheres [74–76, 80, 81, 84, 86].

In addition to the temperature used in the heat treatment, the cooling procedure has also been highlighted to be important in avoiding the formation of impurities. Minakshi et al. reported the formation of Li_3PO_4 and NiO impurities in $LiNiPO_4$ samples when it is rapidly cooled down to room temperature after the final treatment, whereas a phase-pure $LiNiPO_4$ sample was obtained when a slow cooling rate of 0.5°C/min was employed [74,79]. The other reported impurities include metal oxides(NiO_x, Co_3O_4, FeO, Fe_2O_3, Fe_3O_4), metal phosphides(Ni_3P,Fe_2P,Fe_3P), metal pyrophosphates($Ni_2P_2O_7$, $Fe_2P_2O_7$) , $Li_4P_2O_7$ and $Li_2Ni_3(P_2O_7)_2$. [78,81,82,87–89].

Guided by these reported synthesis strategies and findings, this work investigated synthesis procedures incorporating ball milling using a vibrating ball mill equipped with stainless steel jars. Different atmospheric conditions for heat treatments were tested using a tube furnace, while the heat treatments conducted under air were carried out in a muffle furnace with alumina crucibles. The details of the synthesis attempts, along with the challenges faced, are discussed in chapter 5.

4.1.2 Bulk characterization

Characterization of macroscopic properties, in particular magnetization, is an essential first step in obtaining an overview of the magnetic behaviour of the materials. In this work, the temperature and field dependence of the magnetization of powder samples were determined. These measurements allow the determination of magnetic ordering temperatures, effective magnetic moment and In addition to this Curie Weiss temperature provides an initial idea about the dominant interaction type.The bulk characterization serves as a guideline to conduct further studies to determine microscopic properties, including magnetic structure, using other techniques such as neutron scattering.

Magnetization measurements were carried out using the Vibration Sample Magnetometry (VSM) option of Quantum Design Physical Property Measurement System (PPMS) at DTU Chemistry. The operational principle of the VSM is Faraday's law , which states that a change in magnetic flux induces a voltage in the pickup coil given by the equation;

$$V_{\text{coil}} = \frac{d\Phi}{dt} = \left(\frac{d\Phi}{dz}\right)\left(\frac{dz}{dt}\right), \tag{4.2}$$

Where Φ is the magnetic flux enclosed by the pick up coil, z is the vertical position of sample with respect to the pick up coil and t is the time. In practice, the VSM option of the PPMS works by sinusoidally vibrating the sample near the pickup coil at a frequency of 40 Hz and with an amplitude of 1-3 mm. The magnetic flux change due to this periodic motion induces a voltage in the pickup coil. The induced voltage is then processed in the VSM detection module which only extracts the component of the voltage that is in-phase with the sample motion, that is proportional to the magnetic moment of the sample. The conversion of detected voltage to manetic moment is obtained by instrument calibration using a standard of known magnetic moment. The PPMS is equipped with a cryostat that enables cooling down to 1.5 K and allows the application of a magnetic field of up to 9 T along the vertical direction. [90]

In this work, powder samples with an average mass of 30 mg were sealed in standard Quantum Design VSM powder sample holders (polycarbonate capsules). The temperature-dependent susceptibility was measured under a applied magnetic field of 1 T in the temperature range 1.5 K - 300 K. In addition, field-dependent magnetization curves were collected up to ± 9 T at selected temperatures.

4.2 Neutron and X-ray scattering

Following section describes the X-ray and Neutron diffraction techniques used in this thesis.

4.2.1 X-ray powder diffraction

X-ray powder diffraction data obtained in this work were acquired using an in-house Panalytical diffractometer equipped with a Cu K_α radiation source ($\lambda = 1.5406$ Å) shown in figure 4.1 . The instrument was operated in Bragg-Brentano geometry, in which the source and detector are mounted on a goniometer circle with the sample fixed at its centre. The source and detector move symmetrically along this circle so that the Bragg condition is always satisfied. The diffraction patterns were collected in the 2θ range of 5-90°. The finely ground powder sample was mounted on a flat Si sample holder to minimise background scattering.

Rietveld refinements of the collected diffraction patterns were performed using the Mag2Pol software [91] to verify the phase purity of the samples and to provide a primary structural characterization prior to detailed neutron diffraction studies. In the Rietveld refinement, the peak positions, profile functions and instrumental parameters are taken into account to produce a caluclated intenity profile which is fitted to observed intensities, where it uses a weighted least square method to minimize the quantitiy

$$\chi^2 = \sum_i \left(\frac{y_{\text{obs},i} - y_{\text{cal},i}}{\sigma_i} \right)^2 .$$

where y_{cal} and y_{obs} are observed and caluclated intensity . The crystallographic R_F factor is given by

$$R_F = 100 \cdot \frac{\sum_Q |F_{\text{obs},Q} - F_{\text{cal},Q}|}{\sum_Q F_{\text{obs},Q}}.$$

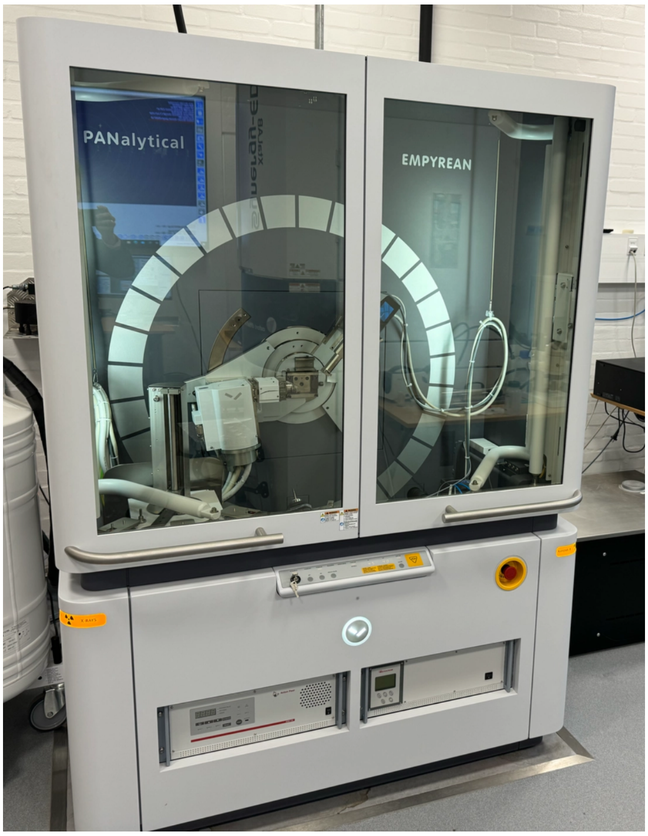

Figure 4.1: Image of the PANalytical Empyrean X-ray diffractometer used for the measurements presented in this work at DTU Chemistry.

4.2.2 Neutron diffraction

The following section discuss the different neutron diffraction techniques used in this work. It includes powder diffraction , single crystal diffraction and spherical neutron polarimetry . These techniques are used in combination with each other to address the scientifc questions of the current work.

Powder diffraction

The neutron powder experiments in this thesis were conducted using the D1B,D2B and D20 powder diffractometers at the Institut Laue Langevin (ILL). A schematic of the D1B diffractometer illustrating the layout of a typical powder diffractometer is shown in figure 4.2.

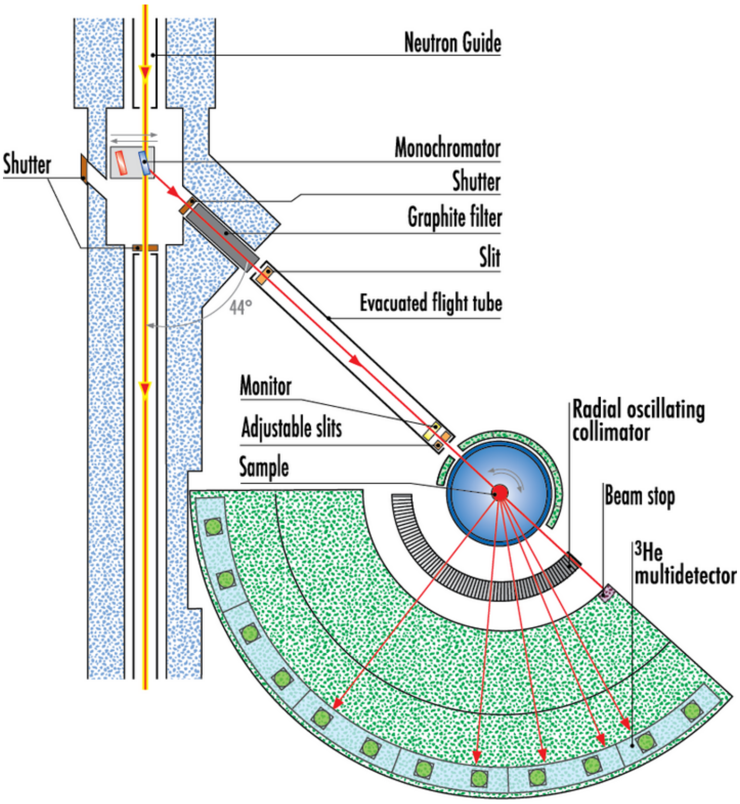

Figure 4.2: Diagram of powder neutron diffractometer D1B. Figure taken from Ref [92]

The first optical element in such diffractometers is a monochromator, which is used to select a single well-defined wavelength from the broad distribution of incident neutron wavelengths. When a polychromatic neutron beam impinges on a single crystal, different lattice planes satisfy Bragg's law for different wavelengths and give rise to reflections in corresponding directions. By exploiting this principle, single crystals with well-known lattice constants such as Germanium and Pyrolytic graphite are aligned at a particular orientation (Ge[311],PG[002]...) with respect to the incident beam so that only the desired wavelength allowed by Bragg's law is reflected towards the sample. A filter is placed after the monochromator in some cases to eliminate higher order harmonics of the desired wavelength allowed by Bragg's law ($\lambda/2$,$\lambda/3$...), depending on the choice of the monochromator. For instance, if the chosen monochromator is a Germanium single crystal, its diamond structure leads to systematic absence of second order reflections from lattice planes with all odd miller indices, there by eliminating $\lambda/2$ contribution in the reflected beam. Slits are used to define the size of the beam at the sample position and to reduce the background. The monitor before the sample counts the neutrons arriving at the sample position. The diffracted beam is then collected by the detectors, producing a diffraction pattern representing scattered intensity as a function of the scattering angle. [93]

Approximately 3g of sample was loaded into a cylindrical vanadium sample holder, which was mounted in a cryostat, enabling diffraction measurements in the temperature range 1.5 K to 300 K .

In this thesis, the complementary strengths of the three mentioned powder diffractometers were utilized to determine both the nuclear and magnetic structure of the mixed anisotropy compounds. Data collected on the high-resolution diffractometer D2B provided accurate structural refinements, while the higher wavelength modes in high flux diffractometers D20 and D1B were used to determine the magnetic structure, as they offer better resolution at lower scattering angles, where magnetic peaks are expected.

Single crystal diffraction

While powder neutron diffraction provides information on average nuclear and magnetic structure, it is limited due to peak overlap and loss of directional information. Single-crystal diffraction allows precise measurement of individual Bragg intensities, which enables unambiguous determination of weak magnetic reflections and detailed structural information. The four-circle diffractometer D9 at ILL was used for the single-crystal diffraction experiments in this work. In this instrument sample is mounted on an Eulerian cradle, which provides three independent rotation angles χ,φ,ω for the sample and free movement of the detector arm (2θ) as illustrated in figure 4.3, thereby allowing access to a wide range of reciprocal space. The sample is aligned in the required orientation for the diffraction to occur by adjusting the three angles χ,φ and ω. Then the 2D detector is rotated by an angle 2θ calculated for the specific Bragg reflection. The intensity for the specific Bragg reflection is recorded while the sample is rotated around the vertical axis, and the process is repeated for numerous Bragg reflections. The integrated intensity is then used to determine the magnetic and nuclear structure. [94]

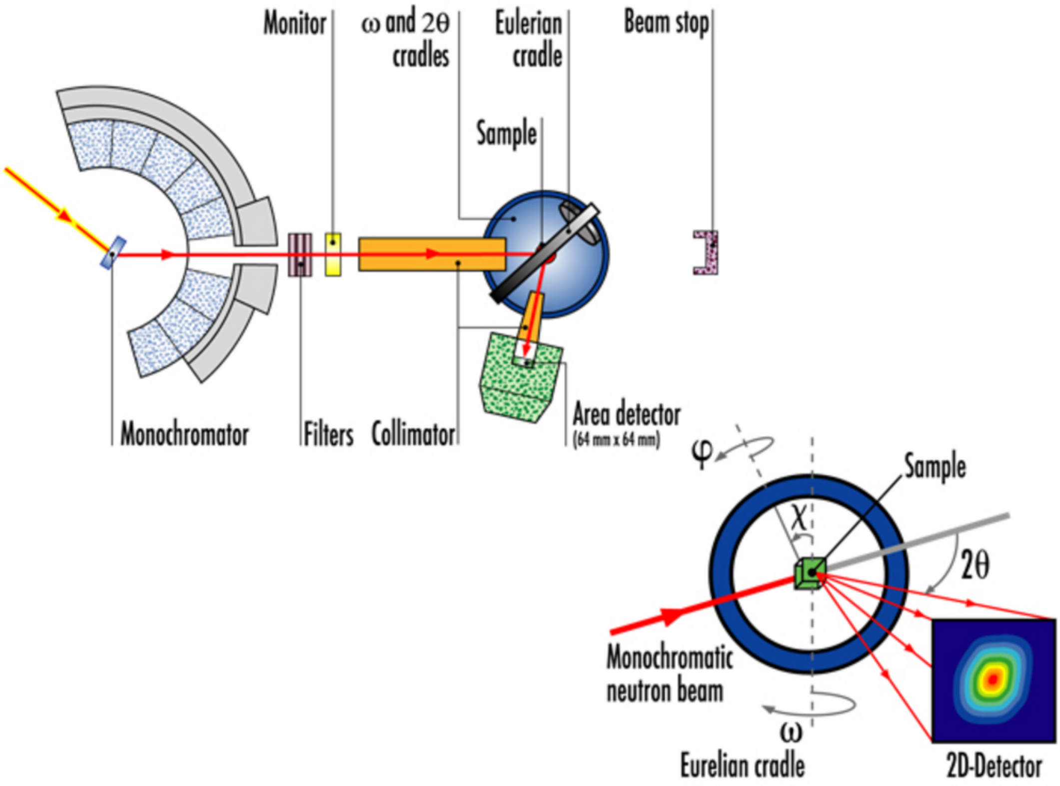

Figure 4.3: Diagram of the hot-neutron diffractometer D9 with the Eulerian cradle shown in the bottom right. The diagram highlights the four adjustable angles that allow access to specific Bragg reflections. The figure is taken from Ref. [94]

Accurate determination of the orientation of the crystal is essential for any single-crystal experiments where measurements along specific crystallographic directions are required. The Laue method is used to determine this, where a polychromatic neutron beam impinges on the single crystal sample. Multiple lattice planes fulfil Bragg's law at different wavelengths, scattering the beam at characteristic angles to a 2D detector. This produces a Laue diffraction pattern consisting of a set of Bragg spots, which is characteristic of the symmetry and orientation of the crystal. In this thesis the Orient Express neutron Laue diffractometer at the ILL was used to align crystals in the required crystallographic direction. The sample is mounted on a 2-stage tilt goniometer that allows ω rotation. The instrument operates in back-reflection geometry and records the diffraction pattern using a scintillator coupled to CCD cameras, allowing the measurement of the Laue diffraction pattern in a very short time [95].

4.2.3 Spherical Neutron Polarimetry

Spherical neutron polarimetry allows the measurement of all three components of scattered neutron polarization independent of the initial polarization direction. This allows measurement of all 9 elements of the polarisation matrix, which gives access to different scattering cross sections and hence allows complete determination of both magnitude and direction of magnetic moment and also helps in distinguishing otherwise non-distinguishable structures such as chiral or 180-degree domains. In this work, a Cryogenic Polarization Analysis Device (CRYOPAD) was used on the hot neutron diffractometer D3 at ILL to realize the conditions needed for spherical neutron polarimetry.

Figure 4.4 represents the top view of the CRYOPAD. Here, the sample is placed in a zero-field chamber achieved by the inner Meissner shield provided by superconducting material. This zero-field chamber ensures that all components of neutron polarization are preserved after scattering from the sample, and that the polarization remains unchanged between the entry guide field and the sample position. The incident neutron beam is polarized along the direction of motion. Nutators positioned on both incoming and outgoing positions of the CRYOPAD provide axial guide fields perpendicular to the direction of the neutron beam. In this region, a gradual change in the guide field allows the neutron spins to rotate towards the guide fields adiabatically. The neutrons coming out of the nutator then pass through the outer Meissner shield, designed to isolate the magnetic fields of the nutator from the precession coils. The primary precession coil is a toroid wound from super-

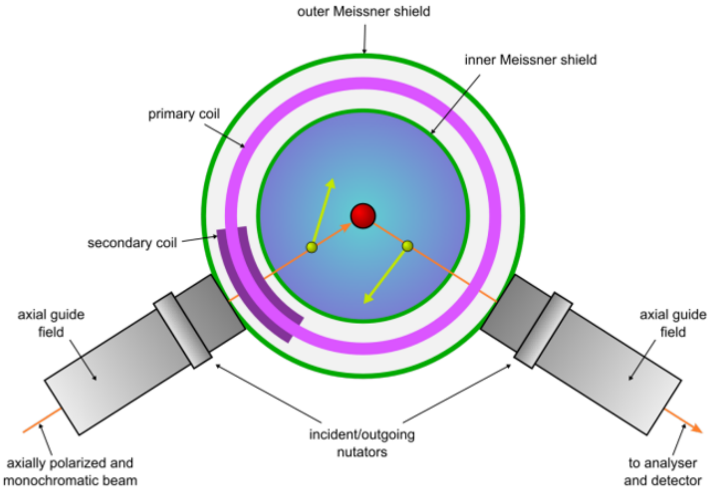

Figure 4.4: Schematic diagram of the CRYOPAD. The combination of nutators and the precession coil allows analysis of all 3 directions of incident and outgoing neutron polarizations. Figure taken from Ref. [96]

conducting wire, and the secondary precession coil is a part of the toroid wound over the primary coil only in the incoming path of the neutron beam. The abrupt magnetic field change in the precession coils causes a non-adiabatic spin rotation around the new field direction, which is precisely controlled by the applied magnetic field, the neutron wavelength, and the path length, thereby defining the incident polarization state of the neutron coming out of the inner Meissner shield to the zero field chamber. So the combination of field change at nutators and the rotations in precession coils defines the direction of polarization of the incident neutron beam. After scattering from the sample, the neutron polarization is modified according to the spin-dependent scattering cross-sections. The polarization state of the outgoing beam is then selected through a combination of rotations in the precession coil and the outgoing nutator, and analyzed using a polarized ^{3}He spin filter. [3, 96]

5

Synthesis

In this chapter, the attempts made to optimize reported solid-state synthesis routes to produce phase-pure samples of $LiFePO_4$, $LiCoPO_4$, $LiNi_{1-x}Fe_xPO_4$ and $LiCo_{1-x}Ni_xPO_4$ are described. The optimisation involves varying the key parameters of the synthesis procedure, including atmospheric conditions, reaction temperatures, and cooling rates, to identify a suitable synthesis route to produce pure phase samples. The optimization trials builds upon the synthesis procedures reported in the references cited in section 4.1.1 and is used without further citation throughout this chapter.

Powder X-ray diffraction (P-XRD) was used as a tool to assess the success of each synthesis attempt. The impurity phases were identified by matching the experimental peaks against reference patterns in the PDF-4 database using Highscore Plus software [97]. Rietveld refinement was employed to quantify the phase composition, where relevant.

The synthesis attempts made to produce pure samples of $LiCo_{1-x}Ni_xPO_4$ is discussed here. More successful attempts are discussed in detail, while the unsuccessful and inconclusive trials are summarised in Table 5.1. The chapter concludes with a summary of key insights on the influence of synthesis conditions and an outlook on potential strategies to attain better phase purity for these compounds.

5.0.1 $LiCoPO_4$ and $LiCo_{1-x}Ni_xPO_4$

The starting materials used were Li_2CO_3, $NH_4H_2PO_4$, $CoC_2O_4{\cdot}2H_2O$ and NiO. The initial synthesis procedure was conducted under an air atmosphere. All of the reagents were weighed and ground in ethanol in a mortar and pestle. Then the resulting mixture was dried by keeping it in the muffle furnace at 80°C for 1 hour.

After regrinding the powder, it was then precalcined at 375°C for 12 hours with a ramp rate of 10°C/min. After cooling down to room temperature, the powder was again reground and sintered at 800°C with a ramp rate of 10°C/min. It was then cooled down at a rate of 0.5°C/min. The PXRD pattern of the product was then recorded and analysed, confirming the formation of a phase-pure compound. The Rietveld refinement of the diffraction patterns was performed, and the results are discussed in Chapter6. The same procedure was repeated to produce samples for 7 compounds in the series $LiCo_{1-x}Ni_xPO_4$ with x = 0, 0.15, 0.3, 0.4, 0.5, 0.6, 0.75.

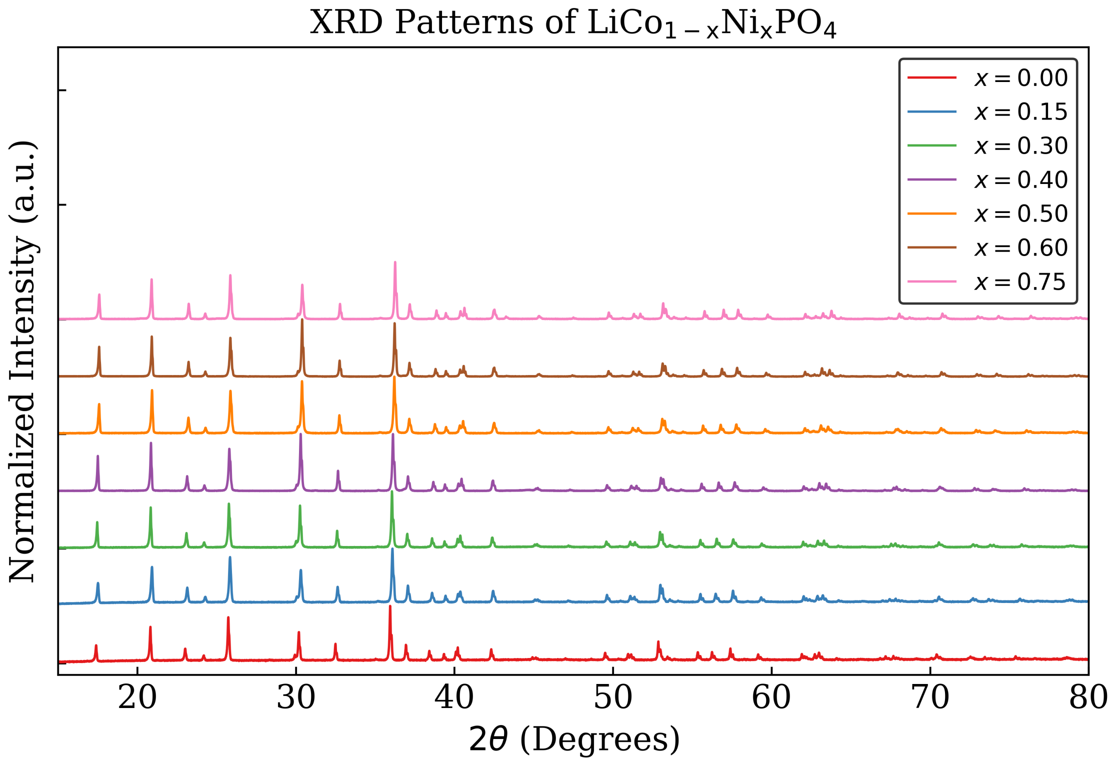

Figure 5.1: Observed P-XRD patterns for compounds in the series $LiCo_{1-x}Ni_xPO_4$ with x = 0, 0.15, 0.3, 0.4, 0.5, 0.6 and 0.75. All samples exhibit diffraction patterns consistent with olivine-type orthorhombic structure. No secondary phases were observed, indicating successful synthesis of phase-pure compounds across the series.

Several synthesis procedures involving different combinations of synthesis parameters were tested before arriving at the successful synthesis procedure described above. The failed synthesis procedures are described in the table 5.1.

Table 5.1: Summary of synthesis procedures and resulting phase compositions for $LiMPO_4$ (M = Fe, Co, Ni) and their solid solutions.

Compound	**Precursors**	**Mixing / Pre-treatment**	**Heat-treatment protocol**	**Atmosphere**	**Impurities / Remarks**
$LiFePO_4$	Li_2CO_3, $NH_4H_2PO_4$, $FeC_2O_4{\cdot}2H_2O$	Ball-milled in acetonitrile, dried under vacuum at 60°C	700°C / 24 h, 1°C/min cooling	N_2 flow	Impurity peak at 30.3° ($Fe_2P_2O_7$, 3–8%)
$LiNi_{1-x}Fe_xPO_4$ (x = 0.2)	Li_2CO_3, $NH_4H_2PO_4$, $FeC_2O_4{\cdot}2H_2O$, $NiC_2O_4{\cdot}2H_2O$	Ball-milled in acetonitrile, dried under vacuum at 60°C	750°C / 24 h, 1°C/min cooling	N_2 flow	$Li_4P_2O_7$ + $Li_2Ni_3(P_2O_7)_2$
			800°C / 24 h, 1°C/min cooling	N_2 flow	$Li_4P_2O_7$ + $Li_2Ni_3(P_2O_7)_2$, no significant improvement from 750°C
$LiNi_{1-x}Fe_xPO_4$ (x = 0.5)	Li_2CO_3, $NH_4H_2PO_4$, $FeC_2O_4{\cdot}2H_2O$, NiO	Ball-milled in acetonitrile, dried under vacuum at 60°C	800°C / 24 h, 1°C/min cooling	Ar flow	$Li_4P_2O_7$ + $Li_2Ni_3(P_2O_7)_2$

Continued on next page

Table 5.1 (continued)

Compound	**Precursors**	**Mixing / Pre-treatment**	**Heat-treatment protocol**	**Atmosphere**	**Impurities / Remarks**
$LiNi_{1-x}Fe_xPO_4$ (x = 0.2)	Li_2CO_3, $NH_4H_2PO_4$, Fe_2O_3, NiO	Manual grinding in ethanol, dried under vacuum at 85°C	175°C / 10 h → 225°C / 5 h → 725°C / 24 h → 750°C / 24 h	Ar flow	$Li_4P_2O_7$ + traces of $Li_2Ni_3(P_2O_7)_2$
		Ball-milled in ethanol, dried under vacuum at 85°C	175°C / 10 h → 225°C / 5 h → 725°C / 24 h → 750°C / 24 h	Ar flow	Same impurity but reduced intensity compared to manual mixing
$LiNi_{1-x}Fe_xPO_4$ (x = 0.5)	Li_2CO_3, $NH_4H_2PO_4$, $FeC_2O_4{\cdot}2H_2O$, NiO	Ball-milled in ethanol, dried under vacuum at 85°C; pre-calcined at 375°C / 10 h	800°C / 24 h, 1°C/min cooling	Ar flow	Minor $Li_2Ni_3(P_2O_7)_2$, improved crystallinity
$LiNiPO_4$	Li_2CO_3, $NH_4H_2PO_4$, $NiC_2O_4{\cdot}2H_2O$	Ball-milled in ethanol, dried under vacuum at 85°C; pre-calcined at 350°C / 10 h	700°C / 24 h	Ar flow	$Li_4P_2O_7$ + $Li_2Ni_3(P_2O_7)_2$ + Ni_3P

Continued on next page

Table 5.1 (continued)

Compound	**Precursors**	**Mixing / Pre-treatment**	**Heat-treatment protocol**	**Atmosphere**	**Impurities / Remarks**
			800°C / 24 h	Ar flow	Small decrease in the weight percentage of impurities compared to 700°C
		Ball-milled in ethanol, dried under vacuum at 85°C; pre-calcined at 350°C / 10 h	600–800°C / 24 h tested, 1°C/min cooling	Ar flow	$Li_4P_2O_7$ + $Li_2Ni_3(P_2O_7)_2$ + Ni_3P
$LiNiPO_4$	Li_2CO_3, $NH_4H_2PO_4$, NiO	Manual grinding in ethanol, dried under vacuum at 85°C; pre-calcined at 375°C / 12 h	800°C / 24 h, 0.5°C/min cooling	Air	Nearly phase-pure, weak impurity peaks at 27.5° and 43.3°
$LiCoPO_4$	Li_2CO_3, $NH_4H_2PO_4$, $CoC_2O_4 \cdot 2H_2O$	Ball-milled in acetonitrile, dried under vacuum at 60°C; pre-calcined at 375°C / 10 h	800°C / 24 h, 1°C/min cooling	Ar flow	Co_2P + unidentified small peaks at 21.8° and 28.7°

Continued on next page

Table 5.1 (continued)

Compound	**Precursors**	**Mixing / Pre-treatment**	**Heat-treatment protocol**	**Atmosphere**	**Impurities / Remarks**
$LiCo_{1-x}Ni_xPO_4$	Li_2CO_3, $NH_4H_2PO_4$, $CoC_2O_4 \cdot 2H_2O$, NiO	Manual grinding in ethanol, dried under vacuum at 85°C; pre-calcined at 375°C / 12 h	800°C / 24 h, 1°C/min cooling	Ar flow	Impurity peak at 28.6°
		Manual grinding in ethanol, dried under vacuum at 85°C; pre-calcined at 375°C / 12 h	800°C / 24 h, 0.5°C/min cooling	Air	Phase-pure

5.0.2 Conclusion and outlook

A series of solid-state synthesis trials were conducted to optimise the production of phase pure LiMPO4 and their solid solutions. The trials tested different synthesis conditions within the guidelines provided by the synthesis procedures reported in the literature. Although the end members are isostructural, the energy scales controlling their redox equilibria and phosphate condensation reactions differs [80, 88, 89]. This leads to different sensitivity to synthesis conditions.

The oxalate precursor, (eg:$FeC_2O_4 \cdot 2H_2O$) is better for $LiFePO_4$ since the decomposition step of oxalates include evolution of CO and CO_2 gas, the possible pathways for this decomposition is given in [88]. This can produce a transient reducing atmosphere locally before being diffused away and this prevents the oxidation of Fe^{2+} to Fe^{3+} [88]. But for $LiNiPO_4$, this is not favourable since the local pockets of decomposed CO would promote the reduction of Ni^{2+} to Ni^0 or Ni^{1+} which can trigger the condensation of phosphates to form phosphides or pyrophosphates. Since these are stable at 700-800°C, once formed they remain in the product. This can also be attributed to the observation that under the inert atmosphere of Ar flow, $LiNiPO_4$ is not pure. Hence slightly oxidising atmosphere is optimal for $LiNiPO_4$.

This explains the observation from the synthesis trials which show that nearly phase pure $LiFePO_4$ was obtained with a reducing atmosphere N_2 and profit from the self reducing property provided by the oxalate precursors. Whereas nearly phase pure $LiNiPO_4$ was obtained with a oxidising reaction environment (air) with NiO as precursor. These two contrasting tendencies existing in the mixture $LiNi_{1-x}Fe_xPO_4$, adds a degree of difficulty to the synthesis.

Ball-milling was reported to promote homogeneity and lower temperatures for reaction completion than manual grinding. But in the tests for $LiNi_{1-x}Fe_xPO_4$, very modest improvement in phase purity was observed with ball-milling while for $LiCo_{1-x}Ni_xPO_4$, phase pure sample was obtained with manual mixing. Hence, beyond a certain mixing threshold, attainable by manual grinding in a solvent, mixing does not play a significant role in phase purity.

The influence of pelletising where the powder is pressed together to shorten the diffusion pathway was also tested. This produced no significant improvement in the phase purity.This suggests that the reaction is thermodynamically limited rather than limited by diffusion. The observation that the impurities are secondary intermediate phases rather than the unreacted precursors also supports this conclusion. Different heating profiles with single-step sintering and multistep calcination were tested. The two step calcination, with a pre-calcination step intended to decompose the precursors and release gases and then a final sintering to complete the reaction, provided the best results accross all compounds in $LiMPO_4$. Even though literature reports phase pure samples with single-step process [84], this was reproducible only for $LiFePO_4$ (Nearly phase pure) while for the mixed compounds, it consistently produced pyrophosphate impurities. This could be associated with the local reducing environment formed with the evolution of gases from the decomposition step of the precursors as discussed earlier. In addition to this we would also like to highlight the importance of slow cooling rates in producing phase pure samples as reported in the literature. In addition, the results from the synthesis trials confirm the importance of slow cooling rates in agreement with literature reports [74].

The observed pyrophosphate impurities could also originate from lithium defficiency caused by volatility of Li reported in the literature for the temperatures and dwell time required to obtain a crystalline end product, in combination with the oxygen deficient environment.

From the unsuccessful attempts to produce phase-pure samples of $LiNi_{1-x}Fe_xPO_4$, the contrasting redox requirements for Fe^{2+} and Ni^{2+} is the main challenge in solid state synthesis of these materials. The Fe component is prone to oxidation to Fe^{3+}, where Ni component is susceptible to reduction under oxygen deficient environment. In addition to the appropriate choice of precursors discussed earlier, future synthesis attempts could employ a controlled oxygen partial pressure environment such as small O_2 mixed with Ar flow in the range that it stabilize both cations in the $+2$ oxidation state. Further the influence of flow rate of the gas on the phase formation needs to be explored further. The current heating profile at 800°C which resulted in the better phase purity causes significant Li volatility [88]. Using a slight excess of Li precursor beyond the stoichiometric ratio could compensate for this loss and mitigate Li deficiency that drives pyrophosphate formation. A slow cooling rate was employed in the present work. However, the heating rate was not closely controlled. A slower heating rate could be employed to avoid the fast release of the gaseous species during the precursor decomposition.

6

Magnetic Structures and phase transitions in $LiCo_{1-x}Ni_xPO_4$

6.1 Motivation

As discussed in chapter 2, the stoichiometric lithium orthophosphates have attracted scientific interest due to their magnetic and magnetoelectric properties. By contrast, the non-stoichiometric compounds in this family remain comparatively less explored. Since all compounds in this family crystallize in the same olivine structure with nearly collinear antiferromagnetic order only differing in the orientation of the ordered moments, they offer an ideal platform for investigating the effect of competing single-ion anisotropy through chemical substituion. In such mixed systems, the combination of Ni^{2+} with Co^{2+} or Fe^{2+} is highly interesting, as these ions possess orthogonal single-ion anisotropies. As discussed in section 2.0.5, mixed anisotropy magnets are predicted to host chemically tunable and potentially complex magnetic phase diagrams. The competition between anisotropy combined with exchange interactions is expected to give rise to oblique antiferromagnetic phases, in which the ordered moments rotate away from the easy axes of both parent compounds. Such magnetic symmetry changes carry significant implications for the physical properties that are governed by the symmetry of the magnetic ground-state. In particular, the magnetoelectric effect in $LiMPO_4$ is highly sensitive to the symmetry changes of the magnetic structure. A recent study of $LiNi_{1-x}Fe_xPO_4$ have reported the emergence of an oblique antiferromagnetic phase in the low temperature region, as explained in detail in chapter7. Notably, this study reports a change compared to the parent compounds $LiFePO_4$ and $LiNiPO_4$ in the non-zero components of the magnetoelectric tensor of the oblique phase, accompanied by an increase of two orders of magnitude in the dominant magnetoelectric coupling element when compared to the parent compounds [1]. These findings further highlight the potential of mixed-anisotropy systems, demonstrating that chemical substitution can be used to tune the magnetic ground state and thereby engineer associated physical properties for future applications.

This chapter focuses on the series $LiCo_{1-x}Ni_xPO_4$. The symmetry lowering expected from theory and associated changes in magnetoelectric tensor elements are worth exploring, as it can provide deeper understanding of how the symmetry changes influence the magnetoelectric effect in these systems. In addition to this, existence of ferrotoroidic order in $LiCoPO_4$ is experimentally verified as reported by Vaknin et al. [50] and $LiNiPO_4$ fulfills the symmetry requirements to support ferrotoroidic order. The ferrotoroidal order is highly dependent on the magnetic symmetry of the system. Hence the possible symmetry lowering in the mixed system is expected to influence the ferrotoroidal order as well.

Understanding how the magnetic structure evolves with Ni substitution is therefore the prerequisite for eventually tuning ferrotoroidicity in these materials. For $LiCo_{1-x}Ni_xPO_4$, structural studies exist in the literature for the Ni rich side of the phase diagram with $x \geq 0.5$, based on X-ray and Raman scattering techniques [98]. These studies report the formation of a single phase solid solution, where Ni^{2+} and Co^{2+} occupy the 4c Wyckoff site. The magnetic structure study reported for $LiCo_{0.1}Ni_{0.9}PO_4$, reveals a commensurate antiferromagnetic phase and a narrow incommensurate phase in the temperature range 20.2 to 21.0 K similar to $LiNiPO_4$. In the low-temperature commensurate phase the magnetic moment is aligned along the c-axis. The incommensurate phase is described by the propagation vector $\mathbf{K_{IC}} = (0, k, 0)$ with k increasing from 0.10 to 0.12 r.l.u between 20.2 and 21.0 K. The presence of a small percentage of Co is reported to narrow the temperature range in which incommensurate order exists in $LiCo_{0.1}Ni_{0.9}PO_4$ [99] compared to $LiNiPO_4$. The magnetic structure of the mixed compound $LiCo_{0.5}Ni_{0.5}PO_4$ is also reported in the literature. Semkin et al. report the existence of an oblique antiferromagnetic structure for this composition, where the spins are oriented in the bc-plane and a reduced ordering temperature of 14.1 K was identified with neutron diffraction, magnetometry and heat capacity measurements [100].

Although these isolated studies hint at interesting phase evolution within the series, a systematic investigation of the magnetic structure of the $LiCo_{1-x}Ni_xPO_4$ across the full phase diagram remains unexplored. Thus this chapter examines the complete composition-temperature phase diagram of the mixed anisotropy magnet LiCo$_{1-x}$Ni$_x$PO$_4$ as a preliminary step to explore the interesting physcial properties of the system such as magnetoelectric effect and ferrotoroidic effect.

6.2 Rietveld refinement of X-ray patterns

As mentioned in section 5.0.1, X-ray diffraction measurements for LiCo$_{1-x}$Ni$_x$PO$_4$ were performed to verify the phase purity and to monitor the structure evolution with increasing Ni substitution. The Rietveld refinements provide the framework required for the analysis of magnetic and structural neutron diffraction results.
The diffraction patterns were collected at room temperature. The patterns were refined starting from the Pnma olivine structure model reported for LiCoPO$_4$ [17]. Lattice parameters, scale factor, peak shape parameters, isotropic displacement parameter and atomic positions were refined keeping the site occupancy of Ni and Co fixed to the nominal percentage since XRD is not sensitive to differentiate between Ni and Co. This is due to the fact that X-ray scatter from the electron cloud. For the atoms such as Ni and Co,differentiating them based on the X-ray diffraction is not possible.

The lattice parameters from the refinement of XRD pattern are summarized in table 6.1. The lattice parameters exhibit systematic evolution with increase in Ni content in accordance with Vegard's law [101]. Both a and b decrease monotonically

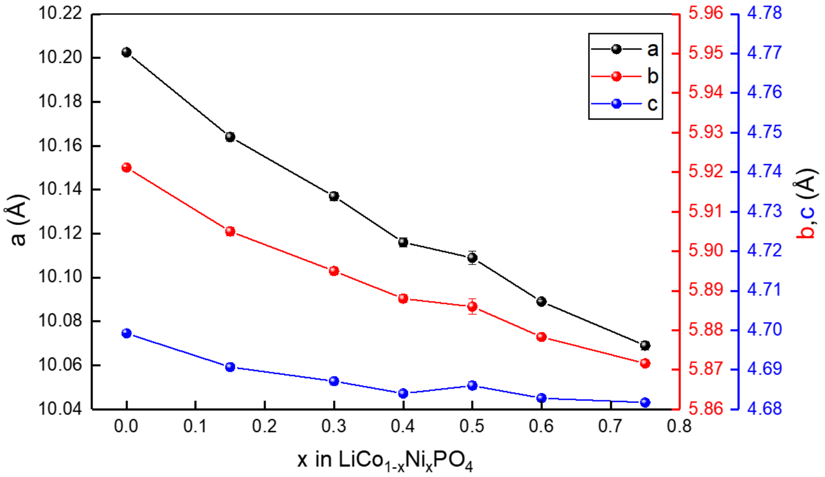

Figure 6.1: Plot of refined lattice parameters against x in LiCo$_{1-x}$Ni$_x$PO$_4$.

while the change in c is minor with increasing Ni concentration. XRD is not sensitive enough to determine the oxygen positions accurately, since in the presence of heavy atoms , the scattering is dominated by these heavy elements and the scattering from light atoms such as oxygen is minimal. The accurate determination of oxygen positions was carried out using neutron diffraction data discussed in the later sections 6.4.

x in LiCo$_{1-x}$Ni$_x$PO$_4$	a (Å)	b(Å)	c(Å)	V(Å^3)
0	10.203(1)	5.921(1)	4.699(1)	283.88(1)
0.15	10.164(2)	5.905(1)	4.691(1)	281.55(9)
0.3	10.137(2)	5.895(1)	4.687(1)	280.09(9)
0.4	10.116(2)	5.888(1)	4.684(1)	278.96(9)
0.5	10.109(3)	5.886(2)	4.686(1)	278.80(9)
0.6	10.089(1)	5.878(1)	4.683(1)	277.72(6)
0.75	10.069(2)	5.872(1)	4.682(1)	276.79(8)

Table 6.1: Refined lattice parameters and cell volume from the room temperature XRD measurements.

The refinements confirmed single-phase behaviour for all compositions. The refinement of all compositions fit with the Pnma space group without any detectable symmetry change or additional peaks. The absence of peak splitting or broadening across the series confirms the formation of a single-phase solid solution without phase segregation. Figure 6.2 illustrates the Rietveld refinements for all LiCo$_{1-x}$Ni$_x$PO$_4$.

6.3 Magnetization measurements analysis

Field dependent and temperature dependent magnetization measurements were carried out to characterize the evolution of magnetic order in LiCo$_{1-x}$Ni$_x$PO$_4$ to act as a guide for the neutron diffraction studies. The measurements were perfomred at DTU Chemistry using a 9T Physical Properties Measurement System (PPMS) from Quantum Design. The results are discussed in the following sections

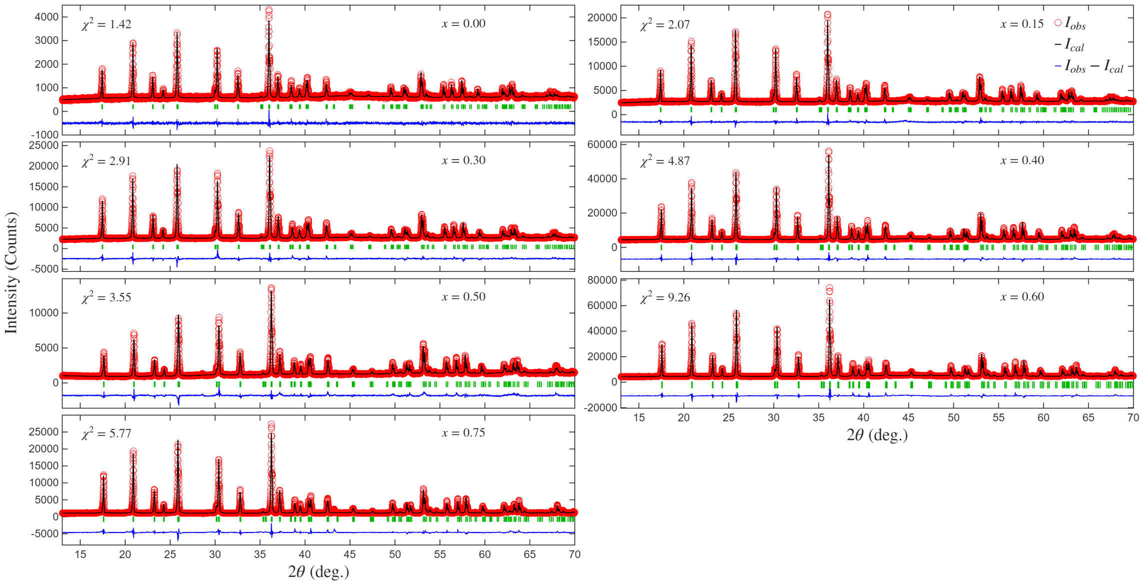

Figure 6.2: Observed (red points) and calculated (black line) X-ray diffraction patterns of LiCo$_{1-x}$Ni$_x$PO$_4$. The green markers denote Bragg peak positions. The blue line represents the difference between the observed and calculated patterns.

6.3.1 Temperature dependent magnetic susceptibility

Temperature dependent magnetic susceptibility can be expressed as

$$\chi(T) = \frac{M(T)}{H}$$

where M(T) is the magnetization of the sample at temperature T and H is the applied magnetic field. The susceptibility represents the magnetic response of a material to an applied magnetic field. The measurements were performed under an applied magnetic field of 10000 Oe. The figure 6.3 illustrates the temperature dependent magnetic susceptibility for all compositions. All compositions exhibit a cusp in magnetic susceptibility at the Néel temperature and exhibit a curve characteristic of an antiferromagnetic ordered state with a slight low-temperature upturn reflecting a small amount of paramagnetic impurities [102]. The Néel temperature was determined from the maximum in the first derivative of the magnetization. The ordering temperature decreases monotonically with increasing Ni concentration up to $x = 0.5$, and then increases up to $x = 0.75$. This trend is consistent with the frustration arising from the competition between different anisotropy energy preferences with increasing Ni concentration. However the second low-temperature transition expected for mixed anisotropy systems as explained in chapter2, was not observed for any composition. This absence could be a result of directional averaging in the powder measurements.

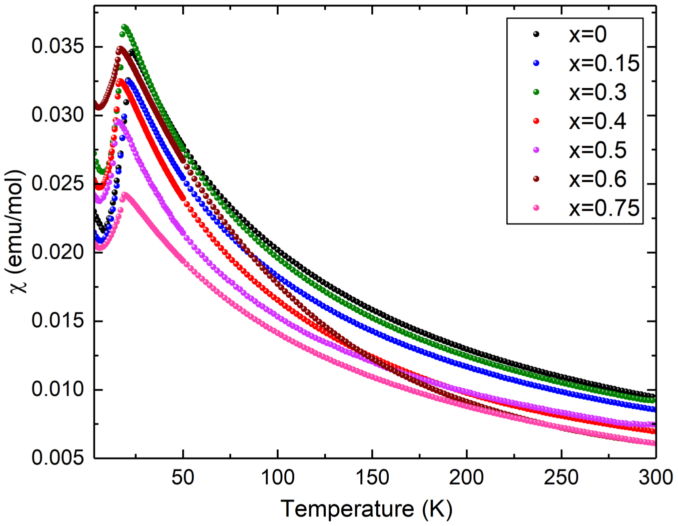

Figure 6.3: Temperature dependent magnetic susceptibility for LiCo$_{1-x}$Ni$_x$PO$_4$.

Although the T_N values exhibit the trend expected for mixed anisotropy systems across the compositions and remain reproducible across different synthesis batches for a given composition, the magnitude and slope of the susceptibility curve exhibit considerable variations. Moreover, these variations do not follow a systematic trend with increasing Ni content. Since the T_N remains reproducible across different batches, deviations from the intended composition can be ruled out as the cause for the observed irregularities. These deviations could result from the experimental uncertainities such as error in sample mass calibration, variations in sample packing, background contributions and factors such as preferred crystallographic orientation and grain size.

The temperature dependent susceptibility curve in the high temperature paramagnetic region is decribed by the Curie-Weiss law [2].

$$\chi = \chi_0 + \frac{C}{T - \theta_\mathrm{CW}}, \tag{6.1}$$

Where C is the Curie constant, θ_CW is the Curie-Weiss temperature and χ_0 is the

x in $\mathrm{LiCo_{1-x}Ni_xPO_4}$	T_N (K)	θ_CW	μ_{eff} (μ_B)
0	21(1)	-89.6(2)	5.64(1)
0.15	20(1)	-81.1(1)	5.19(1)
0.3	18(1)	-74.9(4)	4.91(1)
0.4	15.2(5)	-68(1)	4.90(2)
0.5	14(1.00)	-76(1)	4.64(3)
0.6	15.7(5)	-42.7(1)	4.86(1)
0.75	17(1)	-104.4(2)	5.16(1)
1	23	79	

Table 6.2: Magnetic ordering temperature of $\mathrm{LiCo_{1-x}Ni_xPO_4}$ determined from the maximum of first derivative of magnetization with respect to temperature. Curie-Weiss temperature (θ_CW) and effective magnetic moment obtained from the Curie-Weiss fit of reciprocal magnetic susceptibilities. The values for $\mathrm{LiNiPO_4}$ are taken from reference [17].

temperature independent contribution to the susceptibility including diamagnetic contributions from sample and sample holder. The parameters determined from the Curie-Weiss fitting of the susceptibility curve in the paramagnetic region and the Néel temperature for all the compositions are summarized in the table 6.2. The effective magnetic moment μ_{eff} was calculated from the fitted value of C using the relation $\mu_{eff} = \sqrt{8C}$ in the CGS units [103]. The values of θ_CW are negative across all the compositions indicating the dominant antiferromagnetic interaction in the system. However, the magnitude of θ_CW does not exhibit any systematic trend with increasing Ni concentration. The θ_CW determined for $\mathrm{LiCoPO_4}$ is consistent with the previously reported value. The value of the effective moment μ_{eff}, decreases approximately with increasing x up to $x = 0.5$ and exhibits an upturn for further increase in Ni concentration. The value for the parent compound $\mathrm{LiCoPO_4}$ agrees with the previously reported value in the literature [17]. The fitted value of μ_{eff} is larger than the calculated spin-only values indicating the possible non-zero orbital contribution to the magnetization.

6.3.2 Field dependent magnetic suceptibility

The field dependent magnetization isotherm was measured in the field range of ±9 T at selected temperatures. Since the measurements were performed on polycrystalline samples, the data represent the directional average of the anisotropic magnetic response expected in the $\mathrm{LiCo_{1-x}Ni_xPO_4}$ system.

At all compositions, the MH curves do not exhibit significant hysteresis, confirming the absence of signficant ferromagnetic contributions. None of the compositions exhibits saturation up to the highest applied field, and no sharp anomalies are observed that indicate a field induced magnetic phase transition.

For $LiCoPO_4$, the MH curve remains linear, consistent with the AFM structure. In contrast to the single-crystal measurements with magnetic field applied along b-axis, that reports a weak hysteresis loop attributed to ferromagnetic contribution [43], the powder data in this study show no such contribution. For x=0.15 the magnetization shows a similar linear dependence with the applied field. However, for x=0.3, 0.4 and 0.5 the MH curve measured at low temperature below T_{N} exhibit nonlinear increase in magnetization with applied field. Such nonlinearity has been reported for canted antiferromagnetic materials indicating the onset of canting of magnetic moment in these compositions [104]. At higher Ni concentrations at $x = 0.6$ and 0.75, the MH curve becomes linear again. At $x = 0.5$, the magnetization at highest fields shows slight divergence between different field sweeps.

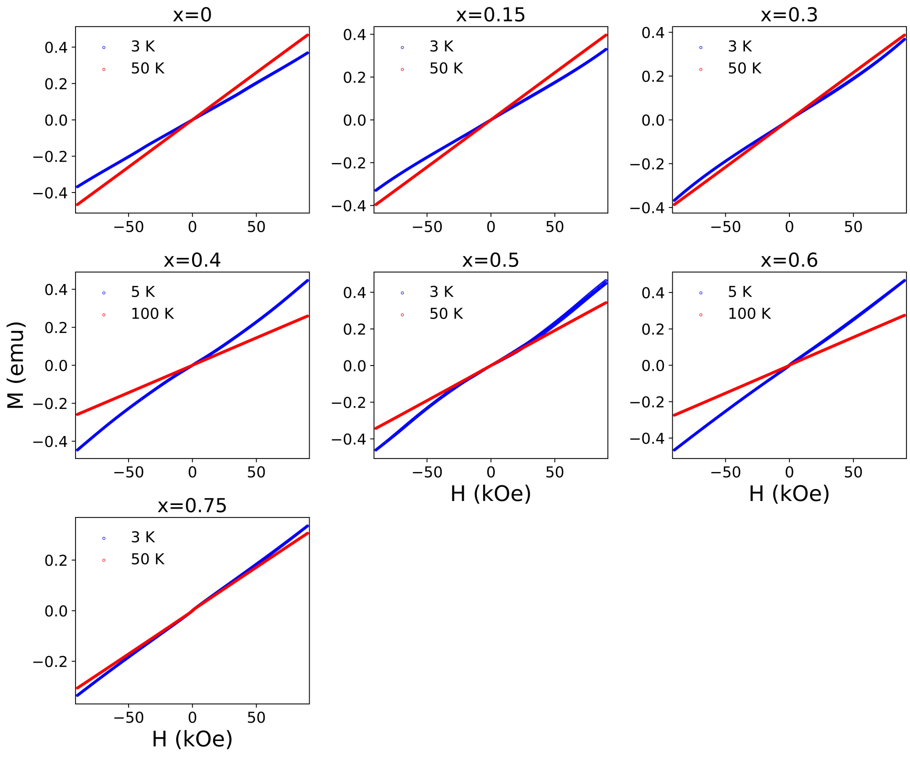

Figure 6.4: Field-dependent magnetization curves of $LiCo_{1-x}Ni_xPO_4$ measured at selected temperatures. Each panel presents a representative low temperature measurement (3 or 5 K) and a high temperature measurement (50 or 100 K) with blue and red symbols respectively.

6.4 Neutron diffraction data and analysis

Neutron powder diffraction experiments were performed to determine the crystal and magnetic structure of $LiCo_{1-x}Ni_xPO_4$. The nuclear and magnetic structure were determined by Rietveld refinement using the Mag2Pol software [91].

6.4.1 Nuclear structure analysis

The neutron diffraction pattern collected on the instruments D2B ($\lambda = 1.59$ Å) and D20 ($\lambda = 1.54$ Å) at the temperature 300 K were analyzed to determine the crystal structure of the compounds $LiCo_{1-x}Ni_xPO_4$. Compared to XRD measurements neutron diffraction allow a direct refinement of the relative Co/Ni occupancies on the transtion metal site due to the distinct scattering lengths of Co (2.49 fm) and Ni (1.03 fm). Furthermore, neutron measurements provide greater precision for oxygen position. The starting model corresponds to orthorhombic olivine structure (space group Pnma, no.62) and the starting parameters were taken from the refinement of XRD patterns.

The peak shapes were described using the profile function Thompson-Cox-Hastings (TCH) pseudo-Voigt and asymmetry corrections were employed while the background was defined manually. For all compositions, refinements yielded excellent agreement factors with $R_F < 2.5$. The refined lattice parameters, atomic positions and the relative occupation of Co^{2+} and Ni^{2+} at the transition metal sites from the refinement are summarized in table 7.2. All compositions were confirmed to crystallize in the same orthorhombic olivine structure as the stoichiometric end compounds $LiNiPO_4$ and $LiCoPO_4$. All the compositions exhibit sharp Bragg peaks with no additional peaks or diffuse features confirming the phase purity and crystallinity of the samples consistent with the XRD results. No peak broadening was detected across the different compositions indicating the absence of Ni and Co clustering and confirming the formation of a solid-solution. Similar to the XRD refinement results, the lattice parameters decrease monotonically with increasing Ni concentrations in accordance with Vegard's law as illustrated in figure 6.5. This contraction is consistent with the difference between the ionic radius of Co^{2+}(0.74 Å) and Ni^{2+}(0.69 Å). The observed contraction is anisotropic with most pronounced contraction along the *a*-axis (1.24 % from x= 0 to 0.75). The contraction along the *b*-axis is around 0.79% and the least decrease is observed along the *c*-axis (0.32%). The results agree

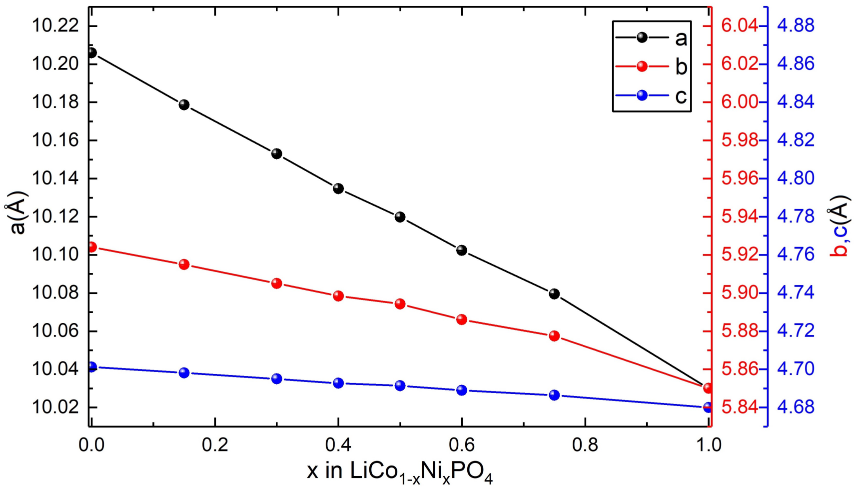

Figure 6.5: Composition dependence of lattice parameters from the refinement of neutron data collected at 300 K

well with the literature reported for $LiCo_{1-x}Ni_xPO_4$ from x= 0.9 to 0.5 [98]. The refined occupation closely agrees with the nominal concentrations.

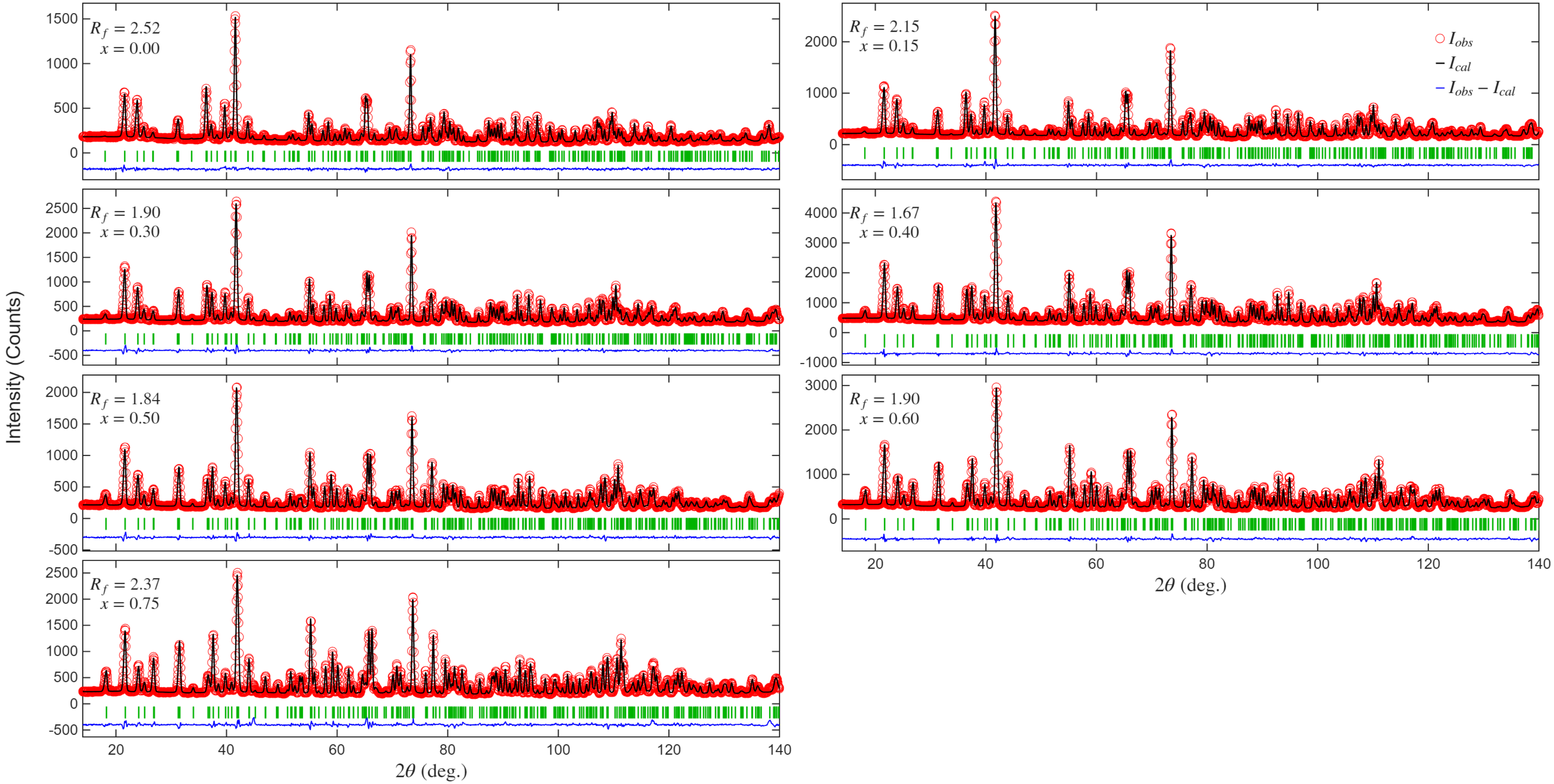

Figure 6.6: Observed (red points) and calculated (black line) neutron powder diffraction patterns of LiCo$_{1-x}$Ni$_x$PO$_4$. The green markers denote Bragg peak positions. The blue line represents the difference between the observed and calculated patterns. The data were collected at T = 300 K using D2B diffractometer.

x	Lattice constants [Å]	Atom	x	y	z	Occ.	R_F
0	a=10.20594(9)	Li	0	0	0	1	2.52
		Co/Ni	0.2771(3)	0.25	0.9793(7)	1 /0	
	b=5.92409(5)	P	0.0942(2)	0.250	0.4188(4)	1	
		O1	0.0983(1)	0.250	0.7413(3)	1	
	c=4.70127(4)	O2	0.4545(1)	0.250	0.2044(3)	1	
		O3	0.1664(1)	0.0445(1)	0.2821(2)	1	
0.15	a=10.17862(8)	Li	0	0	0	1	2.15
		Co/Ni	0.2769(2)	0.250	0.9826(4)	0.841(2)/0.159(2)	
	b=5.91491(5)	P	0.0948(1)	0.250	0.4183(3)	1	
		O1	0.0984(1)	0.250	0.7416(3)	1	
	c=4.69812(4)	O2	0.4540(1)	0.250	0.2046(3)	1	
		O3	0.16629(9)	0.0440(1)	0.2815(2)	1	
0.30	a=10.15296(7)	Li	0	0	0	1	1.90
		Co/Ni	0.2765(1)	0.250	0.9828(3)	0.687(2)/0.313(2)	
	b=5.90505(4)	P	0.0948(1)	0.250	0.4183(3)	1	
		O1	0.0987(1)	0.250	0.7414(3)	1	
	c=4.69497(4)	O2	0.4536(1)	0.250	0.2037(3)	1	
		O3	0.16623(9)	0.0439(1)	0.2805(2)	1	
0.40	a=10.13473(7)	Li	0	0	0	1	1.67
		Co/Ni	0.2765(1)	0.250	0.9835(2)	0.586(2)/0.414(2)	
	b=5.89847(4)	P	0.0943(1)	0.250	0.4177(2)	1	
		O1	0.0987(1)	0.250	0.7420(2)	1	
	c=4.69272(3)	O2	0.4533(1)	0.250	0.2030(2)	1	
		O3	0.16610(8)	0.0431(1)	0.2800(2)	1	
0.50	a=10.11986(7)	Li	0	0	0	1	1.84
		Co/Ni	0.2763(1)	0.250	0.9830(2)	0.506(2)/0.494(2)	
	b=5.89431(4)	P	0.0945(1)	0.250	0.4176(3)	1	
		O1	0.0991(1)	0.250	0.7425(3)	1	
	c=4.69136(3)	O2	0.4525(1)	0.250	0.2027(3)	1	
		O3	0.16625(9)	0.0434(1)	0.2798(2)	1	
0.60	a=10.10232(8)	Li	0	0	0	1	1.90
		Co/ Ni	0.2759(1)	0.250	0.9830(2)	0.400(2)/0.600(2)	
	b=5.88610(4)	P	0.0948(1)	0.250	0.4183(3)	1	
		O1	0.0988(1)	0.250	0.7417(3)	1	
	c=4.68903(3)	O2	0.4523(1)	0.250	0.2032(3)	1	
		O3	0.1659(1)	0.0428(1)	0.2791(2)(3)	1	
0.75	a=10.07956(8)	Li	0	0	0	1	2.37
		Co/ Ni	0.2756(1)	0.250	0.9827(2)	0.249(3)/0.751(3)	
	b=5.87749(5)	P	0.0950(2)	0.250	0.4168(3)	1	
		O1	0.0991(2)	0.250	0.7428(3)	1	
	c=4.68639(4)	O2	0.4509(1)	0.250	0.2019(3)	1	
		O3	0.1663(1)	0.0428(2)	0.2788(2)	1	
1	a=10.0317(1)	Li	0	0	0	1	N/A
		Co/ Ni	0.2756(1)	0.250	0.9825(3)	0/1	
	b=5.8539(1)	P	0.0943(2)	0.250	0.4167(5)	1	
		O1	0.1008(5)	0.250	0.7427(10)	1	
	c=4.6768(1)	O2	0.4492(5)	0.250	0.1978(10)	1	
		O3	0.1668(4)	0.0439(6)	0.2783(7)	1	

Table 6.3: Structural parameters for $LiCo_{1-x}Ni_xPO_4$ at $T = 300$ K. Values for $x = 1$ are taken from Ref. [32]. Those of $x = 0.50$ and $x = 0.60$ agree with Ref. [98].

6.4.2 Magnetic structure analysis

The neutron diffraction patterns for magnetic structure analysis were collected on the instruments D1B (λ=2.52 Å) and D20 (λ= 2.41 Å). The ordering temperatures obtained from the susceptibility measurements were used as guidelines and the diffraction patterns were collected at different temperatures below the ordering temperature. The low-temperature diffraction patterns exhibit additional intensity at scattering angles corresponding to (h,k,l) integer Miller indices. No extra satellite peaks or peak splitting was observed within the instrument resolution. This is consistent with a commensurate magnetic ordering which means magnetic and crystal unit cells are of the same period. For all compositions the magnetic propagation vector was fixed to $\mathbf{k}$ = (0,0,0) for all the refinements which is consistent with the magnetic ground state reported for all lithium orthophosphates $LiMPO_4$ [17, 18].
The magnetic respresentation for the 4c site under the parent group symmetry Pnma is decomposed as $\Gamma = \Gamma_1 + 2\Gamma_2 + 2\Gamma_3 + \Gamma_4 + \Gamma_5 + 2\Gamma_6 + 2\Gamma_7 + \Gamma_8$ with each irreducible representation corresponding to a specific magnetic space group and basis vectors as listed in 1.3.
The crystal structure for all compositions was fixed to the parameters refined from the neutron data collected at shorter wavelength. The magnetic refinements were performed on the low-temperature diffraction patterns at 2 K. Each of the symmetry-allowed models, defined by a single or combined irreps of the Pnma space group was tested systematically. The model yielding the best agreement between the observed and calculated patterns was selected as the solution.

x = 0, 0.15, 0.3:

For compositions with x = 0, 0.15 and 0.3 all observed magnetic reflections could be indexed using the Γ_4 irrep, which corresponds to an antiferromagnetic arrangement of spins along the *b*-axis (C_y). This is consistent with the magnetic structure reported for the parent compound $LiCoPO_4$ [41].
The weak spin canting components reported from the single-crystal studies for $LiCoPO_4$ as explained in section 2.0.3 were not observed in the present powder diffraction data. The spin rotation of 4.6° away from the *b*-axis, corresponding to a C_z component as reported by Vaknin et al. [42] would give rise to non-zero intensity at the (010) peak. As illustrated in the table 6.4, the (010) peak has non-zero structure factor only for *C*-type structure. Since neutrons scatter only from the magnetic moment component perpendicular to the scattering vector, the (010) peak acts as a

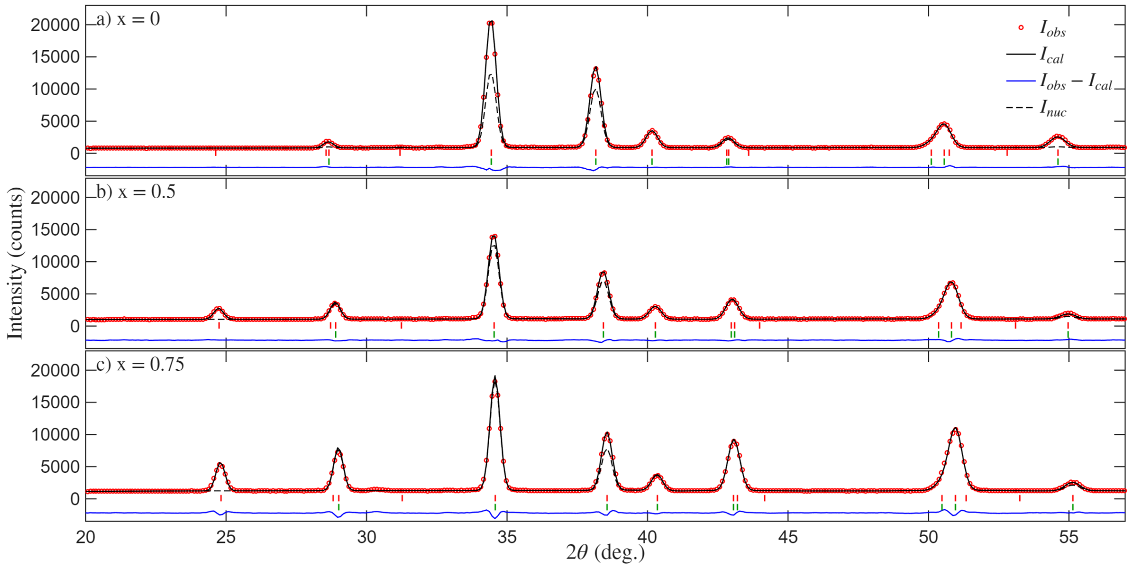

Figure 6.7: Observed (red points) and calculated (black line) neutron diffraction pattern of LiCo$_{1-x}$Ni$_x$PO$_4$. The (a) panel denotes x=0, (b) denotes x=0.5 and (c) panel represent x= 0.75. The green markers denote the symmetry allowed nuclear Bragg reflections and red markers represent the magnetic Bragg reflections. The blue line represents the difference between observed and calculated diffraction patterns. The dotted black line is the nuclear diffraction intensity. The diffraction patterns presented here were measured at 2K at D1B.

fingerprint for the presence of C_x and C_z component.

For the reported spin rotation of 4.6° degrees, the expected intensity of the (010) peak is ≈0.46% of the intensity of the strongest peak (101). If we consider only the reflections with net intensity exceeding three times the signal to noise ratio as unambiguously observable, such a weak signal lies at the boundary of the sensitivity of the analyzed data where the signal to noise ratio is defined as the ratio between intensity of the peak and noise which is defined as $\sqrt{I_{Bkg}}$ where I_{Bkg} is the intensity of the background. No intensity was observed at the (010) position in the current experiment.

Similarly, for the canting of 7° with basis vector A_z reported by Fogh et al., would produce a finite (100) peak intensity. The resulting intensity of the (100) peak would be ≈2.3% of the (101) intensity, Under the sensitivity of the collected data explained earlier this is observable. However, neither the (100) nor the (010) peaks were observed in any of the diffraction pattern for x= 0, 0.15 and 0.3. Therefore based on the absence of these specific peaks and the refinement of the data which accounts for the full set of magnetic reflections, the magnetic structure for

(H,K,L)	$\vert S_R(\mathbf{Q})\vert^2$				$\vert P_i(\mathbf{Q})\vert^2$		
	A (↑↓↓↑)	G (↑↓↑↓)	C (↑↑↓↓)	F (↑↑↑↑)	x	y	z
(301)	0.06	0.19	11.83	3.92	0.34	1	0.66
(100)	15.52	0.48	0	0	0	1	1
(010)	0	0	16	0	1	0	1

Table 6.4: Calculated squared structure and polarization factors for the basis vectors of the key reflections used to distinguish magnetic orders in LiCo$_{1-x}$Ni$_x$PO$_4$. The values are normalized to unit spin length.

x in LiCo$_{1-x}$Ni$_x$PO$_4$	μ_a	μ_b	μ_c	μ_{tot}	R_{fmag}	T_{N}(K)
0	-	3.25(2)	-	3.25(2)	3.40	22.45(0.01)
0.15	-	2.92(2)	-	2.92(2)	3.85	20.60(0.03)
0.3	-	2.58(2)	-	2.58(2)	3.94	18.56(0.10)
0.4	0.3(1)	2.28(2)	0.96(3)	2.49(2)	2.71	15.96(0.04)
0.5	0	1.31(4)	1.40(2)	1.92(3)	4.05	14.94(0.03)
0.6	0.38(8)	0.80(7)	1.87(2)	2.06(4)	2.17	15.85(0.03)
0.75	0.4(1)	-	1.94(2)	1.98(3)	5.60	18.40(0.02)
1	0.3	-	2.2	2.22	-	20.8

Table 6.5: Refined low-temperature average magnetic moments on the transition metal site for LiCo$_{1-x}$Ni$_x$PO$_4$ given in units of Bohr magnetons, μ_{B} along with the corresponding R values of the Rietveld refinements and the ordering temperatures extracted from the power law fits to the neutron diffraction data. The refined magnetic moment value for the x= 0.4 is for the low-temperature magnetic structure.The values quoted for LiNiPO$_4$ (x=1) are taken from Ref. [51].

these three compositions are best described by the Γ_4 model without any detectable spin canting, with magnetic moments completely along the *b*-axis.

The temperature-dependent neutron data collected between 2 K and 50 K were analyzed by fitting the integrated intensity to a power law function to determine the Néel temperature for each of the compositions as illustrated in figure 6.8 for x =0.4. No additional phase transitions were observed below the Néel temperature for any of the three compositions. The refined value of magnetic moment and corresponding reliability factor $R_{F,mag}$ are summarized in the table 6.5. Figure 6.7 illustrates the refinement of LiCoPO$_4$ as a representation of fit quality and the corresponding spin configuration is illustrated in figure 6.9.

x =0.4 :

For x= 0.4, The magnetic order is first observed at $T_{\mathrm{N}} \simeq 16.0$ K, as determined from the temperature dependence of magnetic reflection intensities. At $T_1 \simeq 9.8(4)$ K, a second magnetic phase transition is observed. In the temperature range $T_{\mathrm{N}} > T > T_1$ the observed diffraction pattern is best described by the irrep Γ_4 consistent with the C_y-type antiferromagnetic structure of $x = 0$,0.15 and 0.3 where the spins are aligned along the b-axis.

For temperatures below T_1, an additional magnetic peak appears at 2θ= 23.8° corresponding to the peak (010). The temperature evolution of the intensities of the (301) and (010) peak is indicated in the figure 6.8. The (301) peak contains a minor nuclear contribution which remains constant with temperature. The additional magnetic intensity below T_{N} for the (301) peak indicate an antiferromagnetic ordering of the C-type. The (301) peak has non-zero intensity for all spin directions of C-type structure as presented in table 6.4. In contrast, the (010) peak is purely magnetic and is non-zero only for C-type structures with spins aligned along a or c axis. Hence the absence of the (010) peak above T_1 combined with the presence of magnetic intensity on the (301) peak, confirms that the spins are aligned along b-axis in the temperature range $T_{\mathrm{N}} > T > T_1$. The appearance and growth of the (010) peak intensity below T_1 signifies the emergence of a spin rotation away from the b-axis described by C_x or C_z model. Thus, the different onset of magnetic intensities at the (301) and (010) peaks mark two succesive transitions upon cooling: first the C_y type order in consistant with the parent group magnetic structure, and second a spin reorientation, where the spins rotate away from the easy axis of the parent compound forming an oblique antiferromagnetic structure. The ordering temperatures $T_{\mathrm{N}} = 15.96(4)$ and T_1= 9.8(4) K were determined by fitting the intensities of the (301) and (010) peak to a power-law equation as illustrated in figure 6.8.

The low temperature diffraction pattern below T_1 is best described by a combination of irreps Γ_4+Γ_6 which corresponds to the non-standard setting of magnetic space group $P2_1/c$ $(-c, -a, b + c; 0, 0, 0)$. The refined magnetic structure in this oblique antiferromagnetic structure comprises a dominant C_y component of $2.28(2)\mu_{\mathrm{B}}$, a C_z component of $0.96(3)\mu_{\mathrm{B}}$ and a very small A_x component $0.3(1)\mu_{\mathrm{B}}$. The reliability of the A_x component of the structure is uncertain, as constraining it to zero or allowing it to vary freely does not alter the refinement quality. Hence an unambiguous conclusion on the existence of a magnetic moment component along a axis cannot

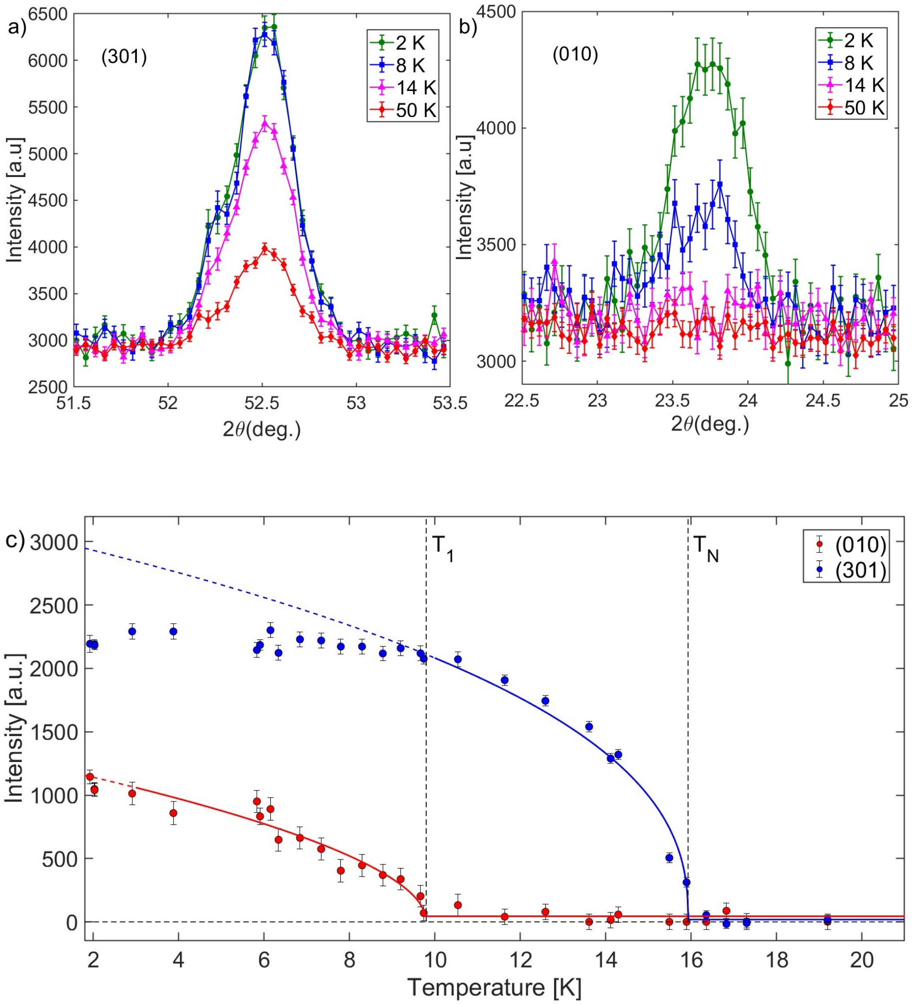

Figure 6.8: Temperature evolution of the observed intensities for (a) the (301) and (b) the (010) reflections. (c) Temperature dependence of the integrated intensities of the (301) and (010) reflections. The nuclear contribution to the (301) reflection has been subtracted, and the red and blue lines represent power-law fits for (010) and (301), respectively.

be drawn from the current data.

x=0.5, 0.6:

For $x = 0.5$ and 0.6, the diffraction patterns are best described by $\Gamma_4 + \Gamma_6$ for all temperatures below T_N. The refined model for x=0.5 yields excellent agreement with the observed diffraction pattern as shown in the figure 6.7 and the spin configuration of the refined oblique magnetic structure is represented in figure 6.9. The refined magnetic structure of x=0.5, closely agrees with the reported magnetic structure by Semkin et al. Although the present powder diffraction results indicate a statistical distribution of Co and Ni at the 4c Wyckoff site, were the literature report demonstrates a ordering of Ni and Co [100].

x=0.75

For x=0.75, the magnetic structure is best described by the irrep Γ_6, for all temperatures below T_N. The refined spins are oriented predominantly along the c axis described by the C_z model with a minor A_x component. This structure is consistent with the magnetic structure reported for the parent compound LiNiPO$_4$, which exhibits a dominant C_z-type structure and a minor spin component described by A_x model, derived from single crystal studies [51]. The refined magnetic structure for x=0.75 is illustrated in figure 6.9 and corresponding refinement results are represented in figure 6.7.

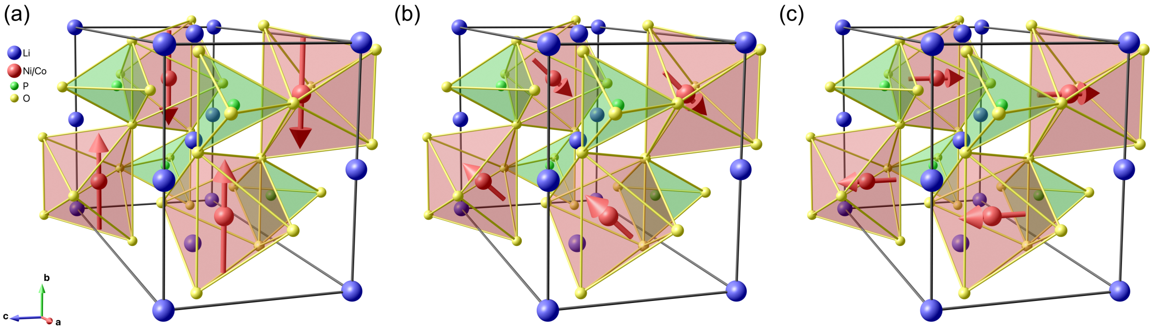

Figure 6.9: Refined magnetic structures for a) LiCoPO$_4$, b) LiCo$_{0.5}$Ni$_{0.5}$PO$_4$ and c) LiCo$_{0.25}$Ni$_{0.75}$PO$_4$. The figure shows the evolution of magnitude and orientation of the magnetic moment with increasing Ni content. The red arrow represents the magnetic moment. The length of the arrow represents the magnitude of the magnetic moment

6.5 Discussion

The composition-temperature phase diagram for LiCo$_{1-x}$Ni$_x$PO$_4$ determined from the neutron diffraction data is illustrated in figure 6.10. The evolution of the magnetic structure upon mixing ions with the ising like anisotropy of Co^{2+} in LiCoPO$_4$ with ions with XY-anisotropy as Ni^{2+} in LiNiPO$_4$ exhibits many features predicted in theory for such a mixed system with few key anomalies that require further discussions. With increasing Ni content, the magnetic structure of the system evolves from the Γ_4 structure of LiCoPO$_4$, in which the moments are parallel to the crystallographic b axis, to an intermediate oblique antiferromagnetic phase described by $\Gamma_4 + \Gamma_6$, where the magnetic moments are predominantly in the bc-plane and finally to the Γ_6 structure of the LiNiPO$_4$, with the magnetic moments along the c-axis. The rotation of the spin direction away from the respective easy axes of the parent compounds reflects the competition between the single-ion anisotropies of Co^{2+} and Ni^{2+}. The reduced value of of magnetic moment at x =0.5 further indicates the frustration arising from the competing anisotropy energies.

To add to the interpretation of the experimental magnetic phase evolution from this work, Monte Carlo simulations were performed as a part of the bachelor project of M. C. Larsen and M. Ravn-Feld under the supervision of N. B. Christensen at DTU Physics [105]. The simulations were based on the spin-Hamiltonian incorporating five exchange interactions (J_{bc}, J_b, J_c, J_{ab}, J_{ac}) as illustrated in figure 2.2 and single-ion anisotropy energy contribution charactrerized by $\mathbf{D}_i = (D_{x_i}, D_{y_i}, D_{z_i})$. The two non-zero components of $\mathbf{D_i}$ define the intermediate and hard axes, while the zero component defines the easy axis. This Hamiltonian has previously been reported to accurately describe the spin-wave spectra of LiMnPO$_4$, LiNiPO$_4$, and LiFePO$_4$ systems [36, 37, 106].

$$\hat{\mathcal{H}} = \sum_{\langle i,j\rangle} J_{ij}\,\mathbf{S}_i \cdot \mathbf{S}_j + \sum_{i,\alpha} D_i^{\alpha}\left(S_i^{\alpha}\right)^2$$

For LiNiPO$_4$, the exchange and anisotropy parameters were taken from the reported values [37], while those for LiCoPO$_4$ were obtained from a preliminary analysis of spin-wave dispersion data recorded for a LiCoPO$_4$ single crystal as summarized in table 6.6. In the mixed system LiCo$_{1-x}$Ni$_x$PO$_4$, the 4c Wyckoff site is randomly occupied by the Co^{2+} and Ni^{2+} ions. The Co-Co and Ni-Ni exchange interactions and anisotropy parameters were assumed to be the same as the parent compound whereas the Co-Ni exchange coupling parameters were taken to be the average of corresponding Co-Co and Ni-Ni terms. These simplifications have been shown to reproduce experimentally observed magnetic phases in the LiNi$_{1-x}$Fe$_x$PO$_4$ system [1].

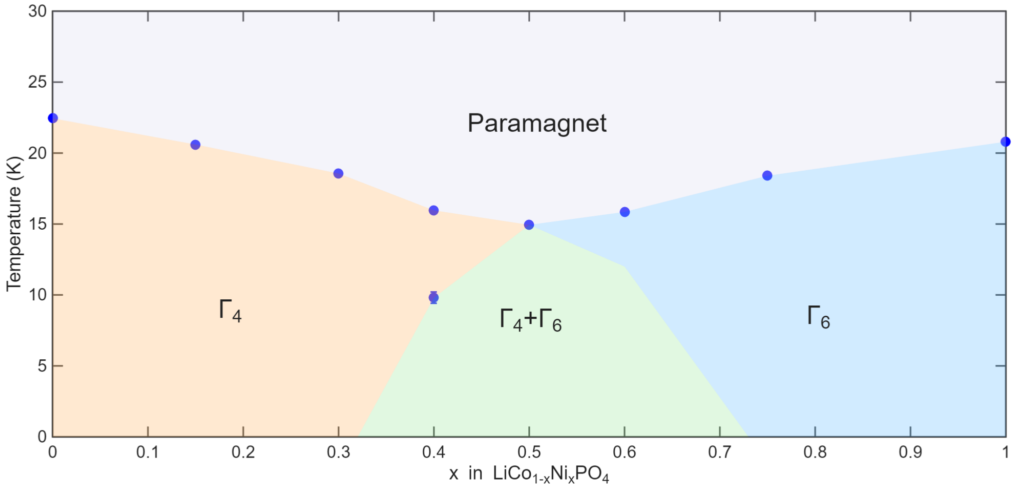

Figure 6.10: Experimental phase diagram of LiCo$_{1-x}$Ni$_x$PO$_4$. The observed points are represented by blue markers. The phase boundary between $\Gamma_4 + \Gamma_6$ and Γ_6 is not experimentally observed but is indicated in the phase diagram to indicate the tetracritical point. The true nature of Γ_4+Γ_6 to Γ_6 boundary needs to be determined in future studies. The value for x= 1 is taken from reference [17].

The simulations reproduce the key qualitative features of the experimentally observed phase diagram. The simulation produces three magnetic phases described by Γ_4, Γ_4+Γ_6 and Γ_6 mirroring the experimental observations. The Monte Carlo results predict a second transition below T_N from Γ_4 to $\Gamma_4 + \Gamma_6$ in the composition range $x \approx$ 0.2-0.5. This is consistent with the experimental obervation of a second-order low-temperature transition for the x = 0.4 composition, which exhibits a transition to the oblique $\Gamma_4 + \Gamma_6$ phase at T_1=9.8(4) K. In contrast the predicted Γ_6 to $\Gamma_4 + \Gamma_6$ low-temperature transition on the Ni-rich side is significantly less pronounced as illustrated in figure 6.11.

The theory outlined in section 2.0.5, predicts a tetracritical point in the composition-temperature phase diagram of a mixed anisotrpy magnets, where four second-order transition lines meet. However, in the current experimental phase diagram 6.10, only three well-defined second-order phase boundaries are detected. The low-temperature second order transition from the Ising-like structure (Γ_4) to the oblique ($\Gamma_4 + \Gamma_6$)

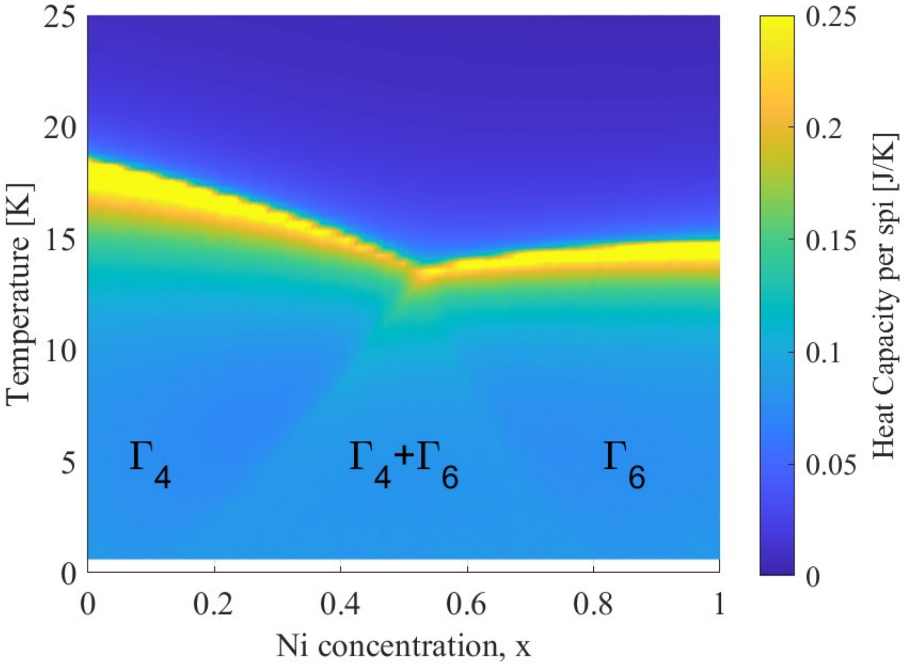

Figure 6.11: The magnetic phase diagram from the Monte Carlo simulations taken from the Bachelor thesis of M. C. Larsen and M. Ravn-Feld [105]

phase is clearly observed for $x = 0.4$ and is unambiguously identified through the appearance of purely magnetic (010) Bragg reflection. In contrast, the expected low-temperature transition from Γ_6 to $\Gamma_4 + \Gamma_6$ on the Ni-rich side of the phase diagram was not detected in the powder data.

The absence of an observable Γ_6 to $\Gamma_4 + \Gamma_6$ transition can be interpreted in terms of the experimental limitations associated with this symmetry change. While the Γ_4 to $\Gamma_4 + \Gamma_6$ transition can be detected by the appearance of the purely magnetic key reflection (010), the transition from Γ_6 to $\Gamma_4 + \Gamma_6$ does not generate a similar easily detectable pure magnetic transition. Hence the refinement is based on the Bragg reflections that have both nuclear and magnetic contributions and is limited by the correlations between nuclear and magnetic parameters, such as atomic positions, absorption etc. reducing the sensitivity to the weak reorientation effects. Moreover, while the data collected at the base-temperature is of high statistical quality to determine the ground-state structure unambiguously, the data sets collected for the temperature evolution, originally collected to identify T_{N}, have low statistical quality. Thus the subtle intensity changes associated with a weak oblique to planar transition may be below the detection threshold of the current powder data.

	S	J_{bc}	J_b	J_c	J_{ab}	J_{ac}	D_a	D_b	D_c
$LiNiPO_4$	1	1.04	0.67	-0.05	0.30	-0.11	0.339	1.82	0
$LiCoPO_4$	3/2	0.34	0.15	-0.11	0.15	0	1.3	0	0.65

Table 6.6: Spin quantum numbers, exchange constants, and single-ion anisotropy parameters (in meV) used in the Monte Carlo simulations [105]. The values for $LiNiPO_4$ is taken from literature [37]. The $LiCoPO_4$ values are from the preliminary spin-wave analysis. D_b was set to zero to reflect the known easy axis direction and J_{ac} was set to zero to reduce the number of parameters.

Beyond the experimental limitations, similar discrepancies in oblique-to-planar phase transition in mixed anisotropy magnets of an Ising-like anisotropy and XY-type anisotropy energies have been reported in systems such as $Fe_{1-x}Co_xBr_2$, $Fe_{1-x}Co_xCl_2$ and $K_2Mn_{1-x}Fe_xF_4$ as discussed in section 2.0.5. These studies highlight the site-dependent random field generated by the local compositional disorder and off-diagonal exchange terms, resulting in smearing of the planar-oblique phase transition into a broadened crossover instead of a sharp transition. In contrast, the Ising to oblique transitions remain comparitively robust under the effect of random-field effects [59, 107]. The absence of a well defined second-order transition between the Γ_6 and $\Gamma_4 + \Gamma_6$ phases may therefore be consistent with the mixed anisotropy systems reported previously.
To resolve the nature of the phase transition and determine the phase diagram more accurately, high-quality single crystal experiments, especially polarized neutron experiments which allow the seperation of different magnetic moment components should be utilized in future works.

The refined magnetic moment decreases with increasing Ni content, reaching a minimum at $x = 0.5$, before increasing slightly for further increase in Ni content. This behaviour paralles the minimum observed in ordering temperature indicating the enhanced frustration derived from the opposing anisotropy energies in the system.
The confirmed existence of toroidal order in $LiCoPO_4$, together with its strong dependence on the magnetic symmetry, suggests that the symmetry changes verified in the present work may have significant consequences for the ferrotroidal order across the series. The evolution of the toroidal moment was calculated by following the equation presented in section 2.0.3 for $LiCoPO_4$, where θ denotes the angle between

the magnetic moment and the b-axis.

$$\mathbf{t} = 2\mu\epsilon a \left(\cos\theta\,\hat{\mathbf{z}} + \sin\theta\,\hat{\mathbf{y}}\right) \tag{6.2}$$

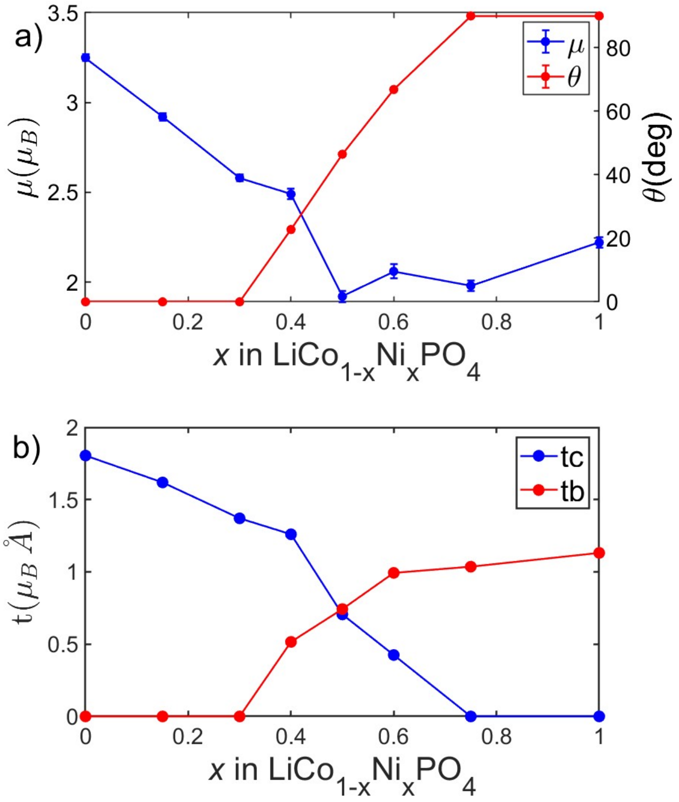

Figure 6.12: a) Compositional dependence of total magnetic moment magnitude and the canting angle θ. b) Compositional dependence of calculated toroidal moment component along b-axis(red) and c-axis(blue).

Figure 6.12 (a) illustrates the composition dependence of θ, demonstrating the increasing rotation of the magnetic moment from the b-axis towards the c-axis as Ni is introduced. This collinear rotation of magnetic moments produces a corresponding rotation of torroidal moment, illustrated in Figure6.12 (b). With increase in the Ni content, the component of the toroidal moment along the b axis increases, where as the component of toroidal moment along the c-axis decreases. Within the oblique phase, the toroidal moment lies in the bc-plane. This results in four symmetry allowed ferrotoroidal domains with different direction of toroidal moment. These results highlight the potential for domain manipulation and suggest possibilities of exploring the toroidal domain poling in this system, which could be of interest for multi-state memory systems.

The influence of this symmetry change of the system with chemical substitution on the magnetoelectric effect also warrants further investigation. In the similar mixed system of $\mathrm{LiNi}_{1-x}\mathrm{Fe}_x\mathrm{PO}_4$, 100-fold increase in the magnitude of magnetoelectric effect together with the appearance of magnetoelectric tensor elements that are prohibited by symmetry in both parent compounds are reported by Fogh et al. [1]. Similar studies on focusing on $\mathrm{LiCo}_{1-x}\mathrm{Ni}_x\mathrm{PO}_4$ could therefore provide important insight into how anisotropy driven symmetry lowering and emergence of oblique phase influence the magnetoelectric effect.

In summary, the $\mathrm{LiCo}_{1-x}\mathrm{Ni}_x\mathrm{PO}_4$ series, demonstrates the chemical tunability of the magnetic ground state and the experimental confirmation of the existence of oblique antiferromagnetic phase at the intermediate concentrations. The associated rotation of toroidal moment with composition present broader potential to explore competing anisotropies as a route to chemically tune physical properties governed by symmetry.

7

Magnetic Structures and phase transitions in $\mathrm{LiNi}_{1-x}\mathrm{Fe}_x\mathrm{PO}_4$

7.1 Motivation

In contrast to the mixed anisotropy system $\mathrm{LiCo}_{1-x}\mathrm{Ni}_x\mathrm{PO}_4$ examined in the previous chapter, substituting Ni^{2+} ions with Fe^{2+} ions in $\mathrm{LiNi}_{1-x}\mathrm{Fe}_x\mathrm{PO}_4$ provide interesting platform with the two parent compounds representing the orthogonal limiting cases within the lithium orthophosphate family: Ni^{2+} possesses an easy axis along c, which coincides with the hard axis of Fe^{2+}, while easy axis of Fe^{2+} along b-axis coinciding with the hard axis of Ni^{2+}. Exploring the composition phase diagram in $\mathrm{LiNi}_{1-x}\mathrm{Fe}_x\mathrm{PO}_4$ therefore provides a potential to explore magnetic moment rotation perpendicular to the easy axes of parent compounds and associated rich phase diagram predicted by theory in such mixed-systems.

Earlier experimental works on $\mathrm{LiNi}_{1-x}\mathrm{Fe}_x\mathrm{PO}_4$ for $\mathrm{LiNi}_{0.99}\mathrm{Fe}_{0.01}\mathrm{PO}_4$ from Mössbauer spectroscopy results and second harmonic generation (SHG) studies on $\mathrm{LiNi}_{0.94}\mathrm{Fe}_{0.06}\mathrm{PO}_4$ reported a magnetic structure similar to LiNiPO_4, with spins aligned along the c-axis and identified an incommensurate phase analogous to that of LiNiPO_4 [108, 109]. The significant motivation for the present work, however arises from the the neutron diffraction and magnetoelectric study reported by Fogh et al. for $\mathrm{LiNi}_{0.8}\mathrm{Fe}_{0.2}\mathrm{PO}_4$ [1]. The study reports two distinct magnetic phase transitions from magnetic susceptibility measurements and from polarized neutron experiments. A transition at 25 K into a antiferromagnetically ordered state with spins aligned along b-axis, followed by a second transition at 21 K to an oblique antiferromagnetic phase, where the spins rotate towards a-axis.Note that given the hard and easy axes of Ni^{2+} and Fe^{2+} ions, the rotation towards a is the best compromise from an energy perspective [1]. Moreover, the study reports an enhancement of magnetoelectric response by two orders of magnitude and the emergence of magnetoelectric tensor elements that are forbidden in both parent compounds, highlighting the sensitivity of the magnetoelectric effect to symmetry lowering induced by competing anisotropies. Monte Carlo simulations from the same study further predict a composition phase diagram for LiNi$_{1-x}$Fe$_x$PO$_4$ with an extended oblique antiferromagnetic phase where the spins are within the ab-plane.

These observations demonstrate the possibility and high impact of chemical tuning of the magnetic ground state on the physical properties such as the magnetoelectric effect. Importantly, the authors concluded that while the symmetry lowering alters magnetoelectric tensor and even though the magnetoelectric tensor is still governed by the symmetry of the magnetic structure in the oblique phase, the precise way the symmetry properties apply to the magnetoelectric effect remains unresolved. Hence mapping the exact evolution of magnetoelectric effect across the phase diagram could prove useful in providing insights on these key questions. A necessary first step in this direction is to determine the magnetic structure evolution across the composition phase diagram of the LiNi$_{1-x}$Fe$_x$PO$_4$. The present chapter aims to address this gap by exploring the compositional dependence of magnetic structure across the entire substituion phase diagram of LiNi$_{1-x}$Fe$_x$PO$_4$. The results from this chapter tracking the anisotropy driven magnetic symmetry changes through chemical substitution could provide a basis for the future studies on evolution and tuning of the symmetry governed physical properties such as magnetoelectric effect.

7.2 Temperature dependent magnetization measurements

The samples for this study was obtained from the collaboration with the research group of Prof. Efrain. E. Rodriguez at University of Maryland. LiNi$_{1-x}$Fe$_x$PO$_4$ single crystals used in this study was produced by the PhD students Hector Cein Mandujano and Cecilia Machiko Wheeler using a two step process. First step consisted of the solid state preparation of the precursors Li$_2$CO$_3$, NH$_4$H$_2$PO$_4$, FeC$_2$O$_4$ and NiCO$_3$ by mixing in ethanol. Then the mixed powder was subjected to a heat treatement at 250°C under Ar flow to decompose the ammonium phosphate and then it was rapidly heated to 780 °C to produce LiNi$_{1-x}$Fe$_x$PO$_4$, which contain

minor oxide impurities. The next step consisted of a LiCl flux growth, where the powder sample from the first step was mixed with LiCl in the molar ratio 1:3. The heat treatment was performed at 800°C under Ar. After cooling down, this procedure produced millimeter sized crystals of LiNi$_{1-x}$Fe$_x$PO$_4$ which was obtained by dissolving the flux in water and manually seperating the impurity Li$_3$PO$_4$.
The powder samples studied in this chapter was synthesized as single crystals and ground into powder form for x =0, 0.1, 0.2, 0.3, 0.5, 0.6 and 0.7. The temperature dependent magnetization for x =0.1, 0.2, 0.3, 0.5 and 0.6 was measured in the temperature range 2 - 300 K for powder samples at an applied magnetic field of 10000 Oe. These measurements were performed by. S. Guchhait and M. A. Dunstan using a Quantum Design Physical Properties Measurement System (PPMS) at DTU Chemistry. Figure 7.1 illustrates the measured susceptibility curves.

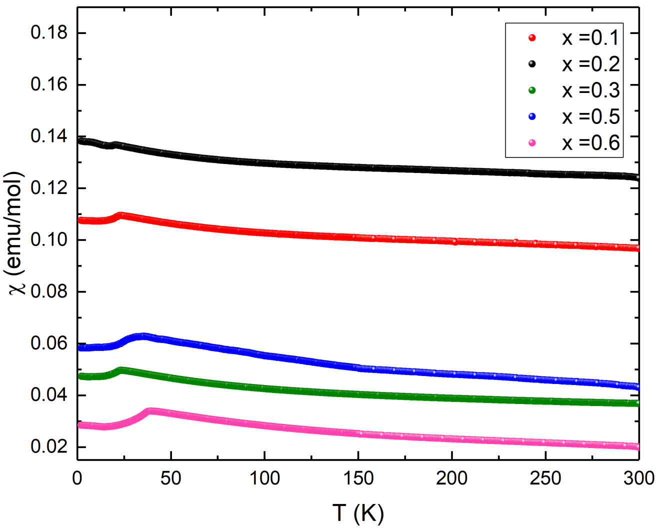

Figure 7.1: Temperature dependent magnetic susceptibility curves for LiNi$_{1-x}$Fe$_x$PO$_4$, x =0.1, 0.2, 0.3, 0.5 and 0.6. The measurements were perfomed in an external magnetic field of 10000 Oe.

The overall magnetic susceptibility in LiNi$_{1-x}$Fe$_x$PO$_4$, does not exhibit a monotonic trend from x = 0.1 to 0.6. All of them exhibit a cusp at the ordering temperature, characteristic of antiferromagnetic systems. A broadening of the cusp is observed for x =0.5 compared to other compositions. From the first derivative of the susceptibility the ordering temperatures were extracted and are summarized in table 7.1.

x in LiNi$_{1-x}$Fe$_x$PO$_4$	T_1	T_N
0.1	20.4(2)	22.2(2)
0.2	19.6(2)	-
0.3	20.0(2)	22.2(2)
0.5	25.0(2)	-
0.6	-	36.0(2)

Table 7.1: Ordering temperatures obtained from the first derivatives curve of the temperature-dependent magnetization.

7.3 Neutron diffraction data and analysis

Neutron powder diffraction measurements were employed to determine the nuclear and magnetic structure across the LiNi$_{1-x}$Fe$_x$PO$_4$ series. Rietveld refinement results and associated interpretations are explained in the following sections. The nuclear structure refinements were carried out using data collected on the instrument D2B with a wavelength of 1.59 Å, whereas magnetic structure analysis was performed using data acquired on the instrument D1B with a longer wavelength of 2.52 Å.

7.3.1 Nuclear structure analysis

Neutron diffraction data for the six compositions of LiNi$_{1-x}$Fe$_x$PO$_4$ were recorded at 100 K and 2K. The refinements were carried out with the structure defined by the orthorhombic space group $Pnma$, which is the established structure for the stoichiometric compounds in the lithium orthophosphate family [18]. The atomic positions and lattice parameters of the samples were refined with a manually defined background. The peak profiles were modelled using the TCH Pseudo-voigt function and asymmetry corrections were applied. The resulting lattice parameters and atomic positions from the refinements are summarized in table 7.2.

The refinement revealed the existence of a non magnetic secondary phase Li$_3$PO$_4$ for all compositions except for $x = 0.5$, for which no impurity peaks were detected above the noise level. For Ni rich compositions, additional unidentified weak impurity peaks were observed in the 2θ range of 40 to 50°. The site occupancies of Ni and Fe at the transition-metal site were fixed to the nominal composition, because the similar scattering length of Ni (1.03 fm) and Fe (0.94 fm) prevents the reliable refinement of the individual occupancies.

The refined lattice parameters across the series is plotted in figure 7.2. Although the lattice parameter variation does not follow Vegard's law strictly, a general expansion of the unit cell with increse in Fe content is observed. The deviation from the linear behaviour could be attributed to the change from the nominal concentration of Ni and Fe. From $x = 0.1$ to 0.7, a increases by approximately 0.83% and b increases by 0.78%, whereas the increase in c is only 0.02%. This suggests an anisotropic expansion predominantly within the ab plane of the olivine structure, while the c axis remains largely unaffected by Fe substitution. The observed and calculated diffraction patterns from the refinements of the 100K data are illustrated in figure 7.3.

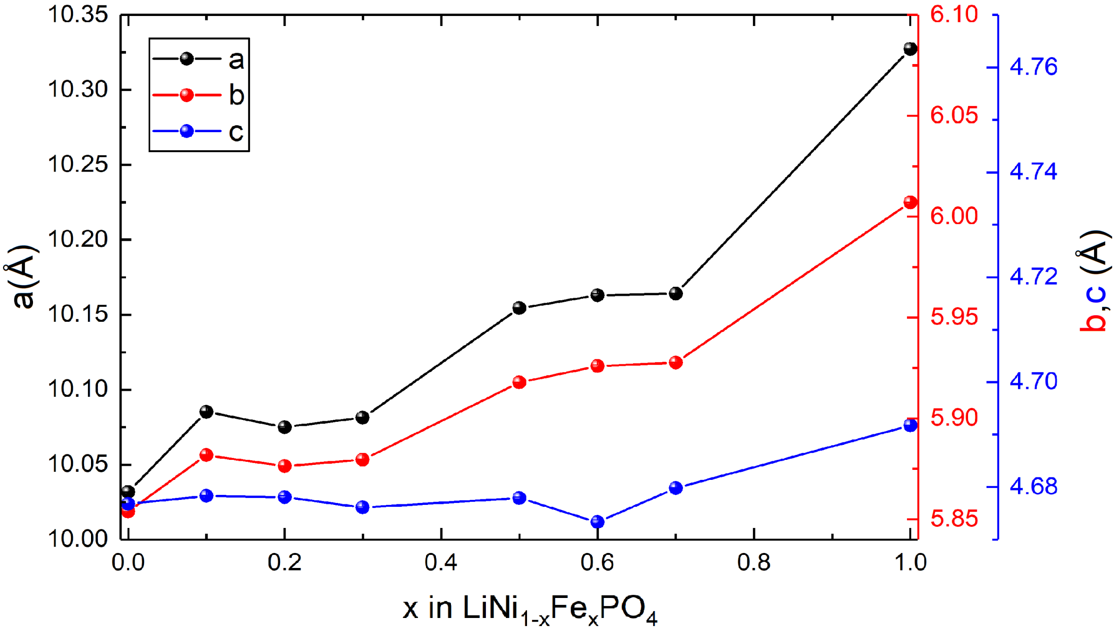

Figure 7.2: Composition dependence of the orthorhombic lattice parameters from the refinement of diffraction data collected at 100 K.

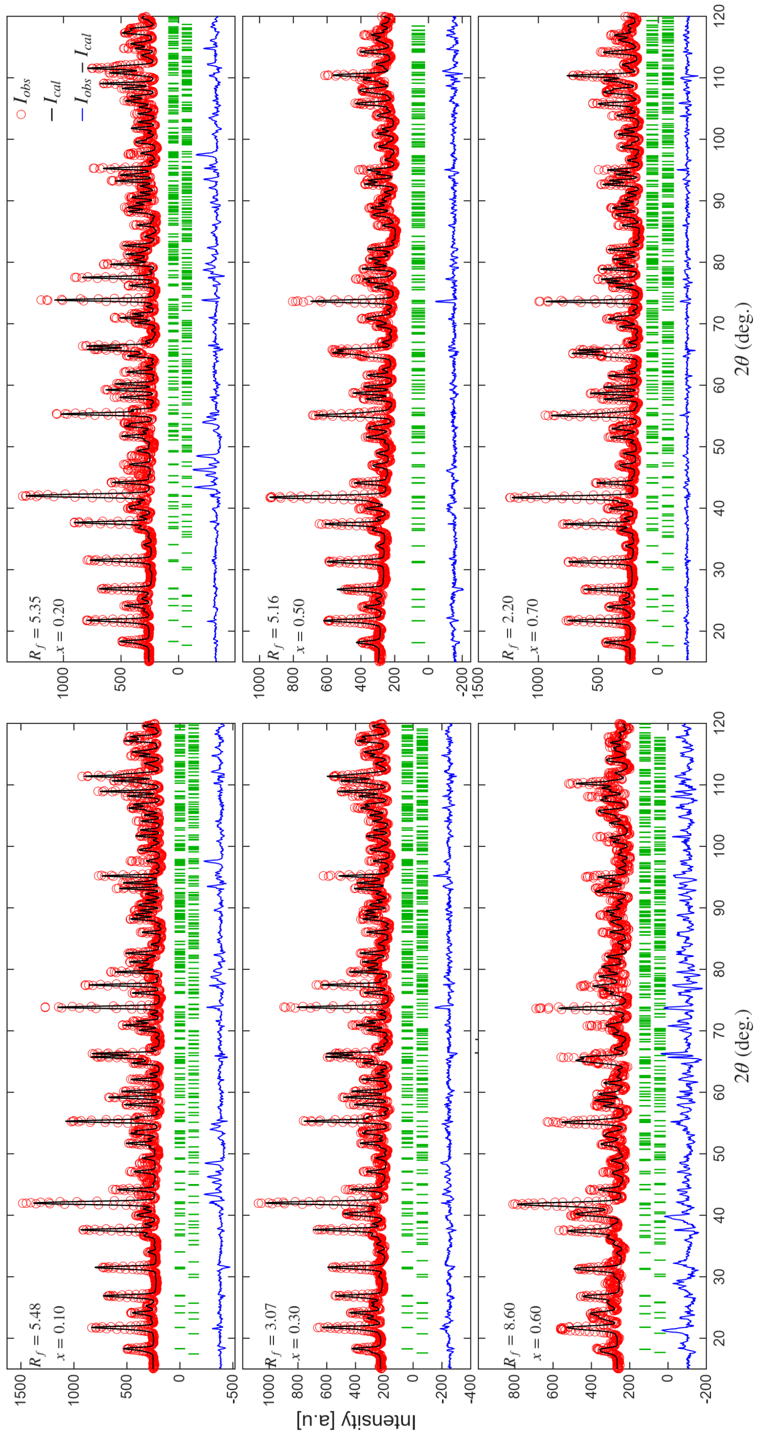

Figure 7.3: Observed (red marker) and calculated (black line) diffraction patterns from rietveld refinement of LiNi$_{1-x}$Fe$_x$PO$_4$. The first row of green ticks represents the Bragg peak positions for LiNi$_{1-x}$Fe$_x$PO$_4$ and the second row represents the Bragg positions for secondary phase Li$_3$PO$_4$.

x	Lattice constants [Å]	Atom	x	y	z	Occ.	R_f	Impurity (Normalized weight %)
0	a=10.0317(1)	Li	0	0	0	1		
		Fe/ Ni	0.2756(1)	0.250	0.9825(3)	0/1		
	b=5.8539(1)	P	0.0943(2)	0.250	0.4167(5)	1		
		O1	0.1008(5)	0.250	0.7427(10)	1	N/A	
	c=4.6768(1)	O2	0.4492(5)	0.250	0.1978(10)	1		
		O3	0.1668(4)	0.0439(6)	0.2783(7)	1		
0.1	a=10.0852(3)	Li	0	0	0	1		
		Fe/Ni	0.2770(2)	0.250	0.9812(5)	0.1/0.9		
	b=5.8818(2)	P	0.0954(4)	0.250	0.4182(8)	1		
		O1	0.0988(4)	0.250	0.7415(8)	1	5.48	3.9(5)
	c=4.6783(1)	O2	0.4517(4)	0.250	0.2035(8)	1		
		O3	0.1660(3)	0.0421(4)	0.2780(5)	1		
0.2	a=10.0749(5)	Li	0	0	0	1		–
		Fe/Ni	0.2768(4)	0.250	0.9822(9)	0.2/0.8		
	b=5.8764(3)	P	0.0942(8)	0.250	0.417(1)	1		
		O1	0.0987(7)	0.250	0.740(1)	1	5.35	10.6(6)
	c=4.6781(3)	O2	0.4508(6)	0.250	0.205(1)	1		
		O3	0.1659(5)	0.0416(7)	0.2788(9)	1		
0.3	a=10.0813(4)	Li	0	0	0	1		
		Fe/Ni	0.2772(2)	0.250	0.9818(6)	0.3/0.7		
	b=5.8796(2)	P	0.0944(5)	0.250	0.4183(9)	1		
		O1	0.0990(5)	0.250	0.7396(9)	1	3.07	22.4(4)
	c=4.6761(2)	O2	0.4515(4)	0.250	0.2032(9)	1		
		O3	0.1672(3)	0.0419(5)	0.2781(6)	1		
0.50	a=10.1543(4)	Li	0	0	0	1		
		Fe/Ni	0.2788(2)	0.250	0.9750(5)	0.5/0.5		
	b=5.9178(2)	P	0.0950(4)	0.250	0.4179(8)	1		
		O1	0.0945(4)	0.250	0.7450(9)	1	5.16	–
	c=4.6779(2)	O2	0.4532(4)	0.250	0.2041(8)	1		
		O3	0.1652(3)	0.0420(4)	0.2785(6)	1		
0.60	a=10.163(1)	Li	0	0	0	1		
		Fe/Ni	0.2786(5)	0.250	0.972(1)	0.6/0.4		
	b=5.9259(7)	P	0.096(1)	0.250	0.424(2)	1		
		O1	0.090(1)	0.250	0.736(2)	1	8.60	26.7(7)
	c=4.6733(5)	O2	0.4524(9)	0.250	0.204(2)	1		
		O3	0.1637(8)	0.041(1)	0.276(1)	1		
0.70	a=10.1640(2)	Li	0	0	0	1		
		Fe/Ni	0.2782(1)	0.250	0.9781(3)	0.7/0.3		
	b=5.9277(1)	P	0.0940(3)	0.250	0.4179(5)	1		
		O1	0.0979(2)	0.250	0.7438(5)	1	2.20	5.0(2)
	c=4.6798(1)	O2	0.4539(2)	0.250	0.2049(5)	1		
		O3	0.1659(2)	0.0440(3)	0.2808(3)	1		
1	a=10.32731(5)	Li	0	0	0	1		
		Fe/Ni	0.28218(2)	0.250	0.97473(4)	1/0		
	b=6.00707(3)	P	0.09482(3)	0.250	0.41824(6)	1		
		O1	0.09695(3)	0.250	0.74267(4)	1	N/A	
	c=4.69175(2)	O2	0.45714(3)	0.250	0.20568(7)	1		
		O3	0.16550(2)	0.04682(3)	0.28506(4)	1		

Table 7.2: Refined Structural parameters for LiNi$_{1-x}$Fe$_x$PO$_4$ at $T = 100$ K. Values for $x = 1$ and $x = 0$ are from the structures reported in Refs. [32, 33]

7.3.2 Magnetic structure analysis

Neutron diffraction data were obtained at base temperature to determine the magnetic ground state of the system. In addition, temperature dependent diffraction data were recorded to determine the ordering temperatures and to track the magnetic structure evolution with temperature. At the base temperature, additional magnetic intensities appear at the integer (h,k,l) positions, consistent with the propagation vector $\mathbf{k} = (0, 0, 0)$ for all compositions. This is consistent with the low temperature magnetic structure reported for the stoichiometric compounds and for the mixed compositions of x =0.06 and 0.2 [1, 18, 51, 109, 110].

For the refinement of the low temperature data, the crystal parameters were taken from the results of Rietveld refinement of diffraction data collected on D2B with shorter wavelengths. Each of the symmetry allowed irreducible representation was tested to determine the magnetic structure model that yield the best agreement between observed and calculated diffraction patterns as described in 6.

x = 0:

For the parent compound, LiNiPO$_4$, temperature dependent measurements were carried out to probe the reported existence of commensurate to incommensurate transition at 20.8 K represented by the appearance of satellite peaks at (010) reported by Vaknin et.al [52]. They reported the appearance of satellite peaks in the range of K=0.9-0.92 and K=1.08-1.1, at the temperature 20.99 K. In the present work the satellite peaks are expected to appear in the 2θ range of ≈22.3°-22.9° and at ≈26.9°-27.5° with the wavelength of λ = 2.52Å and b=5.8539Å. However, in the neutron powder diffraction experiment, the reported satellite peaks were not observed as represented in figure 7.4. A single magnetic phase transition from paramagnetic to antiferromagnetic transition was observed at approximately 21.47 K.

x = 0.1, 0.3, 0.5, 0.6 :

For the compositions x = 0.1, 0.3, 0.5 and 0.6, two magnetic phase transitions are observed upon cooling. This is consistent with the expected behaviour of mixed anisotropy antiferromagnets, where the competing single-ion anisotropies stabilize an oblique antiferromagnetic phase at intermediate concentrations. The above mentioned compositions first orders at the temperature T_N, identified by the appearance of magnetic Bragg intensities consistent with the irreducible represesentation Γ_4, where the magnetic moment are aligned along the b axis (C_y). This magnetic structure is similar to the dominant magnetic component in the end compound LiFePO$_4$.

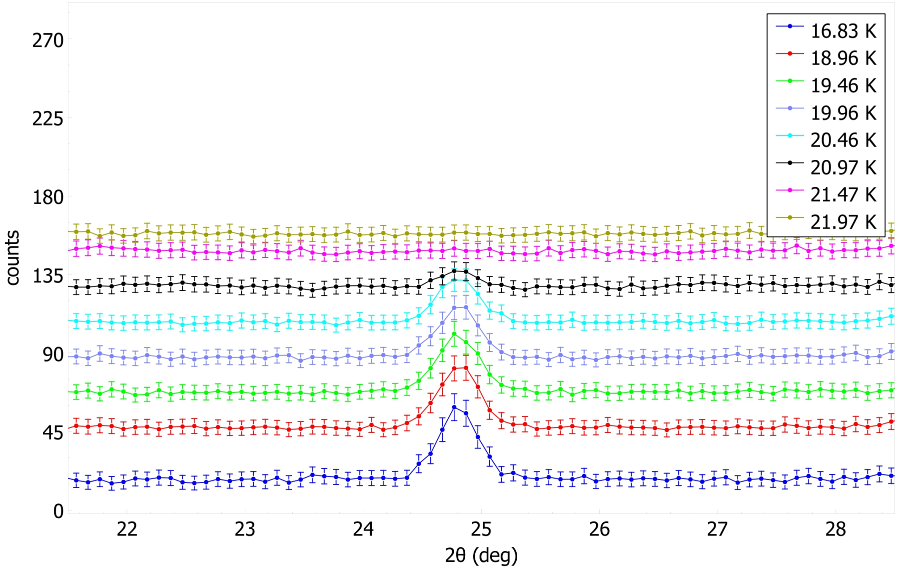

Figure 7.4: The (010) peak intensity evolution near the transition temperature. The diffraction patterns are shifted in intensity for clarity.

An ordering of this type give rise to magnetic intensity at reflections such as (101) and (301).

As the temperature is lowered further, a second magnetic phase transition is observed, signalled by the emergence of intensity at the (010) peak. The appearance of this peak indicates the introduction of a magnetic moment component perpendicular to the b axis, corresponding to the C_x or C_z basis vector, as discussed in detail in chapter 6. Since the (301) and (101) reflections possess non-zero structure factors for all C-type magnetic moment orientations, whereas the (010) is sensitive only to C_x and C_y (table 6.4), the different onset temperatures of (010) and (301)/(101) peaks clearly mark the phase transition driven by the rotation of spins away from the b axis in these compositions.

The ordering temperatures associated with the two magnetic transitions were obtained by the power law fit of the integrated intensities of the relevant peaks over a temperature range extending from base temperature to the paramagnetic region. The lower transition temperature, at which the system enters an oblique antiferromagnetic phase is denoted by T_1.

For all compositions exhibiting two transitions, refinement of the diffraction patterns in the intermediate temperature region $T_1 < T < T_N$ confirm that the magnetic structure in this range is of the Γ_4 type. In contrast, the refinements of the base temperature data ($T < T_1$) yield the best agreement with the combination of irreps $\Gamma_2 + \Gamma_4$. The Γ_2 representation allows C_x and A_z components, however in the refined structures, A_z is close to zero. The resulting oblique antiferromagnetic structure thus consists of magnetic moments collinearly rotated away from the *b* axis and confined to the *ab*-plane.

It is important to note that powder diffraction data of the current data quality cannot unambiguously distinguish between the mixed representations $\Gamma_2 + \Gamma_4$ and $\Gamma_4 + \Gamma_6$, the latter corresponding to a rotation of magnetic moments in the *bc*-plane. The refinement using both combinations produce fits with similar quality. In this work, however the $\Gamma_4 + \Gamma_6$ structure is considered less possible on the basis of single crystal polarized neutron diffraction and magnetic susceptibility results for $\mathrm{LiNi}_0.8\mathrm{Fe}_0.2\mathrm{PO}_4$ reported by Fogh et al. [1]. This study unambiguously demonstrated the existence of a significant component of magnetic moment along *a*-axis and contradicts the magnetic moment rotation towards *c*-axis suggested from SHG measurements reported by Zimmermann et al. [109].

The two transitions observed for each composition are indicated in figure 7.5 thorugh the different onset temperature of the peks (010) and (301)/(101). From this a clear trend in ordering temperatures can be identified, with increasing Fe content, the upper transition temperature increases and the separation between the two phase transitions grows correspondingly. The refined magnetic moment and the the transition temperatures for all compositions are summarized in table 7.3.

x = 0.7:

For the composition x =0.7, only a single magnetic transition is observed at T_N = 38.0(1) K. Below this temperature, the system orders with magnetic moment along *b*-axis, and the magnetic structure at all temperatures is described by Γ_4. The magnetic structure refinement at base temperature yields a good quality fit as represented in figure 7.6.

x = 0.2

For the composition x =0.2, the behaviour in this study contrasts with previous reports. Two magnetic transitions, one at 25 K, below which the system orders with spins along *b* axis, and the second at 21 K below which the magnetic moment rotates towards *a* axis as described by irrep $\Gamma_2 + \Gamma_4$ were reported for this composition. In the present measurements only one transition at T_N = 20.0(1) K was observed. For

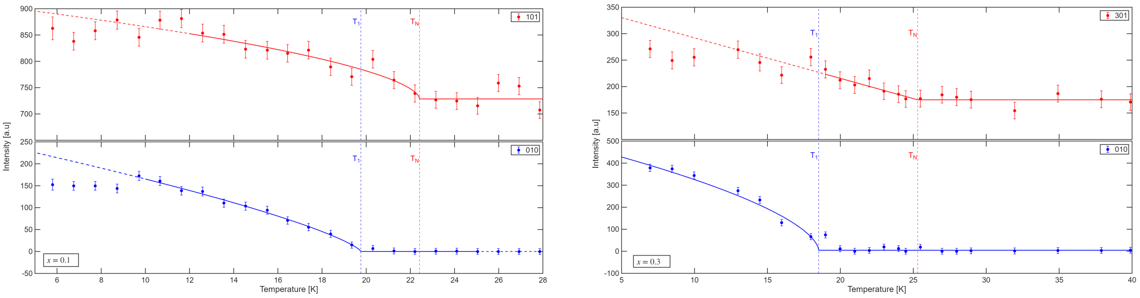

(a) x = 0.1

(b) x = 0.3

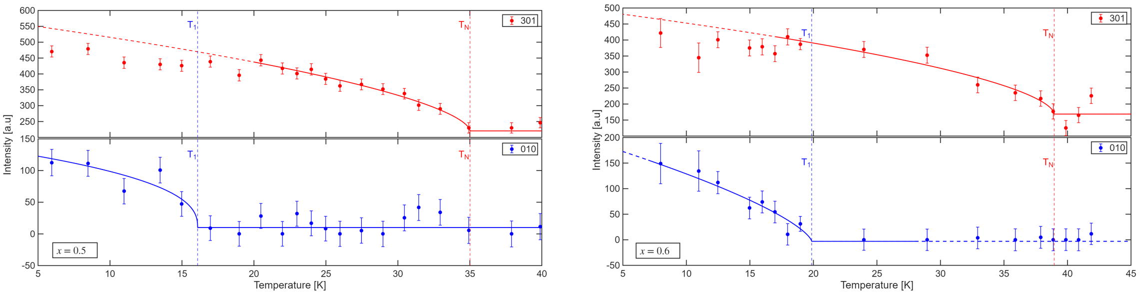

(c) x = 0.5

(d) x = 0.6

Figure 7.5: Temperature dependence of magnetic Bragg intensities for four compositions, $x = 0.1$, 0.3, 0.5 and 0.6.

all temperatures below T_N, the (010) peak exhibits considerable intensity which indicates the absence of reported Γ_4 only intermediate phase. The refinement of neutron powder diffraction data at base temperature, yields similar quality of fit for Γ_6 structure, identical to that of the end member LiNiPO$_4$ and for the combination of irreps $\Gamma_2+\Gamma_4$, corresponding to the oblique antiferromagnetic phase observed in for other compositions and also the reported for x =0.2 in literature. In additon to these models, the combination of irreps Γ_2+Γ_6 yields a slightly improved fit for the powder diffraction data with non-zero C_x and C_z components. This suggests a rotation of the spins within the ac-plane, a scenario that contradicts both the experimentally established magnetic structure for the compositionally accurate x=0.2 sample and the proposed antiferromagnetic phases in the phase diagram from

Monte Carlo simulations in LiNi$_{1-x}$Fe$_x$PO$_4$ reported by Fogh et al. [1]. Owing to this ambiguity, the magnetic structure of x=0.2 composition is further discussed in the next section using the spherical neutron polarimetry technique.

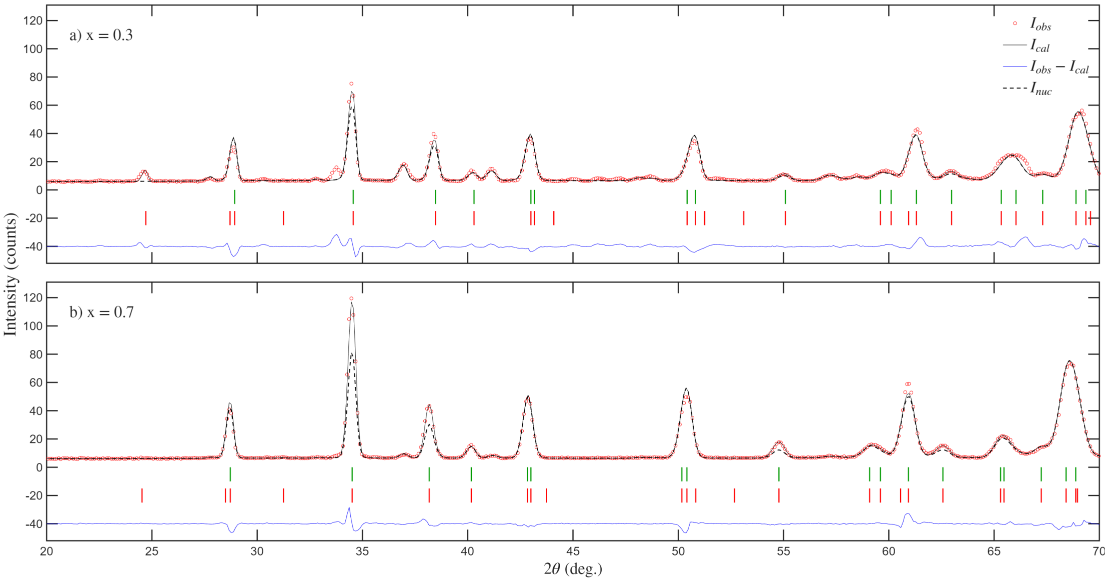

Figure 7.6: Refined powder diffraction pattern recorded at 2K. a) top panel illustrates the observed and calculated pattern for $x = 0.3$, representing the refinement result for $\Gamma_2 + \Gamma_4$ model structure observed in the system. b) Observed and calculated pattern for $x = 0.7$ for the base temperature Γ_4 model. The green ticks on the first row represent the nuclear Bragg peak positions whereas red ticks on the second row represent magnetic Bragg peak positions. The dotted black line represent the calculated pattern for nuclear contribution.

7.3.3 Spherical neutron polarimetry of LiNi$_{0.8}$Fe$_{0.2}$PO$_4$

To further investigate the magnetic structure of the $x = 0.2$ composition, spherical neutron polarimetry (SNP) measurements were performed on a single crystal selected from the same batch used for the powder diffraction studies. SNP measurements allows different components of the magnetic moment to be distinguished. In antiferromagnets, the sign and magnitude of the off-diagonal elements of the polarization matrix provide a characteristic fingerprint of the magnetic moment orientation, if there is a population difference between the symmetry allowed domains. The mechanism responsible for domain selection and the detailed interpretation of the polarization matrix elements are discussed in chapter 8 in detail. This section focuses on the magnetic structure refinement of the x=0.2 crystal used for the powder diffraction and the reason for the deviation from the reported behaviour for the x=0.2 compound studied in Ref. [1].
The crystal was aligned with b-axis along the vertical direction and ac-plane in the scattering plane. According to the SNP coordinate convention, the vertical direc-

x	μ_a	μ_b	μ_{total}	Rf$_mag$	T$_2$	T$_N$
0	0.3	-	2.22	-	-	20.8
0.1	1.74(6)	1.5(1)	2.30(8)	14.23	19.7(4)	22.4(6)
0.2	1.40(4)	1.46(9)	2.03(7)	8.21	-	20.0(1)
0.3	1.30(9)	1.4(2)	1.9(2)	7.67	18.2(2)	25.9(6)
0.5	0.66(9)	2.73(7)	2.81(7)	6.18	16.0(1.0)	35.0(1)
0.6	0.8(2)	2.9(1)	3.0(1)	12.53	19.0(1.0)	38.0(2)
0.7	-	3.0(3)	3.0(3)	3.59	-	38.0(1)
1	0.067	4.09	4.09	-	-	50

Table 7.3: Refined magnetic moment values and the ordering temperature determined from the temperature dependency of Bragg peak intensities. The refined magnetic moment values correspond to the structure observed at base temperature (2 K) . The values for $x=$ 0 and 1 are taken from references [38, 51]. The values indicated for x=0.2 is for the $\Gamma_2 + \Gamma_4$ magnetic structure which gave reasonable results for the refinement of the powder diffraction data. The structure and magnetic moment components of x=0.2 is discussed further in section 7.3.3.

tion is defined as the z axis, the scattering vector Q defines the x axis, and the y axis completes the right-handed coordinate system. The field cooling procedure that has successfully demonstrated to generate reproducible domain imbalance in LiNi$_{0.8}$Fe$_{0.2}$PO$_4$ (See Chapter 8), was applied to the present crystal to preferentially populate one of the symmetry allowed domains. Where an electric field is applied along b-axis and magnetic field is applied at an angle of 30 ° to the a-axis in the ac-plane.

For the reported structure [1] of a $x = 0.2$ sample, the expected oblique structure at the base temperature is described by $\Gamma_2 + \Gamma_4$, with the moments in the ab plane. With the present alignment of the crystal, and in case of domain imbalance, a magnetic moment along the b axis produces a non-zero P_{xy} term in polarization matrix which is sensitive to the z component of the magnetic moment, while a magnetic moment in the (ac) scattering plane produces a non-zero P_{xz} term which is sensitive to the y component of the magnetic moment. The full polarization matrices for the reflections (101), (201), (202),(301) and (400) were recorded at 2K and refined in correlation with the powder diffraction data.
Even prior to the refinement, the measured polarization matrix exhibited a small P_{xy} with a significantly non-zero P_{xz}, as illustrated in table 7.4, which compares the polarization matrices measured at 30 K (paramagnetic region) and at 2K for the

reflection (101). This indicates the absence of magnetic moment along the SNP z direction which is along the crystallographic *b*-axis and the existence of a magnetic moment component in in the *ac*-plane.

Q	$T = 2\,\mathrm{K}$			$T = 30\,\mathrm{K}$		
(1 0 1)	0.686(4)	−0.027(4)	−0.099(4)	0.929(4)	−0.038(5)	0.002(5)
	0.021(4)	0.932(3)	0.017(4)	−0.038(5)	0.926(4)	0.007(5)
	0.078(4)	0.008(4)	0.695(4)	−0.008(5)	0.005(5)	0.931(4)

Table 7.4: Observed polarization matrix measured at the (101) reflection at 2K and at 30K (paramagnetic region)

Figure 7.7 illustrates the temperature dependence of diagonal elements of the polarization matrix elements measured at the (101) reflection. In the paramagnetic regime, all three elements approach unity as there is only a nuclear contribution. As discussed in section 8.3, P_{xx} is sensitive to the total magnitude of the ordered moment whereas P_{yy} and P_{zz} are sensitive to the magnetic moment direction. Throughout the measured temperature range, P_{yy} remains nearly temperature independent, close to the nuclear value, consistent with the absence of magnetic moment component along z axis. In contrast, P_{xx} and P_{zz} exhibits almost similar temperature dependence. Upon cooling from the high temperature to the base temperature, P_{xx} and P_{zz} drop rapidly below 25 K, indicating magnetic ordering, reaching values of approximately 0.70 at the base temperature. The temperature independence of P_{yy} and the nearly identical magnitude and temperature dependence of P_{xx} and P_{zz} indicate that the magnetic interaction vector is nearly entirely perpendicular to the z-axis (crystallographic *b*-axis). The dominant trend in the measured diagonal elements is consistent with the temperature dependence of magnetic Bragg peak intensities observed in the powder diffraction data. A more finely resolved temperature measurements in the range 18-25 K is needed to unambiguously rule out the existence of a pure Γ_4 high-temperature phase, although no indication of such a intermediate phase is observed in the present data set.

Correlated refinements of the polarization matrices and the powder diffraction data were tested for the structure models that provided the best agreement with powder diffraction data: Γ_6, $\Gamma_2+\Gamma_4$ and $\Gamma_2+\Gamma_6$. Compared to the Γ_6 model, better agreement factors for the correlated refinements were obtained for the $\Gamma_2+\Gamma_4$ model, in which the C_y component associated with Γ_4 is driven to zero. The resulting mag-

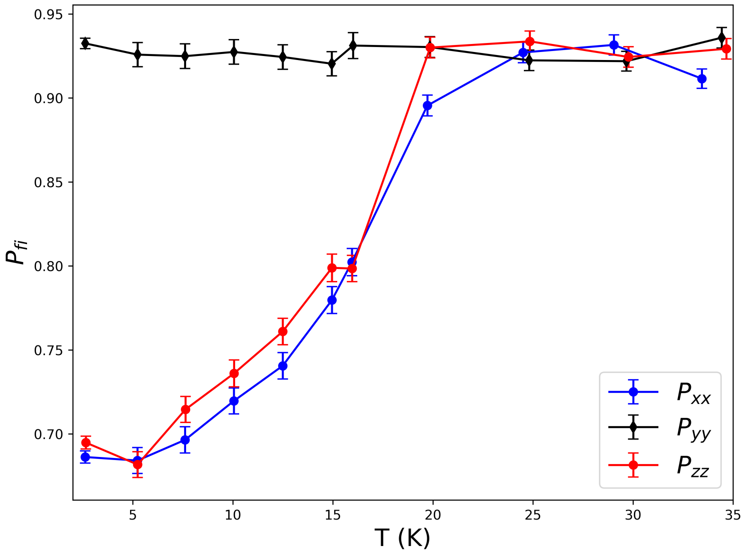

Figure 7.7: The temperature dependence of diagonal elements of the polarization matrix at the reflection (101)

Irreps	μ_a	μ_b	μ_c	μ_{total}	Rf_{mag}
$\Gamma_2+\Gamma_6$	1.62(7)	-	1.11(5)	1.96(9)	8.59
$\Gamma_2+\Gamma_4$	3.04(4)	0	-	3.04(4)	10.83

Table 7.5: Refined magnetic moments from correlated refinement of SNP and powder diffraction data (Figure 7.8) and the corresponding agreement factors for x=0.2

netic structure therefore reduces to Γ_2 with only non-zero component of C_x-type, consistent with the observed large P_{xz} and near absence of P_{xy}. The $\Gamma_2+\Gamma_6$ model provide the best agreement factor among the three considered models. For this model, C_x and C_z are non-zero agreeing with the powder diffraction results. This model also agrees with the absence of magnetic moment component along b-axis and accounts for the observed non-zero P_{xz} term of the (400) reflection which possesses non-zero structure factors for C_y and C_z components better than the pure Γ_2 model.

For a fully unambiguous determination of magnetic structure, SNP measurements can be complemented by single crystal neutron diffraction experiments to better model extinction parameters and for better determination of magnetic moment magnitude. Figure 7.8 presents the results of the correlated refinements for $\Gamma_2+\Gamma_4$ and $\Gamma_2+\Gamma_6$ model for the x=0.2 sample.

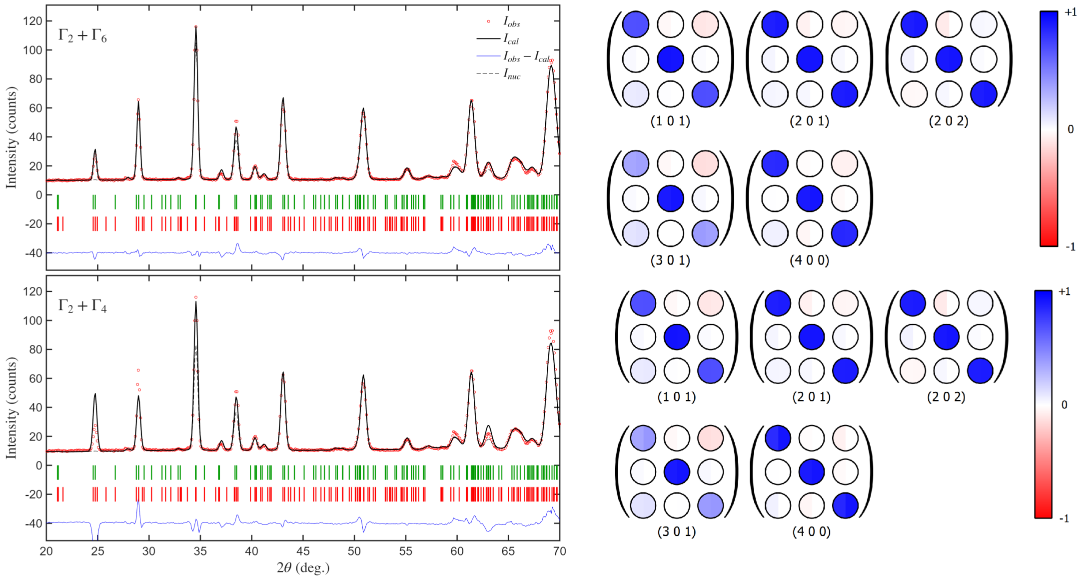

Figure 7.8: Results from correlated refinement of powder diffraction and spherical neutron polarimetry data for $x = 0.2$. The top panel represents the fit for $\Gamma_2 + \Gamma_6$ model and bottom panel the fit for $\Gamma_2 + \Gamma_4$ model. The polarization matrices for the four observed reflections are represented in the figure. The left and right part of each matrix elements represent the observed and calculated values according to the color code from the bar represented next to the matrices.

7.3.4 Discussion

The composition-temperature phase diagram for LiNi$_{1-x}$Fe$_x$PO$_4$ reveals a rich evolution of magnetic structures arising from the competition of single-ion anisotropies and exchange interactions. Mixing LiNiPO$_4$ with c, a and b as easy, intermediate and hard axes respectively, with LiFePO$_4$ where b, a and c are the easy, intermediate and hard axes, produces a phase-diagram that exhibits characteristic features expected for the mixed anisotropy antiferromagnets.

For compositions $x = 0.1$, 0.3, 0.5 and 0.6, two magnetic phase transitions are observed upon cooling: a high temperature transition to a LiFePO$_4$ like Γ_4 structure and a lower temperature second order phase transition to a oblique antiferromagnetic phase described by $\Gamma_2 + \Gamma_4$. For x=0.7, a single magnetic phase is observed with Γ_4 structure similar to LiFePO$_4$. Refinements below the ordering temperature for the end compound LiNiPO$_4$ confirm the stabilization of the Γ_6 magnetic structure on the Ni rich side of the phase diagram. These observations mirror the qualitative trends predicted by the Monte Carlo simulations of Fogh et al. [1], while also exhibiting important deviations.

While the MC simulations for x=0.1 predicts an initial transition to the oblique phase at high temperature followed by a second transition to Γ_6 upon cooling, experimentally the x=0.1 sample undergoes a transition to Γ_4 first, followed by a transition to the oblique antiferromagnetic phase where the spins are rotated in the *ab*-plane. This could indicate a possible deviation of the composition of the measured sample towards higher Fe content, on comparing with the MC phase diagram. In addition, the previously reported narrow incommensurate phase of $LiNiPO_4$ was not detected. This may be attributed to the resolution limitations. However no peak broadening indicative of incommensurate structure were observed near the transition temperature.

The most significant deviation from earlier reports is observed for the nominal x=0.2 composition. Contrary to the previously published study by Fogh et al, our sample exhibit only one magnetic transition at 20.0(1) K and a pure Γ_4 phase is not observed for this compound. Comparison with the MC phase diagram suggest that the ambigous magnetic structure of this sample is likely rooted in a deviation from the intended concentrations ($x < 0.2$). However, according to the MC simulations, for a deviation of this type (Ni-rich composition), the magnetic structure would be a narrow Γ_4 phase followed by a second transition to the *ab*-plane oblique antiferromagnetic phase or for an even high Ni concentrations, a transition to oblique and then to a Γ_6 phase is expected. In the present case, the analysis from spherical neutron polarimetry data and powder diffraction data, indicate that the magnetic structure with $\Gamma_2 + \Gamma_6$ provides slightly better result than $\Gamma_2 + \Gamma_4$ model and Γ_6 model. This phase is not predicted in the MC phase diagram.

Theoretical considerations for mixed-anisotropy systems by Oguchi and Ishikawa [61] provides predicted phase diagrams for such systems. Their model treats a mixture of an antiferromagnet A with easy, intermediate and hard axes x, z and y, with another antiferromagnet B with easy, intermediate and hard axes y, z and x. The model predics two types of phase diagrams. The first phase diagram (Type 1) contains a single oblique antiferromagnetic phase where the spins rotate within the xy plane, i.e. the plane formed by the easy axes of A and B. The second phase diagram (Type 2) features three distinct oblique antiferromagnetic phases where the spins lie in the xz and yz planes and along z-axis. The balance between the

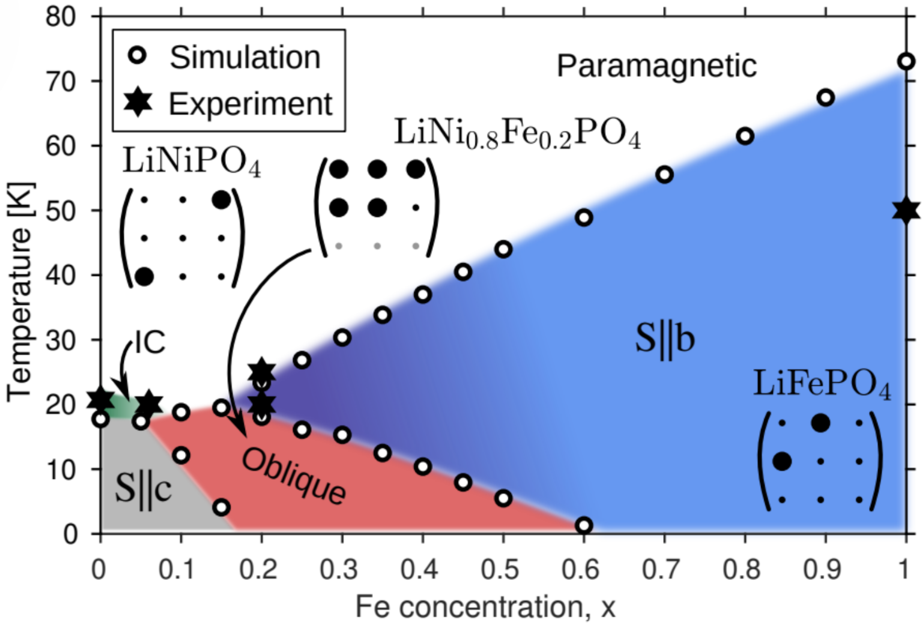

Figure 7.9: Monte-Carlo phase diagram for LiNi$_{1-x}$Fe$_x$PO$_4$.Figure taken from [1]

anisotropy energies determine the type of phase diagram realized in a given system. The phase diagram for the system Ni$_x$Co$_{1-x}$Cl$_2$.6H$_2$O is an example for the type 2 phase diagram (figure 7.10) [61]. In LiNi$_{1-x}$Fe$_x$PO$_4$, a $\Gamma_2+\Gamma_4$ oblique phase is already predicted by MC simulation and validated by the experimental work in Ref. [1] and by the present experimental observations. The observation of $\Gamma_2+\Gamma_6$ which contradicts with the MC simulation results, is validated from the theory models for similar systems as seen in reference [61]. However in comparison with the theoretically predicted model, the expected third oblique phase described by Γ_2 was not observed in the system. In the experiments and in simulations by Fogh et al., an extended oblique antiferromagnetic phase without a stabilization of a long-range a-axis phase at any concentration of Fe is indicated. intermediate a-axis phases, predicted by theory can be suppressed or be entirely absent in experimental systems due to factors such as local anisotropy fluctuations, chemical disorder, exchange frustration and site dependent interactions.

The experimental phase diagram with the exception of x=0.2 is illustrated in figure 7.11, where the indicated phase boundaries are obtained by interpolating experimentally determined transition temperatures. The indicated tetracritical point is obtained by extrapolating the experimentally observed transitions for x=0.1 and

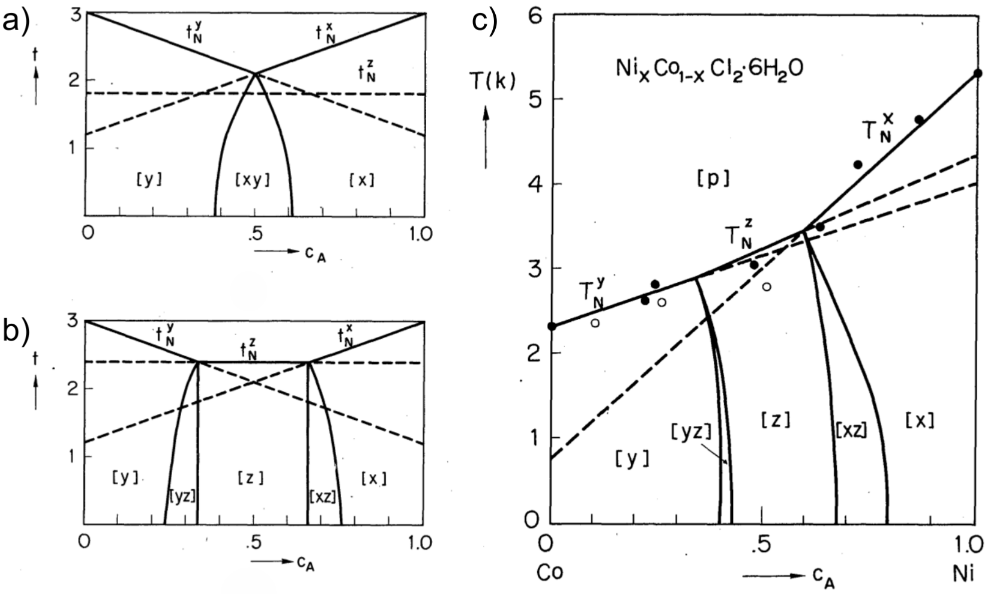

Figure 7.10: Theoretically predicted phase diagrams of mixed anisotropy magnets where a) Represent type 1 phase diagram where a single oblique antiferromaagnetic phase is present with spins in the plane spanned by the easy axes of parent compounds b) Type2 phase diagram where three oblique antiferromagnetic phases are present. Figure taken from [61]. c)Magnetic phase diagram of Ni$_x$Co$_{1-x}$Cl$_2$.6H$_2$O taken from Ref. [61].

previously reported phase transitions for x=0.06 [110]. A central source of uncertainity in the experimental phase diagram arises from the inability to determine the relative concentration of Ni^{2+} and Fe^{2+} using neutron diffraction. Small deviations from the nominal stoichiometry can modify the phase diagram, in particular for small values of x. To eliminate this ambiguity in future studies, techniques such as inductively coupled plasma optical emission spectroscopy (ICP-OES), Mössbauer spectroscopy and X-ray fluorescence spectroscopy should be employed to accurately determine the Ni:Fe ratio.

Magnetic and toroidic moments: For the mixed compounds the magnetic moment magnitude increases with Fe content, with the exception of x=0.2 and 0.3 samples. Figure 7.12 illustrates the compositional dependence of magnetic moment magnitude and orientation. As the Fe content increases, the component of the magnetic moment along the a-axis decreases and the angle, θ, between the magnetic moment and b-axis within the ab-plane drops to zero.

The toroidal moment in LiNi$_{1-x}$Fe$_x$PO$_4$ can be derived following the microscopic

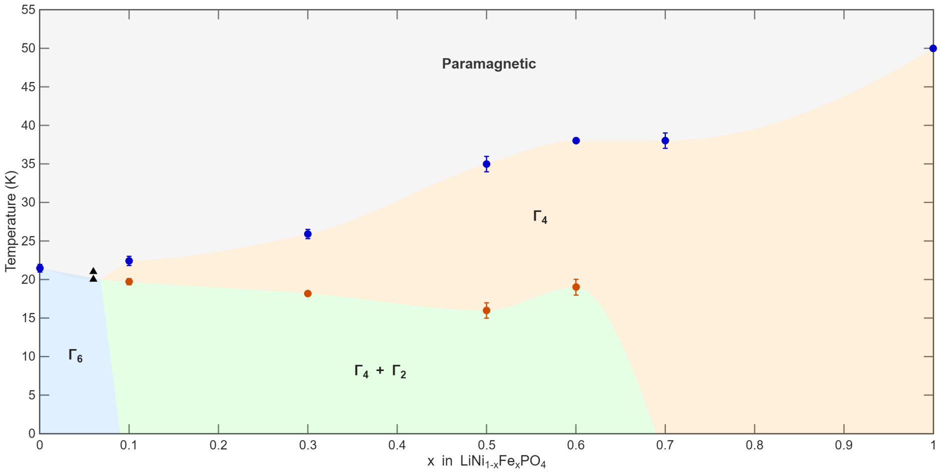

Figure 7.11: Experimental phase diagram of LiNi$_{1-x}$Fe$_x$PO$_4$. The experimental points are marked by circle markers with error bars. The value for x=1 is taken from the reference [38]. The phase boundaries indicated are obtained by extrapolating the line between the experimentally observed points. The indicated tetracritical point is obtained by extrapolating the measured transition temperature for x =0.1 and the previously reported transition temperature to the commensurate phase for x=0.06 [110], indicated by black triangle markers. The phase observed for x =0.2 is excluded in the illustrated phase diagram due to the ambiguity regarding its precise composition.

theory developed by Ederer et al. [31] for LiCoPO$_4$, as discussed in the section 2.0.3, with the modification that in the present system the magnetic moment rotation is within the ab-plane. Since LiNi$_{1-x}$Fe$_x$PO$_4$ is a fully compensated antiferromagnet with zero net magnetization, the derivation presented in Ref. [31] for the compensated part of the magnetic structure is valid for the entire magnetic moment. For a set of localized magnetic moment $\mathbf{m}_i$ at positions $\mathbf{r}_i$, the origin-independent toroidal moment is defined as

$$t^{(0)} = \tfrac{1}{2}\sum_i \mathbf{r}_i \times \mathbf{m}_i$$

For the oblique antiferromagnetic structure of LiNi$_{1-x}$Fe$_x$PO$_4$ described in figure 7.11, where the magnetic moment is rotated by an angle θ from b axis this gives

$$t^{(0)} = \frac{\mu}{2}\begin{pmatrix} 0 \\ 0 \\ 4\epsilon a\cos\theta - b\sin\theta \end{pmatrix}.$$

The macroscopic toroidization ($\mathbf{T}$) is defined as the toroidal moment per unit

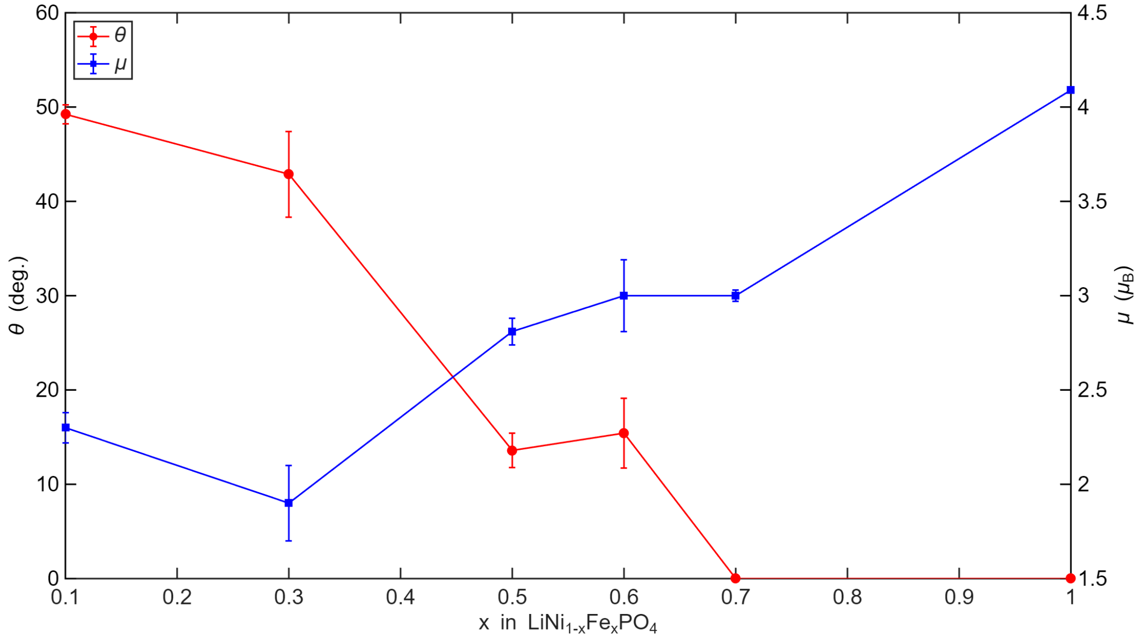

Figure 7.12: Compositional dependence of the angle, θ, between the magnetic moment and b-axis within the ab plane and the magnitude, μ, of the refined magnetic moment.

cell volume (Ω). But different lattice translations generate multiple allowed values of toroidization and the set of possible toroidization branches possible for a general translation (n, m, l) from equation 1.9 is

$$\mathbf{T}_{nml} = \frac{\mu}{2\Omega}\left[\cos\theta \begin{pmatrix} 0 \\ -lc \\ (4\epsilon + n)a \end{pmatrix} + \sin\theta \begin{pmatrix} 0 \\ lc \\ -(m+1)b \end{pmatrix}\right].$$

Only the difference in toroidization between two such branches is physically meaningful and the only non-trivial part of the toroidization is the component along the c-axis. Although the expression for $\mathbf{T}_{nml}$ contains a term proportional to -$b\sin\theta$, this contribution is branch-dependent and can be eliminated by an allowed translation of m = -1. Hence the spontaneous toroidization following the decomposition provided by Ederer et al. is given by

$$\mathbf{T}_s = \frac{2\mu\,\epsilon\,a}{\Omega}\cos\theta\,\hat{\mathbf{c}}, \tag{7.1}$$

Importantly, in contrast to the change in direction of calculated toroidal moment with chemical substitution in $\mathrm{LiCo}_{1-x}\mathrm{Ni}_x\mathrm{PO}_4$ (equation 9.1), the chemical substitution in $LiNi_{1-x}Fe_xPO_4$, only affects the magnitude of the toroidal moment. In $LiNi_{1-x}Fe_xPO_4$, the symmetry allows two toroidal domains while the chemical substitution induced rotation towards *a*-axis produces two orientation domains. The domain manipulation and its potential in this system is further explored in the next chapter.

The strong sensitivity of the magnetic ground state in $LiNi_{1-x}Fe_xPO_4$ to chemical composition highlights the delicate balance of competing anisotropy and exchange interactions in the system. The additional deviation observed for the compositionally ambiguous x=0.2 sample, further motivates a future study combining precise compositional characterisation with single crystal neutron diffraction and SNP to validate the existence of the $\Gamma_2 + \Gamma_6$ phase. The previously reported magnitude increase and modification of magnetoelectric tensor in x=0.2 is linked to the symmetry lowering associated with the oblique antiferromagnetic phase. With the detailed insight into the magnetic structure evolution across the composition phase diagram obtained in this work, a systematic investigation of magnetoelectric effect across the phase diagram would provide an oppurtunity to clarify how symmetry lowering due to chemical substituion influence the magnetoelectric tensor, which could prove useful for future application-driven developments in mixed-anisotropy materials.

8

Selective poling of toroidal domains in $LiNi_{0.8}Fe_{0.2}PO_4$

8.1 Motivation

The increasing demands for faster and higher density data storage drive research interest into magnetelectric materials to be utilized for next generation spintronic devices. Magnetoelectric coupling provides the prospect of a more energy efficient alternative to the traditional data storage methods. In addition to this, magnetoelectric and multiferroic materials provide access to multistate logic that allows the increase in data storage density by allowing the stabilization of more than two states that can be controlled externally. Several multiple state logic systems have been realized in the literature. However, all the established multi state systems to date utilizes composite heterostructures in which at least one of the component is ferro or ferrimagnetic. As a consequence, they remain vulnerable to stray fields [111–117].

This motivates the investigation for an antiferromagnetic system that exhibit multiple domain states that can be selectively populated. In this work, an antiferromagnetic system that is a potential host to ferrotoroidal order is considered. As discussed in sections 1.3.1 and 2.0.3, the existence of toroidal order has been demonstrated in $LiCoPO_4$, where the toroidal domains can be manipulated using the cross product of electric and magnetic fields as a conjugate field [49]. Such control has also been reported in systems such as $LiFeSi_2O_6$ [118]. These examples highlight the potential of toroidicity as an additional handle for domain manipulation. The mixed anisotorpy lithium orthophosphate series discussed in chapter 7, provides an ideal platform to explore these concepts. In $LiNi_{1-x}Fe_xPO_4$, the competing anisotropies of Ni^{2+} and Fe^{2+} drives the rotation of magnetic moment away from the crystallographic b-axis. This generates four distinct antiferromagnetic domains in the low temperature phase compared to the two domain states in parent compounds. The symmetry considerations further indicate the possibility of existence of a macroscopic toroidal moment making the system a potential host for ferrotoroidal order.

The ability to control the four different domains individually is a fundamental step towards realizing a multistate antiferromagnetic system. This chapter therefore aims first to confirm the existence of ferrotroidal order in the specific composition $LiNi_{0.8}Fe_{0.2}PO_4$ and subsequently to explore the possibility of selectively populating the four antiferromagnetic domains using suitable conjugate fields. The single crystal used in this study is the same as that used in the study reported by Fogh et al. [1], where the rotation of magnetic moments away from the b-axis is reported at 21 K and the first antiferromagnetic ordering at 25K, where the system orders with magnetic moment along b-axis. The demonstration of selective poling of four different domains in a single phase antiferromagnetic material represents an important step for spintronic devices that use multistate logic as it offers robustness against stray fields and ultrafast spin dynamics.

8.2 Magnetic symmetry and domain multiplicity in $LiNi_{0.8}Fe_{0.2}PO_4$

As discussed in chapter 7, upon cooling below the Néel temperature $T_2 = 25\text{K}$, $LiNi_{0.8}Fe_{0.2}PO_4$ is reported to enter a collinear antiferromagnetic structure with spins aligned along b-axis. A second transition occurs at temperature $T_4 = 21$ K, below which the spins collinearly rotate towards a-axis. The rotation angle is reported to increase continuously upon cooling and reach the value of 60° at 2 K [1].

In the temperature interval $T_4 < T < T_2$, the magnetic symmetry is described by the magnetic space group $Pnma'$ as denoted in table 1.3. This group preserves all spatial symmetry elements of the crystallographic space group $Pnma$ and breaks only the time inversion symmetry ($1'$) associated with the magnetic ordering. Magnetic domain formation is allowed whenever the magnetic space group symmetry is lower than that of the paramagnetic phase and the number of distinguishable domains are given by p/m where the p and m denote the orders of the crystallographic and magnetic space groups respectively. Breaking time reversal alone, allows two magnetic domains known as the 180° domains. These two domains are related by the reversal of all spin direction and are otherwise structurally identical [3]. Throughout this chapter, the two 180° domains in the temperature range $T_4 < T < T_2$ are labelled $\{a_2, b_2\}$.

Below T_4, the onset of collinear rotation of spins towards a-axis further lowers the magnetic symmetry by breaking additional spatial symmetries of $Pnma$ as indicated by the combination of 2 irreps. The resulting magnetic structure is described by the monoclinic magnetic space group $P112_1/a'$, which contains only four symmetry elements as indicated in table8.1. Since the paramagnetic space group $Pnma$ contains 16 symmetry operations when time reversal is included, the reduction to a magnetic space group of order 4 implies that four distinct magnetic domains exist in the low-temperature phase.

Magnetic space group	Symmetry operators							
	1	$2_1 \parallel z$	$2_1 \parallel y$	$2_1 \parallel x$	$\bar{1}$	$a \perp z$	$m \perp y$	$n \perp x$
$Pn'm'a'$	1	1	1	1	$1'$	$1'$	$1'$	$1'$
$Pnma'$	1	1	$1'$	$1'$	$1'$	$1'$	1	1
$P112_1/a'$	1	1			$1'$	$1'$		

Table 8.1: Symmetry operators of the magnetic space groups involved in the low temperature phase of $LiNi_{0.8}Fe_{0.2}PO_4$. 1 and $1'$ represent the symmetry operations with and without the time inversion respectively.

In addition to the two 180° domains discussed earlier, breaking of the 2_1 screw axis along y give rise to orientation domains. According to the domain classification in reference [3], orientation domains form when the magnetic ordering breaks rotational or mirror symmetries present in the parent crystallographic space group. For the collinear magnetic arrangement of spins in the interval $T_4 < T < T_2$, the spins are aligned parallel to the b axis. This magnetic structure retains the screw axis parallel to y. However, once the spins collinearly rotate away from the b axis below T_4, the inclination of the ordered moments breaks $2_1 \parallel y$ symmetry. This loss of rotational symmetry give rise to two opposite directions of a-axis component of the magnetic moment, generating two orientation domains related by the lost $2_1 \parallel y$

rotation operation as indicated in figure 8.1 from reference [3]. Thus below T_4, the system possess two orientation domains and two 180° domains giving rise to four domain states denoted by

$$\{a'_4,\ a''_4,\ b'_4,\ b''_4\}$$

where the a/b indicate the time reversal domains (180°), whereas the primes distinguish the two different orientation domains. The four domains realized in LiNi$_{0.8}$Fe$_{0.2}$PO$_4$ system are visualized in figure 8.3.

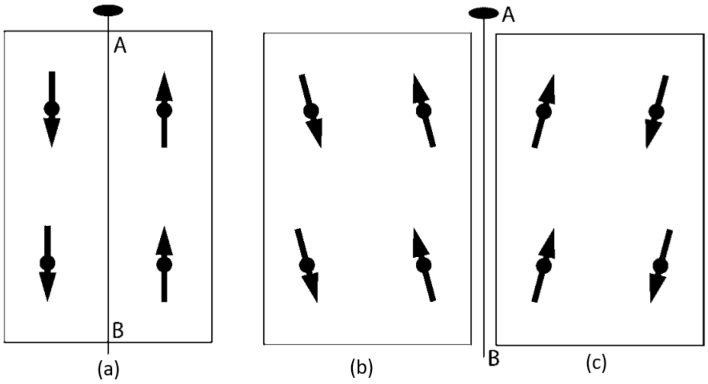

Figure 8.1: Schematic representation of orientation domains arising from the loss of rotational symmetry about the axis AB. Figure taken from reference [3]

8.2.1 Ferrotoroidal order and domains

Following from the equation 7.1 presented in the section 7.3.4, the collinear spin arrangement in LiNi$_{0.8}$Fe$_{0.2}$PO$_4$, produce toroidization along the $\hat{c}$ direction arising from the cross product of the individual magnetic moments and their position vectors as expressed by equation 1.8.

In the temperature range $T_4 < T < T_2$, two 180° domains, related by the time reversal symmetry operation is allowed. Since the toroidal moment is odd under time reversal, these two 180° domains give rise to two toroidal domains with toroidal moment along $+\hat{c}$ and $-\hat{c}$ directions. Therefore in this case, the 180° domains are the same as the toroidal domain. However, this is not a general result and is specific to this system. In all cases 180° need not be always ferrotoroidal domains.

Below T_4, the spin rotation towards the a axis preserves the collinearity of the spin arrangements. As derived in section 7.3.4, the rotation of spins modify only the magnitude of the toroidal moment, leaving the direction of toroidal moment unchanged. Hence the direction of toroidization remains fixed along the c direction throughout the temperature driven phase changes in the system and allows only two toroidal domains with toroidization either along the positive or negative c axis determined from the configuration of spins as indicated in figure 8.2.

8.3 Spherical neutron polarimetry

To explore the domain manipulation in $LiNi_{0.8}Fe_{0.2}PO_4$, it is necessary to employ an experimental technique that can differentiate between the domains. To do this it is necessary to access the full vectorial information of magnetic interaction vector ($\mathbf{M}\perp$) which is defined as the component of the magnetic structure factor $\mathbf{M}$ perpendicular to the scattering vector $\mathbf{Q}$. Normal diffraction experiments probe only the magnitude of the magnetic structure factor. But the symmetry allowed magnetic domains differ only in the direction of magnetic interaction vector. Spherical neutron polarimetry (SNP) provides access to both magnitude and direction of magnetic interaction vector and hence allows to discriminate between the antiferromagnetic domains discussed in section 8.2.

The transformation of the neutron spin through the scattering process can be explained through the Blume-Maleev equations which express the scattered neutron spin polarization in terms of the incident neutron polarization and the nuclear, magnetic and nuclear-magnetic interference scattering cross-sections [3, 119, 120]. This can be written in matrix form as

$$\mathbf{P_f} = P_0 + P\mathbf{P_i}$$

Where P is the matrix describing the rotation of polarization in the scattering process known as the polarization matrix. P_0 is the term that describes the polarization created during scattering. In SNP a right-handed set of orthogonal axes are defined, where x axis is defined to be parallel to the scattering vector $\mathbf{Q}$, z axis is the vertical axis and y completes the right-handed set. A general polarization matrix is given by

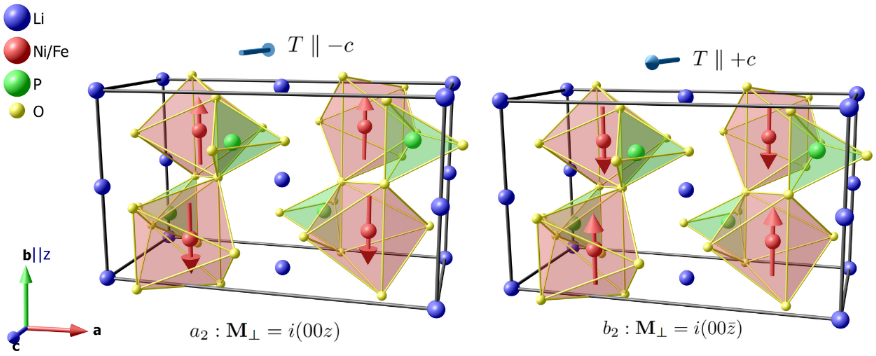

Figure 8.2: Two 180° domains represented by a_2 or b_2 in the temperature range $T_4 < T < T_2$. The corresponding direction of toroidal moment in each domain are indicated by the arrow on top.

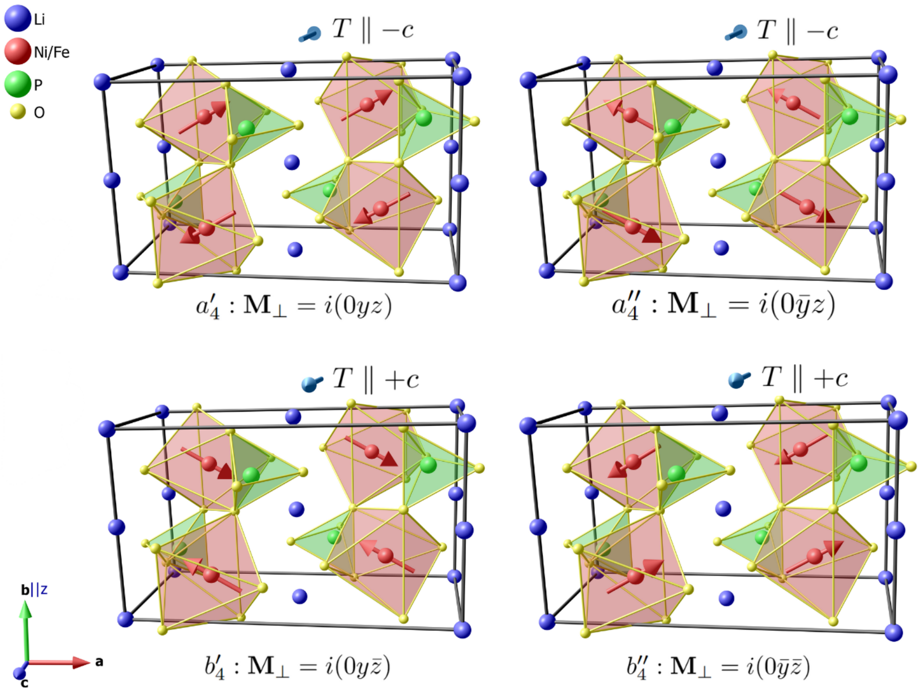

Figure 8.3: Four antiferromagnetic domains in the low temperature phase $T < T_4$. The 180° domains are represented by the labels a/b. The different orientation domains are represented by primed or double primed domains. The magnetic interaction vector corresponding to each domain is also represented.

$$P_{f,i} = \begin{pmatrix} p_{fx}\frac{p_{ix}(N^2-M_\perp^2)-J_{yz}}{I_x} & p_{fx}\frac{-p_{iy}J_{nz}-J_{yz}}{I_y} & p_{fx}\frac{p_{iz}J_{ny}-J_{yz}}{I_z} \\ p_{fy}\frac{p_{ix}J_{nz}+R_{ny}}{I_x} & p_{fy}\frac{p_{iy}(N^2+M_{\perp y}^2-M_{\perp z}^2)+R_{ny}}{I_y} & p_{fy}\frac{p_{iz}R_{yz}+R_{ny}}{I_z} \\ p_{fz}\frac{-p_{ix}J_{ny}+R_{nz}}{I_x} & p_{fz}\frac{p_{iy}R_{yz}+R_{nz}}{I_y} & p_{fz}\frac{p_{iz}(N^2-M_{\perp y}^2+M_{\perp z}^2)+R_{nz}}{I_z} \end{pmatrix}$$

Where

$$I_x = N^2 + M_\perp^2 + p_{ix}J_{yz}$$

$$I_y = N^2 + M_\perp^2 + p_{iy}R_{ny}$$

$$I_z = N^2 + M_\perp^2 + p_{iz}R_{nz}$$

with

$$R_{ni} = 2\,\mathrm{Re}(NM_{\perp i}^*)$$

$$J_{ni} = 2\,\mathrm{Im}(NM_{\perp i}^*)$$

$$J_{yz} = 2\,\mathrm{Im}(M_{\perp y}M_{\perp z}^*)$$

$$R_{yz} = 2\,\mathrm{Re}(M_{\perp y}M_{\perp z}^*)$$

Here N is the nuclear structure factor and $M_\perp$ is the magnetic interaction vector defined as $M_\perp(\mathbf{Q}) = \mathbf{Q} \times (\mathbf{M} \times \mathbf{Q})$ and $M(\mathbf{Q})$ is the magnetic structure factor given by $M(\mathbf{Q}) = \sum_j S_j f_j(\mathbf{Q}) e^{-i\mathbf{Q}\cdot\mathbf{r}_j}$.

For the magnetic structure of LiNi$_{0.8}$Fe$_{0.2}$PO$_4$,the magnetic moments related by the inversion center are antiparallel and this leads to purely imaginary magnetic structure factors. As a result, many contributions from different scattering cross sections becomes zero such as $R_{ni} = J_{yz} = 0$ and $I_x = I_y = I_z = N^2 + M_\perp^2$. These considerations simplifies the polarization matrix to the form of a pure rotation matrix which can be expressed as

$$\mathbf{P_f} = P\mathbf{Pi}$$

$$P = \frac{1}{I}\begin{pmatrix} N^2 - M_\perp^2 & -J_{nz} & J_{ny} \\ J_{nz} & N^2 + M_{\perp y}^2 - M_{\perp z}^2 & R_{yz} \\ -J_{ny} & R_{yz} & N^2 - M_{\perp y}^2 + M_{\perp z}^2 \end{pmatrix}$$

Experimentally, for a specific Bragg reflection, SNP measures how the neutron spin evolves during a scattering process using the CRYOPAD setup explained in section 4.2.3. This is done by measuring all 9 elements of the polarization matrix corresponding to the incident polarization along x, y, z and scattered neutron polarization directions x, y, z where each matrix element P_{fi} is obtained from the spin parallel (n_{fi}^{++}) and antiparallel (n_{fi}^{+-}) to the analysis direction:

$$P_{fi} = \frac{n_{fi}^{++} - n_{fi}^{+-}}{n_{fi}^{++} + n_{fi}^{+-}}.$$

8.4 Experimental setup

The crystal was aligned with b-axis along the vertical direction corresponding to the z axis in the SNP coordinates, while the scattering plane $(h0l)$ was accessible for measurements. As discussed in section 8.2.1, the toroidization in $\mathrm{LiNi_{0.8}Fe_{0.2}PO_4}$ is along the crystallographic c-axis. The two toroidal domains correspond to toroidization either along $+c$ or $-c$ directions. To selectively populate one of these domains, it is necessary to apply a conjugate field to toroidization that breaks both time and space reversal symmtery simultaneously as described in section 1.3.1. The simplest experimental realisation of such a field is a configuration of perpendicular electric and magnetic fields where the toroidization couples to the cross product $\mathbf{E} \times \mathbf{H}$. Thus in order to confirm the existence of ferrotoroidal order and to explore the selective domain population, the experimental setup must allow the simultaneous application of electric and magnetic fields with their cross product aligning along positive or negative c-axis during the cooling of the sample.

8.4.1 Field cooling protocols

To achieve a cross product of electric and magnetic field, along the crystallographic c axis, an electric field stick and electromagnet setup available on the D3 instrument at the ILL were utilized. An electric field was applied using the electric field stick which allows the application of electric field in the vertical direction. The single crystal ($5 \times 5 \times 5$ mm^3) was glued diectly onto the bottom capacitor plate. The distance between the capacitor plates were about 5.5 mm. The electric field was applied between these capacitor plates while the sample chamber of ($\approx$ 2cm^3) was continuously pumped to reduce the arcing when applying high voltages. The electric field stick was inserted into a cryostat capable of reaching temperatures down to 2K. The thin tail of the cryostat was positioned within the bores of an electromagnet that provided magnetic fields up to ±1T, either within the scattering plane or perpendicular to it.

In the present work, The electric field was applied parallel to the b axis by applying a voltage difference of up to ± 7 kV. Althogh the application of a higher electric field was allowed by the setup, a voltage above 7 kV could not be applied due to electric arcing. The magnetic field was restricted to the ac-plane with a magnitude of ± 1 T, as illustrated schematically in figure 8.4. This results in a conjugate field $\mu_0 HE$ of magnitude of up to 13 T kV/cm. Figure 8.5 shows the original crystal and the electromagnet setup at D3.

Because the Cryopad environment used for SNP cannot tolerate external magnetic fields, as it perturbs the neutron polarization direction, the sample was cooled in perpendicular fields ex situ. The field cooling protocol employed through out this work was to apply the electric and magnetic field in the paramagnetic state and then cool the sample down to the desired temperature range. At the desired temperature, all fields were turned off and the cryostat was transferred into the cryopad to perform SNP measurements in the zero-field environment.

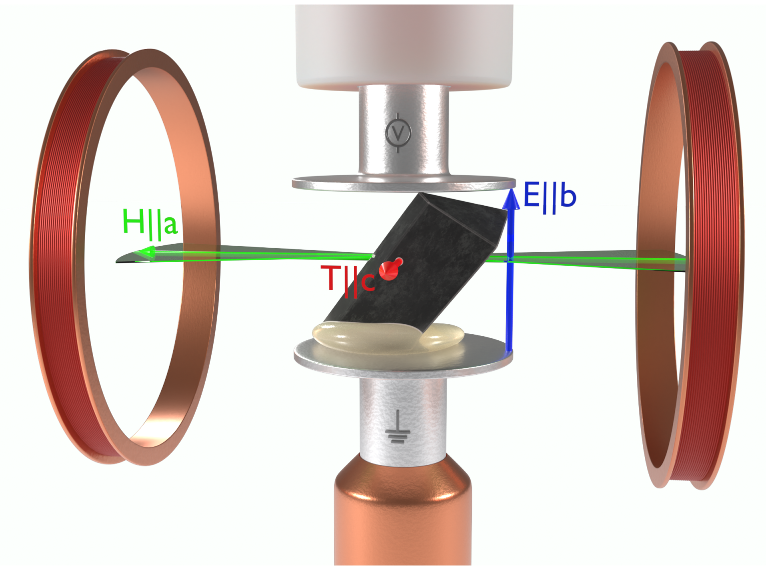

Figure 8.4: Experimental setup at D3 illustrating the sample with the b-axis aligned along the vertical direction and glued to the bottom capacitor plate. Applied electric field along the b-axis is represented with the blue arrow and the magnetic field in the ac -plane is shown in green arrow.

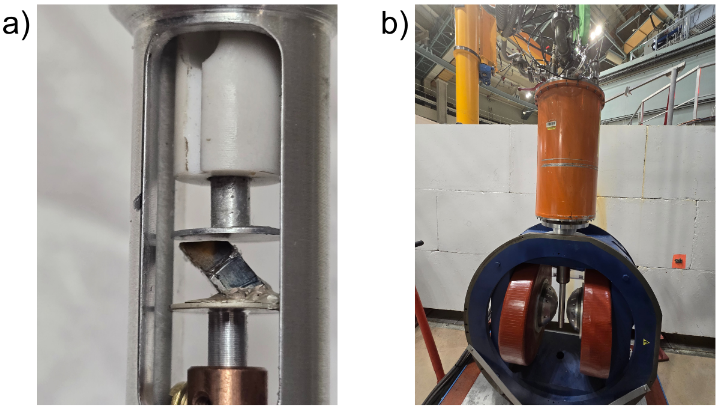

Figure 8.5: a) $LiNi_{0.8}Fe_{0.2}PO_4$ single crystal glued onto the lower capacitor plate. b) The magnetic field setup at D3

8.5 Magnetic structure factor and $M_\perp$

To interpret the SNP measurements, it is necessary to understand the form of magnetic interaction vector for the accessible reflections in the $(h0l)$ plane. In this chapter, we adopt the definition of scattering vector $\mathbf{Q}$ as $\mathbf{Q} = \mathbf{k}_f - \mathbf{k}_i$ where $\mathbf{k}_f$ and $\mathbf{k}_i$ are the final and incident wave vectors respectively. With this choice the magnetic structure factor is given by

$$\mathbf{M}(\mathbf{Q}) = \sum_j \mathbf{S}_j f_j(\mathbf{Q}) \exp(-i\mathbf{Q}\mathbf{r}_j) \tag{8.1}$$

where $\mathbf{S}_j$ is the magnetic moment vector of the jth atom at position $\mathbf{r}_j$ in the unit cell and $f_j(\mathbf{Q})$ is its magnetic form factor.

The magnetic ions in $LiNi_{0.8}Fe_{0.2}PO_4$, occupy $4c$ wyckoff position with fractional coordinates given in equation 1.5. Here the metal ions at r_1 and r_3 are related by inversion symmetry, and similarly $r_2$and r_4 form another inversion pair. The experimentally established magnetic structure in $LiNi_{0.8}Fe_{0.2}PO_4$ [1], follows the sign pattern (+, +, -, -) for both the a and b components of the magnetic moment. Thus each inversion related pair contribute terms of the form $\mathbf{S}\exp[-2\pi i(r^x + r^z)]$ and $-\mathbf{S}\exp[-2\pi i(r^x + r^z)]$, where $\mathbf{S} = (S^a, S^b, 0)$. Approximating $r^x \approx \frac{1}{4}$ and $r^z \approx 0$ and summing over all four sites, the magnetic structure factor for the Bragg peak

(101) simplifies to the purely imaginary form

$$\mathbf{M}(101) = -4if(101)(S^a, S^b, 0)$$

Only the component of $\mathbf{M}$ perpendicular to the $\mathbf{Q}$ contributes to magnetic neutron scattering. The projection of the magnetic structure factor known as magnetic interaction vector is given by $M_\perp(\mathbf{Q}) = \mathbf{Q} \times (\mathbf{M} \times \mathbf{Q})$.

For the (101) reflection the nuclear structure factor is less than zero($N < 0$). The scattering vector corresponding to this reflection $\mathbf{Q}$ lies in the ac plane. In the SNP coordinates $x \parallel \mathbf{Q}$, while the vertical z-axis is parallel to crystallographic b-axis and the y axis completes the right handed set. Hence the projection of the structure factor results in a magnetic interaction vector of the form

$$\mathbf{M}_\perp = i(0, \pm M_{\perp y}, \pm M_{\perp z})$$

where $M_{\perp y}$ is sensitive to the a component of the magnetic moment yielding a positive $M_{\perp y}$ for positive S^a and $M_{\perp z}$ is sensitive to the b component of the magnetic moment yielding a positive $M_{\perp z}$ for positive S^b.

8.6 SNP fingerprints of magnetic domains

As discussed in section 8.2, the magnetic domains that arise in LiNi$_{0.8}$Fe$_{0.2}$PO$_4$ below T_4 are related to each other by two symmetry operations of time reversal ($1'$) and a screw axis $2_1 \parallel y$. These domains differ only by the direction of the magnetic moment components. So that each domain corresponds to a distinct combination of signs of the y and z component of the $\mathbf{M}_\perp$. The off-diagonal nuclear-magnetic interference terms in the polarization matrix 8.3, depend linearly on $M_{\perp y}$ and $M_{\perp z}$. Since these components reverse sign for different domains, the sign and magnitude of off-diagonal elements provide unambiguous fingerprints of the different domains and their relative population.

8.6.1 Time reversal domains

In the temperature range $T_4 < T < T_2$, the ordered moments are aligned strictly along the b axis. Consequently, the only non-zero component of magnetic interaction vector is $M_{\perp z}$. In this phase, symmetry allows two domains a_2, b_2, which are related by the time-reversal symmetry. Since this results in the reversal of all magnetic

Domains	$M_\perp$	P_{xy}	P_{xz}
a_4'	$i(0, M_{\perp y}, M_{\perp z})$	negative	positive
a_4''	$i(0, -M_{\perp y}, M_{\perp z})$	negative	negative
b_4'	$i(0, M_{\perp y}, -M_{\perp z})$	positive	positive
b_4''	$i(0, -M_{\perp y}, -M_{\perp z})$	positive	negative

Table 8.2: Magnetic interaction vectors and signs of the off-diagonal terms for the (101) Bragg peak ($N < 0$) for the 4 domains present below T_4.

moments, it transforms as

$$M_{\perp z} \to -M_{\perp z}$$

The off-diagonal polarization matrix element $P_{xy} = -P_{yx} = -J_{nz} = 2\,\mathrm{Im}(NM^*_{\perp z})$, probes the sign of $M_{\perp z}$ and hence reveals which one of the 180° domains (toroidal domains) is populated.

8.6.2 Orientation domains below T_4

Below T_4 the ordered magnetic moment possess a non-zero component along a axis, which gives rise to a non-zero component of magnetic interaction vector along y ($M_{\perp y}$). The orientation domains related by the $2_1 \parallel y$ operation changes the component of magnetic moment along a from $S^a \to -S^a$, while keeping S^b unchanged. This results in a rotation of the magnetic interaction vector in the yz plane by

$$M_\perp = i(0, M_{\perp y}, M_{\perp z}) \to i(0, -M_{\perp y}, M_{\perp z})$$

In contrast the 180° domains result in a reversal of both $M_\perp$ components as.

$$M_\perp = i(0, M_{\perp y}, M_{\perp z}) \to i(0, -M_{\perp y}, -M_{\perp z})$$

The off diagonal term $P_{xz} = -P_{zx} = J_{ny} = 2\,\mathrm{Im}(NM^*_{\perp y})$ is sensitive to the sign changes of $M_{\perp y}$ and therefore reveals which of the orientation domains are populated. The four different sign combination of P_{xy} and P_{xz} , uniquely identify all four magnetic domains in the low temperature phase as summarized in table 8.2

8.7 Control of toroidal domains at 22K

The SNP measurements were first carried out at T = 22K ($T_4 < T = 22K < T_2$), where the system is expected to exhibit two domains, a_2 and b_2, giving rise to opposite orientation of the toroidization and two different toroidal domains as discussed in section 8.2.1. The measurement at 22K therefore provide direct insight into whether $LiNi_{0.8}Fe_{0.2}PO_4$ hosts ferrotoroidal order. All polarization matrices presented in this chapter are corrected to the initial polarization on D3, $p_0 \approx 0.92$, and to the decay of ^{3}He spin filter efficiency which was tracked at regular time intervals by measuring the P_{zz} element of the (002) nuclear Bragg peak.

Zero field cooling: To establish a reference state, the sample was cooled to 22K without any applied field and a polarization matrix of the Bragg reflection (101) was measured. The diagonal elements P_{xx} and P_{yy} exhibit small deviations from 1, which indicates the presence of magnetic ordering. The observed polarization matrix is given by

$$\begin{pmatrix} 0.9130(7) & -0.038(1) & 0.004(1) \\ 0.025(1) & 0.9148(7) & 0.005(1) \\ -0.012(1) & -0.003(1) & 1.0000(6) \end{pmatrix} \qquad (1\ 0\ 1)$$

The measured matrix exhibits an off-diagonal term P_{xy} which is zero within the instrumental sensitivity window of ±0.02, indicating equal population of the two domains. This is consistent with the characteristics of a classical antiferromagnetic material with two degenerate 180° domains. The zero field cooling polarization matrix is presented in figure 8.7.

Crossed field cooling ($\mathbf{E} \times \mathbf{H} \neq 0$): The field cooling protocol explained in the section 8.4.1 were followed with a $\mathbf{E}$ =7 kV parallel or antiparallel to the b axis and $\mathbf{H} = 1$T parallel or antiparallel to the a-axis. The four different field cooling protocols yield $\mathbf{E} \times \mathbf{H} \parallel \pm c$.

The resulting matrices for the four different protocols are presented in figure 8.7 for the Bragg peak (101). The measured polarization matrices exhibit a non-zero P_{xy} term for all four field treatments, indicating a domain imbalance. Furthermore, it can be seen that the P_{xy} term changes sign depending on the direction of $\mathbf{E} \times \mathbf{H}$, and not with the polarity of $\mathbf{E}$ or $\mathbf{H}$ independently. Specifically

- $+\mathbf{E} \times +\mathbf{H} = -\mathbf{E} \times -\mathbf{H} \parallel -c$ yield $P_{xy} < 0$, corresponding to preferential population of the a_2 domain.
- $+\mathbf{E} \times -\mathbf{H} = -\mathbf{E} \times +\mathbf{H} \parallel +c$ yield $P_{xy} > 0$, corresponding to b_2 domain.

As expected at this temperature from the magnetic structure with spins aligned entirely along the b-axis, the P_{xz} and P_{yz} terms are zero within the sensitivity of the instrument in the observed matrices.

E only and H only field cooling: To demonstrate that the electric field nor the magnetic field acting alone act as the conjugate fields to the toroidal order, measurements were conducted following field-coolings in an electric field only, and in a magnetic field only field protocol. The observed matrices for the **E** only measurements exhibit zero off-diagonal elements indicating equal population of domains a_2 and b_2. These results demonstrate that the individual **E** field have no effect on toroidal domain selection. The magnetic field only measurements produce a much smaller P_{xy} term compared to the crossed field treatments. The origin of this effect is discussed in section 8.8.2.

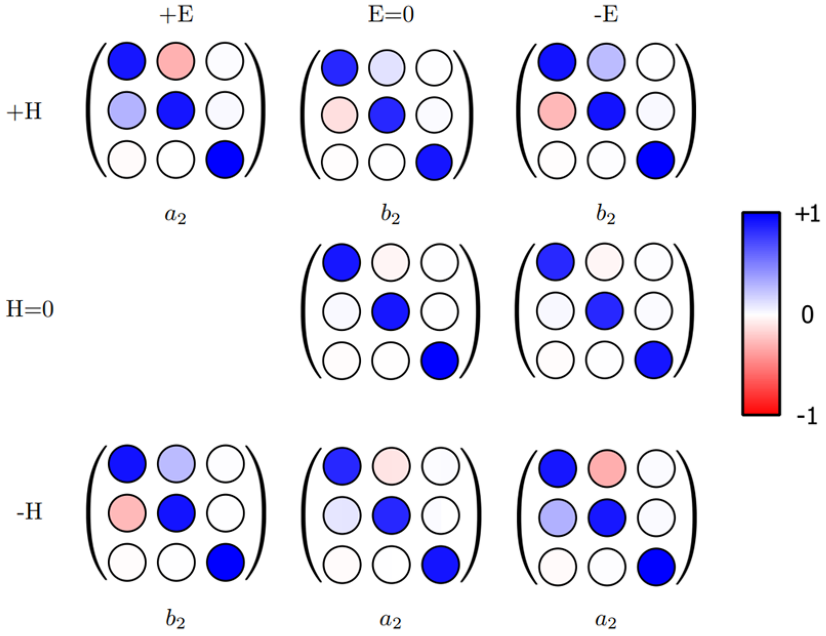

Figure 8.6: Observed polarization matrices for the Bragg peak (101) after different field cooling procedures. All data were obtained at 22 K. The majority domain corresponding to each observed matrix is labelled below the matrix.

Refinement of domain populations: The precise domain populations were obtained by refining the polarization matrices collected for different field treatements using the software Mag2POl. The magnitude of ordered magnetic moment was refined using the polarization matrices of (101), (103), (201) and (202) collected under the $+\mathbf{E} \times -\mathbf{H}$ field cooling, starting from the previously reported nuclear and magnetic structures [1, 18]. The refinement results are illustrated in figure8.7. The refinement yields an ordered magnetic moment of 0.84(2) μ_B along the b-axis. The magnetic moment magnitude was then fixed for the other field treatments of (101) and the domain populations were refined. The resulting domain populations for (101) under different field cooling protocols are summarized in table 8.3.

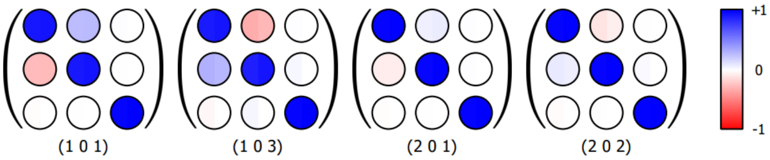

Figure 8.7: Refined polarization matrices under the $+\mathbf{E} \times -\mathbf{H}$ field cooling at 22 K. Observed polarization elements are represented by left half of the circle and the calculated elements are represented by right half of the circle.

It is worth noting that the first attempt at producing a domain imbalance by applying perpendicular fields with $+\mathbf{E} \times -\mathbf{H}$ were carried out using an applied voltage of only 2 kV (attempts to increase the voltage difference lead to arcing). The magnetic field magnitude was 1 T. This produced a small non-zero P_{xy} and a refined majority domain population of 58(1)%, whereas the same field treatment with a voltage of 7 kV produced a 86(2)% domain imbalance. This suggests that the efficiency of domain selection increases with the strength of the applied fields. Assuming linear dependence of the domain population on the conjugate field, the figure 8.9 represent the linear fit of the observed domain population at the three conjugate field points. The conjugate field is calculated as the product of applied electric field and magnetic field , where the electric field is calculated by dividing the applied voltage by capacitor plate distance in centimeters. The extrapolation of the linear fit suggests the domain population saturation at a conjugate field of 18.7TkVcm^{-1} which correspond to an applied electric field of 10.3 kV. This magnitude of voltage can be achieved with the current experimental setup if arcing can be avoided. This warrants further investigation, particularly to identify the minimum and maximum field thresholds to stabilize and saturate the domain population respectively.

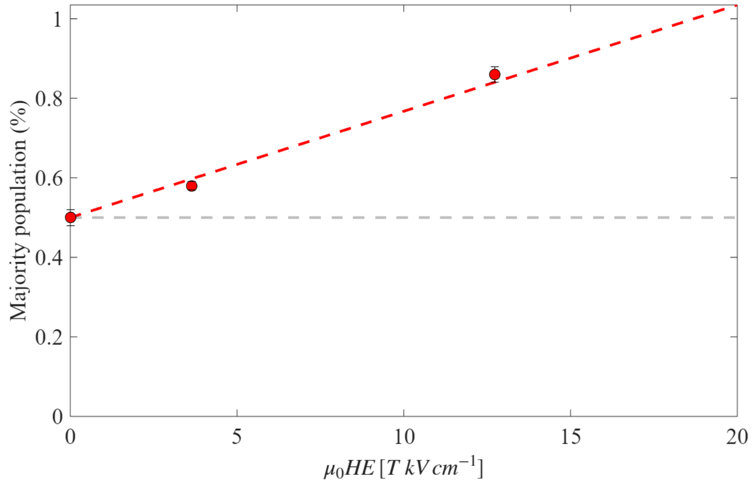

Figure 8.8: Majority domain population as a function of conjugate field. The grey line represent the equal population and the red line represent the linear fit. The refined domain population is shown with red markers.

In summary, the observations at 22K demonstrates that $\mathrm{LiNi_{0.8}Fe_{0.2}PO_4}$ hosts ferrotoroidal order, and the toroidal domains couple to $\mathbf{E}\times\mathbf{H}$. This is demonstrated by the change in sign of P_{xy} term only upon change in sign of the cross product not individual electric or magnetic field.

8.8 Selective poling of four domains at 2K

At 2K$< T_4$ the magnetic moment possesses a non-zero a component and there can be four domains as explained in section 8.6.2. Zero field cooling measurements similar to those described in 8.7 were carried out at 2K for the reflection (101). The diagonal elements P_{xx}, P_{yy} and P_{zz} are significantly smaller than 1 at 2K indicating well-developed magnetic ordering. However, the off-diagonal elements P_{xy} and P_{xz} are zero indicating equal population of the expected four domains as illustrated in figure 8.11

Crossed field cooling with magnetic field along the a axis: A magnetic field along a-axis does not introduce an energy preference between the two orientation domains. Hence applying crossed field with the electric field along the b-axis and the magnetic field along the a-axis, selectivey populates toroidal domains but not orientation domains. This results in non-zero P_{xy} values while the P_{xz} value remain close to zero as illustrated in figure8.9.

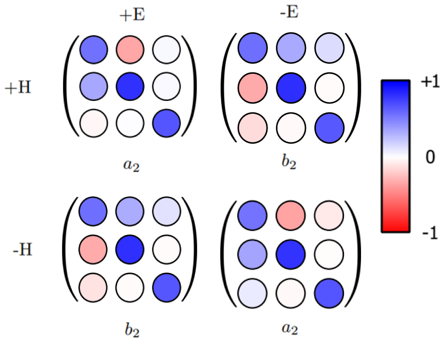

Figure 8.9: Observed polarization matrices for (101) under different field protocols as indicated by the labels.

8.8.1 Domain selection under rotated magnetic fields

In an effort to selectively populate the orientation domains, the magnetic field was rotated away from the a axis by an angle ϕ towards either the positive c-axis(ϕ_+) or negative c-axis (ϕ_-) as shown in figure 8.10. The resulting two components of the magnetic field $\mathbf{H}_a$ and $\mathbf{H}_c$, influence the domain population in two distinct way.

- $\mathbf{H}_a$ combined with an electric field along the b axis, depending on the direction of cross product stabilizes one of the toroidal domains labelled as a or b.
- $\mathbf{H}_c$ lifts the degeneracy between two orientation domains by minimizing the Dzyaloshinskii-Moriya energy as discussed in section 8.8.2. This stabilizes either primed or double-primed domains.

For all results discussed in this section, the magnetic field was rotated by $\phi \approx 20°$. Using the two different handles for domain population control, the selective population of four different domains using four different combination of the applied fields were achieved as illustrated in figure 8.11, which shows the full polarization matrix for (101) under corresponding field coolings. As summarized in table 8.2, the selective population of four domains in the low temperature phase can be identified by the four different sign combinations of the off-diagonal matrix elements P_{xy} and P_{xz}. In the current set of field cooling procedures, $\pm\mathbf{E} \times -\mathbf{H}_a$ parallel to $\pm c$ were used to stabilize one of the toroidal domains in $\{a'_4, a''_4, b'_4, b''_4\}$, as indicated by the sign of P_{xy}. The signs of P_{xy} are consistent with those observed at 22K for the same direction of $\mathbf{E} \times \mathbf{H}$. The component, $\pm H_c$, of the magnetic field along c now determines which of the two orientation domains arising from each toroidal domain is being stabilized i.e. selects between a'_4-a''_4 or between b'_4- b''_4. This is indicated by the sign of P_{xz}. The sign of P_{xz} follows from the sign of $-(\mathbf{E} \times \mathbf{H}_a) \cdot \mathbf{H_c}$. Hence from the four different sign combinations of P_{xy} and P_{xz} achieved through four different combinations of applied fields, the selective poling of four domains in the low-temperature phase is demonstrated. Note that all the SNP measurements were recorded in zero field conditions after the ex-situ field cooling of the sample, confirming the non-volatile nature of the four state domain distribution.

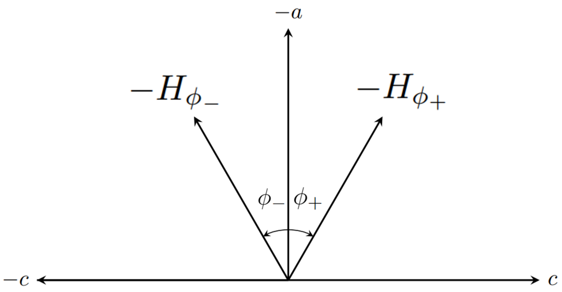

Figure 8.10: Rotated magnetic field setup used for the four domain selection below T_4. The magnetic field is rotated in the ac-plane, where it makes an angle ϕ with the -a-axis.

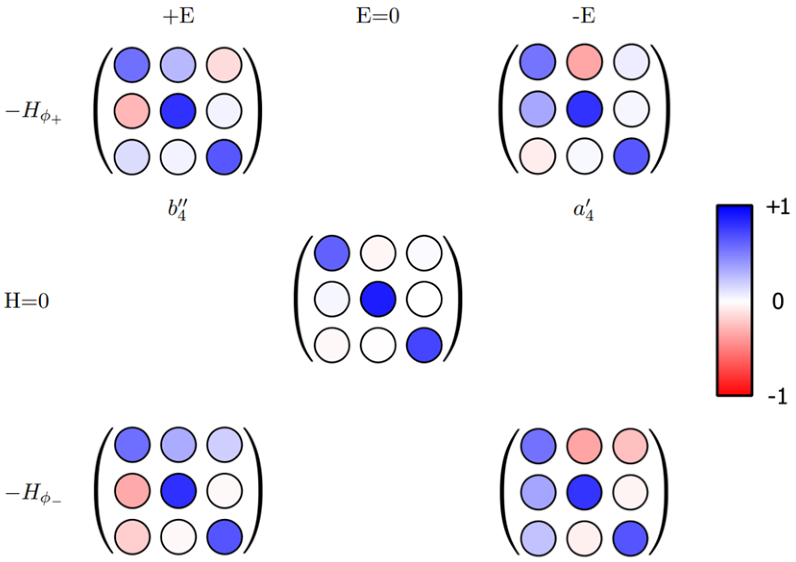

Figure 8.11: Observed polarization matrix under different field coolings for the reflection (101). The corresponding domains are labelled below the matrix.

Refinement of domain populations: The magnetic structure was refined using polarization matrices of the reflections (101), (103), (201) and (202) recorded under the $+\mathbf{E} \times +\mathbf{H}$ field cooling protocol at 2K. The refined magnetic moment magnitude yields $2.28(2)\mu_B$ and a spin rotation of angle $60.4(6)°$ away from b-axis. This value is in good agreement with the angle $\sim 60°$ obtained by Fogh et al. [1]. The refinement results are illustrated in figure 8.12.

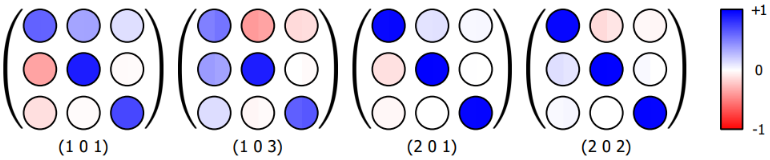

Figure 8.12: Refined polarization matrices corresponding to $+\mathbf{E} \times +\mathbf{H}$ field cooling protocol at 2K. Observed polarization elements are shown by the left half of the circles and the refined polarization matrix element is represented by the right half of the circle.

The SNP refinements obtain the best results with the C_x symmetry of the a-axis magnetic moment component confirming the magnetic structure defined by the combination of irrep $\Gamma_2 + \Gamma_4$ below T_4. The magnetic structure was then fixed to the value obtained from this refinement and the relative populations of the four domains were refined for the (101) polarization matrices recorded under the four different field-coolings. The results from the refinement is summarized in table 8.3. The toroidal domain imbalance is calculated as $\eta_T = (a'_4 + a''_4) - (b'_4 + b''_4)$. The most efficient toroidal domain selection was up to 92% for the $-\mathbf{E} \times -\mathbf{H}_{\phi_-}$ field protocol, while the most efficient orientation domain imbalance ($\eta_R = (a'_4 + b'_4) - (a''_4 - b''_4)$) of 40% was achieved with the same field configuration.

8.8.2 Dzyaloshinskii-Moriya interaction and domain selection

The theoretical considerations concerning the role of the Dzyaloshinskii-Moriya (DM) interaction presented here are in analogy to the ones presented for LiCoPO$_4$ [44] and LiNiPO$_4$ [51]. The magnetic susceptibility tensor elements χ_{ab} and χ_{ac} associated with the non-zero magnetoelectric tensor elements α_{ab} and α_{ac} reported in LiNi$_{0.8}$Fe$_{0.2}$PO$_4$, allows the coupling of S^a and S^b and S^a and S^c respectively. To capture the dominant contribution, only the nearest neighbour interaction between the spin pairs S_1-S_4 and S_3-S_2 are considered

$$\mathcal{H}_1^{\mathrm{DM}} = \mathbf{D}_{14} \cdot (\mathbf{S}_1 \times \mathbf{S}_4) + \mathbf{D}_{32} \cdot (\mathbf{S}_3 \times \mathbf{S}_2). \tag{8.2}$$

Since the midpoints between these spin pairs lie on general position of the space group *Pnma*, all components of the DM vector **D** are allowed. Furthermore, since the midpoints are related by inversion operator,

$$\mathbf{D}_{14} = -\mathbf{D}_{32}$$

Thus the two symmetry allowed DM interactions are

$$H_1^{\mathrm{DM}} = D_{14}^{c}\left(S_1^a S_4^b - S_1^b S_4^a - S_3^a S_2^b + S_3^b S_2^a\right). \tag{8.3}$$

$$H_1^{\mathrm{DM}} = -D_{14}^{b}\left(S_1^a S_4^c - S_1^c S_4^a - S_3^a S_2^c + S_3^c S_2^a\right). \tag{8.4}$$

In the two-domain state in the temperature interval $T_4 < T < T_2$, the ordered moment lies along b-axis. However,an applied magnetic field along the $+a$-axis induces a small ferromagnetic component along $+a$ of the magnetic moments on all four sites. Then if $D_{14}^c > 0$ in the allowed DM interaction 8.3, it couples the field-induced S^a to the ordered moment S^b and stabilizes the (+,+,-,-) sequence of spin component along b axis thus selecting one of the two 180° domains. Hence this explains the domain selection observed, even in the absence of an electric field in section 8.7 with an applied magnetic field $\mathbf{H} \parallel \pm a$. The magnetic field only poling results in a domain imbalance of 67(2)% which is less efficient than the crossed-field poling as seen in table 8.3.

Applying the same logic to the $T < T_4$ region, an ordered moment component along a exists and a ferromagnetic moment along c due to an applied magnetic field along $\mathbf{H} \parallel \pm c$ is induced. Then DM interaction vector along b-axis8.4 couples these two spin components. The induced ferromagnetic component along $+c$ axis, stabilizes a (-,-,+,+) sequence of spins on the a axis component if $D_{14}^b > 0$, hence lowering the energy for one of the orientation domain and explains the selection of one out of the primed and double primed domains.

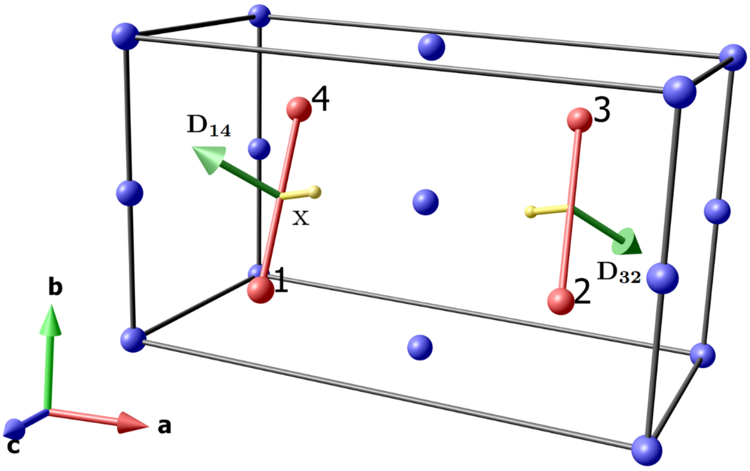

Figure 8.13: The figure illustrates the Dzyaloshinskii-Moriya interaction vectors $\mathbf{D_{14}}$ and $\mathbf{D_{32}}$ in LiNi$_{0.8}$Fe$_{0.2}$PO$_4$. The figure shows four magnetic ions (red), the oxygen atom (yellow) mediating the DM-interaction and the displacement, x, of the oxygen away from the lines connecting magnetic ions.

The magnitude of individual component of DM vector is determined by the geometry of the superexchange pathway. The orientation of $\mathbf{D}$ is proportional to $\mathbf{r_{14}} \times \mathbf{x}$ where $\mathbf{r_{14}}$ is the unit vector between the spins 1 and 4 and $\mathbf{x}$ is the displacement of oxygen ion from that line [121]. The projection of $\mathbf{D_{14}}$ onto the *bc* plane makes an angle of 35°angle with the *c* axis. Therefore, $D^b < D^c$ and this in combination with the experimental condition of $H_c < H_a$ results in a slightly less efficient selection of orientation domains of upto 66(2)% compared to the selection of 180° domains using magnetic field only.

8.9 Temperature dependence of magnetic moment rotation

The temperature evolution of magnetic structure was investigated using the measurements of selected polarization matrix elements of the (101) peak with $+\mathbf{E} \times -\mathbf{H}$ field cooling. The diagonal elements P_{xx}, P_{yy}, P_{zz} were measured because they probe the square of the magnetic interaction vector and therefore allowing the characterization of magnetic structure independent of the domain distribution.

The magnetic structure for each temperature point was refined while keeping the structural values fixed to the values determined in reference [1]. The magnetic moment magnitude and the spin rotation angle θ from b axis was refined. The magnetic space group of $Pnma'(\Gamma_4)$ was used for the $T_4 < T < T_2$ region while the monoclinic group $P112_1/a'$ $(\Gamma_2 + \Gamma_4)$ was employed below the temperature T_4. The observed and refined values of the diagonal elements are illustrated in figure 8.14.

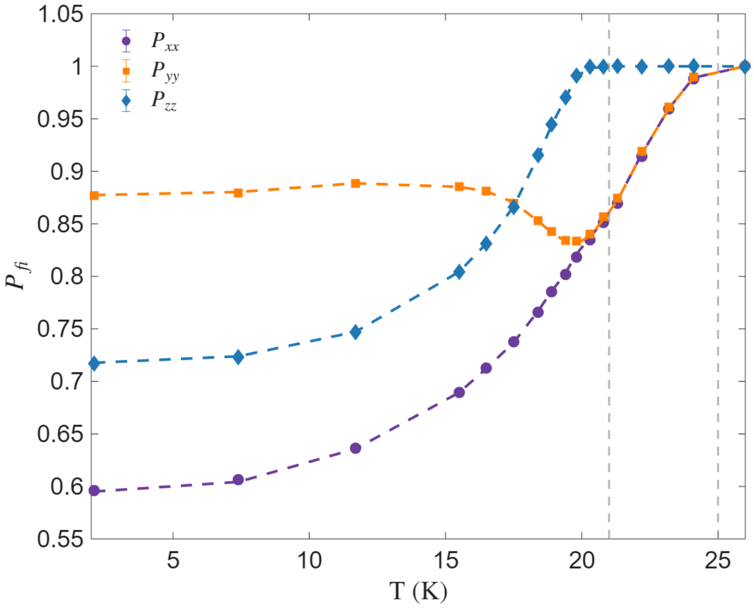

Figure 8.14: Temperature dependence of the diagonal elements of the polarization matrix of the Bragg peak (101) recorded for the field cooling procedure with $+\mathbf{E} \times -\mathbf{H}$. The markers denote the observed value while the dotted line follow the refined value of the diagonal elements evaluated from the polarization matrix observed at specific temperature points.

As discussed in the polarization matrix 8.3, P_{xx} is sensitive to the total magnitude of the $M_{\perp}$, while P_{yy} probes the spin flip channel contribution from the $M_{\perp z}$ which is sensitive to the magnetic moment component along b-axis. The P_{zz} element has spin flip contribution from the $M_{\perp y}$ component, which is sensitive to the a axis component of magnetic moment. As illustrated in figure 8.3, in the paramagnetic region $(T > T_2)$, all three diagonal elements approach unity corresponding to the nuclear only contribution which does not alter the neutron spin state.

In the temperature region $T_2 < T < T_4$, the increase in the magnitude of ordered magnetic moment along b axis is reflected in the identical decrease in P_{xx} and P_{yy} upon cooling, which indicate that the only magnetic contribution is from magnetic moment along b -axis. In this region, P_{zz} remain close to 1 consistent with the absence of $M_{\perp y}$. Below T_4, the onset of spin rotation towards a axis is reflected in

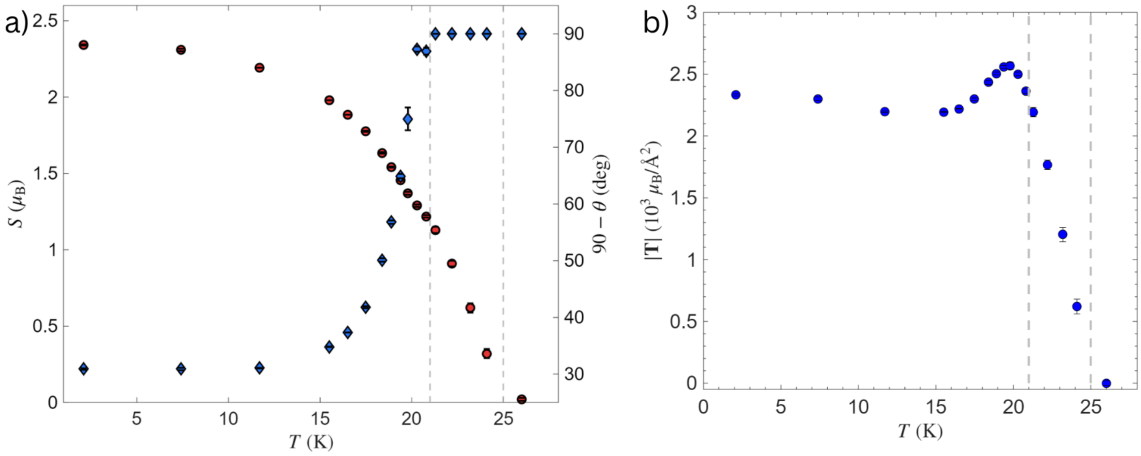

Figure 8.15: a) The magnetic moment magnitude and the magnetic moment rotation away from b axis (θ) from the refined polarization matrices at different temperature points. b) Calculated toroidization using the refined magnetic structure at each temperature point.

the decrease of P_{zz} due to the increase in $M_{\perp y}$. The P_{xx} decreases monotonically with decreasing temperature below T_4, indicating the overall increase in magnitude of ordered magnetic moment. P_{yy} first decreases below T_4 reaching a minimum at 20K, due to the increasing contribution from $M_{\perp y}$, then increasing with further increase in $M_{\perp y}$. The ordering temperatures observed from the SNP data, agrees with the T_2 and T_4 reported by Fogh et al. [1].

The magnitude and the angle of spin rotation from b axis of the ordered moment extracted from the refinements are plotted in the figure 8.15. Below T_4, the angle θ increases continuously, reaching 60° at 2K, in good agreement with the previously reported value [1].

The calculated toroidization from the refined magnetic structure using the equation1.8, in the direction c is plotted in figure 8.15. The toroidization increases monotonically below T_2 due to the increase in ordered magnetic moment. Below T_4, the toroidization decreases slightly due to the onset of spin rotation θ before stabilizing.

8.10 Temperature dependence of domain imbalance

The off-diagonal elements P_{yx} and P_{zx} were measured for the same temperature points were the diagonal elements were measured under the field cooling configuration of $+\mathbf{E} \times -\mathbf{H}$. The domain imbalances were refined together with the ordered magnetic moment magnitude and direction which can be refined using the diagonal elements as explained in the section 8.9. The $+\mathbf{E} \times -\mathbf{H}$ field treatement with magnetic field strictly along a axis does not produce significant orientation domain imbalance as indicated by the P_{zx} value which is within the instrumental sensitivity to exact zero values (± 0.02). The large P_{yx} values produced by this field treatement indicated the successive poling of toroidal domains. The refiened and observed value of P_{zx} and P_{yx} is illustrated in figure 8.16.

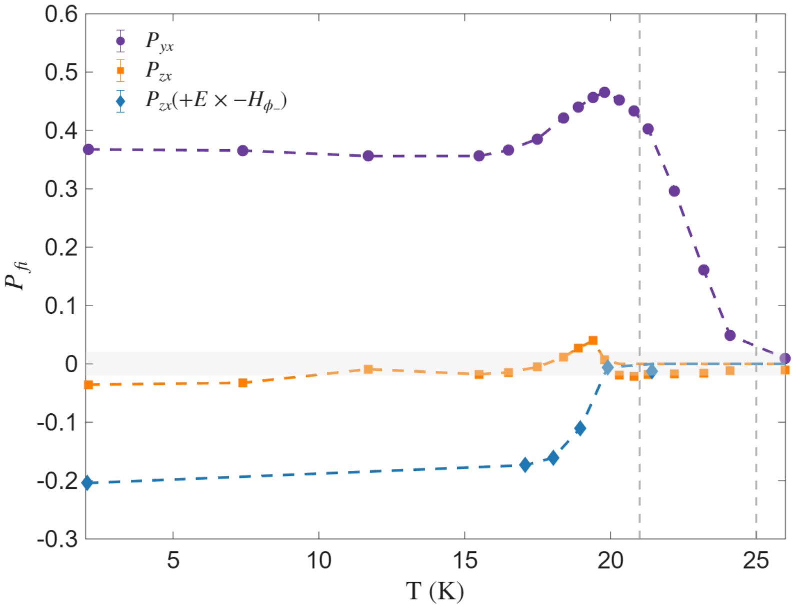

Figure 8.16: Temperature dependence of the P_{yx} and P_{zx} elements of the polarization matrix of the Bragg peak (101) recorded for the field cooling procedure with $+\mathbf{E} \times -\mathbf{H}$. The Temperature dependence of P_{zx} under the field treatment $+\mathbf{E} \times -\mathbf{H}_{\phi\_}$ is also illustrated in the figure.The markers denote the observed value while the dotted line follow the refined value of the diagonal elements evaluated from the polarization matrix observed at specific temperature points. The grey zone indicate the SNP sensitivity.

The toroidal domain imbalance η_T and η_R extracted from the refinements are plotted in figure8.17. The toroidal domain imbalance η_T remain stable throughout the temperature range below T_4. With increase in temperature above T_4, η_T continuously decreases reaching zero at T_2 when system becomes paramagnetic. The refinement of orientation domain, results in oreientation domain imbalance that is close to zero within the zero polarization window below T_4, exhibiting large fluctu-

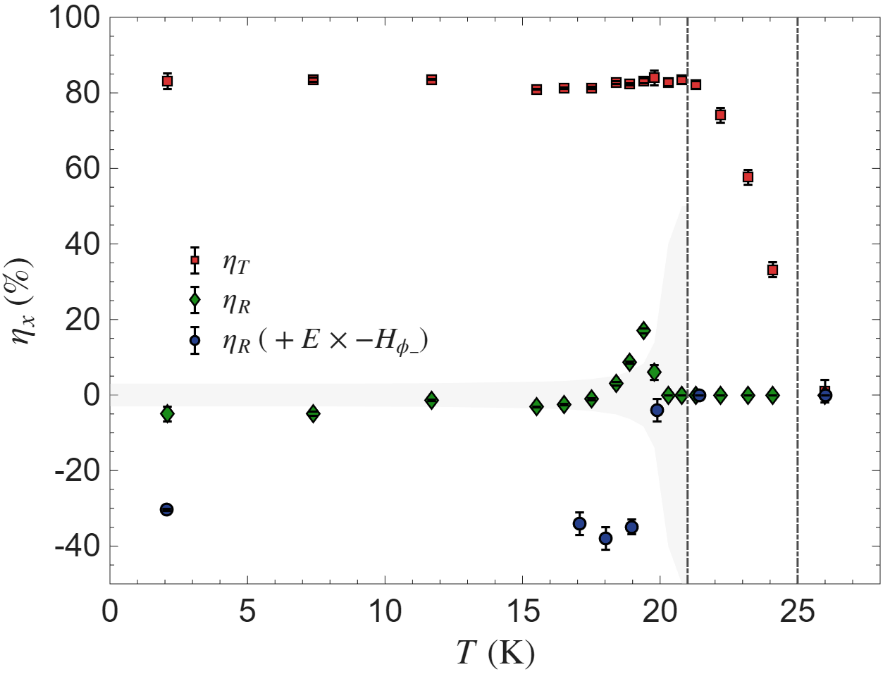

Figure 8.17: Temperature dependence of toroidal domain imbalance (η_T) and the otrientation domain imbalance (η_R) under the field treatment $+\mathbf{E} \times -\mathbf{H}$ from the refinement of polarization matrices. The orientation domain imbalance under the field treatment $+\mathbf{E} \times -\mathbf{H}_{\phi\_}$ clearly indicate the selective population of orientation domains.

ation just below T_4, as the significance of $M_{\perp y}$ and in turn the term P_{zx} becomes negligible as the spins approach b-axis.

An additional temperature dependece of P_{zx} element is illustrated in figure8.16 for a different field configuration of $+\mathbf{E} \times -\mathbf{H}_{\phi\_}$ as described in section 8.8.1. This produces large P_{zx} values and correspondingly result in large η_R values from the refinements. This observed domain imbalance is stable in the whole temperature below T_4 independent of the variation in magnetic moment rotation angle.

Domain response to temperature cycling: Figure 8.18 illustrates the temperature dependence of P_{yx} and P_{zx} with an applied magnetic field of $-\mathbf{H}_{\phi\_}$ with $\phi = 10°$. As shown in figure the sample exhibits a reproducible domain imbalance when it is heated to temperatures just below T_4 as represented by the identical values of P_{xy}. In the illustrated data, the sample was first cooled down to 2K and the temperature dependent P_{xy} and P_{xz} were measured when the temperature was increased upto 19 K, then cooled down again while measuring the matrix elements.

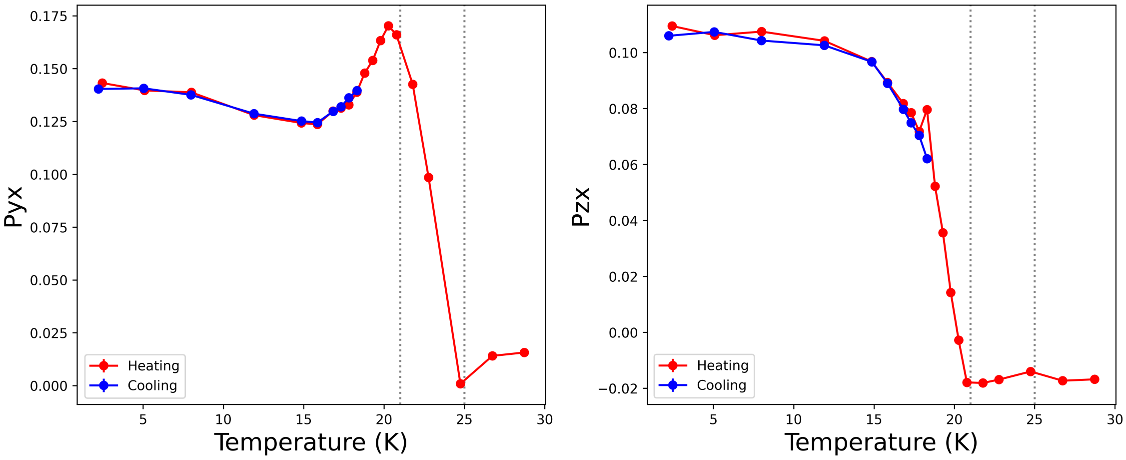

Figure 8.18: P_{yx} and P_{zx} temperature dependence under the field cooling with $-\mathbf{H}_{\phi_-}$. The figure illustrates the reproducibility of P_{yx} and P_{zx} in turn indicating the reproducibility of domain population distribution when the temperature is cycled under T_4

8.11 In-situ switching trials for toroidal and orientation domains

In-situ switchability of the domains, where the domain selection can be switched without heating above the ordering temperature is highly interesting in the perspective of future application-oriented research. Such in-situ switching has been demonstrated in the compound $LiCoPO_4$ using second harmonic generation techniques unambiguously, where the full hysteresis loop of toroidal moment as a function of the conjugate field $\mathbf{E} \times \mathbf{H}$ have been reported [49]. These measurements reveal a ferrotoroidal moment switching at a well defined coercive field. A key observation from this study was that the coercive threshold decreases rapidly as the temperature approaches transition temperature. With an increase in temperature by 0.7 K, the threshold field decreases by nearly two orders of magnitude reaching a value of 0.25T.kV cm^{-1}. This motivates switching attempts closer to the transition temperature.

In the present work, switching attempts were carried out at 19K, 2K below T_4 which corresponds to half the temperature difference from the transition temperature in the $LiCoPO_4$ study. The conjugate field strength of 13 T.kV cm^{-1} was used for the switching.

Electric-field driven switching: The switching was attempted by reversing the conjugate field direction by reversing the electric field direction. The system was first cooled down to 2K under a field configuration of $-\mathbf{E} \times -\mathbf{H}_{\phi_-}$ with $\phi = 20°$. Upon heating to 19 K, the measured P_{yx} and P_{zx} were positive identifying the a_4'' domain as the populated state in this configuration. The switching was attempted by applying a $+\mathbf{E} \times -\mathbf{H}_{\phi_-}$ followed by rotation of the magnetic field to ϕ_+. Reversal of the toroidal domain would manifest as a sign change in P_{yx} while same sign of P_{zx} is expected. However, the measurement after the application of switching fields does not reveal any change in the signs of both P_{yx} and P_{zx} indicating a failed switching.

Magnetic field driven switching: Together with the attempts to switch the domain population under the transition temperature, attempts were made to improve the orientation domain selection from the observed population of 66% for the majority domain.

To maximize the orientation domain imbalance, the sample was first cooled to $T_4 < T = 22.8K < T_4$ with $-\mathbf{E} \times -\mathbf{H}$ magnetic field along $-a$ axis. At 22.8 K, the electric field was removed and the magnetic field was rotated by 90° towards $+c$ axis. The sample was further cooled down to 2 K. However this field protocol did not succeed in producing a better domain imbalance. The orientation domains were nearly equally populated (49(4) %), indicating that the complete removal of toroidal poling field may introduce fluctuations that could destabilize the orientation domain imbalance. However a toroidal domain imbalance of 89(4)% is observed. With this initial configuration, an attempt to switch the toroidal domains were made by heating upto 19K and reintroducing a crossed field setup $-\mathbf{E} \times +\mathbf{H}$ with magnetic field along $+a$. No change in P_{yx} was observed indicating failed switching.

In the next field protocol, In order to maximize the orientation domain imbalance, the sample was cooled to 23.5 K under $+\mathbf{E} \times -\mathbf{H}$ with magnetic field along $-a$ axis. After which the magnetic field was rotated 45° towards $-c$ axis in order to increase the poling field for orientation domains (H_c), while keeping a finite toroidal poling field and the sample was cooledd down to 2 K. This field cooling protocol was successful in achieving the most efficient orientation domain selection observed in this work with $P_{zx} = 0.457(1)$. The refinement of the polarization matrix with this field cooling procedure yields a majority domain population of 78(2)% for the b_4' domains. Hence indicating that the increase in H_c with a presence of toroidal poling field incresese the orientation domain selection efficiency. Notably, repeating the same field cooling procedure with appropriate signs for the field configuration, did not yield comparable efficiencies for other domains.

Switching attempts were made with the high efficiency domain selection field procedure discussed, with $+\mathbf{E} \times -\mathbf{H}$ along $-a$ down to 23.5 and then rotating the magnetic field to 45° towards $+c$ axis. At 2K the P_{yx}=-0.325(1) and $P_{zx} = 0.076(1)$ was observed identifying the populated state as b''_4 domain. At 19 K, switching of the orientation domain was attempted by rotating the magnetic field 45° towards $-c$ axis. The measurment after the application of switching field, showed no change in P_{yx} and P_{zx} indicating failed switching.

Despite the several switching attempts with the 13 T.kV cm^{-1} strength of conjugate field, no switching of toroidal domains or orientation domains were observed. Considering the higher transition temperature for the toroidal domain of T_2, the attempts to switch the toroidal domains below T_4 in the four domain state might be too low in temperature. The orientation domain switching attempts also failed with the current field magnitude of ≈ 0.7 T. Eventhough robust domain populations can be selected with cooling under combined fields, domain switching was not possible in-situ proving the domain population distribution under T_4 to be resistant against stray fields.

8.12 Discussion

The results presented in this chapter unambiguously demonstrate the controllable four-domain state in LiNi$_{0.8}$Fe$_{0.2}$PO$_4$, originating from the spin rotation away from the b-axis. Moreover, this chapter provides direct experimental evidence for the existence of ferrotoroidal order in the mixed anisotropy lithium orthophosphate system LiNi$_{0.8}$Fe$_{0.2}$PO$_4$. The ferrotoroidal nature of the system provides two different handles for toroidal and orientation domain manipulation. In particular, the cross product of electric and magnetic field allows the manipulation of toroidal domains, while the magnetic field along c-axis provide the handle for orientation domain manipulation. Together with the demonstrated non-volatility and the robustness of the domains, these results position LiNi$_{0.8}$Fe$_{0.2}$PO$_4$, to the best of our knowledge, as the only single phase antiferromagnet where controllable four-state domains have been realized.

Further insight into the domain behaviours is provided by the results from different field cooling procedures discussed in this chapter. The high efficiency procedure explained in section 8.11 achieves the orientation domain selection with majority domain population of 78(2)%. However, the pronounced domain dependency of the efficiency suggests possible local anisotropy variations due to the Ni/Fe occupancy and domain pinning effects that makes certain domains easier to stabilize than others. A systematic investigation of how the selection efficiency depends on the magnitude of the conjugate field would be valuable for establishing poling procedures and exploring the switching behaviours more efficiently in this compound and in other related memebers of the lithium orthophosphate family.

Attempts to switch the domain states within the ordered phase exhibited a clear contrast with the reported behaviour of $LiCoPO_4$ [49]. In $LiNi_{0.8}Fe_{0.2}PO_4$, even higher conjugate fields from that reported for $LiCoPO_4$, was unsuccessful to induce domain switching at comparable temperature window with respect to the transition temperature. This absence of switching is consistent with the enhanced pinning effects due to chemical disorder and local anisotropy variations. Thus eventhough selective poling of toroidal and orientation domains are achievable in $LiNi_{0.8}Fe_{0.2}PO_4$, the domains remain relatively rigid compared to the $LiCoPO_4$. Switching behaviours of the system should be further explored using different field stregths especially for the orientation domain switching to assess whether the switching threshold can be achieved. Further compositions within the $LiNi_{1-x}Fe_xPO_4$ series, that exhibit similar spin rotation as discussed in chapter 7 should be investigated to determine if the absence of switching arises from sample specific pinning or from intrinsic effects associated with mixed anisotropy disorders.

The high degree of controllability combined with the non-volatility implies borader significance for the four domain state in $LiNi_{0.8}Fe_{0.2}PO_4$. A robust four-state antiferromagnetic ground state is of considerable interest for device development that require multiple stable logic states such as quatenary memory concepts. Further, the lithium orthophosphate family offers a tunable platform where chemical substitution works as a handle to control the competing anisotropy driven spin rotation and therefore giving rise to a spectrum of contollable magnetic structure governed physical properties as discussed in chapter 6 and 7. The multi domain states can be developed further in such systems and their toroidal nature can be utilized as an additional handle for domain control. The behaviour demonstrated here therefore present proof of concept for engineering controllable multi domain antiferromagnets by exploiting anisotropy competition.

	P_{xy}/P_{yx}		P_{xz}/P_{zx}		Domain population (%)			
E × **H**	obs.	cal.	obs.	cal.	a_2		b_2	
$+\times+$	-0.306(1) 0.297(1)	-0.302 0.302	0.011(1) -0.017(1)	0 0	**90(2)**		10(2)	
$+\times-$	0.266(1) -0.274(1)	0.270 -0.270	0.009(1) -0.012(1)	0 0	14(2)		**86(2)**	
$-\times+$	0.263(1) -0.279(1)	0.271 -0.271	0.005(1) -0.006(1)	0 0	14(2)		**86(2)**	
$-\times-$	-0.319(1) 0.304	-0.312 0.312	0.014(1) -0.021(1)	0 0	**91(2)**		9(2)	
0×0	-0.038(1) 0.025	-0.032 0.032	0.004(1) -0.012(1)	0 0	54(2)		46(2)	
$0\times+$	0.125(1) -0.136(1)	0.13 -0.13	0.005(1) -0.008(1)	0 0	33(1)		**67(1)**	
E × **H**$_\phi$					a'_4	a''_4	b'_4	b''_4
$+\times-_+$	0.304(1) -0.310(1)	0.307 -0.307	-0.150(1) 0.150(1)	-0.150 0.150	8(2)	5(2)	31(2)	**56(2)**
$+\times-_-$	0.361(1) -0.365(1)	0.363 -0.363	0.206(1) -0.204(1)	0.205 -0.205	6(2)	0(2)	**59(2)**	35(2)
$-\times-_-$	-0.385(1) 0.383(1)	-0.384 0.384	-0.269(1) 0.260(1)	-0.264 0.264	30(2)	**66(2)**	0(2)	4(2)
$-\times-_+$	-0.380(1) 0.375(1)	-0.378 0.378	0.077(1) -0.082(1)	0.079 -0.079	**55(2)**	40(2)	1(2)	4(2)
0×0	-0.035(1) 0.034(1)	-0.035 0.035	0.021(1) -0.026(1)	0.023 -0.023	27(2)	27(2)	24(2)	22(2)

Table 8.3: Observed and calculated values of P_{xy}, P_{xz} and refined domain populations for the different field coolings. The upper part of the table corresponds to field coolings carried out at 22K, while the lower part corresponds to the field coolings carried out at 2K. The polarity of the applied electric and magnetic fields are represented by "+" or "-". For the 2K field cooling procedures, the third polarity entry denotes the direction of magnetic field rotation ϕ

9

Single crystal studies of $LiCoPO_4$ and $LiFePO_4$

9.1 Motivation

The lithium orthophosphate family has been extensively studied. Its members are generally described as collinear antiferromagnetic compounds with propagation vector $\mathbf{k}$=0 [17, 18]. However, the literature contains a large amount of contradictory evidence for deviations from the collinear structure for $LiCoPO_4$ and $LiFePO_4$. Even subtle deviation from collinearity of the magnetic structure carry significant implications for the symmetry governed properties, such as magnetoelectric effect and toroidal order.

Within the collinear antiferromagetic structure with compensated magnetic moment reported for $LiCoPO_4$ with C_y basis vector, the allowed magnetoelectric tensor elements are α_{xy} and α_{yx}. Notably, $LiCoPO_4$ exhibits the largest reported magnetoelectric coefficients among $LiMPO_4$ family. Rivera et al. [122], while confirming the expected magnetoelectric tensor form, also revealed the unusually large absolute value and the existence of a strong butterfly type magnetoelectric loop for fields along b-axis. These features are inconsistent with the collinear antiferromagnetic order with compensated magnetic moment and hints at possible symmetry lowering existing in this compound.

Later Kharchenko et al. reported the possible existence of a weak ferromagnetic component along b-axis, based on SQUID magnetometry measurements on a high quality single crystal. They observed a spontaneous magnetic moment of the order 0.1G along b-axis at 15 K. This also suggests the lowering of symmetry from the original structure suggested for $LiCoPO_4$ [43].

Further, neutron diffraction studies of $LiCoPO_4$ suggest the existence of transverse magnetic moment components. Vaknin et al. [42] reported a weak magnetic peak at the (010) position, that is forbidden under the collinear C_y structure. They interpreted this as the evidence for collinear rotation of magnetic moment in the *bc*-plane by an angle of 4.6° away from the *b*-axis. This lowered symmetry magnetic structure is described by the combination of basis vectors C_y+C_z.

More recent neutron studies by Fogh et al. [44], identified a zero field magnetic ground state where in addition to the dominant magnetic structure described by C_y an additional minor component described by the basis vector A_z is reported. They reported the canting angle in the *bc*-plane to be about 7(1)° by comparing the intensities of the Bragg reflection (301) (indicating C_y structure) and the (100) reflection which indicates an A_z component and is forbidden under the collinear magnetic structure.

$LiFePO_4$ presents a similar case. As in $LiCoPO_4$, the dominant magnetic structure has been established to be of C_y type. However, neutron diffraction studies by Li et al. [106] revealed a non-zero intensity at the symmetry forbidden reflection (010). Based on the intensity ratio of the reflections (210) and (010), they inferred a rotation of the ordered magnetic moments by an angle 7.5(5)° towards *c*-axis, or equivalently about 3 ° towards the *a*-axis. In a later neutron diffraction and magnetoelectric study, Toft-Petersen et al. [38] reported a significantly smaller canting angle of about 1.3° with components along both the *a* and *c* axes described by the combination of basis vectors $C_x + A_z$ in addition to the dominant component of C_y type.

This chapter is motivated by these long-standing unresolved questions regarding the minor canting components of the $LiCoPO_4$ and $LiFePO_4$. In the present work, the existing ambiguity surrounding the symmetry and existence of canting components is addressed by utilizing a combination of single crystal neutron diffraction and spherical neutron polarimetry measurements. Having demonstrated the ability to selectively pole the four antiferromagnetic domains in a mixed-anisotropy compound in the chapter8, this chapter explores the same logic in order to test the existence and symmetry of orientation domains which arise from the existence of deviations from the strict collinear antiferromagnetic structure. Although the proposed canting components are small in magnitude, they represent a lowering of magnetic structure symmetry and therefore influence the symmetry governed properties of these materials. For example, in the ferrotoroidal material $LiCoPO_4$, the spin rotation proposed by Vaknin et al., generates a finite component of the toroidal moment along b-axis, as expressed in equation 9.1 [31,50]. Similarly, recently reported existence of a weak finite diagonal magnetoelectric tensor element α_{aa} in LiFePO$_4$ also indicates a symmetry lowering [39]. These observations highlight the importance of confirming the symmetry and existence of such canting components. This chapter therefore attempt to resolve the canting components comprehensively to establish a solid foundation for understanding the implications of this symmetry lowering on the physical properties.

9.2 Single crystal neutron diffraction of LiCoPO$_4$

Single crystal diffraction measurements were performed at the four-circle hot neutron diffractometer D9 at ILL Grenoble with a neutron wavelength of λ= 0.835Å. A high quality LiCoPO$_4$ single crystal was glued on to the sample holder with b-axis vertical. Integrated intensities were collected at 50 K and 2K over a wide set of symmetry allowed and nominally forbidden reflections to enable a precise determination of both nuclear and magnetic structure. The integrated intensity for each Bragg peak is collected following the method described in section 4.2.2. The integrated intensity represent the area under the omega scan for each Bragg peak. The figure 9.1 shows the 2D detector image for the (101) peak at a specific omega step.

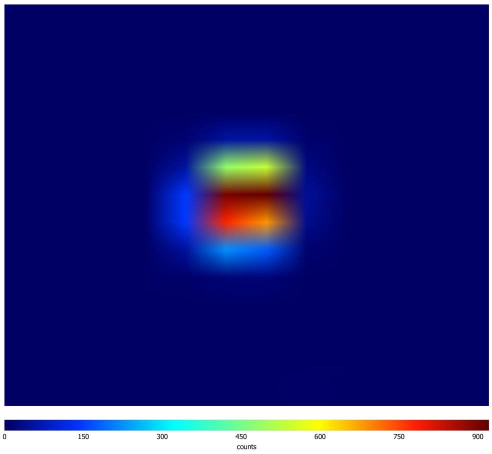

Figure 9.1: 2D detector image for the (101) peak at a specific omega step

9.2.1 Nuclear and magnetic structure refinement

A comprehensive refinement of the nuclear structure was carried out using the 50 K data, which is well above the reported Néel temperature ($T_N \approx 21K$ [17]), A total of 307 unique reflections were measured, corresponding to 166 symmetry inequivalent reflections. The crystal structure was refined in the space group $Pnma$. The scale factor, extinction parameters as well as atomic positons and anisotropic displacement parameters for all atoms were refined. Refinement with $Pnma$ space group resulted in an agreement factor of $R_F = 1.93$. As illustrated in the figure 9.2, indicative of an internally consistent structural model.The result of the refinement is summarized in table 9.1. The correlated refinement combining D9 data and the powder diffraction data from D2B, similarly exhibits excellent agreement factors, demonstrating the consistency across techniques. The fit quality for the correlated refinements are illustrated in figure9.3.

Atom	Site	x	y	z	Occ.
Li	$4a$	0	0	0	1
Fe	$4c$	0.27788(9)	1/4	0.9793(2)	1
P	$4c$	0.09394(5)	1/4	0.41815(9)	1
O1	$4c$	0.09726(4)	1/4	0.74212(9)	1
O2	$4c$	0.45425(4)	1/4	0.20544(8)	1
O3	$8d$	0.16619(3)	0.04403(5)	0.28189(6)	1

Table 9.1: Refined atomic position of $LiCoPO_4$ from the refinement of single crystal neutron diffraction data collected at 50 K. The refinement yields an agreement factor of R_f=1.93

Magnetic structure refinement: Magnetic structure refinement was performed at 2 K, including the forbidden peaks under the crystallographic structure described by the space group $Pnma$. Particular attention was given to weak purely magnetic reflections that could indicate canting of the magnetic moment. The refinements were attempted for 3 different models

- $\Gamma_2 + \Gamma_4$ - Tests the presence of magnetic moment canting of the type A_z along the c-axis as discussed in table 1.3, previously proposed in the reference [44].
- Γ_4 - This model corresponds to the widely accepted main component of the magnetic moment along b-axis and absence of any canting.

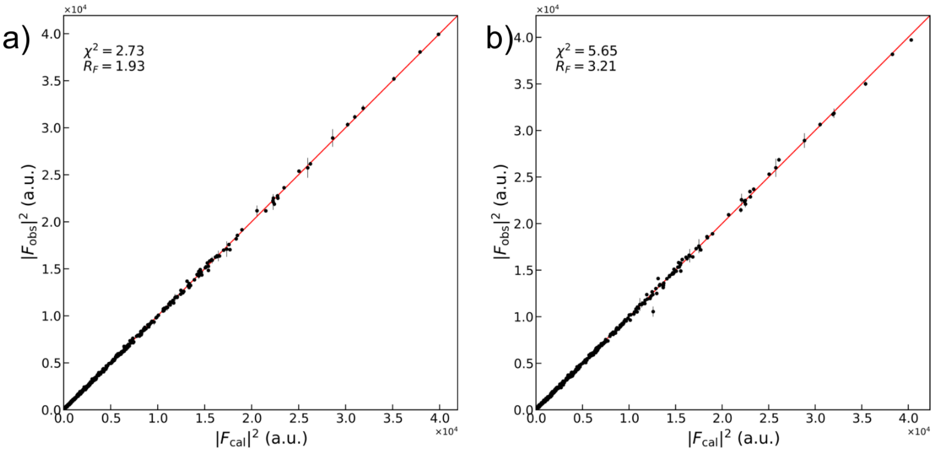

Figure 9.2: a)Crystal structure refinement result for single crystal data collected at 50 K b) Magnetic structure refinement for $\Gamma_2 + \Gamma_4$ model at 2K. Both data were collected on D9 instrument with wavelength of λ= 0.835 Å

- $\Gamma_4 + \Gamma_6$- This model incorporates a canting of the type C_z along the *c*-axis reported in reference [42].

Each magnetic model was refined against the full data set including the symmetry forbidden reflections. The best agreement factor was achieved for the $\Gamma_2 + \Gamma_4$ model with an R_F of 3.21 while the strictly collinear Γ_4 model yields an agreement factor of R_F= 3.49. The refinements yield a dominant C_y component of $3.51(2)\mu_B$, consistent with previously reported values for LiCoPO$_4$ [17, 42–44]. In addition a small canting of $A_z = 0.37(2)\ \mu_B$ is obtained. This corresponds to a canting angle of θ=6.0(3)° from the *b*-axis. The value is in close agreement with the canting angle of 7(1)° reported for the same symmetry in reference [44]. Refining the C_x component allowed by the Γ_2 irrep improves the agreement factor slightly and yields a value of $0.29(3)\mu_B$.
Both $\Gamma_4 + \Gamma_6$ and $\Gamma_2 + \Gamma_4$ improve the quality of the refinement compared to the Γ_4 model with magnetic moments strictly along *b*-axis. The refined magnetic moments within each magnetic model and the corresponding agreement factors are summarized in table 9.2. The figure 9.2 shows the refinement results for $\Gamma_2 + \Gamma_4$. Notably, the $\Gamma_4 + \Gamma_6$ model produces an angle $\theta = 3.8(7)°$ with non-zero minor component of the type C_z, while the previously proposed canting angle with this symmetry component was 4.6 ° [42].

Although both $\Gamma_4 + \Gamma_6$ and $\Gamma_2 + \Gamma_4$ improve the quality of the fit compared to the collinear model Γ_4, the extracted canting component must be interpreted with

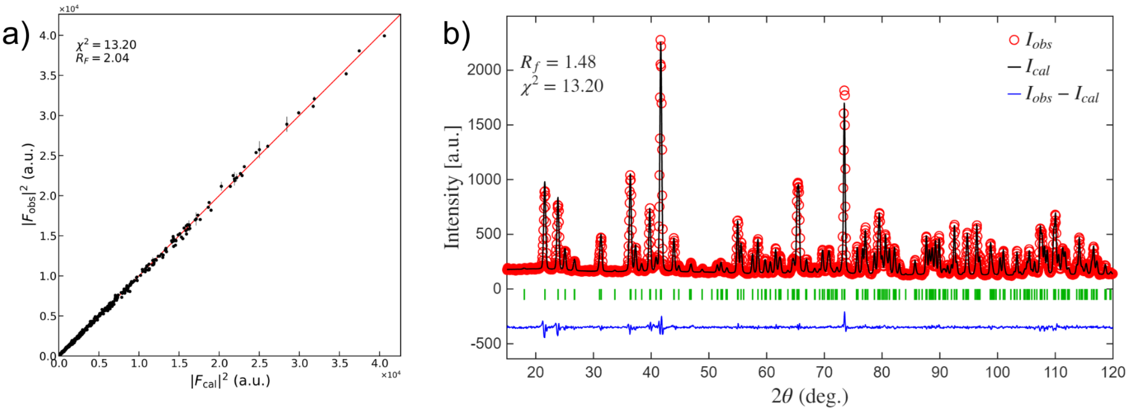

Figure 9.3: Correlated refinement result for single crystal data collected at 50 K on D9 instrument with wavelength of $\lambda = 0.835$ Å and the powder data collected on D2B with $\lambda = 1.594$ Å.

Magnetic structure	μ_a	μ_b	μ_c	μ_{total}	R_f
$\Gamma_2 + \Gamma_4$	0.29(3)	3.51(2)	0.37(2)	3.54(2)	3.21
Γ_4	-	3.45(2)	-	3.45(2)	3.49
$\Gamma_4 + \Gamma_6$	0.38(3)	3.46(2)	0.23(4)	3.49(2)	3.31

Table 9.2: Refined magnetic moment and corresponding agreement factors for the three tested magnetic structures of LiCoPO$_4$

caution. The symmetry forbidden peaks that lead to finite canting components in the refinement could have considerable contribution from multiple scattering and background artefacts. In the next section, the temperature dependence and ψ scans of key reflections are discussed to interpret their true nature.

9.2.2 Temperature dependence and ψ-scans of key reflections

To further assess the validity of the refined magnetic structure and to search for possible signatures of weak canting-related intensity contributions, temperature dependent measurements were carried out on the reflections (3 0 0), (0 -3 0), (0 -1 -2), (3 0 1) and (1 0 1). The relevant magnetic structure factors for the basis vectors and corresponding polarization factors contributing to these peaks are summarized in table 9.3. The temperature dependence of the reflections (3 0 0), (0 1 2), (3 0 1) and (1 0 1) were measured in the temperature range 4-300 K, while the (0 -3 0) reflection was recorded in the temperature range 9 to 26 K. The temperature dependence for all the peaks in the range 4 to 80 K is visualized in figure 9.4.

Magnetic reflections (1 0 1), (3 0 1) and (0 -1 -2) :

The reflections (1 0 1), (3 0 1) and (0 -1 -2) are allowed magnetic Bragg peaks for the Γ_4 model, which contains the basis vector C_y and therefore corresponds to a magnetic moment aligned strictly along the *b*-axis. All three reflections exhibit a temperature dependence characteristic of magnetic ordering. The reflection intensities drop rapidly above 20.5 K, reaching background level in the range 20.5 - 25K. This behaviour is consistent with the established Neél temperature of $LiCoPO_4$ ($T_N \approx 21.6$ K).

The absence of additional anomalies above T_N indicates the well-defined magnetic ordering for the Bragg reflections that correspond to C_y basis vector in the reported ordering temperature range. This validates the existence of C_y- type magnetic ordering.

Symmetry forbidden reflections (3 0 0) and (0 -3 0):

Both (3 0 0) and (0 -3 0) are forbidden by symmetry under the *Pnma* space group and therefore have zero nuclear structure factor. Any intensity at these positions must therefore originate from a secondary basis vector if the magnetic symmetry is lowered due to the rotation of spins away from the *b*-axis or from effects such as multiple scattering.

As can be seen from table 9.3, the reflection (3 0 0) has a non-zero intensity if the magnetic structure possess components of the type A_y or A_z. Therefore, the intensity of this reflection is expected to show an order-parameter like temperature dependence where a clear ordering temperature is visible if the minor magnetic moment components of the type A_z exist. However the observed scattering at (3 0 0) position is extremely weak and exhibit random intensity fluctuations comparable to statistical uncertainity. The absence of any anomaly at the ordering temperature implies that the intensity at this position is originating from the instrumental background or multiple diffraction contributions. Hence the temperature independent behaviour of (3 0 0) indicates the possible absence of a A_z type minor component within the detection limits of the instrument.

A similar argument applies to the (0 -3 0) reflection position, which exhibits non-zero intensity only for magnetic structures containing components of the type C_x and C_z. Therefore if the finite C_z minor components suggested from the refinement results exist, then the temperature dependence should exhibit an order-parameter dependent temperature evolution with a drop to background level at T_N. However, the measured intensity at this position consists of a very weak signal with large un-

H,K,L	$\lvert S_R(\mathbf{Q})\rvert^2$				$\lvert P_i(\mathbf{Q})\rvert^2$		
	A (↑↓↓↑)	G (↑↓↑↓)	C (↑↑↓↓)	F (↑↑↑↑)	x	y	z
(301)	0.06	0.19	11.83	3.92	0.34	1.00	0.66
(101)	0	0.2	15.3	0.5	0.80	1.00	0.20
(0-1-2)	0	0.99	15.01	0	1.00	0.86	0.14
(300)	12.02	3.98	0	0	0	1.00	1.00
(0-30)	0	0	16	0	1.00	0	1.00
(1-20)	15.52	0.48	0	0	0.92	0.08	1.00
(201)	1.83	13.92	0.22	0.03	0.54	1.00	0.46

Table 9.3: Calculated squared structure factor and polarization factors for the reflections on which temperature dependence was measured. The structure factor and the polarization factor are discussed in section 3.4.

certainities and random fluctuations, with no drop in intensity observed at T_N. This indicates the possible absence of a C_z type spin rotation away from b-axis. Similar to (3 0 0), this indicates the origins of intensity at this position not being magnetic diffraction.

The following section discusses the ψ scans of two symmetry forbidden reflections to evaluate the possibility that the canting components inferred from the refinement originate from multiple scattering.

Ψ scans of (0 -3 0) and (1 -2 0):

The measurements on D9 were performed using a short wavelength (λ= 0.835Å). Such conditions produce a large radius of Ewald's sphere and consequently increase the possibility of mulitple reciprocal lattice points intersecting the sphere simultaneously. These conditions enhance the probability of multiple diffraction events significantly. Multiple diffraction occurs when the diffractometer is setup to measure a specific reflection of (hkl), and a second refection $(hkl)'$ lies on the Ewald's sphere. The incident neutron with wave vector $\mathbf{k_i}$ is then diffracted by this secondary reflection $(hkl)'$, producing an intermediate wave vector $\mathbf{k}'$. This wave vector may fulfill the Bragg condition for a third reflection $(hkl)_{diff}$ = (hkl)-$(hkl)'$ and result in final wave vector k_f which is detected at the same angular position as the original reflection (hkl). The resulting intensity is much smaller than the intensity of a Bragg peak, however, this contribution becomes significant when the original considered Bragg peak is weak or extinct by symmetry [123–126]. This is particularly relevant in the present case, where the reflections that suggest weak canting components in

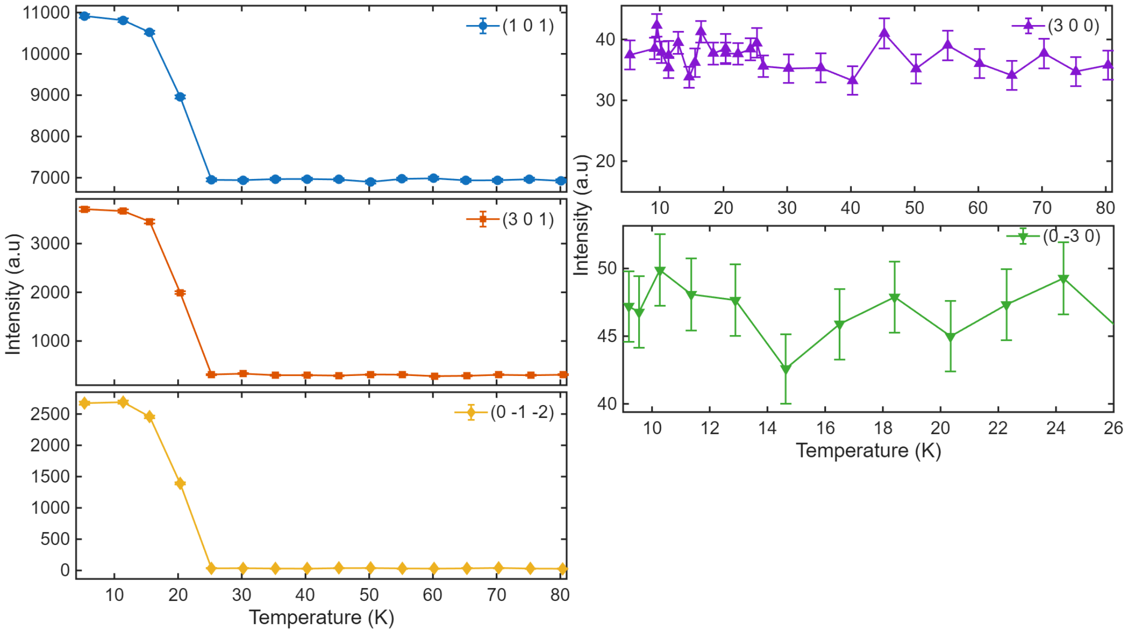

Figure 9.4: Temperature dependence of the Bragg peaks in the temperature range 4-80 K recorded on D9 instrument with wavelength of λ= 0.835 Å

the refinement are symmetry forbidden under the Γ_4 model, making them susceptible to contamination from multiple diffraction.

ψ scans are one of the methods that can be utilized to differentiate intrinsic diffraction from multiple diffraction. In a ψ scan, the crystal is rotated about the scattering vector of the selected reflection. For a true Bragg reflection, the integrated intensity is independent of ψ as it does not alter the diffraction condition for that reflection. In contrast, multiple diffraction occurs only for specific geometric alignments. As a consequence the intensity contribution from multiple diffraction varies strongly as a function of ψ. This forms the basis for analysing the weak canting components of $LiCoPO_4$ allowing to distinguish multiple diffraction intensities that exhibit strong ψ dependence from weak intensity from magnetic diffraction due to symmetry lowering.

Figure 9.5 illustrates the ψ-scans for the (0 -3 0) and (1 -2 0) reflections. As discussed earlier, these reflections acquire non-zero intensity in the presence of weak canting components of type C_z and A_z, respectively. For both reflections ψ scans were performed at 2 K in the magnetically ordered phase and at 50 K, well above the Néel temperature of $LiCoPO_4$.

The integrated intensity of the (0 -3 0) reflection exhibits pronounced variations

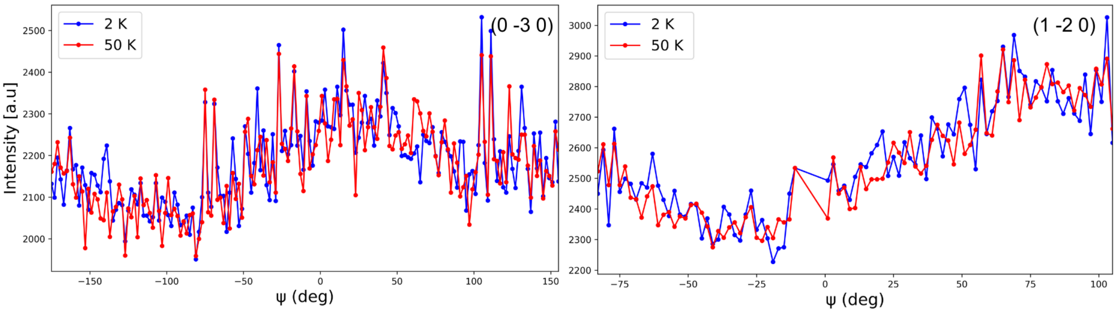

Figure 9.5: ψ-scans of (0 -3 0) and (1 -2 0) recorded on the instrument D9 with wavelength of λ= 0.835 Åat 2K and at 50K temperatures illustrated by blue and red markers respectively.

with ψ. Moreover, the integrated intensity recorded at 2K and 50K overlaps almost perfectly. Notably, no reduction in intensity was observed on heating above the ordering temperature. This behaviour indicates that the observed signal at (0 -3 0) is dominated by multiple diffraction rather than by a true C_z magnetic contribution. Similarly for (1 -2 0), the integrated intensity exhibits ψ dependency and the signal is almost temperature independent between 2K and 50 K. This likewise indicates the possible multiple diffraction origin for (1 -2 0).

The combined temperature dependence and the ψ-scans results rule out the presence of weak canting components associated with C_z and A_z within the sensitivity limits of the D9 experiment. The non-zero canting components obtained in refinements therefore most likely arise from multiple diffraction contribution rather than from real symmetry lowering. The intensity on the (0 -3 0) in bisecting condition (i.e. $\psi = 0$) is contaminated by the additional intensity that is roughly the difference between intensity at $\psi = 0$ and the minimum intensity in the ψ curve. Therefore, $LiCoPO_4$ adopts a purely $C_y(\Gamma_4)$ magnetic structure within the detection limits of single crystal neutron diffraction at D9. Nevertheless, single crystal neutron diffraction is fundamentally limited in its ability to resolve small canting components. In contrast, SNP provides better sensitivity to weak canting components as it allows to distinguish between different magnetic moment directions. Therefore, the next section discusses the SNP measurements for $LiCoPO_4$ to unambiguously determine the weak canting component of the magnetic moment.

9.3 Spherical neutron polarimetry of $LiCoPO_4$

9.3.1 Experimental setup

Spherical neutron polarimetry measurements were carried out on the same single crystal of $LiCoPO_4$ as the one used for single crystal neutron diffraction experiment on D9. The crystals was glued to the bottom capacitor plate with the b-axis along the vertical direction. The experimental setup follows the configuration described previously in section 8.4.

As discussed in section 6.5, $LiCoPO_4$ is a ferrotoroidic material and the toroidal moment in $LiCoPO_4$ is given by the equation

$$\mathbf{t} = 2\mu\epsilon a\,(\cos\theta\,\hat{\mathbf{z}} + \sin\theta\,\hat{\mathbf{y}}) \tag{9.1}$$

Where, θ represents the angle of collinear rotation of the type C_z away from the b-axis. The dominant component of the magnetic moment in $LiCoPO_4$ corresponds to spins aligned along the b-axis of the type C_y producing a toroidal moment along the c-axis. Therefore, to selectively populate one of the toroidal domains the cross product of $\mathbf{E} \times \mathbf{H}$ should be along the $\pm c$ axis, following from the discussion in the section 8.2.1.

To populate one of the toroidal domains in $LiCoPO_4$, the sample was cooled below the Néel temperature with an electric field along $+b$ axis and a magnetic field primarily along $-a$ axis in order to achieve the conjugate field $\mathbf{E} \times \mathbf{H}$ along $\mathbf{c}$. Motivated by our successful poling of orientation domains reported in chapter 8, we have further applied a c component of the magnetic field by rotating the magnetic field in the a-c plane, which is the only degree of freedom in the current exprimental configuration. Depending on the symmetry and existence of canting components, the magnetic field component along c-axis can induce a potential orientation domain imbalance, which can be detected using the off-diagonal elements of the polarization matrix.

9.3.2 SNP analysis of $LiCoPO_4$

The Γ_4 structure of $LiCoPO_4$ yields a magnetic interaction vector component $M_{\perp z}$, corresponding to spins aligned along b-axis. Any weak spin canting, away from the b-axis, produces an additional magnetic moment component in the ac-plane generating a non-zero magnetic interaction vector component $M_{\perp y}$. Therefore, even if an equal population of the orientation domains suppress the off-diagonal element P_{xz}, which contains terms linear in $M_{\perp y}$, the presence of canting components can still be detected. This is because the diagonal elements of the polarization matrix contain terms that depend on the square of the magnetic interaction vector component $M_{\perp y}$ which is independent of the domain distribution as can be seen from the polarization matrix 8.3. The deviations of diagonal elements from their value corresponding to the Γ_4 structure, therefore allow the detection of canting components in this experimental configuration.

The full polarization matrices were measured for selected Bragg reflections that exhibit non-zero structure factors for the canting basis vectors C_z and A_z. The calibration of the cell efficiency was done using the nuclear peak (0 0 2).

The field cooling was carried out with an applied voltage of 7 kV and a magnetic field of 1 T with $\phi = 30°$, where ϕ is the angle between magnetic field and a-axis in the ac-plane. The polarization matrix observed for field cooling with $+\mathbf{E} \times -\mathbf{H}_{\phi\_}$ for the selected peaks is represented in figure9.6. As can be seen from the figure, for all measured reflections, the P_{xz} term remains zero within experimental uncertainity. This can arise either from the absence of canting components or from equal population of orientation domains in the presence of weak canting. Therefore, the decisive elements are the diagonal elements. Refinement results of the full polarization matrices at 2 K are represented in figure 9.6. The refinement was carried out using the structural parameters obtained from the D9 single crystal neutron diffraction measurements. For both proposed models ($\Gamma_2 + \Gamma_4$ and $\Gamma_4 + \Gamma_6$), the canting components, A_z and C_z, converge to zero within the error bars, upon refining the SNP data indicating zero canting. However, it is important to emphasize the scale of the expected signatures. The proposed canting angle of 4.6° for C_z type produces a difference between P_{xx} and P_{yy} of ≈ 0.01 for the measured reflections in this geometry, and an even smaller signature is expected for A_z-type canting for the selected Bragg reflections. Such a difference approaches the limit of detectability under the current experimental configuration.

Tilted scattering plane: In this section instead of aligning the b-axis along the vertical direction, a tilted configuration is adapted. The reciprocal space vector (00.990.10) is aligned parallel to the vertical direction, resulting in a $\approx 6.7°$ tilt of the b-axis relative to the vertical with (1 0 0)-(0 1 -6) plane in the scattering plane. The electric field is applied along the vertical direction with an applied voltage of 10 kV along with a magnetic field of 1 T along the a-axis. This configuration allows

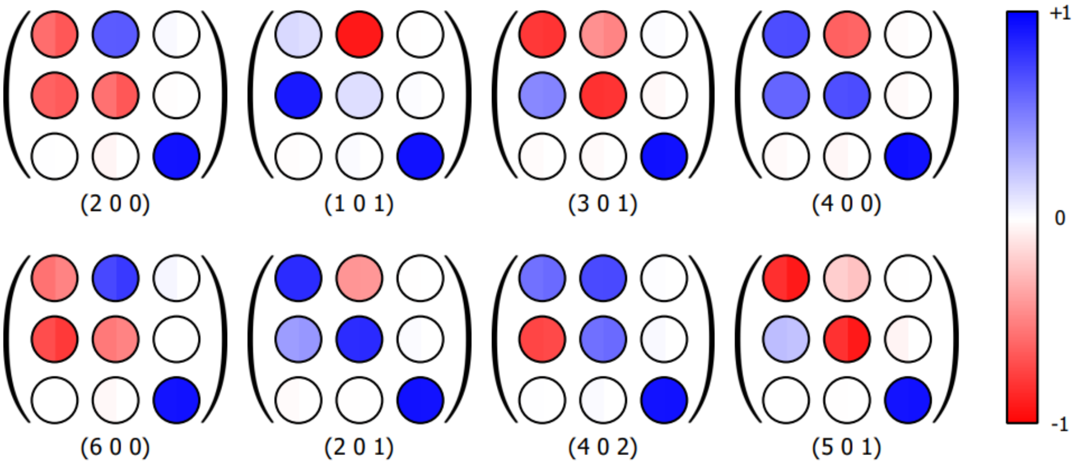

Figure 9.6: Refined polarization matrices for selected Bragg reflections at 2 K. The left half of the circle represent the observed value and the right half represent the calculated value for the magnetic structure model $\Gamma_2 + \Gamma_4$.

a cross product of $\mathbf{E} \times \mathbf{H}$ along the b-axis in addition to the major component along c-axis. An increased voltage was used for the electric field to increase the component of cross product along b-axis. This additional conjugate field along the b axis can preferentially stabilize one of the toroidal moment components along the b-axis and thereby stabilize one of the orientation domains in the case of collinear rotation of C_z for which the toroidal moment calculation is carried out in equation 9.1. A full polarization matrix was measured for the reflection (2 0 0), which possesses non-zero intensity for the C_z type canting. The nuclear peak used for calibrating the cell efficiency over time was (216). As in the previous configuration, the refinement of the polarization matrix yields a vanishing canting component. The refined polarization matrix for the (2 0 0) peak is shown in figure9.7.

Across both geometries, the SNP analysis detects no measurable canting within the instrument sensitivity. The combined results from single crystal diffraction and SNP measurements on $LiCoPO_4$ carried out in this work, therefore did not detect any canting component that has been previously reported in the literature for $LiCoPO_4$ within the detection limits of the discussed data. However, the expected signatures for the canting in the measured geometry and selected reflections are small and improved sensitivity to the canting components could be achieved using specialized experimental geometries aimed to produce a preferential population between the orientation domains and can be optimized for peaks that exhibit the largest signature within the diagonal elements. In the first configuration explained in this work,

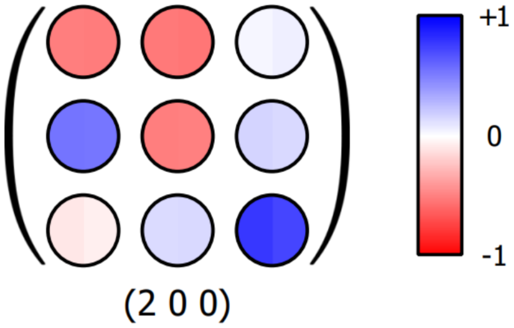

Figure 9.7: Refined polarization matrix for the reflection (200) at 2 K. The left half of the circle represent the observed value and the right half represent the calculated value for the magnetic structure model $\Gamma_4 + \Gamma_6$.

the biggest signature for the canting A_z is observed for the peak (2 0 1) among the measured peaks which corresponds to P_{xx}-P_{yy}=0.008. Similarly for C_z canting, the biggest signature among the observed peaks is for the reflection (6 0 0) corresponding to P_{xx}-P_{yy}=0.01.

9.4 Single crystal neutron diffraction of $LiFePO_4$

The single crystal diffraction measurements for the $LiFePO_4$ compound were carried out at the D9 instrument at the ILL with a wavelength of λ =0.835Å. The $LiFePO_4$ single crystal was glued to the sample holder with the *b*-axis along the vertical direction. Integrated intensities of both symmetry allowed and symmetry forbidden reflections were recorded at 2 K, 80 K and 300K. The following section discusses the nuclear and magnetic structure refinements from these measurements.

9.5 Nuclear and magnetic structure refinement

The nuclear structure refinement was performed using the data collected at 300 K and 80K, above the reported ordering temperature $T_{\mathrm{N}} = 50$ K [18]. Integrated intensity of a wide range of reflections were recorded including 1074 unique reflections of which 616 are symmetry inequivalent, in addition, 124 symmetry forbidden reflections were measured.

The nuclear refinements were carried out within the orthorhombic space group *Pnma*. The atomic positions, extinction parameters, scale factor and anisotropic displacement parameters were refined. Absorption correction for the data were applied using the 3D model of the sample implemented in the Mag2Pol software using a series of 360° images of the crystal mounted on the instrument. The $LiFePO_4$ crystal was bigger and deviates from near spherical shape of the $LiCoPO_4$ crystal. Therefore the absorption correction accounts for the geometric absorption effects. The nuclear refinements at 300K yielded an agreement factor of R_F= 7.83 for 300K and R_F = 9.67 for 80 K. The refinement failed to fully reproduce the observed integrated intensities. Noticeable deviations between observed and calculated intensities are present in the refinement results at 300 K and 80K as illustrated in figure 9.8.

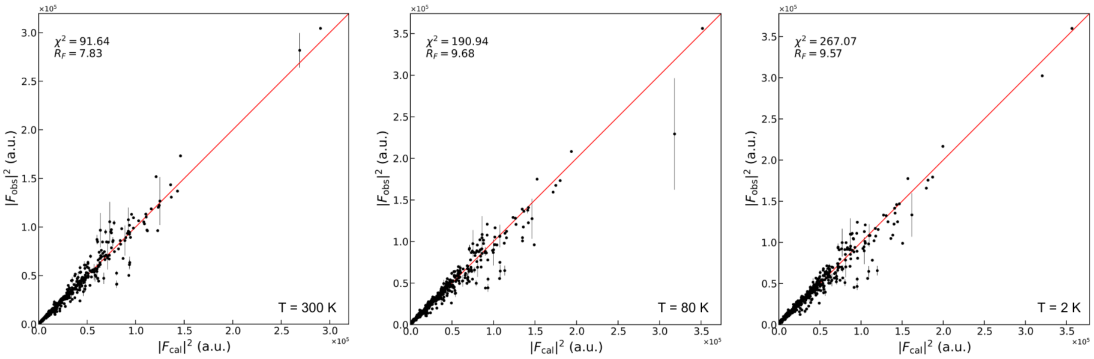

Figure 9.8: Refinement of single crystal data collected on D9 with wavelength of λ= 0.835 Åat 300 K , 80 K and at 2K with magnetic structure $\Gamma_2 + \Gamma_4$

Magnetic structure refinement: The magnetic structure refinement was performed under the crystallographic space group *Pnma*, using the 2 K dataset in which all forbidden reflections under *Pnma* are included. In $LiFePO_4$, recent studies have suggested additional minor spin components in addition to the dominant *b*-axis moment. Toft-Petersen et al [38] proposed minor spin components with C_x and A_z basis vectors described by the model $\Gamma_2 + \Gamma_4$, where the spin rotation away from *b*-axis is around 1.3(1)°. In contrast, Jiying Li et al [106] suggest a larger spin rotation either towards the *c*-axis or the *a*-axis with an angle of 3-7° depending on the direction of spin rotation.

This study therefore compares three models - Γ_4 model with no canting, $\Gamma_2 + \Gamma_4$ with minor components described by the basis vectors C_x+A_z and $\Gamma_4 + \Gamma_6$ which allows canting with basis vectors A_x and C_z.

Among the three tested models, both $\Gamma_2 + \Gamma_4$ and $\Gamma_4 + \Gamma_6$ models yield comparable agreement factors of R_F=9.56 and 9.57 respectively. The refined magnetic moments and the agreement factors for all three models are summarized in table 9.4. Both

Magnetic structure	μ_a	μ_b	μ_c	μ_{total}	R_f
$\Gamma_2 + \Gamma_4$	0.6(1)	3.7(2)	0.5(1)	3.7(2)	9.56
Γ_4	-	3.7(2)	-	3.7(2)	9.87
$\Gamma_4 + \Gamma_6$	0.6(1)	3.6(2)	0.6(1)	3.7(2)	9.57

Table 9.4: Refined magnetic moment and the corresponding agreement factors for magnetic structure models $\Gamma_2 + \Gamma_4$, Γ_4 and $\Gamma_4 + \Gamma_6$

models that permit non-zero canting components improve the fit quality compared to the Γ_4 model where spins are aligned strictly along the *b*-axis (R_f= 9.87).

The refined magnitude of the magnetic moment $\mu = 3.7(2)\ \mu_B$ is consistent with the previously reported values [76, 106, 127]. The refined canting components result in a rotation of the magnetic moment away from the *b*-axis by approximately 12°, which is significantly higher than previously reported values. Even though the refinement stabilizes the magnetic structures with lowered symmetry with non-zero canting components, as discussed in section 9.2.1, the contributions from multiple diffraction and background contributions can generate apparent intensities at the forbidden reflection angle positions. Such artefacts can artificially stabilize the canting components in refinements. Therefore, the validity of such reflections must be verified using ψ scans and temperature dependent measurements before reaching a conclusion regarding the presence of canting components.

9.6 Temperature dependence and ψ scans of key reflections

The temperature evolutions of the three reflections (012), (300) and (030) are illustrated in figure 9.9 and their corresponding structure factors are listed in table 9.3. The reflection (012) is dominated by the intensity contribution from the C_y-type structure. The integrated intensity of this reflection exhibits a pronounced temperature dependence, where it drops to background level on heating above the Néel temperature of 50 K, which is consistent with the previously reported ordering temperature. The peak exhibits a characteristic second order disppearance of long-range ordered magnetic moment associated with the dominant C_y basis vector.

The reflection (030) possesses a non-zero structure factor for both C_x and C_z-type canting components and is forbidden under *Pnma* space group, therefore possessing zero nuclear structure factor. Although this reflection exhibits a considerable intensity at 2 K, the integrated intensity does not vanish upon heating above the ordering temperature. The integrated intensity exhibits a monotonic decrease from 2K to 300 K instead of a sharp transition associated with an ordered magnetic moment component of the symmetry type C_x or C_z. The absence of critical behaviour strongly suggests that the signal observed at this position is contaminated by multiple diffraction or other instrumental effects rather than originating from a true canting component.

A similar behaviour is observed for the (3 0 0) reflection, which is sensitive to the A_z canting component and possess zero nuclear structure factor. The observed signal for (3 0 0) is extremely weak at 2 K and does not exhibit a sharp transition at T_{N} expected for a magnetic ordering. Instead it exhibits a weak temperature dependence, gradually dropping to background levels at 300 K.

The weak temperature dependence of these intensities could be due to the change in Debye-Waller factor and cast significant uncertainities regarding the canting component stabilized in the refinements. The behaviour is more consistent with the contribution from multiple scattering or other experimental backgrounds rather than with genuine canting components.

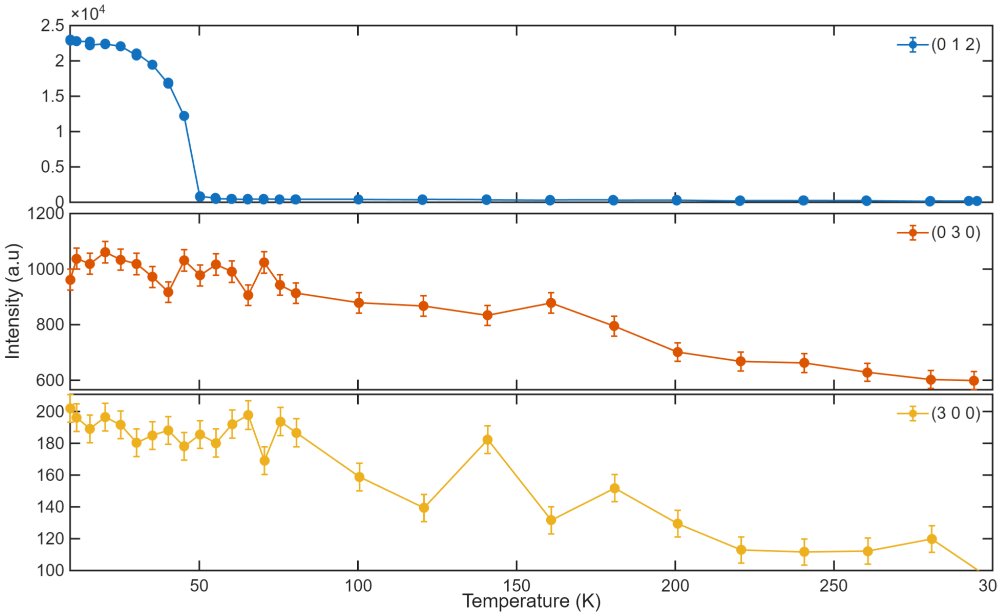

Figure 9.9: Temperature dependence of the Bragg peaks in the temperature range 9-300 K recorded on D9 instrument with wavelength of λ= 0.835 Åfor $LiFePO_4$

The figure 9.10 illustrates the ψ scan recorded for (030) at 300 K and at 80 K. At both temperatures, the integrated intensity is dependent on the angle ψ indicating the presence of possible multiple diffraction at this reflection position. To determine the canting components of the $LiFePO_4$ unambiguously, SNP measurements were carried out for $LiFePO_4$ at the D3 instrument.

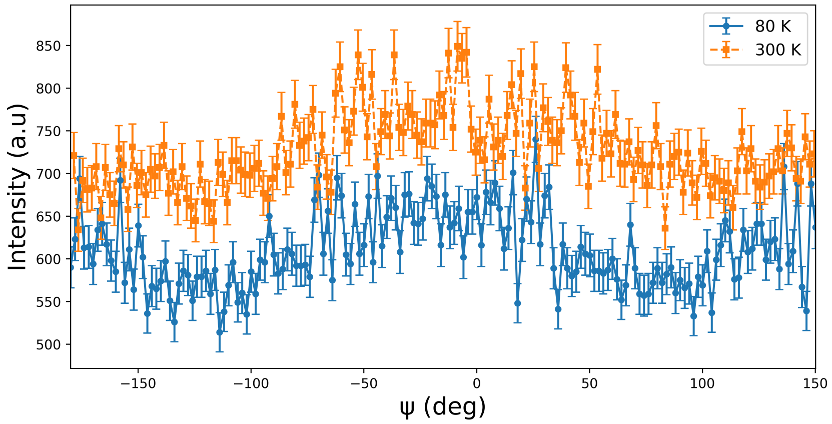

Figure 9.10: ψ-scan of the reflection (030) of $LiFePO_4$ recorded on D9 instrument with wavelength of $\lambda = 0.835$ Å

9.7 Spherical neutron polarimetry of $LiFePO_4$

Spherical neutron polarimetry measurements for $LiFePO_4$ were carried out using the same experimental setup described in section 9.3.1. The $LiFePO_4$ single crystal used for the D9 measurements was glued on to the lower capacitor plate with the b-axis oriented along the vertical direction. An electric field was applied along $+b$ axis with an applied voltage of 9.3 kV, while the magnetic field was applied within the ac plane at an angle of 30° to the a-axis. In the current configuration the magnetic field was applied along negative a axis with 30° rotation towards positive c-axis ($+\mathbf{H}_{\phi_+}$). Analogous to the considerations for $LiCoPO_4$ in section 9.3.1 and for the mixed anisotropy system $LiNi_{0.8}Fe_{0.2}PO_4$ in chapter 8, the major magnetic moment component in $LiFePO_4$ belongs to the Γ_4 model with spins aligned along the b-axis. This component gives rise to toroidal domains with a toroidal moment along $\pm c$, which can be in principle selectively populated with a conjugate field of $\mathbf{E} \times \mathbf{H}$ along $\pm c$ axis. However, the formation and detectability of the orientation domains depends on the presence and symmetry of the proposed canting components.

Following the arguments presented in section 9.3.2, full polarization matrices for selected Bragg peaks were measured at 2 K after field cooling. The nuclear structural parameters for the refinement of the observed polarization matrices were taken from the single crystal diffraction measurements on D9. For all measured reflections, the P_{xz} value was close to zero indicating that if canting components exist, the corresponding orientation domains are populated nearly equally.

Refinement of the observed matrices yielded the best agreement factors for the $\Gamma_2 + \Gamma_4$ model, with canting components of C_x =0.6(1)μ_B and A_z=0.4(3)μ_B while the dominant component is $C_y = 4.17(6)\mu_B$. The refined magnetic moment and the agreement factors for the three considered magnetic structures are summarized in table 9.5. The resulting magnetic moment magnitude 4.23(7)μ_B is comparable to the value reported in reference [38]. However, the refined canting angle of 9.8(2.5)° is significantly higher than the value reported. In interpreting this result, it is important to note that the SNP refinements utilize the structural parameters from the D9 single-crystal refinement, which failed to achieve a satisfactory agreement with observed and calculated intensities. The error in atomic positions or extinction parameters extracted from D9 data can introduce deviations in the calculated nuclear structure factor in SNP refinement, which it compensates for by artificially enhancing the canting components and the magnetic moment magnitude in general as can be seen from the refined values of magnetic moment magnitude from D9 and SNP. Therefore the large canting angle obtained from the refinement is unlikely to

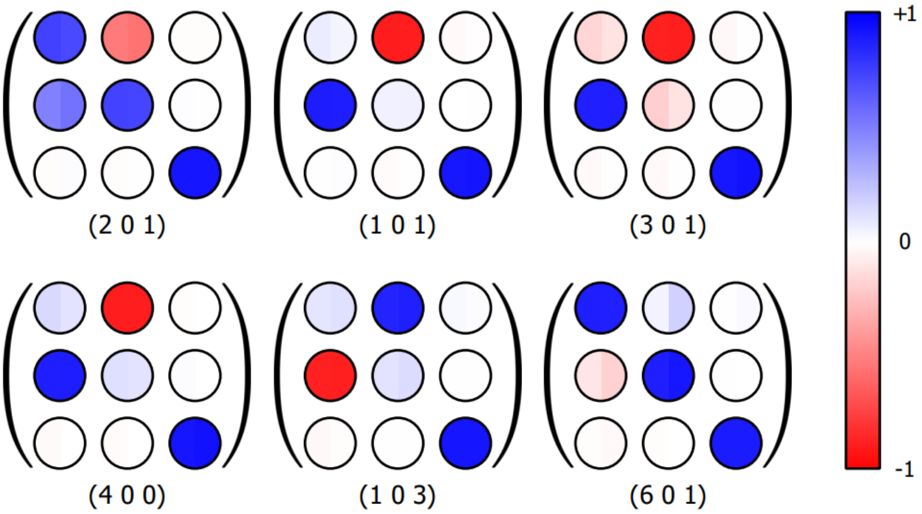

Figure 9.11: Refined polarization matrices for the selected Bragg reflections for the model $\Gamma_2 + \Gamma_4$ with canting components C_x and A_z

be intrinsic to $LiFePO_4$ and is most plausibly arising from the limitations of the underlying structural model.

Combining the single crystal diffraction and SNP results, although both refinements stabilize non-zero canting components, the evidence for the canting is not robust. The limitations of the structural model derived from the single crystal measurements significantly influence the interpretation of SNP results. In order to obtain a more reliable determination of the canting components in $LiFePO_4$, a more accurate structural model need to be established, especially in light of the previously reported canting angle of 1.3°. A single crystal diffraction experiment could be attempted with another crystal to determine if the poor structure modelling in this work arises from the imperfections in the single crystal used here. In addition, specialized SNP experimental geometries need to be investigated that is optimized to unambiguously determine the canting components in $LiFePO_4$.

Magnetic model	μ_a	μ_b	μ_c	μ_{tot}	Domain population (%)				χ_r^2
					a'_4	a''_4	b'_4	b''_4	
$\Gamma_2 + \Gamma_4$	0.6(1)	4.17(6)	0.4(3)	4.23(7)	46(3)	52(3)	0(3)	2(3)	233.39
Γ_4	–	4.16(6)	–	4.16(6)	98(2)		2(1)		256.09
$\Gamma_4 + \Gamma_6$	0.5(3)	4.16(6)	0.6(2)	4.23(7)	46(3)	52(3)	2(3)	0(3)	250.70

Table 9.5: Refined magnetic moments, domain population and χ_r^2 value for the tested magnetic structure models of $LiFePO_4$ using the polarization matrices of reflections indicated in figure 9.11. For the model Γ_4, the indicated domain population is for the two 180°domains as the orientation domains does not exist in this model.

9.8 Discussion

The combined single crystal neutron diffraction and spherical neutron polarimetry investigations presented in this chapter provides a reassessment to the differing reports of existence and symmetry of the minor magnetic moment compponents in the $LiCoPO_4$ and $LiFePO_4$. This chapter highlights the strong susceptibility of key reflections that have been interpreted as signatures of canting in the previous reports to the contaminations from multiple scattering and the limitations introduced by a poor structural model.

This is particularly evident in the case of $LiCoPO_4$, where the initial single crystal refinements with an excellent agreement factor stabilize canting components with angles consistent with those reported in the literature. However, further verifications using the temperature evolution of intensities and ψ scans demonstrate that these reflections are dominated by the contaminations from multiple diffraction rather than by the magnetic reflection from canting, within the detection limits of the instrument. This is further confirmed by the SNP experiments. The ability to selectively populate the orientation domains should be investigated in future studies to determine the existence of canting as this study rules out the existence of canting above the magnitude that can be resolved through the refinement of polarization matrices which rely on the signature of canting on the diagonal elements alone.

The results from $LiFePO_4$ are less robust than the results from $LiCoPO_4$ owing mainly to the poor structural model from single crystal diffraction refinements even with extensive abosorption corrections. Even though, both single crystal and SNP measurements stabilize canting components, dedicated temperature evolution studies on key reflections undermines the reliability of these results. In addition, significantly higher canting angles resulting from both techniques point towards the possibility of artificial stabilization of the canting angle in the refinement to compensate the errors originating from underlying structure parameters.

In conclusion, this chapter demonstrate the comprehensive attempt to resolve the minor canting components in $LiCoPO_4$ and $LiFePO_4$, that are of particular interest due to their influence on the assoicated physical properties such as magnetoelectric effect and toroidal order. This work explores the combination of single crystal diffraction and SNP measurements as a pathway to resolve the minor spin canting components. Even though the diagonal elements of the polarisation matrices are sensitive to the magnetic moment magnitude for different components, for canting angles of the magnitude reported for these compounds, higher focus should be given to the selective poling of orientation domains that arise when the canting is present, as demonstrated in chapter 8.

Conclusions and outlook

This thesis investigates chemical substituion in $LiMPO_4$ antiferromagnets as a tool to tune the magnetic ground state through competing anisotropy and exchange interactions. The chemical substitution phase diagrams of $LiCo_{1-x}Ni_xPO_4$ and $LiNi_{1-x}Fe_xPO_4$ were investigated using neutron powder diffraction, revealing the emergence of oblique antiferromagnetic structure in the mixed-anisotropy regime. Within the stabilized oblique antiferromagnetic structure in $LiNi_{1-x}Fe_xPO_4$, the identified composition hosting a four domain state was explored using spherical neutron polarimetry, through which the control of four domains were demonstrated and there by establishing the system as a single phase antiferromagnetic system that provide conceptual basis for quaternary memory systems. Finally, leveraging the domain selection mechanism developed in the mixed-anisotropy system, the parent compounds $LiCoPO_4$ and $LiFePO_4$ were revisited to determine the existence and symmetry of the canting components.

Chapter5 details the different synthesis strategies undertaken to synthesize phase pure polycrystalline samples of $LiCo_{1-x}Ni_xPO_4$ and $LiNi_{1-x}Fe_xPO_4$, motivated by the numerous synthesis procedures reported in literature. For the $LiCo_{1-x}Ni_xPO_4$ series, the synthesis procedure was successfully optimized to produce phase pure samples whose purity was confirmed by X-ray diffraction measurements. In contrast, the synthesis for $LiNi_{1-x}Fe_xPO_4$ did not yield a phase pure material, indicating additional challenges for this series that could not be fully resolved within the scope of this work.

Chapter6, presents a comprehensive investigation of the evolution of the magnetic structure in $LiCo_{1-x}Ni_xPO_4$ as a function of Ni content, using neutron powder diffraction and bulk magnetization measurements. Introducing Ni^{2+}, which has an easy axis along c, into the $LiCoPO_4$, where the easy axis of the Co^{2+} is b axis, leads to a rotation of spins across the compoisition range. The competing single-ion anisotropies and exchange interactions stabilize an oblique antiferromagnetic phase in the intermediate compositions, which is a characteristic of mixed anisotropy antiferromagnets. Although, the powder results clearly indicate the spin rotaion and symmetry lowering, further single crystal neutron diffraction measurements are required to determine the phase boundaries accurately in this series. The calculations of the toroidal moment for the refined magnetic structures in this series clearly indicate the emergence of four toroidal domain states arising in the oblique antiferromagnetic regions of the composition phase diagram. Highlighting this compositon range as a promising platform to explore controllable multidomain states in a single phase antiferromagnetic system.

Building on the observations from the $LiCo_{1-x}Ni_xPO_4$ series, the investigation of mixed anisotropy systems in $LiMPO_4$ family of compounds was extended to the series $LiNi_{1-x}Fe_xPO_4$, in chapter7. This series, presents a different case of anisotropy competition compared to the $LiCo_{1-x}Ni_xPO_4$ series. Here the easy axis of the Ni^{2+} coincides with the hard axis of the Fe^{2+} and vice versa. This offered an oppurtunity to assess the generality of spin rotation and the characteristics of the composition phase diagram for the $LiMPO_4$. Neutron powder diffraction reveals an extended oblique antiferromagnetic phase in which the spin is rotated away from the *b*-axis towards the *a*-axis within the *ab*-plane. This is in contrast to the $LiCo_{1-x}Ni_xPO_4$ system, where the oblique antiferromagnetic strucutre possess spins in the plane spanned by the easy axes of the end compounds. The major oblique magnetic phase identified in $LiNi_{1-x}Fe_xPO_4$ agreed with the previous experimental and theoretical observations reported in the literature. However, for the nominal composition x =0.2, the present work indicates a magnetic structure with spins in the *bc*-plane, which is different from the major oblique antiferromagnetic phase observed in this series and also contradicts experimental observation reported in literature for this composition. As neutron diffraction alone does not conclusively determine the precise occupation ratio of Ni and Fe compositional variation is a plausible explanation for this deviation. The major oblique antiferromagnetic phase described by the $\Gamma_2 + \Gamma_4$ model, is identified as a magnetic structure which host four symmetry allowed antiferromagnetic domains and also satisfies the symmetry conditions to host ferrotoroidal order. These characteristics makes this series a promising candidate for domain engineered functionalities.

The insights gained in chapter 7 directly motivated the investigations presented in chapter8, where the specific composition $LiNi_{0.8}Fe_{0.2}PO_4$ was examined using spherical neutron polarimetry to verify the existence of ferrotoroidal order and to explore selective poling of the four domain states in the $LiNi_{0.8}Fe_{0.2}PO_4$. At low temperatures, this composition exhibits a magnetic structure with spin components along both b-axis and a-axis as established in literature. In this structure, two 180° domains which correspond to the toroidal domains in the case of existing ferrotoroidal order and two orientation domains are allowed by symmetry. In this work, the existence of ferrotoroidal order was confirmed by the high efficiency selective population of toroidal domains using the conjugate field $\mathbf{E} \times \mathbf{H}$. Moreover, the orientation domain selection were also demonstrated by exploiting the Dzyaloshinskii-Moriya coupling between the induced magnetic moment along c-axis, arising under an applied magnetic field along c-axis and the ordered spin component along the a-axis. The combination of these two mechanisms, enable the selective and non-volatile stabilization of four antiferromagnetic domains through four different combinations of applied fields. These results establish a concrete physical basis for quaternary memory concepts using a single phase antiferromagnetic material, thereby positioning mixed-anisotropy systems as an important model platform for multistate antiferromagnetic spintronics.

Motivated by the successful domain selection mechanisms demonstrated in the mixed-anisotropy systmes, the long standing questions regarding the minor canting components in $LiCoPO_4$ and $LiFePO_4$ were addressed in the chapter 9. This chapter explores the debated canting components using a combination of single crystal neutron diffraction and spherical neutron polarimetry. In $LiCoPO_4$, no evidence of the proposed canting components were detected within the sensitivity of SNP experiment, whereas in $LiFePO_4$, a definitive conclusion regrading the canting components was hindered primarily by the limitations of the structural model developed in this work.

A natural next step following the results presented in this thesis is to study the magnetoelectric response across the substitution phase diagram of both $LiCo_{1-x}Ni_xPO_4$ and $LiNi_{1-x}Fe_xPO_4$. In the substitution series $LiNi_{1-x}Fe_xPO_4$, the significant magnitude increase and the modification of magnetoelectric tensor form have already been demonstrated for the x=0.2 sample in the literature. With the additional insight gained in this work regarding the magnetic ground state across the substitution phase diagram of the $LiNi_{1-x}Fe_xPO_4$ series, magnetoelectric response for other compositions could provide a deeper understanding of the influence of symmetry lowering on the magnetoelectric response. In the $LiCo_{1-x}Ni_xPO_4$, the symmetry of the oblique phase differs from that of the $LiNi_{1-x}Fe_xPO_4$, therefore furute studies on the magnetoelectric behaviour in the oblique antiferromagnetic phase of this series could provide insight into how the symmetry lowering tunes the magnetoelectric re-

sponse. Such investigations would clarify the extent to which chemical substitution can be used as a method to tailor the magnetoelectric response.
The successful demonstration of selective poling of four domains in $LiNi_{0.8}Fe_{0.2}PO_4$, motivates further research into the in-situ switchability of these domains which was only briefly explored in the present work. Further studies could employ higher field magnitudes and measurements of different samples to rule out the effect of domain pinning due to the presence of impurites. Moreover, switching experiments should be attempted for different composiitons to determine whether the domain rigidity is introduced by the chemical disorder inherent to the mixed-systems. Further, the powder diffraction study have identified suitable compositions within the $LiCo_{1-x}Ni_xPO_4$, where four toroidal domains are allowed by symmetry . These compositions allows the exploration of toroidal domains with similar domain selection mechanisms using different directions of crossed electric and magnetic field.
The results presented in this thesis demonstrate that the chemical substitution in $LiMPO_4$, provides a powerful route to engineer competing anisotropies and thereby stabilize distinct magnetic ground state. This tunability, in turn enables a control on domain structure and other symmetry governed physical properties. Beyond the established scientific relevance of the $LiMPO_4$ family as magnetoelectric materials, this work establishes the mixed-anisotropy series of this family as a potential rare platform for pursuing future research into multistate logic systems based on single phase antiferromagnetic materials .

Bibliography

[1] Ellen Fogh, Bastian Klemke, Manfred Reehuis, Philippe Bourges, Christof Niedermayer, Sonja Holm-Dahlin, Oksana Zaharko, Jürg Schefer, Andreas B Kristensen, Michael K Sørensen, et al. Tuning magnetoelectricity in a mixed-anisotropy antiferromagnet. *Nature Communications*, 14(1):3408, 2023.

[2] Stephen Blundell. *Magnetism in Condensed Matter.* OUP Oxford, 2001.

[3] Tapan Chatterji. *Neutron Scattering from Magnetic Materials.* Elsevier, 2005.

[4] C Timm. Theory of magnetism: International max planck research school for dynamical processes in atoms. *Molecules and Solids (Technische Univ. Dresden, Institute for Theoretical Physics, Dresden, Germany, 2015)*, 2011.

[5] Charles Kittel and Paul McEuen. *Introduction to Solid State Physics.* John Wiley & Sons, 2018.

[6] Theo Hahn, Uri Shmueli, and JC Wilson Arthur. *International tables for crystallography*, volume 1. Reidel Dordrecht, 1983.

[7] Norberto Majlis. *The Quantum Theory of Magnetism.* World Scientific, 2007.

[8] A Wills. Magnetic structures and their determination using group theory. *Le Journal de Physique IV*, 11(PR9):Pr9–133, 2001.

[9] I Kornev, J-P Rivera, S Gentil, AGM Jansen, M Bichurin, H Schmid, and P Wyder. Optical absorption of Co^{2+} in $LiCoPO_4$. *Physica B: Condensed Matter*, 270(1-2):82–87, 1999.

[10] G Rousse, J Rodriguez-Carvajal, S Patoux, and C Masquelier. Magnetic structures of the triphylite $LiFePO_4$ and of its delithiated form $FePO_4$. *Chemistry of materials*, 15(21):4082–4090, 2003.

[11] En-cai Xiao, Zhikai Cao, Jianzhu Li, Xue-Hui Li, Mengting Liu, Zhenxing Yue, Ying Chen, Guohua Chen, Kaixin Song, Huanfu Zhou, et al. Crystal structure, dielectric properties, and lattice vibrational characteristics of $LiNiPO_4$ ceramics sintered at different temperatures. *Journal of the American Ceramic Society*, 103(4):2528–2539, 2020.

[12] Gang Yang, Huan Ni, Haidong Liu, Po Gao, Hongmei Ji, Soumyajit Roy, João Pinto, and Xuefan Jiang. The doping effect on the crystal structure and electrochemical properties of $LiMn_xM_{1-x}PO_4$ (M= Mg, V, Fe, Co, Gd). *Journal of Power Sources*, 196(10):4747–4755, 2011.

[13] Helmut Ehrenberg, Natalia N Bramnik, Anatoliy Senyshyn, and Hartmut Fuess. Crystal and magnetic structures of electrochemically delithiated $Li_{1-x}CoPO_4$ phases. *Solid State Sciences*, 11(1):18–23, 2009.

[14] Tôru Moriya. Anisotropic superexchange interaction and weak ferromagnetism. *Physical review*, 120(1):91, 1960.

[15] Igor Dzyaloshinsky. A thermodynamic theory of “weak” ferromagnetism of antiferromagnetics. *Journal of physics and chemistry of solids*, 4(4):241–255, 1958.

[16] LC Chapon. An introduction to the use of representation analysis for studying magnetoelectrics and multiferroics. In *EPJ Web of Conferences*, volume 22, page 00013. EDP Sciences, 2012.

[17] R Santoro. Magnetic properties of $LiCoPO_4$ and $LiNiPO_4$. *Journal of Physics and Chemistry of Solids*, 27(6-7):1192–1193, 1966.

[18] RP Santoro and RE Newnham. Antiferromagnetism in $LiFePO_4$. *Acta Crystallographica*, 22(3):344–347, 1967.

[19] Thomas Bagger Stibius Jensen. *Magnetic structures, phase diagram and spin waves of magneto-electric $LiNiPO_4$*. Risø National Labratory, 2007.

[20] Vinod Wadhawan. *Introduction to ferroic materials*. CRC press, 2000.

[21] Nicola A Spaldin, Manfred Fiebig, and Maxim Mostovoy. The toroidal moment in condensed-matter physics and its relation to the magnetoelectriceffect. *Journal of Physics: Condensed Matter*, 20(43):434203, 2008.

[22] Namjung Hur, Soonyong Park, Peter Anand Sharma, JS Ahn, Sabyasachi Guha, and Sang-Wook Cheong. Electric polarization reversal and memory in a multiferroic material induced by magnetic fields. *Nature*, 429(6990):392–395, 2004.

[23] Ramaroorthy Ramesh and Nicola A Spaldin. Multiferroics: progress and prospects in thin films. *Nature materials*, 6(1):21–29, 2007.

[24] Nicola A Spaldin, Sang-Wook Cheong, and Ramamoorthy Ramesh. Multiferroics: Past, present, and future. *Physics today*, 63(10):38–43, 2010.

[25] Manish Kumar, S Shankar, Arvind Kumar, Avneesh Anshul, M Jayasimhadri, and OP Thakur. Progress in multiferroic and magnetoelectric materials: applications, opportunities and challenges. *Journal of Materials Science: Materials in Electronics*, 31(22):19487–19510, 2020.

[26] Nicola A Spaldin and Manfred Fiebig. The renaissance of magnetoelectric multiferroics. *Science*, 309(5733):391–392, 2005.

[27] Wilma Eerenstein, ND Mathur, and James F Scott. Multiferroic and magnetoelectric materials. *nature*, 442(7104):759–765, 2006.

[28] Stephanie Gnewuch and Efrain E Rodriguez. The fourth ferroic order: Current status on ferrotoroidic materials. *Journal of Solid State Chemistry*, 271:175–190, 2019.

[29] Manfred Fiebig. Revival of the magnetoelectric effect. *Journal of Physics D: Applied Physics*, 38(8):R123, 2005.

[30] Hans Schmid. Some symmetry aspects of ferroics and single phasemultiferroics. *Journal of Physics: Condensed Matter*, 20(43):434201, 2008.

[31] Claude Ederer and Nicola A Spaldin. Towards a microscopic theory of toroidal moments in bulk periodic crystals. *Physical Review B—Condensed Matter and Materials Physics*, 76(21):214404, 2007.

[32] I Abrahams and KS Easson. Structure of lithium nickel phosphate. *Crystal Structure Communications*, 49(5):925–926, 1993.

[33] Wojciech A Sławiński, Helen Y Playford, Stephen Hull, Stefan T Norberg, Sten G Eriksson, Torbjörn Gustafsson, Kristina Edström, and William R

Brant. Neutron pair distribution function study of $FePO_4$ and $LiFePO_4$. *Chemistry of Materials*, 31(14):5024–5034, 2019.

[34] F Kubel. Crystal structure of lithium cobalt double orthophosphate, $LiCoPO_4$. *Zeitschrift für Kristallographie-Crystalline Materials*, 209(9):755–755, 1994.

[35] V Koleva, R Stoyanova, and E Zhecheva. Nano-crystalline $LiMnPO_4$ prepared by a new phosphate–formate precursor method. *Materials Chemistry and Physics*, 121(1-2):370–377, 2010.

[36] Jiying Li, Wei Tian, Ying Chen, Jerel L Zarestky, Jeffrey W Lynn, and David Vaknin. Antiferromagnetism in the magnetoelectric effect single crystal $LiMnPO_4$. *Physical Review B—Condensed Matter and Materials Physics*, 79(14):144410, 2009.

[37] Thomas Bagger Stibius Jensen, Niels Bech Christensen, M Kenzelmann, Henrik M Rønnow, C Niedermayer, Niels Hessel Andersen, Kim Lefmann, M Jiménez-Ruiz, F Demmel, J Li, et al. Anomalous spin waves and the commensurate-incommensurate magnetic phase transition in $LiNiPO_4$. *Physical Review B—Condensed Matter and Materials Physics*, 79(9):092413, 2009.

[38] Rasmus Toft-Petersen, Manfred Reehuis, Thomas BS Jensen, Niels H Andersen, Jiying Li, Manh Duc Le, Mark Laver, Christof Niedermayer, Bastian Klemke, Kim Lefmann, et al. Anomalous magnetic structure and spin dynamics in magnetoelectric $LiFePO_4$. *Physical Review B*, 92(2):024404, 2015.

[39] Ellen Fogh, Bastian Klemke, Alexandre Pages, Jiying Li, David Vaknin, Henrik M Rønnow, Niels B Christensen, and Rasmus Toft-Petersen. The magnetoelectric effect in $LiFePO_4$–revisited. *Physica B: Condensed Matter*, 648:414380, 2023.

[40] Sofie Holm-Janas, Mitsuru Akaki, Ellen Fogh, Takumi Kihara, Manh Duc Le, Paola Catarina Forino, Stanislav E Nikitin, Tom Fennell, Adheena Painganoor, David Vaknin, et al. Magnetic structure and magnetoelectric properties of the spin-flop phase in $LiFePO_4$. *Physical Review B*, 109(17):174413, 2024.

[41] Stephanie Gnewuch and Efrain E Rodriguez. Distinguishing the intrinsic antiferromagnetism in polycrystalline $LiCoPO_4$ and $LiMnPO_4$ olivines. *Inorganic Chemistry*, 59(9):5883–5895, 2020.

[42] D Vaknin, JL Zarestky, LL Miller, J-P Rivera, and H Schmid. Weakly coupled antiferromagnetic planes in single-crystal $LiCoPO_4$. *Physical Review B*, 65(22):224414, 2002.

[43] NF Kharchenko, Yu N Kharchenko, R Szymczak, M Baran, and Hans Schmid. Weak ferromagnetism in the antiferromagnetic magnetoelectric crystal $LiCoPO_4$. *Low Temperature Physics*, 27(9):895–898, 2001.

[44] Ellen Fogh, Oksana Zaharko, Jürg Schefer, Christof Niedermayer, Sonja Holm-Dahlin, Michael Korning Sørensen, Andreas Bott Kristensen, Niels Hessel Andersen, David Vaknin, Niels Bech Christensen, et al. Dzyaloshinskii-moriya interaction and the magnetic ground state in magnetoelectric $LiCoPO_4$. *Physical Review B*, 99(10):104421, 2019.

[45] NF Kharchenko, VM Khrustalev, and Savitskiĭ. Magnetic field induced spin reorientation in the strongly anisotropic antiferromagnetic crystal $LiCoPO_4$.

[46] Ellen Fogh, Rasmus Toft-Petersen, Eric Ressouche, Christof Niedermayer, Sonja Lindahl Holm, Maciej Bartkowiak, Oleksandr Prokhnenko, Steffen Sloth, Frederik Werner Isaksen, David Vaknin, et al. Magnetic order, hysteresis, and phase coexistence in magnetoelectric $LiCoPO_4$. *Physical Review B*, 96(10):104420, 2017.

[47] VM Khrustalyov, VM Savytsky, and MF Kharchenko. Magnetoelectric effect in antiferromagnetic $LiCoPO_4$ in pulsed magnetic fields. *Low Temperature Physics*, 42(4):280–285, 2016.

[48] VM Khrustalyov, VN Savytsky, and MF Kharchenko. (h, ti)-diagram of magnetic transformations induced by a pulsed magnetic field in antiferromagnetic $LiCoPO_4$. *Low Temperature Physics*, 43(11):1332–1337, 2017.

[49] Anne S Zimmermann, Dennis Meier, and Manfred Fiebig. Ferroic nature of magnetic toroidal order. *Nature communications*, 5(1):4796, 2014.

[50] Bas B Van Aken, Jean-Pierre Rivera, Hans Schmid, and Manfred Fiebig. Observation of ferrotoroidic domains. *Nature*, 449(7163):702–705, 2007.

[51] Thomas Bagger Stibius Jensen, Niels Bech Christensen, Michel Kenzelmann, Henrik Moodysson Rønnow, Christof Niedermayer, Niels Hessel Andersen,

Kim Lefmann, Jürg Schefer, Martin v. Zimmermann, Jiying Li, et al. Field-induced magnetic phases and electric polarization in $LiNiPO_4$. *Physical Review B—Condensed Matter and Materials Physics*, 79(9):092412, 2009.

[52] David Vaknin, Jerel L Zarestky, J-P Rivera, and Hans Schmid. Commensurate-incommensurate magnetic phase transition in magnetoelectric single crystal $LiNiPO_4$. *Physical review letters*, 92(20):207201, 2004.

[53] Ellen Fogh, Takumi Kihara, Rasmus Toft-Petersen, Maciej Bartkowiak, Yasuo Narumi, Oleksandr Prokhnenko, Atsushi Miyake, Masashi Tokunaga, Kenichi Oikawa, Michael Korning Sørensen, et al. Magnetic structures and quadratic magnetoelectric effect in $LiNiPO_4$ beyond 30 t. *Physical Review B*, 101(2):024403, 2020.

[54] Michel Mercier. *Étude de l'effet magnetoelectrique sur de composés de type olivine, perovskite et grenat.* PhD thesis, Ph. D. thesis, Université de Grenoble, 1969.

[55] Rasmus Toft-Petersen, Ellen Fogh, Takumi Kihara, Jens Jensen, Katharina Fritsch, Jooseop Lee, Garrett E Granroth, Matthew B Stone, David Vaknin, Hiroyuki Nojiri, et al. Field-induced reentrant magnetoelectric phase in $LiNiPO_4$. *Physical Review B*, 95(6):064421, 2017.

[56] Amnon Aharony and Shmuel Fishman. Decoupled tetracritical points in quenched random alloys with competing anisotropies. *Physical Review Letters*, 37(23):1587, 1976.

[57] Amnon Aharony. Critical phenomena in disordered systems. *Journal of Magnetism and Magnetic Materials*, 7(1-4):198–206, 1978.

[58] Hiroshi Mano. Possible phase diagrams of systems with competing anisotropies. *Progress of Theoretical Physics Supplement*, 101:597–610, 1990.

[59] Shmuel Fishman and Amnon Aharony. Phase diagrams and multicritical points in randomly mixed magnets. ii. ferromagnet-antiferromagnet alloys. *Physical Review B*, 19(7):3776, 1979.

[60] Fumitaka Matsubara and Sakari Inawashiro. Mixture of two anisotropic antiferromagnets with different easy axes. *Journal of the Physical Society of Japan*, 42(5):1529–1537, 1977.

[61] Takehiko Oguchi and Takuma Ishikawa. Theory of a mixture of two anisotropic antiferromagnets with different easy axes. *Journal of the Physical Society of Japan*, 45(4):1213–1220, 1978.

[62] L Bevaart, E Frikkee, JV Lebesque, and LJ De Jongh. Magnetic and neutron scattering experiments on the antiferromagnetic layer-type compounds $K_2Mn_{1-x}M_xF_4$ (M= Fe, Co). *Physical Review B*, 18(7):3376, 1978.

[63] L Bevaart, E Frikkee, JV Lebesque, and LJ De Jongh. Composition vs transition temperature phase diagram of a random two-component magnetic system with competing spin-anisotropies. *Solid State Communications*, 25(8):539–542, 1978.

[64] K Katsumata, H Yoshizawa, G Shirane, and RJ Birgeneau. Successive ising phase transitions in a random antiferromagnet with competing anisotropies. *Physical Review B*, 31(1):316, 1985.

[65] P-Z Wong, PM Horn, RJ Birgeneau, and G Shirane. $Fe_{1-x}Co_xCl_2$: Competing anisotropies and random molecular fields. *Physical Review B*, 27(1):428, 1983.

[66] Po-zen Wong, PM Horn, RJ Birgeneau, CR Safinya, and G Shirane. Competing order parameters in quenched random alloys: $Fe_{1-x}Co_xCl_2$. *Physical Review Letters*, 45(24):1974, 1980.

[67] K Katsumata, J Tuchendler, and S Legrand. Magnetic phase transitions in a random mixture with competing ising and xy spin anisotropies. *Physical Review B*, 30(3):1377, 1984.

[68] Andrew T Boothroyd. *Principles of Neutron Scattering from Condensed Matter.* Oxford University Press, 2020.

[69] John RD Copley. *The fundamentals of neutron powder diffraction.* US Governmen, 2001.

[70] Philip Willmott. *An introduction to synchrotron radiation: techniques and applications.* John Wiley & Sons, 2019.

[71] NF Berk. Outline of neutron scattering formalism. *Journal of research of the National Institute of Standards and Technology*, 98(1):15, 1993.

[72] Gordon Leslie Squires. *Introduction to the theory of thermal neutron scattering.* Courier Corporation, 1996.

[73] P. Barnes, S. Jacques, and M. Vickers. Powder diffraction course material: Powder diffraction. Course material.

[74] Manickam Minakshi, Neeraj Sharma, David Ralph, Dominique Appadoo, and Kalaiselvi Nallathamby. Synthesis and characterization of $LiCo_{0.5}Ni_{0.5}PO_4$ cathode for li-ion aqueous battery applications. *Electrochemical and Solid-State Letters*, 14(6):A86, 2011.

[75] J Wolfenstine and J Allen. $LiNiPO_4$–$LiCoPO_4$ solid solutions as cathodes. *Journal of Power Sources*, 136(1):150–153, 2004.

[76] Atsuo Yamada, Sai-Cheong Chung, and Koichiro Hinokuma. Optimized $LiFePO_4$ for lithium battery cathodes. *Journal of the electrochemical society*, 148(3):A224, 2001.

[77] PJ Baker, I Franke, FL Pratt, T Lancaster, D Prabhakaran, W Hayes, and SJ Blundell. Probing magnetic order in $LiMPO_4$ (M= Ni, Co, Fe) and lithium diffusion in Li_xFePO_4. *Physical Review B*, 84(17):174403, 2011.

[78] CM Julien, A Mauger, K Zaghib, R Veillette, and H Groult. Structural and electronic properties of the $LiNiPO_4$ orthophosphate. *Ionics*, 18(7):625–633, 2012.

[79] Manickam Minakshi, Pritam Singh, Dominique Appadoo, and Danielle E Martin. Synthesis and characterization of olivine $LiNiPO_4$ for aqueous rechargeable battery. *Electrochimica Acta*, 56(11):4356–4360, 2011.

[80] Natalia N Bramnik, Dmytro M Trots, Heiko J Hofmann, and Helmut Ehrenberg. Mixed $LiCo_{0.6}M_{0.4}PO_4$ (M= Mn, Fe, Ni) phosphates: cycling mechanism and thermal stability. *Physical Chemistry Chemical Physics*, 11(17):3271–3277, 2009.

[81] M Piana, M Arrabito, Silvia Bodoardo, A D'epifanio, D Satolli, Fausto Croce, and B Scrosati. Characterization of phospho-olivines as materials for Li-ion cell cathodes. *Ionics*, 8(1):17–26, 2002.

[82] P Subramanya Herle, B Ellis, N Coombs, and LF Nazar. Nano-network electronic conduction in iron and nickel olivine phosphates. *Nature materials*, 3(3):147–152, 2004.

[83] JL Dodd, Rachid Yazami, and Brent Fultz. Phase diagram of Li_xFePO_4. *Electrochemical and Solid-State Letters*, 9(3):A151, 2006.

[84] Jun Sugiyama, Hiroshi Nozaki, Masashi Harada, Kazuya Kamazawa, Yutaka Ikedo, Yasuhiro Miyake, Oren Ofer, Martin Månsson, Eduardo J Ansaldo, Kim H Chow, et al. Diffusive behavior in $LiMPO_4$ with M= Fe, Co, Ni probed by muon-spin relaxation. *Physical Review B—Condensed Matter and Materials Physics*, 85(5):054111, 2012.

[85] K Rissouli, K Benkhouja, JR Ramos-Barrado, and C Julien. Electrical conductivity in lithium orthophosphates. *Materials Science and Engineering: B*, 98(3):185–189, 2003.

[86] Sylvain Franger, Frederic Le Cras, Carole Bourbon, and Hélène Rouault. Comparison between different $LiFePO_4$ synthesis routes and their influence on its physico-chemical properties. *Journal of power Sources*, 119:252–257, 2003.

[87] Min Zhang, Nuria Garcia-Araez, and Andrew L Hector. Understanding and development of olivine $LiCoPO_4$ cathode materials for lithium-ion batteries. *Journal of Materials Chemistry A*, 6(30):14483–14517, 2018.

[88] Alexei V Churikov, Alexander V Ivanishchev, Arseni V Ushakov, Irina M Gamayunova, and Ilya A Leenson. Thermodynamics of $LiFePO_4$ solid-phase synthesis using iron (ii) oxalate and ammonium dihydrophosphate as precursors. *Journal of Chemical & Engineering Data*, 58(6):1747–1759, 2013.

[89] Stefan M Rommel, Norbert Schall, Christian Brünig, and Richard Weihrich. Challenges in the synthesis of high voltage electrode materials for lithium-ion batteries: a review on $LiNiPO_4$. *Monatshefte für Chemie-Chemical Monthly*, 145(3):385–404, 2014.

[90] Quantum Design. Vibrating sample magnetometer (vsm) option user's manual. *Quantum Design*, 6325, 2011.

[91] Navid Qureshi. Mag2pol: A program for the analysis of spherical neutron polarimetry, flipping ratio and integrated intensity data. *Applied Crystallography*, 52(1):175–185, 2019.

[92] . D1b - high intensity two-axis powder diffractometer. https://www.ill.eu/for-ill-users/instruments/instruments-list/d1b/description/instrument-layout.

[93] E Arzi, Charles Alfred Taylor, University of Wales (Cardiff), and Union internationale de cristallographie. Commission on Crystallographic Teaching. *Introduction to neutron powder diffractometry.* International Union of Crystallography, 1984.

[94] . D9 - hot neutron four-circle diffractometer. https://www.ill.eu/for-ill-users/instruments/instruments-list/d9/description/instrument-layout.

[95] B Ouladdiaf, J Archer, GJ McIntyre, AW Hewat, D Brau, and S York. Orientexpress: A new system for laue neutron diffraction. *Physica B: Condensed Matter*, 385:1052–1054, 2006.

[96] Navid Qureshi. Instrumental aspects. In *EPJ Web of Conferences*, volume 155, page 00002. EDP Sciences, 2017.

[97] Thomas Degen, Mustapha Sadki, Egbert Bron, Uwe König, and Gwilherm Nénert. The highscore suite. *Powder diffraction*, 29(S2):S13–S18, 2014.

[98] MA Semkin, NV Urusova, M Rajesh Kumar, NA Kulesh, MO Kalinkin, KV Grzhegorzhevskii, DK Kuznetsov, AA Ostroushko, and AN Pirogov. Raman analysis and crystal structure of polycrystalline $LiNi_{1-x}Co_xPO_4$ (x= 0–0.5). *Applied Physics A*, 127(1):67, 2021.

[99] MA Semkin, NV Urusova, A Hoser, AI Beskrovnyi, and AN Pirogov. Magnetic structures of the $LiNi_{0.9}Co_{0.1}PO_4$ crystal. *Journal of Surface Investigation: X-ray, Synchrotron and Neutron Techniques*, 15(5):890–895, 2021.

[100] MA Semkin, NV Urusova, A Hoser, DS Neznakhin, and AN Pirogov. Models of Ni-and Co-ion occupation in $LiNi_{0.5}Co_{0.5}PO_4$ orthophosphate and its magnetic structure. *Journal of Physics: Condensed Matter*, 34(16):165801, 2022.

[101] Alan R Denton and Neil W Ashcroft. Vegard's law. *Physical review A*, 43(6):3161, 1991.

[102] J. H. Van Vleck. On the theory of antiferromagnetism. *J. Chem. Phys.*, 9(1):85–90, 01 1941.

[103] Sam Mugiraneza and Alannah M Hallas. Tutorial: a beginner's guide to interpreting magnetic susceptibility data with the curie-weiss law. *Communications Physics*, 5(1):95, 2022.

[104] Xiang Ma, Junjie Wu, Lizhen Huang, Xiangbiao Shi, Ruimin Li, Mengyang Chang, Yalin Lu, and Bin Xiang. Unconventional magnetic and magneto-transport properties in a canted antiferromagnet Fe_3SnSb. *Precision Chemistry*, 2025.

[105] M. C. Larsen and M. Ravn-Feld. *Monte Carlo simulations of Lithium orthophosphates.* Bachelor Thesis, Technical University of Denmark, 2024.

[106] Jiying Li, Vasile O Garlea, Jerel L Zarestky, and David Vaknin. Spin-waves in antiferromagnetic single-crystal $LiFePO_4$. *Physical Review B—Condensed Matter and Materials Physics*, 73(2):024410, 2006.

[107] David Mukamel. Phase diagrams and multicritical points in randomly mixed alloys. *Physical Review Letters*, 46(13):845, 1981.

[108] Woochul Kim, Chan Hyuk Rhee, Hyung Joon Kim, Seung Je Moon, and Chul Sung Kim. Strong crystalline field at the fe site and spin rotation in olivine $LiNi_{0.99}Fe_{0.01}PO_4$ material by mössbauer spectroscopy. *Applied Physics Letters*, 96(24), 2010.

[109] Anne S Zimmermann, Elke Sondermann, Jiying Li, David Vaknin, and Manfred Fiebig. Antiferromagnetic order in $Li(Ni_{1-x}Fe_x)PO_4$ (x= 0.06, 0.20). *Physical Review B—Condensed Matter and Materials Physics*, 88(1):014420, 2013.

[110] Ellen Fogh. Magnetic and magnetoelectric properties of lithium orthophosphates. 2018.

[111] Martin Gajek, Manuel Bibes, Stéphane Fusil, Karim Bouzehouane, Josep Fontcuberta, Agnès Barthélémy, and Albert Fert. Tunnel junctions with multiferroic barriers. *Nature materials*, 6(4):296–302, 2007.

[112] Noel D'Souza, Jayasimha Atulasimha, and Supriyo Bandyopadhyay. Four-state nanomagnetic logic using multiferroics. *Journal of Physics D: Applied Physics*, 44(26):265001, 2011.

[113] Taehee Yoo, Sungwon Khym, Hakjoon Lee, Sangyeop Lee, Sanghoon Lee, Xiaomei Liu, Jacek K Furdyna, Dong Uk Lee, and Eun Kyu Kim. Quaternary memory device fabricated from a single layer fe film. *Journal of Applied Physics*, 111(7), 2012.

[114] Chad S Watson, Courtney Hollar, Kimball Anderson, William B Knowlton, and Peter Müllner. Magnetomechanical four-state memory. *Advanced Functional Materials*, 23(32):3995–4001, 2013.

[115] HM Yau, ZB Yan, NY Chan, K Au, CM Wong, Chi Wah Leung, FY Zhang, XS Gao, and JY Dai. Low-field switching four-state nonvolatile memory based on multiferroic tunnel junctions. *Scientific reports*, 5(1):12826, 2015.

[116] Changjun Jiang, Fenglong Wang, Chunhui Dong, Cai Zhou, Lei Wu, and Desheng Xue. A non-volatile four-state magnetic memory in a Co/(011) Pb (Mg1/3Nb2/3)O3-PbTiO$_3$ heterostructure. *Applied Physics Letters*, 108(3), 2016.

[117] Yanping Wei, Cunxu Gao, Zhendong Chen, Shibo Xi, Weixia Shao, Peng Zhang, Guilin Chen, and Jiangong Li. Four-state memory based on a giant and non-volatile converse magnetoelectric effect in FeAl/PIN-PMN-PT structure. *Scientific Reports*, 6(1):30002, 2016.

[118] M Baum, K Schmalzl, P Steffens, A Hiess, LP Regnault, M Meven, P Becker, L Bohatỳ, and M Braden. Controlling toroidal moments by crossed electric and magnetic fields. *Physical Review B—Condensed Matter and Materials Physics*, 88(2):024414, 2013.

[119] M Blume. Polarization effects in the magnetic elastic scattering of slow neutrons. *Physical Review*, 130(5):1670, 1963.

[120] SV Maleev, VG Bar'yakhtar, and RA Suris. The scattering of slow neutrons by complex magnetic structures. *Soviet Phys.-Solid State (English Transl.)*, 4, 1963.

[121] Sang-Wook Cheong and Maxim Mostovoy. Multiferroics: a magnetic twist for ferroelectricity. *Nature materials*, 6(1):13–20, 2007.

[122] J-P Rivera. The linear magnetoelectric effect in LiCoPO$_4$ revisited. *Ferroelectrics*, 161(1):147–164, 1994.

[123] Lara Kiefer, Felix Wirth, Alexandre Bertin, Petra Becker, Ladislav Bohatỳ, Karin Schmalzl, Anne Stunault, J Alberto Rodríguez-Velamazán, Oscar Fabelo, and Markus Braden. Crystal structure and absence of magnetic order in single-crystalline RuO_2. *Journal of Physics: Condensed Matter*, 37(13):135801, 2025.

[124] Elisabeth Rossmanith. Approximate calculation of multiple-diffraction patterns based on renninger's kinematicalsimplest approach'. *Applied Crystallography*, 33(3):921–927, 2000.

[125] WH Zachariasen. Multiple diffraction in imperfect crystals. *Acta Crystallographica*, 18(4):705–710, 1965.

[126] M Renninger. „umweganregung ", eine bisher unbeachtete wechselwirkungserscheinung bei raumgitterinterferenzen. *Zeitschrift für Physik*, 106(3):141–176, 1937.

[127] Yong-Nian Xu, Sung-Yoon Chung, Jason T Bloking, Yet-Ming Chiang, and WY Ching. Electronic structure and electrical conductivity of undoped $LiFePO_4$. *Electrochemical and Solid-State Letters*, 7(6):A131, 2004.

Paper I

Magnetic structure and magnetoelectric properties of the spin-flop phase in $\mathbf{LiFePO_4}$

S. Holm-Janas, M. Akaki, E. Fogh, T. Kihara, M. D. Le, P. C. Forino, S. E. Nikitin, T. Fennell, **A. Painganoor**, D. Vaknin, M. Watanabe, N. B. Christensen, H. Nojiri, and R. Toft-Petersen

Physical Review B ***109****, 174413 (2024)*

This paper reports the magnetic structure and magnetoelectric effect in the high magnetic field region above 31 T for $LiFePO_4$. Contributions were made to the neutron experiments performed at the instrument EIGER during first year of PhD.

PHYSICAL REVIEW B **109**, 174413 (2024)

Editors' Suggestion

Magnetic structure and magnetoelectric properties of the spin-flop phase in $\mathrm{LiFePO_4}$

Sofie Holm-Janas,[1] Mitsuru Akaki,[2] Ellen Fogh,[3] Takumi Kihara,[2,4] Manh Duc Le,[5] Paola Catarina Forino,[1,3]
Stanislav E. Nikitin,[6] Tom Fennell,[6] Adheena Painganoor,[1,7] David Vaknin,[8] Masao Watanabe,[9]
Niels Bech Christensen,[1] Hiroyuki Nojiri,[2] and Rasmus Toft-Petersen[1,10,*]
[1]*Department of Physics, Technical University of Denmark, 2800 Kongens Lyngby, Denmark*
[2]*Institute for Materials Research, Tohoku University, Sendai 980-8577, Japan*
[3]*Laboratory for Quantum Magnetism, Institute of Physics, École Polytechnique Fédérale de Lausanne (EPFL), 1015 Lausanne, Switzerland*
[4]*Research Institute for Interdisciplinary Science, Okayama University, Okayama, 700-8530, Japan*
[5]*ISIS Neutron and Muon Source, Rutherford Appleton Laboratory, Didcot OX11 0QX, United Kingdom*
[6]*Laboratory for Neutron Scattering and Imaging, Paul Scherrer Institut, 5232 Villigen PSI, Switzerland*
[7]*Institut Laue-Langevin, 71 avenue des Martyrs, CS 20156, Grenoble, 38042 Cedex 9, France*
[8]*Ames National Laboratory and Department of Physics and Astronomy, Iowa State University, Ames, Iowa 50011, USA*
[9]*Materials and Life Science Division, J-PARC Center, Tokai, Ibaraki 319-1195, Japan*
[10]*European Spallation Source ERIC, P.O. Box 176, SE-221 00, Lund, Sweden*

(Received 11 March 2024; accepted 18 April 2024; published 6 May 2024)

We investigate the magnetic structure and magnetoelectric(ME) effect in the high-field phase of the antiferromagnet $\mathrm{LiFePO_4}$ above the critical field of 31 T. A neutron diffraction study in pulsed magnetic fields reveals the propagation vector to be $\mathbf{q} = 0$ for the high-field magnetic structure. Pulsed-field electric polarization measurements show that, at the critical field, the low-field off-diagonal ME coupling α_{ab} is partially suppressed, and the diagonal element α_{bb} emerges. These results are consistent with a spin-flop transition where the spin direction changes from primarily being along the easy b axis below the transition to being along a above. The persistence of off-diagonal ME tensor elements above the critical field suggests a lowering of the magnetic point-group symmetry and hence a more complex magnetic structure in the high-field phase. In addition, neutron diffraction measurements in low magnetic fields show no observable field-induced spin canting, which indicates a negligible Dzyaloshinskii-Moriya interaction. The observed spin-flop field supports the Hamiltonian recently deduced from inelastic neutron studies and indicates that the system is less frustrated and with a larger single-ion anisotropy than originally thought. Our results demonstrate the effectiveness of combining pulsed-field neutron diffraction and electric polarization measurements to elucidate the magnetic structures and symmetries at the highest attainable field strengths.

DOI: 10.1103/PhysRevB.109.174413

I. INTRODUCTION

Multiferroics and magnetoelectric (ME) materials carry the prospect for applications, such as electrical-field control of skyrmions and low-power-consumption logic devices [1–6]. To date, the vast majority of realized devices adopts alternating layers, e.g., of piezoelectric and magnetostrictive materials, where the mechanical coupling between layers creates an artificial ME material with the desired functionality. However, some of these innovative designs employ distinct ME layers, and a fundamental understanding of single-phase MEs is crucial for progress in the field. The allowed ME coupling tensor elements α_{ij} between an applied magnetic field H_j and electric polarization $P_i = \alpha_{ij} H_j$ are dictated by the magnetic point-group symmetry [7]. In this respect, the magnetic phase diagrams of ME materials serve as testing grounds for model spin Hamiltonians since distinct ME coupling tensors may be realized within the same compound by temperature and magnetic-field control of the ground state [8,9].

The lithium orthophosphates are a well-studied family of orthorhombic ME materials [10] of chemical formula $\mathrm{Li}M\mathrm{PO_4}$ (M = Mn, Fe, Co, Ni), all ordering antiferromagnetically(AFM) below Néel temperatures in the range $T_N = 20$–$50\,\mathrm{K}$ [11–18]. The single-ion anisotropy in the system depends on the transition metal ion M in question. Thus, different magnetic point-group symmetries are realized in the AFM ground state depending on M, which in turn results in different ME tensor forms [10,19,20]. Two mechanisms for the physical origin of the ME coupling have been proposed in this class of materials, based on exchange striction [21–24] and orbital magnetism [25].

$\mathrm{LiFePO_4}$, the focus of this paper, orders with spins predominantly along the easy b axis below $T_N = 50\,\mathrm{K}$ with intermediate axis a and hard axis c [17]. The zero-field magnetic ground state has been determined in detail (see Sec. II) and has a lower symmetry than what was initially expected. This may be explained by a recent observation of strong magnetostriction peaking at T_N in $\mathrm{LiFePO_4}$, as measured by

---

[*] rasp@fysik.dtu.dk

dilatometry [26]. The excitations have been investigated in great detail using both neutron spectroscopy [8,12,23], electron spin resonance (ESR) spectroscopy [27], and terahertz absorption spectroscopy [28]. Recently, the latter revealed a veritable zoo of excitations, including electromagnons and other ME active modes [28]. Extensive work on modeling the exchange interactions and single-ion anisotropy constants of $LiFePO_4$ has been undertaken [8,20,23,27,28]. While the different models agree on the order of magnitude of the interactions, the level of exchange frustration in $LiFePO_4$ is debated.

Neutron spectroscopy measurements reveal mild exchange frustration in all the different lithium orthophosphates [15,16,23,29]. The competition between exchange and single-ion anisotropy governs the magnetic phase diagrams, which vary in complexity for the different family members [8,15,18,20,21,26,30,31]. The Mn analog $LiMnPO_4$ has the simplest phase diagram with a spin-induced transition to an incommensurate, elliptic spin cycloid at ∼12 T applied magnetic field [13]. This is followed by a spin-flop transition at higher magnetic fields, where the system becomes commensurate again. $LiNiPO_4$, on the other hand, first exhibits a spin-density phase upon cooling down in zero field before entering the AFM ground state at low temperatures. Upon applying a magnetic field, $LiNiPO_4$ undergoes a succession of transitions between commensurate and incommensurate phases. Intriguingly, in $LiNiPO_4$, the same ME coupling tensor α_{ij} is observed in the high-field commensurate phases as in zero field. These phases also have the same $\mathbf{q} = 0$ propagation vector, which indicates that the high-field commensurate phases are magnetized variants of the zero-field commensurate phase rather than a spin-flop phase.

The behavior of $LiFePO_4$ differs somewhat from these two sister compounds. From the similarity of the XY-like anisotropy in $LiFePO_4$ to that of $LiNiPO_4$, one might also expect to observe incommensurate (spiral or spin-density wave) phases in $LiFePO_4$. However, unlike $LiNiPO_4$, with its multiple phase transitions as a function of magnetic field, magnetization measurements on $LiFePO_4$ reveal only a single clear field-induced phase transition at $\mu_0 H \simeq 32\,\mathrm{T}$ [26], demonstrating the robustness of the zero-field structure against the application of a magnetic field. The transition is speculated to be of the spin-flop type, but this has not yet been verified experimentally [26–28].

In this paper, we combine neutron diffraction and electric polarization measurements, both performed with pulsed magnetic fields, to determine the high-field magnetic structure in $LiFePO_4$. We find the phase transition at 31 T to be of the spin-flop type with spins reorienting to point dominantly along the *a* axis. However, the high-phase ME tensor components imply a more complex magnetic structure than a colinear AFM structure with magnetic moments oriented along the *a* axis. Furthermore, in a different neutron diffraction experiment, we find no further field-induced spin canting, which indicates a negligible Dzyaloshinskii-Moriya (DM) interaction. Finally, we perform mean-field(MF) calculations to determine the phase diagram based on previously estimated sets of exchange parameters to compare with the experimentally obtained phase diagram and find that the less frustrated set of exchange parameters, with larger spin anisotropies, provide a better description of all data. This demonstrates that studies of magnetic phase diagrams are complementary to studies of magnetic excitations, when the magnetic Hamiltonian is complex.

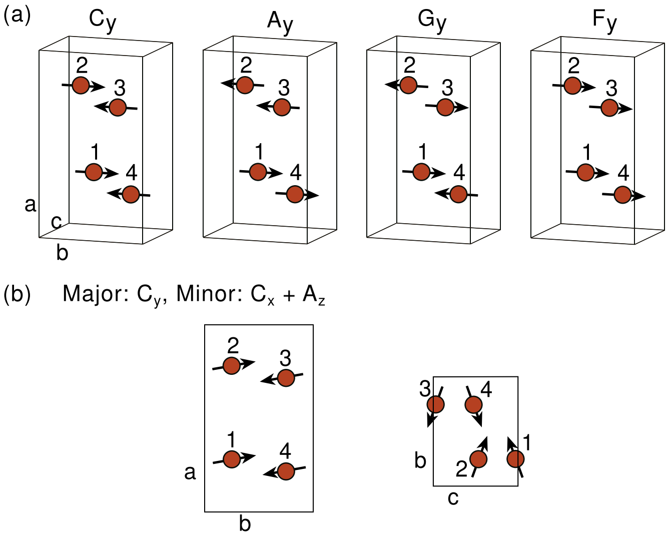

FIG. 1. (a) The basis vectors of Li*M*PO_4 for $\mathbf{q} = 0$ structures in the *Pnma* space group. Only the lattice of magnetic ions is shown. The arrows represent the spin orientation on the four magnetic sites labeled 1–4 as shown. (b) Projections onto the (*b*, *c*) and (*a*, *b*) planes for the zero-field magnetic structure of $LiFePO_4$, $[C_y + C_x + A_z]$. Canting angles are exaggerated for clarity.

II. MAGNETIC STRUCTURES AND THE ME TENSOR

The crystal structure of the lithium orthophosphates has historically been assumed to belong to the *Pnma* space group [11]. The four Fe^{2+} ions are located on the Wyckoff position 4*c*: $\mathbf{r}_1 = (\frac{1}{4} + x, \frac{1}{4}, -z)$, $\mathbf{r}_2 = (\frac{3}{4} + x, \frac{1}{4}, \frac{1}{2})$, $\mathbf{r}_3 = (\frac{3}{4} - x, \frac{3}{4}, z)$, and $\mathbf{r}_4 = (\frac{1}{4} - x, \frac{3}{4}, \frac{1}{2} - z)$, where $x = 0.03$ and $z = 0.025$ in the orthorhombic unit cell [23]. The spin structure can be described by the four irreducible basis vectors: $A = (\uparrow\downarrow\downarrow\uparrow)$, $C = (\uparrow\uparrow\downarrow\downarrow)$, $G = (\uparrow\downarrow\uparrow\downarrow)$, and $F = (\uparrow\uparrow\uparrow\uparrow)$. Here, ↑ and ↓ denote the relative orientation of the four spins in a unit cell which are enumerated 1–4, see Fig. 1(a). The four basis vectors combined with magnetic moment orientations along the three perpendicular crystallographic axes (*a*, *b*, and *c*) then allow for a full description of the magnetic structures. There are eight irreducible representations (IRs) for *Pnma*, denoted Γ_i for $i = 1, \ldots, 8$, see. e.g.. Ref. [23]. Only some of these are realized in the lithium orthophosphates. The main magnetic structure element for all the compounds in the lithium orthophosphate family is of *C* type with major spin components along either *a* ($LiMnPO_4$), *b* ($LiCoPO_4$ and $LiFePO_4$), or *c* ($LiNiPO_4$), see Table I for a summary.

The ME properties depend intimately on the magnetic point group in the ordered ground state. Of all the 122 possible magnetic point groups, only 58 allow the linear ME effect. The specific point-group symmetry dictates the form of the ME tensor, see, e.g., Ref. [7]. The resulting ME tensor for the point groups relevant to the lithium orthophosphates are listed in Table I.

TABLE I. IRs for the *Pnma* space group and the allowed tensor forms for the linear ME effect in the lithium orthophosphates. The first two columns list the IR(s), the second column gives the point group symmetry, andthe third the ME tensor form. Small dots indicate vanishing tensor elements, and large dots show elements that may be finite. The last column specifies which (if any) lithium orthophosphate displays the corresponding low-temperature, zero-field structure.

IR No. 1	IR No. 2	Point group	ME tensor	Compound
$\Gamma_5(C_x, A_z)$		$m'm'm'$	$\begin{pmatrix} \bullet & \cdot & \cdot \\ \cdot & \bullet & \cdot \\ \cdot & \cdot & \bullet \end{pmatrix}$	$LiMnPO_4$
$\Gamma_7(C_z, A_x)$		$mm'm$	$\begin{pmatrix} \cdot & \cdot & \bullet \\ \cdot & \cdot & \cdot \\ \bullet & \cdot & \cdot \end{pmatrix}$	$LiNiPO_4$
$\Gamma_8(C_y)$		mmm'	$\begin{pmatrix} \cdot & \bullet & \cdot \\ \bullet & \cdot & \cdot \\ \cdot & \cdot & \cdot \end{pmatrix}$	
$\Gamma_8(C_y)$	$\Gamma_5(C_x, A_z)$	$2_z/m'_z$	$\begin{pmatrix} \bullet & \bullet & \cdot \\ \bullet & \bullet & \cdot \\ \cdot & \cdot & \bullet \end{pmatrix}$	$LiFePO_4$
				$LiCoPO_4$
$\Gamma_5(C_x, A_z)$	$\Gamma_7(C_z, A_x)$	$2_y/m'_y$	$\begin{pmatrix} \bullet & \cdot & \bullet \\ \cdot & \bullet & \cdot \\ \bullet & \cdot & \bullet \end{pmatrix}$	
$\Gamma_8(C_y)$	$\Gamma_7(C_z, A_x)$	$2'_x/m_x$	$\begin{pmatrix} \cdot & \bullet & \bullet \\ \bullet & \cdot & \cdot \\ \bullet & \cdot & \cdot \end{pmatrix}$	

It was previously shown that the dominant component of the magnetic structure of $LiFePO_4$ is C_y but that there are additional subdominant components C_x and A_z corresponding to the spins rotating off the crystallographic b axis. The refined moment along the b axis is $\mu_y = 4.09(4)\,\mu_B$ (from the C_y component), while the refined canted moments are $\mu_x = 0.067(5)\,\mu_B$ along the a axis and $\mu_z = 0.063(5)\,\mu_B$ along the c axis, corresponding to an overall rotation of $1.3(1)^\circ$ off the b axis [23]. The structure is shown in Fig. 1(b) with exaggerated canting angles [23].

The major component C_y belongs to the Γ_8 IR under the *Pnma* space group. The minor components C_x and A_z belong to Γ_5, meaning that two different IRs are involved, and hence, the magnetic point-group symmetry is lowered from mmm' (purely Γ_5) to $2_z/m'_z$ ($\Gamma_5 \otimes \Gamma_8$). This in turn relaxes the constraints on the ME tensor (Table I). Indeed, a recent study of the ME couplings at low fields found a weak but finite signal corresponding to the diagonal element α_{aa} [22], consistent with $2_z/m'_z$ symmetry. This highlights the strength in using the ME coupling tensor to support magnetic structure determination and indicates that the crystal structure of $LiFePO_4$ at zero field is of lower symmetry than *Pnma* [23].

In Ref. [26], a spin flop was suggested at the 31 T transition. Assuming that the symmetry of the dominant structure component remains C, the ME tensor form above the critical field would follow that of point group $m'm'm'$ (C_x) or $mm'm$ (C_z). Given that the c axis is the hard axis of $LiFePO_4$, it seems most likely that the system would flop to a structure dominated by C_x. For a structure exclusively described by the C_x basis vector, one would expect the ME tensor to change to contain only finite diagonal elements (α_{ii}, $i = a, b, c$), while a structure involving a linear combination of sizable C_x and C_z would also give rise to finite off-diagonal elements (α_{ab} and α_{ba}) in addition to the diagonal elements (cf. Table I).

III. EXPERIMENTAL DETAILS

$LiFePO_4$ single crystals were grown via the standard flux growth technique, using LiCl as the flux and a stoichiometric mixture of high-purity $FeCl_2$ and Li_3PO_4. The composition and structure were confirmed via x-ray powder diffraction (XRD) [12].

To probe the structure of the high-field phase with neutron diffraction, pulsed magnetic fields are required to reach sufficiently elevated fields. Neutron diffraction in pulsed magnetic fields has become an established technique within the last decade [32–39] and was already used to elucidate the field-induced phases in $LiNiPO_4$ [21,39]. However, the low duty cycle of the magnet coils and the resulting long counting times as well as the limited scattering geometry imposed by the coils present a number of experimental challenges linked to this technique. To align the magnet and neutron pulse, the time delay Δt between the two pulses must be adjusted such that the maximum field coincides with the desired scattering vector $\mathbf{Q}$. The principle of the technique is illustrated in Fig. 2. So far, these pulsed-field experiments have all been performed in forward-scattering geometry [21,32–39]. In the case at hand, however, it is necessary to probe scattering vectors $\mathbf{Q}$ parallel to the field $\mathbf{H}$, i.e., $\mathbf{Q} \parallel \mathbf{H}$, which for solenoids can only be done in backscattering geometry. This was challenging for a number of reasons. First, longer wavelengths are needed in backscattering than forward scattering for any given $\mathbf{Q}$. The Japan Proton Accelerator Research Complex (J-PARC) moderator has lower brilliance at these wavelengths [40]. In addition, the Q range covered in the time span of a field pulse is significantly smaller in backscattering geometry, necessitating many different field settings and hence many more magnet pulses to cover the desired region in $(\mathbf{Q}, H)$ than experiments performed in forward scattering.

To directly probe the magnetic structure of $LiFePO_4$ at high magnetic fields, a time-of-flight (ToF) neutron Laue diffraction experiment was performed at NOBORU, the Neutron Source Diagnostic & Test Port, at J-PARC [40]. A pulsed polychromatic neutron beam was incident on the sample and the scattered neutrons captured by a position sensitive area detector. The detector was operated in integration mode with a 30 μs bin size. The pulsed magnetic field was generated by recently developed wide-angle magnet coils with a maximum field strength of $B_{\max} = 35$ T and pulse duration of 5 ms [41]. The coils have maximum and minimum scattering angles 2θ of 42° and 138°, for forward and backwards scattering, respectively. The coil is immersed in liquid nitrogen. The sample in vacuum was attached to a 7-diameter single-crystalline sapphire rod connected to a closed-cycle refrigerator with a base temperature of 4.5 K.

A 60 mg ($2.6 \times 2.2 \times 3.0$ mm^3) single crystal was oriented with the crystallographic b axis (easy axis) parallel to the direction of the applied magnetic field and with $\mathbf{Q} = (HK0)$ in

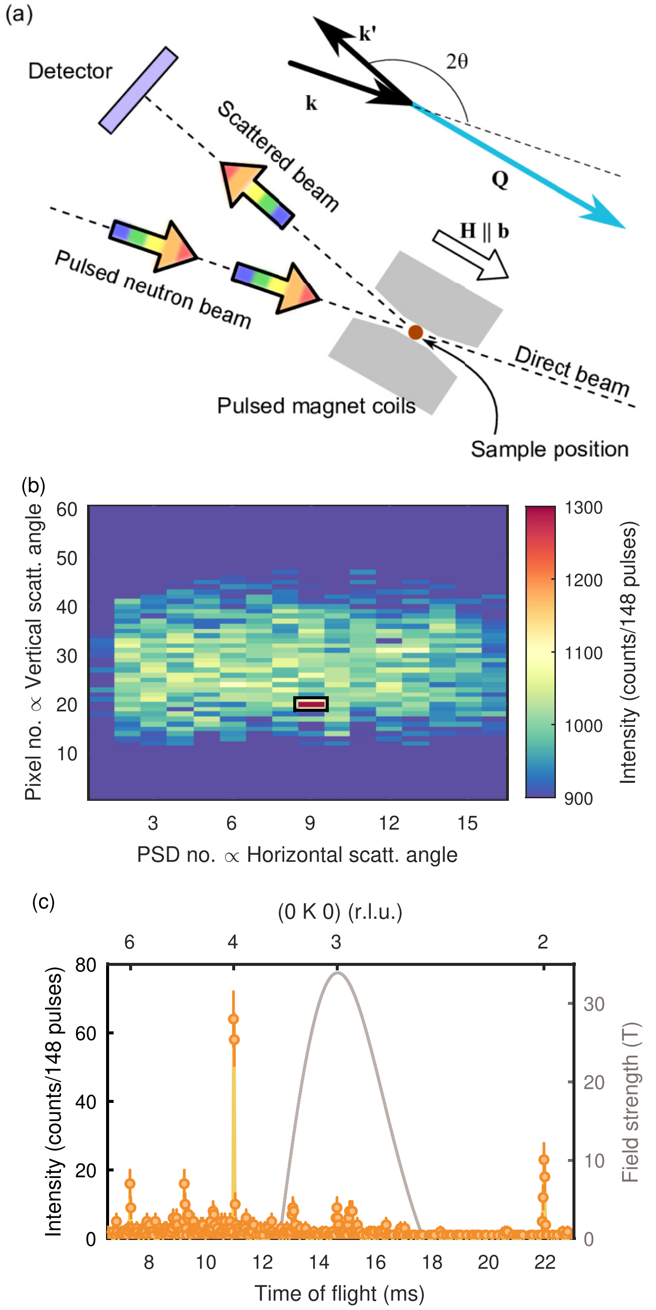

FIG. 2. (a) Schematic of the neutron Laue diffraction backscattering setup at NOBORU. The incoming beam is polychromatic with wave vector **k**, scattered wave vector **k**′, and scattering vector $\mathbf{Q} = \mathbf{k} - \mathbf{k}'$. The pulsed magnet coils (gray) allow a maximum $2\theta = 42^\circ$. The magnetic field is parallel to the b axis of the sample. (b) Position-sensitive detector image for a pulsed-field measurement. The detector has 16 vertical tubes, each with 60 pixels. The color represents the neutron intensity integrated over 148 pulses and all neutron flight times. The high-intensity pixel enclosed in the black rectangle corresponds to neutron momentum transfers along $\mathbf{Q} = (0K0)$. (c) Neutron intensity vs time of flight for the high-intensity pixel shown in (b). The top axis shows the corresponding value of K along $\mathbf{Q} = (0K0)$. The magnetic field strength (gray line) is indicated on the right-hand axis. The time delay between the neutron and magnet pulse has been adjusted to reach the maximum field strength of 34 T at $\mathbf{Q} = (030)$.

the horizontal scattering plane, see Fig. 2. This setup allowed us to reach momentum transfers along $(0K0)$ in backscattering geometry. The ToF can be converted to $\mathbf{Q} = (0K0)$ following $K = 2\alpha L \sin\theta/\mathrm{ToF}$, where $\alpha = 252.7\,\mu\mathrm{s\,m^{-1}\,Å^{-1}}$, θ is half the scattering angle, and $L = 14.9\,\mathrm{m}$ is the distance from the neutron target via the sample position to the detector.

Electric polarization measurements with pulsed magnetic fields were performed at the Institute for Materials Research, Tohoku University. The samples used for these measurements were three $\mathrm{LiFePO_4}$ single-crystalline plates of size $\sim 1 \times 1 \times 0.5\ \mathrm{mm^3}$, which were cut from the same crystal as used for neutron diffraction. They were aligned within 5° with respect to the magnetic field direction. The pulsed-field coil delivered a field pulse with a total duration of 6.3 ms. The magnet pulse is split into two parts, each with a full with at half maximum (FWHM) time length of 2.1 ms. In the first part, the maximum field is reached at 35 T followed by an opposing pulse of magnitude 21 T. See Appendix B for details.

We probed each combination of directions of electric polarization and magnetic fields, here denoted by P_iH_j, where $\{i, j\} = \{a, b, c\}$. The measurement procedure was as follows: For each P_iH_j, the sample was cooled down to base temperature of 4.2 K in zero applied magnetic field. Note that no poling was possible with this setup. The electric polarization was then measured during a magnetic field pulse at consecutively increasing temperatures. During such a measurement series, it is assumed that the sample remained in the same domain state. However, for repeated measurements, we observed a slight shift in the measured polarization, likely due to the system settling into a different domain state upon the initial cooling below T_N. The consequence is that temperature and field dependencies may be regarded as reliable within a single measurement series, but absolute values of the electric polarization will vary between separate datasets. Data collected at 60 K were used for background subtraction (except for P_bH_c).

To obtain an estimate for the size of the DM interaction, neutron diffraction with static magnetic fields was performed at the thermal triple-axis spectrometer EIGER at SINQ at the Paul Scherrer Institute [42]. EIGER was operated in elastic mode with incoming and outgoing energy $E = 14.64\,\mathrm{meV}$, and $40'$ collimation both before and after the sample. A pyrolytic graphite filter was placed between the sample and the analyzer to suppress higher-order scattering. Two different experiments were performed, one with magnetic field along the a axis and another along the c axis. The first experiment with $\mathbf{H}||\mathbf{a}$ was performed on the same 30 mg single-crystal as used at NOBORU. It was aligned with $(0KL)$ in the horizontal scattering plane and placed in a vertical ^{4}He cryomagnet with a maximum field of 12 T. The second experiment with $\mathbf{H}||\mathbf{c}$ was performed on a 140 mg single-crystal aligned with $(HK0)$ in the horizontal scattering plane and placed in a vertical ^{4}He cryomagnet with a maximum field of 10 T.

IV. RESULTS

A. Magnetic structure in the high-field phase

The intensity of a Bragg reflection depends on the nuclear and magnetic structure. The intensity arising from the magnetic structure is proportional to the neutron magnetic

TABLE II. Squared structure factors (F^2) and polarization factors (P^2) and nuclear structure factors for selected Bragg reflections in $LiFePO_4$, see Eqs. (1)–(4).

$\mathbf{q}$	$\lvert F_C\rvert^2$	$\lvert F_A\rvert^2$	$\lvert F_G\rvert^2$	$\lvert F_F\rvert^2$	$\lvert F_N\rvert^2$	$\lvert P_x\rvert^2$	$\lvert P_y\rvert^2$	$\lvert P_z\rvert^2$
(020)	0	0	0	16	5300	1	0	1
(030)	16	0	0	0	0	1	0	1

scattering cross-section:

$$I^{\mathrm{Mag}}(\mathbf{q}) \propto f(\mathbf{q})^2 \sum_R \langle S_R\rangle^2 |F_R(\mathbf{q})|^2 \sum_i |P_i(\mathbf{q})|^2, \qquad (1)$$

where $f(\mathbf{q})$ is the ion-dependent magnetic form factor, and $\langle S_R\rangle$ is the thermal average of the magnetic moment for the structure $R = \{A, G, C, F\}$, as explained in Sec. II. The magnetic structure is represented through the squared magnetic structure factor $|F_R(\mathbf{q})|^2$ and spin polarization $|P_i(\mathbf{q})|^2$ for $i = \{x, y, z\}$, which are defined as

$$F_R(\mathbf{q}) = \sum_d \mathbf{m}_d^R \exp(i\mathbf{q}\cdot\mathbf{r}_d), \qquad (2)$$

$$\mathbf{P}(\mathbf{q}) = \mathbf{q} \times (\hat{\mathbf{e}} \times \mathbf{q}). \qquad (3)$$

Here, $\mathbf{m}_d^R$ is the magnetic moment at site $d = 1, ..4$ for the structure R, and $\hat{\mathbf{e}}$ is the unit vector for directions $\{x, y, z\}$. The intensity arising from the nuclear structure is proportional to the nuclear structure factor:

$$F_N(\mathbf{q}) = \sum_j b_j \exp(i\mathbf{q}\cdot\mathbf{r}_j), \qquad (4)$$

where the sum runs over all j atoms in the unit cell (both magnetic and nonmagnetic) with scattering length b_j at position $\mathbf{r}_j$. Table II shows the squared structure and polarization factors for a few selected magnetic Bragg reflections for the different possible structures R. Note that, while a given reflection may have a finite structure factor for a specific basis vector, the intensity can still be vanishing due to the polarization factor.

Figure 3(a) shows the diffraction data obtained in zero field at 4.5 K. The nuclear Bragg reflections are identified as the high-intensity peaks and indicated in the figure. These are present at all applied fields and are a good indication that the sample stayed in position for the duration of the experiment. Lower-intensity peaks are observed in the region $6 - 16$ ms [corresponding to $K = 2.5 - 6$ in $\mathbf{Q} = (0K0)$], stemming from aluminum and copper in the sample environment, see Appendix A for a detailed treatment.

Data combined from 148 magnet pulses collected at 4.5 K and with $B_{\max} = 34$ T are shown in Fig. 3(b) together with the scaled zero-field measurement. The high-field data clearly contain a peak at $\mathbf{Q} = (030)$, which is not present in the zero-field phase to be commensurate with propagation vector $\mathbf{q} = 0$. To understand the further implications of this new magnetic signal, we turn to Table II. The (030) Bragg peak has finite neutron intensity exclusively for a C-type structure with spins oriented along either the a or c axis.

Due to the low flux and the backscattering geometry, the pulsed-field setup employed here is unable to detect weak magnetic Bragg peaks. The observed (030) peak is ~2.5 times weaker than the strong nuclear (020) reflection, demonstrating the ordered C_x moment to be of a similar order of magnitude to the zero-field C_y component and therefore likely the main structural component.

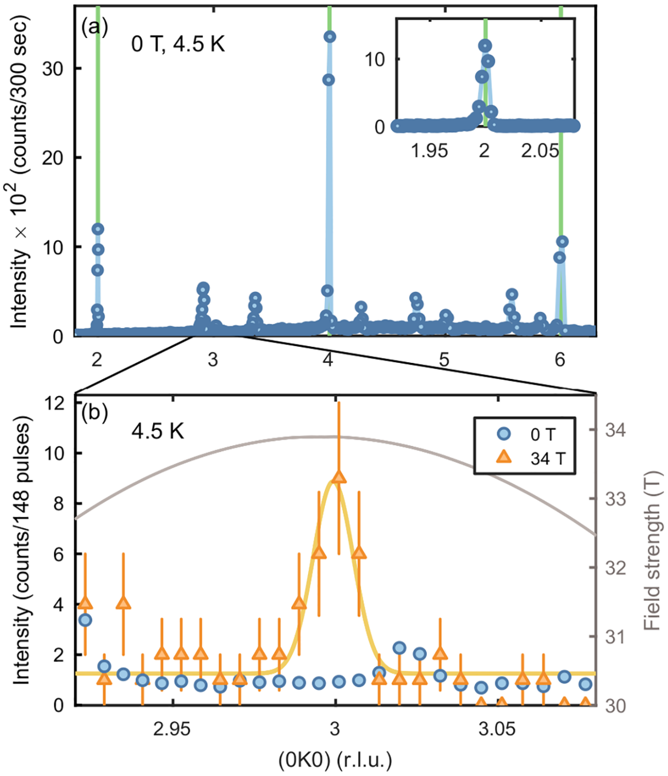

FIG. 3. Neutron diffraction measurement of $LiFePO_4$ with pulsed magnetic fields. (a) Diffraction intensity as a function of K along $\mathbf{Q} = (0K0)$ in zero applied magnetic field. Green lines indicate nuclear Bragg reflections. Inset focuses on the (020) reflection. (b) Diffraction intensity along $\mathbf{Q} = (0K0)$ in pulsed magnetic fields. Zero-field data from (a) has been scaled to use as background. A Gaussian (yellow) line has been fitted to the pulsed-field data as a guide to the eye of the (030) reflection. The strength of the magnetic field pulse is shown on the right-handside in gray.

B. The magnetoelectric effect

Figure 4(a) shows all nine combinations of the electric polarization along i induced in applied magnetic field along j, P_iH_j, $\{i, j\} = \{a, b, c\}$, at different temperatures. The ME coefficients α_{ij} may be extracted from the slopes of P_i as a function of H_j. Three nonzero tensor elements are observed: For fields along a, a linear ME effect is seen for P_b for all field strengths and temperatures, while the other polarization components are zero. For fields along b, a clear phase transition takes place at $B_{\mathrm{SF}} = 31 \pm 1$ T and 4.2 K, where P_a of the low-field phase shows a dip, and simultaneously, P_b appears. This value of the transition field is in accordance with previous observations [26,28,43]. For fields along c, no ME signals are observed within the experimental sensitivity.

The data for $H||b$ are shown in greater detail in Fig. 4(b), where P_aH_b and P_bH_b measured at 4.2 K are compared. For P_aH_b, a linear ME effect is observed at low fields, followed by a sudden drop at B_{SF}. It is worth noting, however, that

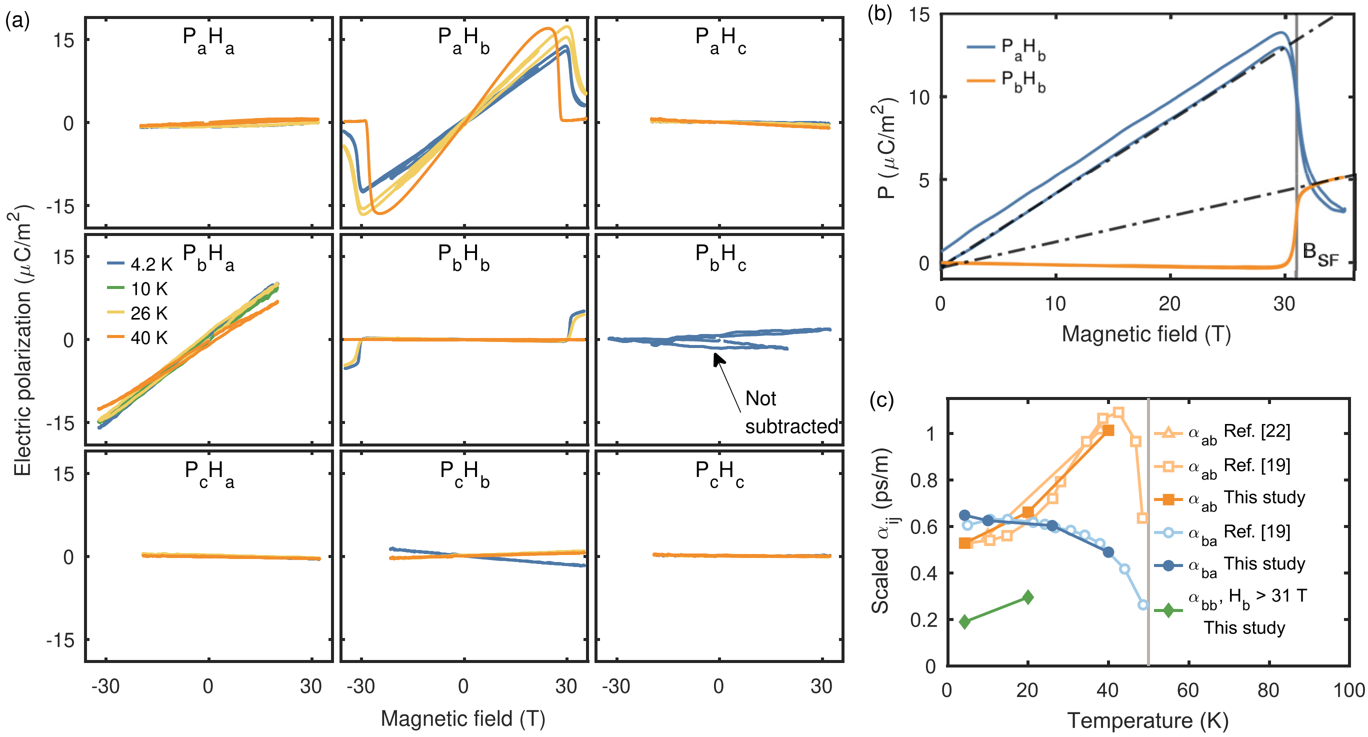

FIG. 4. Electric polarization P_i in applied pulsed magnetic fields H_j. Background measurements obtained at 60 K have been subtracted from all data, except P_bH_c, as explained in the text. (a) Overviewof all nine combinations of P_i and H_j for various temperatures. (b) Electric polarizations P_a and P_b as a function of magnetic fields applied along b clearly show the phase transition. The critical field $B_{\mathrm{SF}} = 31\,\mathrm{T}$ is indicated in by the gray vertical line. The dot-dashed lines represent linear fits to the polarization as a function of field to extract α_{ij}. (c) Temperature dependence of α_{ij}. Notice that the values obtained are merely proportional to α_{ij}. Our values are compared with scaled results from Refs. [19,22].

P_aH_b remains finite above the critical field. For P_bH_b, no ME signal is observed at low fields, but there is a steep increase at the transition whereafter a linear behavior with field is established up to the highest probed field strengths of 35 T.

The temperature dependence of the ME coefficients α_{ij} may be estimated from the experimentally determined electric polarization by fitting a linear function $P_i = P_0 + \alpha_{ij}H_j$ to the linear parts of the data in Fig. 4(a). The results obtained for the three finite tensor elements (α_{ba}, α_{ab}, and α_{bb}) are shown in Fig. 4(c). It should be noted that, while α_{ab} appears to be finite and nonzero above the phase transition, the field interval from B_{SF} to our maximum field is insufficient to distinguish if there is a linear or superlinear field dependence. It should be considered whether this finite α_{ab} could stem from a misalignment of the sample. However, assuming that the domain structure is comparable between measurements, a misalignment of the sample of $\approx 10^\circ$ would be needed to account for this nonzero signal in P_aH_b above B_{SF}. We are confident of the sample alignment within 5°, and hence, the finite P_aH_b above B_{SF} is most likely a real signal.

The ME coefficients for α_{ab} and α_{ba} in the low-field regime have previously been measured [19,22]. Figure 4(c) compares these results with our measurements. While, as already mentioned, the absolute values of α_{ij} cannot be compared directly, the temperature dependencies are still meaningful, and the values obtained for our unpoled setup are smaller than the literature values, as expected. Our temperature dependencies of α_{ab} and α_{ba} agree well with previously published results [19,22].

For the ME coefficients appearing for fields >31 T, we only have data at two temperatures. From these, it appears that α_{bb} in the high-field phase increases slightly with temperature but is otherwise lower than the ME coefficients present in the low-field phase.

We note also that, although a recent study found a weak but distinctly nonzero α_{aa} component in the low-field phase [22] for a poled $\mathrm{LiFePO_4}$ sample, it is beyond our experimental limit to corroborate these findings. This is due to the experimental uncertainty connected to the pulsed-field technique as well as the fact that our sample is not poled. Without poling, multiple domains may be present, which will lower the measured polarization and therefore α_{ij} compared with poled measurements.

C. Possible field-induced spin canting

In both $\mathrm{LiNiPO_4}$ and $\mathrm{LiCoPO_4}$, a field-induced spin canting caused by the DM interaction occurs for magnetic fields applied in the transverse direction [15,44]. Measurements of the field dependence of relevant Bragg peaks reflecting such structure deviations have been used to estimate the strength of the DM interaction in these compounds. Likewise, here, we investigate whether any field-induced spin canting also occurs in $\mathrm{LiFePO_4}$ and thus probe the strength of the DM interaction. We have probed five different Bragg peaks that reflect all

TABLE III. Squared structure factors (F^2) and polarization factors (P^2) and nuclear structure factors for Bragg reflections investigated with EIGER, see Eqs. (1)–(4).

q	$\|F_C\|^2$	$\|F_A\|^2$	$\|F_G\|^2$	$\|F_F\|^2$	$\|F_N\|^2$	$\|P_x\|^2$	$\|P_y\|^2$	$\|P_z\|^2$
(010)	16	0	0	0	0	1	0	1
(001)	0.29	0	16	0	0	1	1	0
(011)	0	16	0	0.29	260	1	0.62	0.38
(021)	0.29	0	16	0	0	1	0.29	0.71
(110)	0	0.49	16	0	0	0.75	0.25	1

possible field-induced cantings, as shown in Table III. The Bragg peaks (010), (001), (011), and (021) were investigated for fields along a, $B||a$, while the (110) peak was investigated for $B||c$. Figure 5 shows the difference in the neutron intensity for zero and finite magnetic fields. No intensity difference is observed for any of the peaks. This is in stark contrast with the Ni and Co compounds, where the intensity of the relevant Bragg peaks increases significantly in applied magnetic fields. This indicates a negligible DM interaction in LiFePO$_4$, to within the limits of sensitivity of the experiment.

V. DISCUSSION

A. Magnetic structure beyond 31 T

The appearance of the (030) Bragg peak >31 T in our pulsed-group symmetry $2_z/m'_z$. These observations rule out a possible C_z structure, and the only structure to satisfy both observations is a high-field phase with a dominant C_x structure and minor components C_y and A_z. This confirms the suggestion of a spin-flop transition put forward in Ref. [26], where the spins reorient from being predominantly along the b axis to being predominantly along the a axis with critical field $B_{SF} = 31$ T. Interestingly, this is the same point group as in the low-field phase but with a different distribution of the major and minor structure components. In the low-field phase, the system has major component C_y with minor C_x and A_z and a total spin canting away from b of $1.3(1)^\circ$ [23]. In the high-field phase, the major component is now C_x and with smaller components of C_y and A_z. We cannot determine the relative weights of these smaller structure components in the high-field phase and thus cannot speculate on the size of the spin canting. However, such components may explain the anomalous magnetization curve above the critical field observed in Ref. [26]. Furthermore, magnetization measurements in the spin-flop phase [26,28] show a magnetization jump to $\approx\frac{1}{2}$ of the saturation magnetization at the spin-flop transition, meaning that a sizable F_y component has been induced. The resulting inferred spin-flop structure is illustrated in Fig. 6(b) for a magnetic field immediately above the transition. The magnetic structures below and above the transition are illustrated in Figs. 6(a) and 6(b).

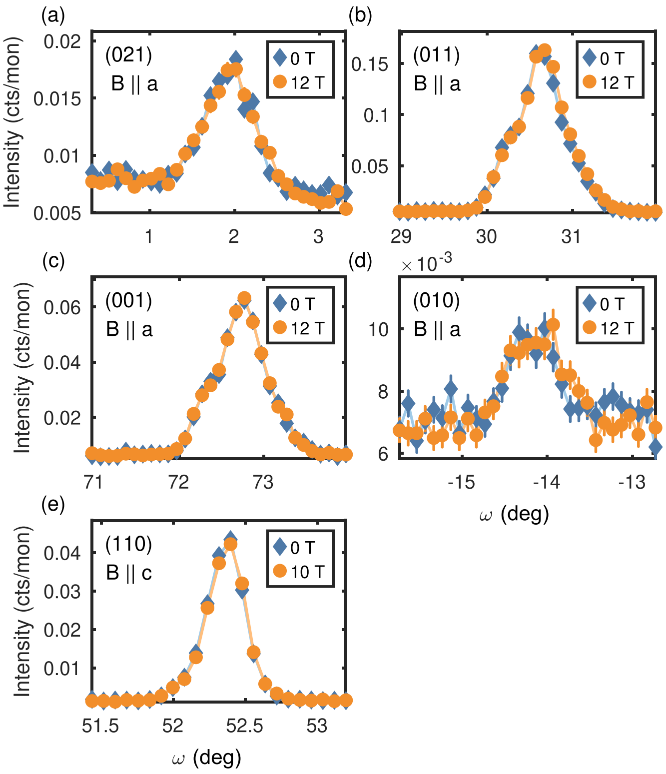

FIG. 5. Sample rotation ω scan of different Bragg peaks at low and high magnetic fields. All scans were performed at 2 K. Scans (a)–(d) are with magnetic fields along a, while scan (e) is with field along c.

B. Phase diagram and Hamiltonian

Figure 6(c) shows the phase diagram obtained of LiFePO$_4$ by combining the magnetization measurements from Refs. [26,28] with our neutron diffraction and electric polarization measurements. Based on anomalies in the magnetization, Werner *et al.* [26] reported a precursor phase just below the spin-flop transition at 1.5 K. We see no evidence of the AFM′ phase in the electric polarization measurements down to 4.2 K. The magnetic structure has now been established in both the low-field phase (cf. Ref. [23]) and the high-field phase (this paper). Combined with the realization that the DM interaction is of negligible size, based on the lack of any field-induced spin canting as seen in our neutron diffraction measurements, we now try to consolidate our understanding of LiFePO$_4$ by use of MF calculations.

The Hamiltonian of LiFePO$_4$ can be written as $\hat{\mathcal{H}} = \frac{1}{2}\sum_{ij} J_{ij}\,\mathbf{S}_i\cdot\mathbf{S}_j + \sum_{\alpha,i}\mathfrak{D}_\alpha (S_i^\alpha)^2$, where J_{ij} are the Heisenberg exchange interactions, and $\mathfrak{D}_\alpha$ is the single-ion anisotropy constant for $\alpha = \{a, b, c\}$ [8,23,28]. A number of different estimates of the exchange interactions and anisotropies of LiFePO$_4$ have been published [8,12,23,27,28]. However, of these studies, only Refs. [8,23] incorporate all the leading exchange interactionsand assume the DM interaction to be negligible. In Refs. [8,23], the couplings were obtained from fitting dispersion relations from linear spin-wave theory to the excitation spectrum measured by neutron spectroscopy. One notable difference between the two studies is that the estimate of Ref. [8] renders LiFePO$_4$ more frustrated in the (b, c) plane than Ref. [23] and with a larger value of the single-ion anisotropy $\mathfrak{D}_c$.

Using these two sets of parameters, we calculated the phase diagram and magnetic structures using a MF calculation as implemented in the program McPhase [45]. The calculations

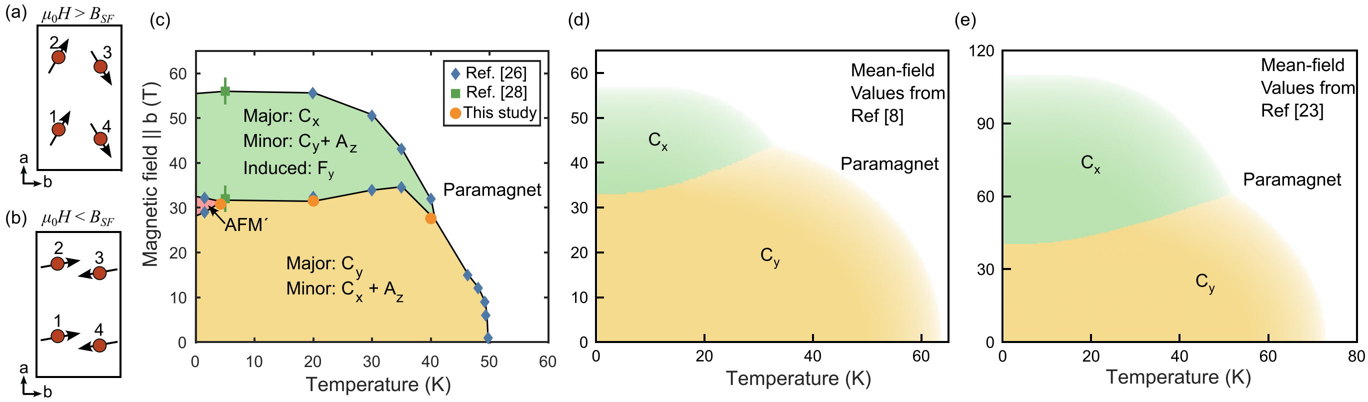

FIG. 6. Magnetic structures of $LiFePO_4$ in (a) the spin-flop and (b) the low-field phase. (c) Experimental phase diagram of $LiFePO_4$ for magnetic fields along *b*. Figure includes results from our neutron diffraction and electric polarization measurements as well as magnetization data from Refs. [26,28]. (d) and (e) Phase diagrams as determined from mean-field calculations with two different sets of parameters [8,23].

consider only the spin moments. We find an insignificant difference if we include the orbital moments and the full crystal field Hamiltonian as was used by Ref. [8], with a slightly lower spin-flop and saturation fields and lower T_N. The resulting phase diagrams are shown in Figs. 6(d) and 6(e). For both sets of parameters, we find C_y AFM order at low temperatures and low fields, as well as a spin-flop transition to C_x AFM order at elevated fields before saturation is reached at yet higher fields. We note that neither set of exchange couplings predict any AFM′ phase at low temperature, as observed in Ref. [26].

It is evident when comparing Figs. 6(a) and 6(d) that the phase diagram for the values in Ref. [8] match the experimental phase diagram well. In fact, the spin-flop and saturation fields obtained using the exchange and anisotropy parameters from Ref. [8] are within ∼5% of the experimental values, while the critical fields for the parameters from Ref. [23] are significantly higher. The Néel temperatures and spin-flop and saturations fields obtained from the MF calculations are summarized in Table IV and compared with the experimental values. Thus, we conclude that the parameters obtained by Yiu *et al.* [8] provide a better description of the phase diagram of $LiFePO_4$.

With regard to the DM interaction, $LiFePO_4$ seems to be distinct from the two relevant family members $LiNiPO_4$ and $LiCoPO_4$ with much smaller zero-field canting. ESR [27] and terahertz [28] spectroscopy estimate the DM interaction to be <0.05 meV, and our neutron diffraction results confirm this, using the same method of investigation used on the other two family members. This is significantly smaller than the DM interactions in the Ni and Co compounds, being 0.4 meV [31] and 0.7 meV [44], respectively. The *Pnma*-allowed DM interaction has the form $\hat{\mathcal{H}}_{\rm DM} = D^b_{12}(S^z_1 S^x_2 - S^x_1 S^z_2) + D^b_{34}(S^z_3 S^x_4 - S^x_3 S^z_4)$. However, the distorted octahedra surrounding the magnetic ions give rise to a low crystal-ion terms of the form [15] $\hat{\mathcal{H}}_{\mathfrak{D}} = -\mathfrak{D}_{xz}(S^z_1 S^x_1 - S^x_2 S^z_2 + S^z_3 S^x_3 - S^x_4 S^z_4)$. The two terms have a similar origin as higher order orbital processes, and are hard to distinguish experimentally.

TABLE IV. Sets of estimated exchange interactions and single-ion anisotropies (in meV) from previous publications [8,23]. Also shown are the predicted MF values of critical temperature and fields at 4 K [see Figs. 6(d) and 6(e)] compared with the experimental values.

	Toft-Petersen *et al.* (2015) [23]	Yiu *et al.* (2017) [8]	
J_{bc}	0.77(2)	0.46(2)	
J_b	0.30(2)	0.09(1)	
J_c	0.14(2)	0.01(1)	
J_{ab}	0.14(2)	0.09(1)	
J_{ac}	0.05(1)	0.01(1)	
$\mathfrak{D}_a$	0.62(1)	0.86(2)	
$\mathfrak{D}_c$	1.56(4)	2.23(2)	
	MF theory		Measured
T_N (K)	73	62	50
$B_{\rm SF}$ (T)	40	33	31
$B_{\rm Sat}$ (T)	110	57	56

VI. CONCLUSIONS

Motivated by the discovery of a phase transition in $LiFePO_4$ at high fields along the crystallographic *b* axis [26], we have combined pulsed-field neutron diffraction and electric polarization measurements. Our results show that the phase transition is of the spin-flop type with $B_{\rm SF} = 31\,{\rm T}$ at 4 K. Above the transition, a ME active phase exists with finite α_{bb} and α_{ba} ME tensor elements. By combining the results from pulsed-field neutron diffraction and electric polarization measurements, we argue that the high-field AFM structure is dominantly C_x with magnetic moments along the *a* axis but also that further subdominant C_y and A_x components are required to explain the nonzero α_{ba}. This indicates a lower-symmetry magnetic point group than a simple spin-flop phase. Furthermore, neutron diffraction experiments in magnetic fields along *c* and *a* showed no field-induced spin canting in $LiFePO_4$, which demonstrates a DM interaction of negligible strength. Phase diagrams calculated using MF theory indicate that the coupling parameters determined by Yiu *et al.* [8] match well the observations for $LiFePO_4$.

ACKNOWLEDGMENTS

We thank Lise Grüner Hanson (DTU Physics) for help with conducting the EIGER neutron experiments. This project was supported by a research grant (No. 35921) from VILLUM FONDEN as well as the European Research Council through the Synergy network HERO (Grant No. 810451) and the Swiss National Science Foundation through Project Grant No. 188648. The neutron experiment at the Materials and Life Science Experimental Facility of the J-PARC was performed under a user program (Proposal No. 2021B0166). The other neutron experiment was performed at the Swiss spallation neutron source SINQ, Paul Scherrer Institute, Villigen, Switzerland. Polarization measurements were performed at the Institute for Solid State Physics, Japan. R.T.P. was supported by GIMRT and ICC-IMR. D.V. and J. L. grew and characterized the crystals. Their research was supported by the U.S. Department of Energy(DOE), Office of Basic Energy Sciences, Division of Materials Sciences and Engineering. Ames National Laboratory is operated for the DOE by Iowa State University under Contract No. DE-AC02-07CH11358. The experimental work was supported by the instrument center DanScatt funded through the Danish Agency for Science, Technology, and Innovation through Grant No. 7129-00003B.

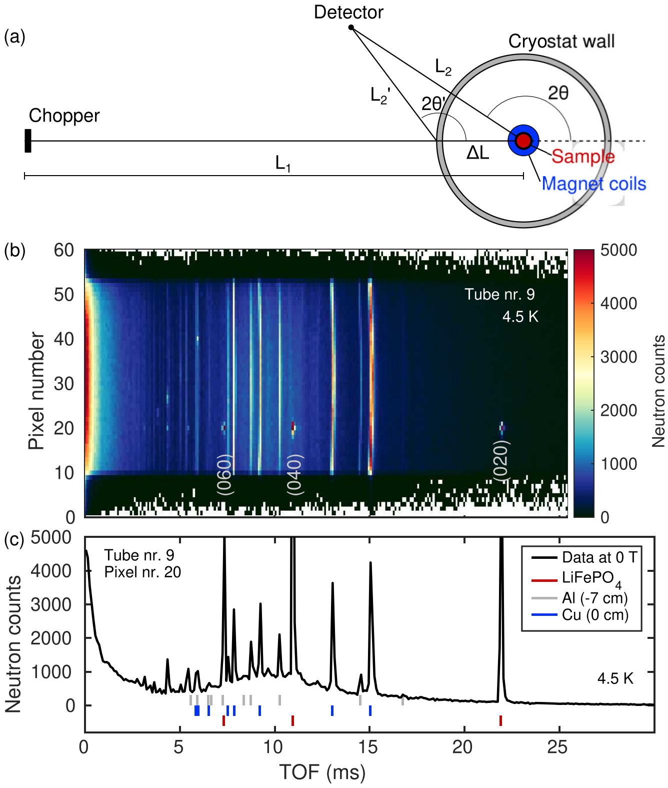

FIG. 7. Identification of powder lines arising from the sample environment (cryostat wall and magnet coils) and nuclear Bragg peaks from the sample. (a) Experimental geometry showing the position of the cryostat wall, magnet coils, and sample. Note that the sketch is not to scale. (b) Neutron diffraction data collected at zero field as a function of pixel number and time of flight(ToF) for detector tube No. 9. Color contours represent the neutron counts. Nuclear Bragg peaks (020), (040), and (060) are observed as high-intensity spots around pixel No. 20. Powder lines have intensity spread out homogeneously over all pixels. (c) Neutron counts as a function of ToF collected at zero field and 4.5 K in detector tube No. 9 and pixel No. 20. Nuclear Bragg peak positions from the sample are marked with red lines. Powder lines from the cryostat wall (aluminum) and magnet coils (copper) are marked with, respectively, gray and blue lines.

APPENDIX A: POWDER LINES AND BACKGROUND AT NOBORU

In addition to the Bragg peaks arising from $LiFePO_4$, our pulsed-field neutron diffraction data contained multiple additional high-intensity peaks. To investigate the origin of these features, we considered scattering from the sample surroundings. Two main sources of polycrystalline elastic scattering were identified: the cryostat wall in aluminum and the magnet coils in copper, positioned as shown in Fig. 7(a). The quantities indicated in the sketch are $L_1 = 14\,\mathrm{m}$, $L_2 = 0.9\,\mathrm{m}$,

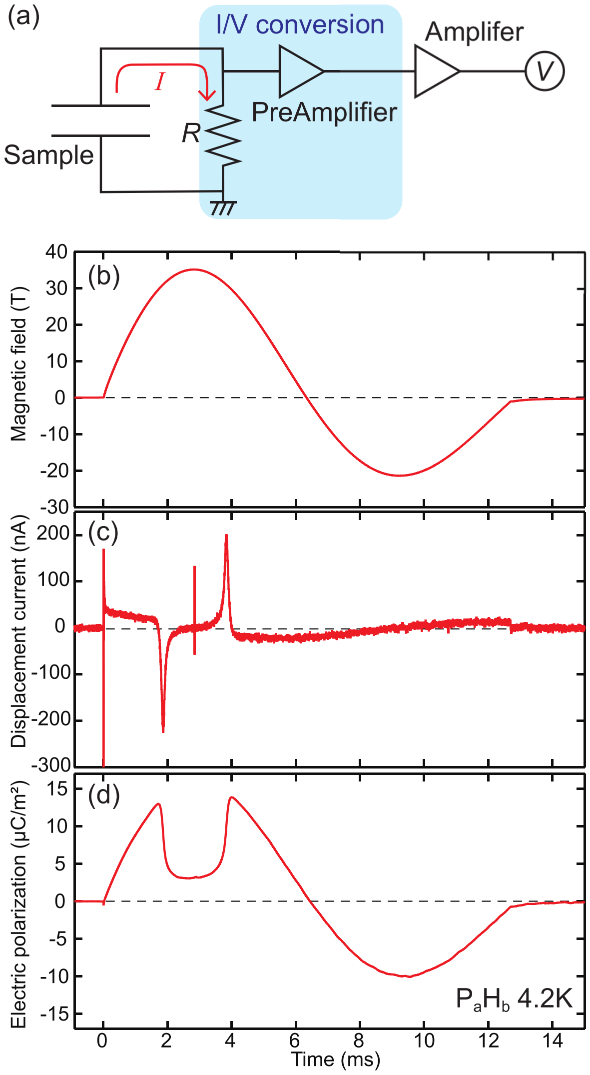

FIG. 8. (a) Experimental setup for polarization measurement. (b) Two consecutive magnetic field pulse of duration 6.1 ms. (c) The measured displacement current during the time of the pulse. (d) The deduced electric polarization. As evident, the electric polarization along a has a plateau in the spin flop phase, for field applied along the b axis, as discussed in the main text.

$2\theta = 150^\circ$, and ΔL in the range $[-15, 0]$ cm, where negative ΔL corresponds to a position before the sample. Bragg peaks from the sample are distinguished from the powder lines as high-intensity spots on the detector, see Fig. 7(b). The cryostat contains several aluminum shields, but most peaks in the diffraction pattern are well accounted for by including a single wall of aluminum positioned 7 cm before the sample and copper at the sample position as shown in Fig. 7(c), considering the second cryostat wall after the sample does not yield any additional insight. Most important for our data analysis is the identification of the lines ~15 ms, which are close to the location of the (030) Bragg peak. It is clear that these arise from the sample environment, and any additional intensity in this area at high magnetic fields must find its origin in the sample itself.

APPENDIX B: POLARIZATION MEASUREMENTS

Lastly, we elaborate on the pulsed-crystal plate is connected to two electrodes, and as the magnetic field changes with time, the ME effect induces a change in bulk polarization and thereby a change in the surface charge on the electrodes. This gives rise to a so-called displacement current in the circuit. A diagram of the circuit is given in Fig. 8(a). For I/V conversion, a LI-76 converter from the NF Corporation was used, and the low-noise voltage preamplifier was a SR560 model from Stanford Research Systems. For obtaining the electric polarization, the displacement current is integrated over time:

$$\begin{aligned} P(T_1) &= P(T_0) - \frac{1}{A}\int_{T_0}^{T_1} I(T)dT \\ &= P(T_0) - \frac{1}{A}\int_{T_0}^{T_1} \frac{V(T)}{R}dT, \end{aligned} \tag{B1}$$

where $I(T)$ and $V(T)$ are the current and voltage, respectively, A is the crystal electrode area, and R is the resistance.

[1] S. Manipatruni, D. E. Nikonov, C. C. Lin, T. A. Gosavi, H. Liu, B. Prasad, Y. L. Huang, E. Bonturim, R. Ramesh, and I. A. Young, Scalable energy-efficient magnetoelectric spin-orbit logic, Nature (London) **565**, 35 (2019).

[2] F. Trier, P. Noël, J.-V. Kim, J.-P. Attané, L. Vila, and M. Bibes, Oxide spin-orbitronics: Spin-charge interconversion and topological textures, Nat. Rev. Mater. **7**, 258 (2022).

[3] M. Fiebig, T. Lottermoser, D. Meier, and M. Trassin, The evolution of multiferroics, Nat. Rev. Mater. **1**, 16046 (2016).

[4] N. A. Spaldin and R. Ramesh, Advances in magnetoelectric multiferroics, Nat. Mater. **18**, 203 (2019).

[5] X. Liang, A. Matyushov, P. Hayes, V. Schell, C. Dong, H. Chen, Y. He, A. Will-Cole, E. Quandt, P. Martins *et al.*, Roadmap on magnetoelectric materials and devices, IEEE Trans. Magn. **57**, 1 (2021).

[6] Y. Ba, S. Zhuang, Y. Zhang, Y. Wang, Y. Gao, H. Zhou, M. Chen, W. Sun, Q. Liu, G. Chai *et al.*, Electric-field control of skyrmions in multiferroic heterostructure via magnetoelectric coupling, Nat. Commun. **12**, 322 (2021).

[7] J. P. Rivera, A short review of the magnetoelectric effect and related experimental techniques on single phase (multi-) ferroics, Eur. Phys. J. B **71**, 299 (2009).

[8] Y. Yiu, M. D. Le, R. Toft-Petersen, G. Ehlers, R. J. McQueeney, and D. Vaknin, Hybrid excitations due to crystal field, spin-orbit coupling, and spin waves in $\mathrm{LiFePO_4}$, Phys. Rev. B **95**, 104409 (2017).

[9] G. Quirion and M. L. Plumer, Landau theory of the magnetic phase diagram of monoclinic multiferroics: Application to $\mathrm{MnWO_4}$ and CuO, Phys. Rev. B **87**, 174428 (2013).

[10] M. Mercier, Étude de l'effet magnetoelectrique sur de composés de type olivine, perovskite et grenat, Ph.D. thesis, Université de Grenoble, 1969.

[11] R. P. Santoro and R. E. Newnham, Antiferromagnetism in $\mathrm{LiFePO_4}$, Acta Cryst. **22**, 344 (1967).

[12] J. Li, V. O. Garlea, J. L. Zarestky, and D. Vaknin, Spin-waves in antiferromagnetic single-crystal $\mathrm{LiFePO_4}$, Phys. Rev. B **73**, 024410 (2006).

[13] E. Fogh, R. Toft-Petersen, E. Ressouche, C. Niedermayer, S. L. Holm, M. Bartkowiak, O. Prokhnenko, S. Sloth, F. W. Isaksen, D. Vaknin *et al.*, Magnetic order, hysteresis, and phase coexistence in magnetoelectric $\mathrm{LiCoPO_4}$, Phys. Rev. B **96**, 104420 (2017).

[14] R.P. Santoro, D.J. Segal, and R.E. Newnham, Magnetic properties of $\mathrm{LiCoPO_4}$ and $\mathrm{LiNiPO_4}$, J. Phys. Chem. Solids **27**, 1192 (1966).

[15] T. B. S. Jensen, N. B. Christensen, M. Kenzelmann, H. M. Rønnow, C. Niedermayer, N. H. Andersen, K. Lefmann, J. Schefer, M. v. Zimmermann, J. Li *et al.*, Field-induced magnetic phases and electric polarization in $\mathrm{LiNiPO_4}$, Phys. Rev. B **79**, 092412 (2009).

[16] D. Vaknin, J. L. Zarestky, J.-P. Rivera, and H. Schmid, Antiferromagnetism in $\mathrm{LiCoPO_4}$ and $\mathrm{LiNiPO_4}$, in *Magnetoelectric Interaction Phenomena in Crystals*, NATO Science Series, edited by M. Fiebig, V. V. Eremenko, and I. E. Chupis (Springer, Dordrecht, 2004), Vol. 164, pp. 203–217.

[17] G. Rousse, J. Rodriguez-Carvajal, S. Patoux, and C. Masquelier, Magnetic structures of the triphylite $\mathrm{LiFePO_4}$ and of its delithiated form $\mathrm{FePO_4}$, Chem. Mater. **15**, 4082 (2003).

[18] R. Toft-Petersen, N. H. Andersen, H. Li, J. Li, W. Tian, S. L. Bud'ko, T. B. S. Jensen, C. Niedermayer, M. Laver, O. Zaharko *et al.*, Magnetic phase diagram of magnetoelectric $\mathrm{LiMnPO_4}$, Phys. Rev. B **85**, 224415 (2012).

[19] M. Mercier, P. Bauer, and B. Fouilleux, Mesures magnétoélectriques sur $\mathrm{LiFePO_4}$, C. R. Acad. Sci. Paris B **267**, 1345 (1968).

[20] E. Fogh, B. Klemke, M. Reehuis, P. Bourges, C. Niedermayer, S. Holm-Dahlin, O. Zaharko, J. Schefer, A. B. Kristensen, M. K. Sørensen *et al.*, Tuning magnetoelectricity in a mixed-anisotropy antiferromagnet, Nat. Commun. **14**, 3408 (2023).

[21] E. Fogh, T. Kihara, R. Toft-Petersen, M. Bartkowiak, Y. Narumi, O. Prokhnenko, A. Miyake, M. Tokunaga, K. Oikawa, M. K. Sørensen *et al.*, Magnetic structures and quadratic magnetoelectric effect in $\mathrm{LiNiPO_4}$ beyond 30 T, Phys. Rev. B **101**, 024403 (2020).

[22] E. Fogh, B. Klemke, A. Pages, J. Li, D. Vaknin, H. M. Rønnow, N. B. Christensen, and R. Toft-Petersen, The magnetoelectric effect in $LiFePO_4$—Revisited, Physica B: Condens. Matter **648**, 414380 (2023).

[23] R. Toft-Petersen, M. Reehuis, T. B. S. Jensen, N. H. Andersen, J. Li, M. D. Le, M. Laver, C. Niedermayer, B. Klemke, K. Lefmann *et al.*, Anomalous magnetic structure and spin dynamics in magnetoelectric $LiFePO_4$, Phys. Rev. B **92**, 024404 (2015).

[24] T. B. S. Jensen, N. B. Christensen, M. Kenzelmann, H. M. Rønnow, C. Niedermayer, N. H. Andersen, K. Lefmann, M. Jiménez-Ruiz, F. Demmel, J. Li *et al.*, Anomalous spin waves and the commensurate-incommensurate magnetic phase transition in $LiNiPO_4$, Phys. Rev. B **79**, 092413 (2009).

[25] A. Scaramucci, E. Bousquet, M. Fechner, M. Mostovoy, and N. A. Spaldin, Linear magnetoelectric effect by orbital magnetism, Phys. Rev. Lett. **109**, 197203 (2012).

[26] J. Werner, S. Sauerland, C. Koo, C. Neef, A. Pollithy, Y. Skourski, and R. Klingeler, High magnetic field phase diagram and failure of the magnetic Grüneisen scaling in $LiFePO_4$, Phys. Rev. B **99**, 214432 (2019).

[27] J. Werner, C. Neef, C. Koo, A. Ponomaryov, S. Zvyagin, and R. Klingeler, Exceptional field dependence of antiferromagnetic magnons in $LiFePO_4$, Phys. Rev. B **103**, 174406 (2021).

[28] L. Peedu, V. Kocsis, D. Szaller, B. Forrai, S. Bordács, I. Kézsmárki, J. Viirok, U. Nagel, B. Bernáth, D. L. Kamenskyi *et al.*, Terahertz spectroscopy of spin excitations in magnetoelectric $LiFePO_4$ in high magnetic fields, Phys. Rev. B **106**, 134413 (2022).

[29] J. Li, W. Tian, Y. Chen, J. L. Zarestky, J. W. Lynn, and D. Vaknin, Antiferromagnetism in the magnetoelectric effect single crystal $LiMnPO_4$, Phys. Rev. B **79**, 144410 (2009).

[30] D. Vaknin, J. L. Zarestky, J. P. Rivera, and H. Schmid, Commensurate-incommensurate magnetic phase transition in magnetoelectric single crystal $LiNiPO_4$, Phys. Rev. Lett. **92**, 207201 (2004).

[31] R. Toft-Petersen, J. Jensen, T. B. S. Jensen, N. H. Andersen, N. B. Christensen, C. Niedermayer, M. Kenzelmann, M. Skoulatos, M. D. Le, K. Lefmann *et al.*, High-field magnetic phase transitions and spin excitations in magnetoelectric $LiNiPO_4$, Phys. Rev. B **84**, 054408 (2011).

[32] K. Kuwahara, S. Yoshii, H. Nojiri, D. Aoki, W. Knafo, F. Duc, X. Fabrèges, G. W. Scheerer, P. Frings, G. L. J. A. Rikken *et al.*, Magnetic structure of phase II in $\mathbf{U}(Ru_{0.96}Rh_{0.04})_2Si_2$ determined by neutron diffraction under pulsed high magnetic fields, Phys. Rev. Lett. **110**, 216406 (2013).

[33] H. Nojiri, S. Yoshii, M. Yasui, K. Okada, M. Matsuda, J. S. Jung, T. Kimura, L. Santodonato, G. E. Granroth, K. A. Ross *et al.*, Neutron laue diffraction study on the magnetic phase diagram of multiferroic $MnWO_4$ under pulsed high magnetic fields, Phys. Rev. Lett. **106**, 237202 (2011).

[34] S. Yoshii, K. Ohoyama, K. Kurosawa, H. Nojiri, M. Matsuda, P. Frings, F. Duc, B. Vignolle, G. L. J. A. Rikken, L.-P. Regnault *et al.*, Neutron diffraction study on the multiple magnetization plateaus in TbB_4 under pulsed high magnetic field, Phys. Rev. Lett. **103**, 077203 (2009).

[35] F. Duc, X. Fabrèges, T. Roth, C. Detlefs, P. Frings, M. Nardone, J. Billette, M. Lesourd, L. Zhang, A. Zitouni *et al.*, A 31 T split-pair pulsed magnet for single crystal x-ray diffraction at low temperature, Rev. Sci. Instrum. **85**, 053905 (2014).

[36] K. Ohoyama, N. Katoh, H. Nojiri, Y. Matsuda, H. Hiraka, K. Ikeda, and H. Shimizu, Neutron diffraction under 30 T pulsed magnetic fields, J. Magn. Magn. Mater. **310**, e974 (2007).

[37] A. Gazizulina, D. L. Quintero-Castro, Z. Wang, F. Duc, F. Bourdarot, K. Prokes, W. Schmidt, R. Daou, S. Zherlitsyn, N. Islam *et al.*, Neutron diffraction of field-induced magnon condensation in the spin-dimerized antiferromagnet $Sr_3Cr_2O_8$, Phys. Rev. B **104**, 064430 (2021).

[38] F. Duc, X. Tonon, J. Billette, B. Rollet, W. Knafo, F. Bourdarot, J. Béard, F. Mantegazza, B. Longuet, J. E. Lorenzo *et al.*, 40-Tesla pulsed-field cryomagnet for single crystal neutron diffraction, Rev. Sci. Instrum. **89**, 053905 (2018).

[39] R. Toft-Petersen, E. Fogh, T. Kihara, J. Jensen, K. Fritsch, J. Lee, G. E. Granroth, M. B. Stone, D. Vaknin, H. Nojiri *et al.*, Field-induced reentrant magnetoelectric phase in $LiNiPO_4$, Phys. Rev. B **95**, 064421 (2017).

[40] K. Oikawa, F. Maekawa, M. Harada, T. Kai, S. Meigo, Y. Kasugai, M. Ooi, K. Sakai, M. Teshigawara, S. Hasegawa *et al.*, Design and application of NOBORU-neutron beam line for observation and research use at J-PARC, Nucl. Instrum. Methods Phys. Res. A **589**, 310 (2008).

[41] M. Watanabe, T. Kihara, and H. Nojiri, Automated pulsed magnet system for neutron diffraction experiments at the materials and life science experimental facility in J-PARC, Quantum Beam Sci. **7**, 1 (2023).

[42] U. Stuhr, B. Roessli, S. Gvasaliya, H. M. Rønnow, U. Filges, D. Graf, A. Bollhalder, D. Hohl, R. Bürge, M. Schild *et al.*, The thermal triple-axis-spectrometer EIGER at the continuous spallation source SINQ, Nucl. Instrum. Methods Phys. Res. A **853**, 16 (2017).

[43] J. Werner, C. Neef, C. Koo, S. Zvyagin, A. Ponomaryov, and R. Klingeler, Antisite disorder in the battery material $LiFePO_4$, Phys. Rev. Mater. **4**, 115403 (2020).

[44] E. Fogh, O. Zaharko, J. Schefer, C. Niedermayer, S. Holm-Dahlin, M. K. Sørensen, A. B. Kristensen, N. H. Andersen, D. Vaknin, N. B. Christensen *et al.*, Dzyaloshinskii-Moriya interaction and the magnetic ground state in magnetoelectric $LiCoPO_4$, Phys. Rev. B **99**, 104421 (2019).

[45] M. Rotter, Using McPhase to calculate magnetic phase diagrams of rare earth compounds, J. Magn. Magn. Mater. **272-276**, E481 (2004).

Paper II

Magnetic and crystal electric field studies of the rare earth based square lattice antiferromagnet $NdKNaNbO_5$

S. Guchhait, **A. Painganoor**, S. S. Islam, J. Sichelschmidt, M. D. Le, M. Aouane, N. B. Christensen, and R. Nath

Physical Review B ***110****, 144434 (2024)*

This paper reports the magnetic properties and crystal electric field scheme of rare-earth square lattice antiferromagnet $NdKNaNbO_5$. Contributions were made to the synthesis of the powder samples, XRD measurements, magnetization measurements and to their analysis during the Master's thesis work at the Indian Institute of Science Education and Research (IISER) Thiruvananthapuram.

PHYSICAL REVIEW B **110**, 144434 (2024)

Magnetic and crystal electric field studies of the rare earth based square lattice antiferromagnet NdKNaNbO$_5$

S. Guchhait,[1] A. Painganoor,[1,2,3] S. S. Islam,[1] J. Sichelschmidt,[4] M. D. Le,[5] M. Aouane,[5]
N. B. Christensen,[2,*] and R. Nath[1,†]

[1]*School of Physics, Indian Institute of Science Education and Research Thiruvananthapuram, Thiruvananthapuram 695551, India*
[2]*Department of Physics, Technical University of Denmark, 2800 Kongens Lyngby, Denmark*
[3]*Institute Laue-Langevin, 38042 Grenoble Cedex 9, France*
[4]*Max Planck Institute for Chemical Physics of Solids, Nöthnitzer Str 40, 01187 Dresden, Germany*
[5]*ISIS Neutron and Muon Source, Science and Technology Facilities Council, Rutherford Appleton Laboratory,*
Didcot OX11 0QX, United Kingdom

(Received 30 August 2024; revised 7 October 2024; accepted 8 October 2024; published 21 October 2024;
corrected 27 June 2025)

The interplay of magnetic correlations, crystal electric field interactions, and spin-orbit coupling in low-dimensional frustrated magnets fosters novel ground states with unusual excitations. Here, we report the magnetic properties and crystal electric field (CEF) scheme of a rare-earth-based square-lattice antiferromagnet NdKNaNbO$_5$ investigated via magnetization, specific heat, electron spin resonance (ESR), and inelastic neutron scattering (INS) experiments. The low-temperature Curie-Weiss temperature $\theta_{\mathrm{CW}} \simeq -0.6$ K implies net antiferromagnetic interactions between the Nd^{3+} ions. Two broad maxima are observed in the low-temperature specific heat data in magnetic fields, indicating multilevel Schottky anomalies because of the effect of CEF. No magnetic long-range order is detected down to 0.4 K. The CEF excitations of Kramers' ion Nd^{3+} ($J = 9/2$) probed via INS experiments evince dispersionless excitations characterizing the transitions among the CEF energy levels. The fit of the INS spectra enabled the mapping of the CEF Hamiltonian and the energy eigenvalues of the Kramers' doublets. The simulation using the obtained CEF parameters reproduces the broad maxima in specific heat in zero field as well as in different applied fields. The significant contribution from $J_z = \pm 1/2$ state to the wave function of the ground-state doublet indicates the role of strong quantum fluctuations at low temperatures. The magnetic ground state is found to be a Kramers' doublet with effective spin $J_{\mathrm{eff}} = 1/2$ at low temperatures.

DOI: 10.1103/PhysRevB.110.144434

I. INTRODUCTION

Frustrated magnetism has been at the forefront of condensed matter research for decades since frustration compels the spin systems to resist magnetic long-range order (LRO) and to exhibit a variety of disordered ground states [1]. In a two-dimensional (2D) square lattice, frustration arises because of competing nearest-neighbor (NN) (J_1) and next-nearest-neighbor (NNN) (J_2) interactions along the edges and diagonals of a square, respectively. Based on the frustration ratio, $\alpha = J_2/J_1$, a series of fascinating phases are predicted theoretically for the spin-1/2 $J_1 - J_2$ model. The two most exciting ones are quantum spin-liquid (QSL) and spin-nematic phases that are predicted at the critical regimes $\alpha \simeq \pm 0.5$, respectively [2,3]. However, to date, no experimental verifications of the existence of these phases have emerged. Most of the frustrated square lattice (FSL) systems experimentally realized so far are based on 3d transition metal ions, but none of them fall within the quantum critical regimes [4–10]. Unfortunately, none of the compounds feature a perfect square lattice, as the underlying crystal symmetries are lower than tetragonal [11].

Recently, rare-earth (4f)-based antiferromagnets (AFM) with strong spin-orbit coupling (SOC) and crystal electric field (CEF) interactions offer an alternate route to realize exotic quantum phenomena [12]. In such systems, CEF is typically weak compared to SOC and splits the spin-orbit entangled ground state into different singlet and doublet states. A system with an odd number of 4f electrons (Kramers' ion) forms Kramers' doublets and often behaves as an effective spin-1/2 system at a temperature that is low compared to the energy gap between the ground and first excited state doublets. The CEF controls the single ion ground-state properties and determines the size and anisotropy of the magnetic moment. Further, from the wave functions of the CEF ground state and excited states, one can extract information about the role of quantum fluctuations, quantum tunneling, and anisotropic spin interactions of the system [13–15]. For instance, if the CEF ground state has significant $|J, J_z\rangle$ components with a large $|J_z|$, quantum fluctuations are suppressed and classical states are stabilized [13]. Here, J is the total angular momentum and J_z is the z component of the angular momentum operator. On the other hand, if the CEF ground state has significant $|J, J_z\rangle$ components with a small $|J_z|$, it would facilitate quantum tunneling and leads the system to host exotic quantum phenomena, such as QSL [16,17]. Thus, in order to understand the nature of the magnetic ground state,

---

[*] Contact author: nbch@fysik.dtu.dk
[†] Contact author: rnath@iisertvm.ac.in

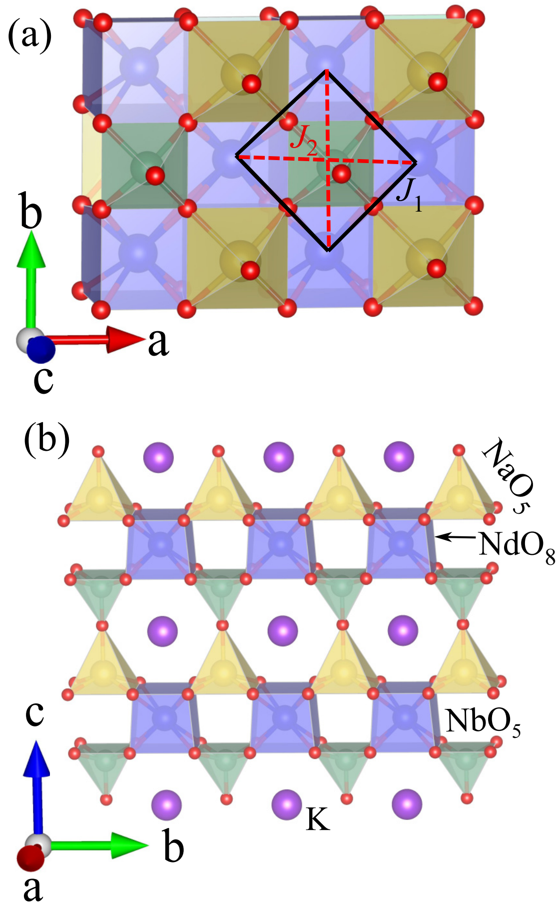

FIG. 1. (a) A section of the $NdNaNbO_5$ layer (square plane) in the *ab* plane highlighting the interactions J_1 (along the sides of the square) and J_2 (along the diagonals of the square). (b) Crystal structure of $NdKNaNbO_5$ projected in the *bc* plane that shows the stacking of two adjacent layers along the *c* axis and their interlayer connectivity via NbO_5 and NaO_5 square pyramids.

especially for rare-earth-based systems, it is essential to analyze the CEF scheme. From the material perspective, while many rare-earth-based frustrated magnets are studied [12,18–29], systems featuring FSL have not yet received much attention because of the unavailability of model compounds. Recently, $NaYbGeO_4$ is reported to be a distorted square-lattice compound, showing magnetic LRO at 0.21 K [30]. Similarly, another compound Bi_2YbO_4Cl displays a perfect square lattice and does not order down to 0.09 K [31].

The family of compounds, $LnKNaNbO_5$ (Ln = rare-earth) exist with a tetragonal structure (space group: $P4/nmm$, i.e., a perfect square lattice), without any structural disorder, making them favorable candidates to explore FSL model. $NdKNaNbO_5$ (NKNNO) belongs to the above family where distorted NdO_8 cubes are edge-shared with the basal edges of NbO_5 and NaO_5 square pyramids and form a layered structure in the *ab* plane, as depicted in Fig. 1(a). Two adjacent $NdNaNbO_5$ layers are interconnected via a common apical oxygen of NbO_5 and NaO_5 units along the *c* axis [see Fig. 1(b)]. K^+ ions occupy the interstitial space. In each layer, Nd^{3+} ions form a perfect square lattice with NN exchange interaction (J_1) arising through Nd-O-Nd pathway while the NNN interaction (J_2) occurring via Nd-O-Nb-O-Nd or Nd-O-Na-O-Nd pathways [see Fig. 1(a)] [32]. Nd^{3+} is a Kramers ion with $4f^3$ configuration ($L = 6$, $S = 3/2$, $J = 9/2$, and Landé g factor $g = 0.73$) for which one expects five doublets with quantum numbers $J_z = \pm\frac{1}{2}, \pm\frac{3}{2}, \pm\frac{5}{2}, \pm\frac{7}{2}$, and $\pm\frac{9}{2}$. The low-temperature magnetic and CEF properties of this compound have not been studied yet. In this paper, we report a comprehensive study of the low-temperature magnetic properties and CEF excitations of Nd^{3+} in NKNNO by means of magnetization, specific heat, electron spin resonance (ESR), and inelastic neutron scattering (INS) measurements. No conventional magnetic LRO is detected down to 0.4 K. We could successfully model the INS spectra using the CEF Hamiltonian and extract information about the CEF energy levels. Finally, the specific heat calculated using the CEF parameters replicates the experimental specific heat data.

II. SYNTHESIS AND METHODS

Polycrystalline samples of NKNNO and the nonmagnetic isostructural compound $LaKNaNbO_5$ (LKNNO) were synthesized by the conventional solid-state reaction method. Stoichiometric amount of Ln_2O_3 (Ln = Nd and La) (Aldrich, 99.9%), Na_2CO_3 (Aldrich, 99.9%), K_2CO_3 (Aldrich, 99.8%), and Nb_2O_5 (Aldrich, 99%) were ground thoroughly inside an Argon-filled glove box and pressed into pellets. Prior to grinding, preheating was done at 1000°C for one day for Ln_2O_3 and at 120°C for overnight for Na_2CO_3 and K_2CO_3. The pellets of LKNNO and NKNNO were heated for several hours at 760°C and 800°C, respectively with intermediate grindings. In each intermediate grinding step, we added an extra amount (5% excess) of Na_2CO_3 and K_2CO_3 to compensate the loss of Na and K during the heating process. The phase purity of the samples were checked by room-temperature powder x-ray diffraction (XRD) measurement using a PANalytical powder diffractometer with Cu K_α radiation ($\lambda_{avg} \simeq 1.5418$ Å) (see Fig. 2). Rietveld refinement of the powder XRD patterns were performed using the FULLPROF software package [33], taking the initial structural parameters from Ref. [32]. The refined atomic coordinates are tabulated in Table I. The lattice parameters and unit cell volumes (V_{Cell}) obtained from the refinement are [$a = b = 5.8032(3)$ Å, $c \simeq 8.2713(4)$ Å, and $V_{Cell} \simeq 278.5$ Å^3] and [$a = b = 5.7367(2)$ Å, $c = 8.2422(1)$ Å, and $V_{Cell} \simeq 271.3$ Å^3] for LKNNO and NKNNO compounds, respectively. These values are in close agreement with the previous report [32].

Magnetization (M) as a function of temperature (T) was measured in the temperature range 0.4–380 K in different magnetic fields using a superconducting quantum interference device (SQUID) (MPMS-3, Quantum Design) magnetometer. Isothermal magnetization (M vs H) was measured at $T = 0.4, 0.6, 1, 1.8, 3$, and 5 K from 0 to 7 T. Measurements below 1.8 K were performed using a ^{3}He insert (iHelium3) to the SQUID magnetometer. Temperature-dependent specific heat at different fields (0–9 T) was measured on a sintered pellet in a large temperature range (0.4 K $\leqslant T \leqslant$ 200 K) using the thermal relaxation technique in PPMS. A ^{3}He insert to the PPMS was used to measure specific heat below 2 K.

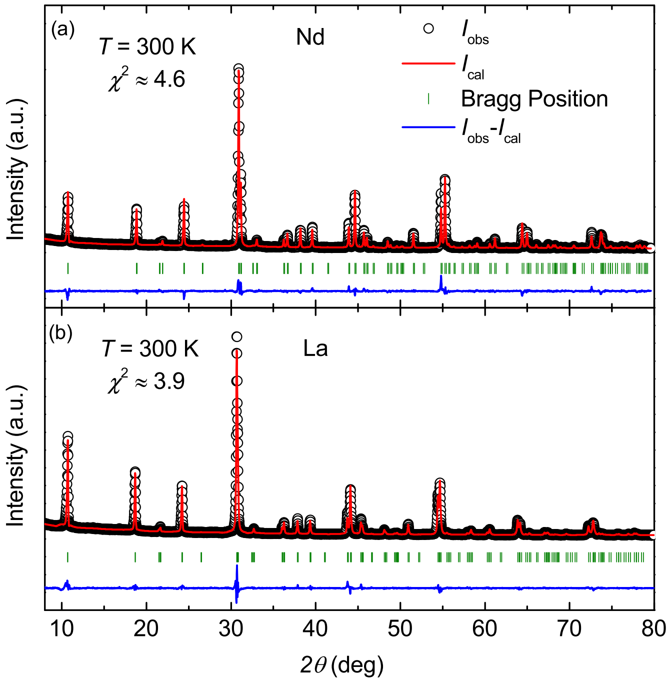

FIG. 2. Room-temperature powder XRD patterns of (a) NKNNO and (b) LKNNO. Black circles denote the observed intensity and the red-solid line represents the Rietveld fit. Green small-vertical bars at the bottom show the Bragg peak positions and the blue-solid line represents the difference between observed and calculated intensities. χ^2 represents the goodness-of-fit of the refinement.

Electron spin resonance (ESR) experiments were performed on the powder sample using a standard continuous-wave spectrometer in the temperature range $3\ \mathrm{K} \leqslant T \leqslant 30$ K. We measured the power P absorbed by the sample from a transverse magnetic microwave field (X-band, $\nu = 9.4$ GHz) as a function of an external static magnetic field. To improve the signal-to-noise ratio, a lock-in technique was employed. The final data were recorded as the derivative of the response signal $\frac{dP}{dH}$ as a function of the field. The ESR g factor was calculated using the resonance condition, $g = \frac{h\nu}{\mu_B H_{\mathrm{res}}}$, where h is Planck's constant, μ_B is the Bohr magneton, ν is the resonance frequency, and H_{res} is the corresponding resonance field.

TABLE I. Structural parameters of (Nd,La)KNaNbO$_5$ obtained from the Rietveld refinement of the powder XRD data at room temperature [structure: tetragonal; space group: $P4/nmm$ (No. 129)]. Listed are the Wyckoff positions, refined atomic coordinates, and occupancies of each atom for NdKNaNbO$_5$ (upper lines) and LaKNaNbO$_5$ (lower lines).

Atom	Wyckoff position	x	y	z	Occ.
Nd/La	2b	0.75	0.25	0.5	1
Nb	2c	0.25	0.25	0.254(1)	1
	2c	0.25	0.25	0.253(6)	1
Na	2c	0.25	0.25	0.761(3)	1
	2c	0.25	0.25	0.751(3)	1
K	2a	0.75	0.25	0.00	1
	2a	0.75	0.25	0.00	1
O1	8j	0.017(5)	0.017(5)	0.317(9)	1
	8j	0.023(7)	0.023(7)	0.326(3)	1
O2	2c	0.25	0.25	0.024(2)	1
	2c	0.25	0.25	0.019(2)	1

For the zero-field inelastic neutron scattering (INS) experiment, we used the direct geometry time-of-flight (TOF) spectrometer MARI at the ISIS Facility, Rutherford Appleton Laboratory, United Kingdom. Powder samples with total mass 3.5 g of NKNNO and LKNNO were packed in an annular geometry inside Al cans, which were cooled using a top-loading closed cycle refrigerator. Data were recorded at 6 and 200 K using incident neutron energies $E_i = 14, 40$, and 100 meV and Gd chopper frequency 400 Hz. The three configurations gave elastic energy resolutions 0.3, 0.9, and 3 meV, respectively. The raw data were processed using the Mantid software [34].

III. RESULTS

A. Magnetization

Figure 3(a) presents the temperature-dependent magnetic susceptibility $\chi[\equiv M/H]$ of NKNNO measured at $\mu_0 H = 0.05$ and 1 T. No indication of magnetic LRO is observed down to 0.4 K. The inverse magnetic susceptibility, $1/\chi$, in the high-temperature region was well fitted by the modified Curie-Weiss (CW) law

$$\chi(T) = \chi_0 + \frac{C}{T - \theta_{\mathrm{CW}}}. \tag{1}$$

Here, χ_0 is the combination of temperature-independent core diamagnetic (χ_{dia}) and Van-Vleck paramagnetic (χ_{VV}) susceptibilities. In the second term, C is the Curie constant and θ_{CW} is the CW temperature. The CW fit for $T \geqslant 100$ K yields $\chi_0 \simeq 5.14 \times 10^{-4}$ cm^3/mol, $C^{\mathrm{HT}} \simeq 1.63$ cm^{3}K/mol, and $\theta_{\mathrm{CW}}^{\mathrm{HT}} \simeq -66$ K. From the C^{HT} value, the effective moment $\mu_{\mathrm{eff}}^{\mathrm{HT}}$ [$= \sqrt{(3k_B C^{\mathrm{HT}}/N_A)}\mu_B$, where N_A is the Avogadro's number, μ_B is the Bohr magneton, and k_B is the Boltzmann constant] is calculated to be $\sim 3.61\mu_B$, which is close to the expected value $3.62\mu_B$ for a free Nd^{3+} ion. Here, the large negative value of $\theta_{\mathrm{CW}}^{\mathrm{HT}}$ does not indicate the presence of strong AFM interactions. It rather reflects the effect of CEF excitations at high temperatures. At high temperatures, all Kramers doublets get thermally populated and contribute to θ_{CW}.

At low temperatures, $1/\chi$ changes its slope because of depopulation of crystal field energy levels. A CW fit to $1/(\chi - \chi_{\mathrm{VV}})$ in the low-T ($9\ \mathrm{K} \leqslant T \leqslant 22$ K) region results in $C^{\mathrm{LT}} \simeq 0.55$ cm^3 K/mol and $\theta_{\mathrm{CW}}^{\mathrm{LT}} \simeq -0.6$ K. The value of χ_{VV} is obtained from the magnetization isotherm analysis (discussed later). The negative value of $\theta_{\mathrm{CW}}^{\mathrm{LT}}$ suggests a weak AFM net interaction among the Nd^{3+} ions. The obtained C^{LT} value corresponds to an effective moment of $\mu_{\mathrm{eff}}^{\mathrm{LT}} \simeq 2.1\mu_B$. The reduced value of effective moment [$\mu_{\mathrm{eff}} = g\sqrt{J_{\mathrm{eff}}(J_{\mathrm{eff}}+1)}\mu_B$] at low-$T$s corresponds to pseudospin $J_{\mathrm{eff}} = 1/2$ with $g \simeq 2.45$, suggesting that the lowest Kramers' doublet is the ground state. As we shall see below, this g value matches with the one obtained from the ESR experiments at low-Ts.

In order to estimate the energy splitting between the ground state and first excited Kramers' doublets in the CEF scheme, $1/\chi(T)$ was also fitted by the effective two-level

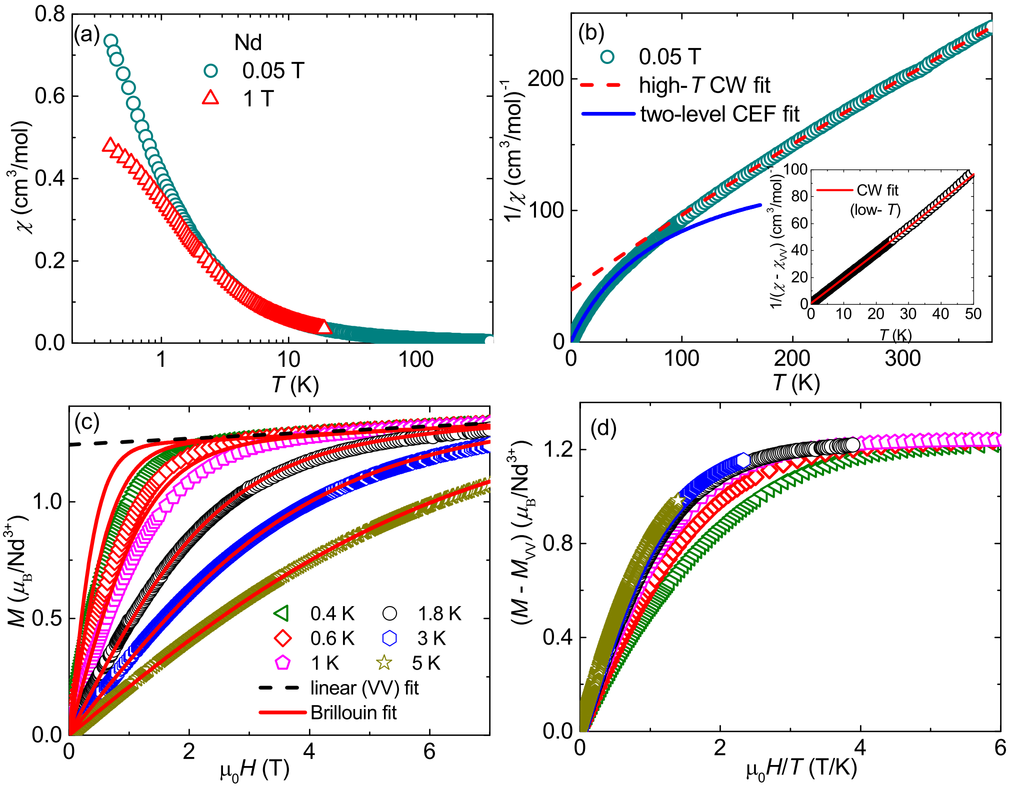

FIG. 3. (a) χ vs T of NKNNO measured at $\mu_0H = 0.05$ and 1 T. (b) $1/\chi$ vs T at $\mu_0H = 0.05$ T. The red dashed line is the high-T CW fit and the solid blue line indicates the two-level CEF fit. (Inset) $1/(\chi - \chi_{\rm VV})$ vs T and the solid line is CW fit in the low-T region. (c) M vs H at $T = 0.4$, 0.6, 1, 1.8 3, and 5 K. The dashed line represents a linear fit to the high-field data for $T = 0.4$ K. The solid lines represent the Brillouin function fits with $J_{\rm eff} = 1/2$ Nd^{3+} moment. (d) $(M - M_{\rm VV})$ vs μ_0H/T to visualize the scaling of magnetization curves.

CEF expression [35,36]

$$\chi(T) = \chi_0 + \frac{1}{8(T - \theta_{\rm CW})} \times \left[\frac{\mu_{\rm eff,0}^2 + \mu_{\rm eff,1}^2 e^{\left(-\frac{\Delta}{k_B T}\right)}}{1 + e^{\left(-\frac{\Delta}{k_B T}\right)}}\right]. \quad (2)$$

Here, $\Delta/k_{\rm B}$ is the energy difference between the ground state and the first excited CEF levels. $\mu_{\rm eff,0}$ and $\mu_{\rm eff,1}$ are the effective moments of the ground state and first excited CEF levels, respectively. The two-level CEF fit for $T \leqslant 20$ K yields $\chi_0 \simeq 7 \times 10^{-3}$ cm^3/mol, $\mu_{\rm eff,0} \simeq 2.06\mu_{\rm B}$/Nd^{3+}, $\mu_{\rm eff,1} \simeq 2.2\mu_{\rm B}$/Nd^{3+}, $\Delta/k_{\rm B} \simeq 18$ K, and $\theta_{\rm CW} \simeq -0.32$ K. It should be noted that this is a simple two-level model fit that neglects higher-lying Kramers doublets for a tentative estimation of the energy difference between ground and first excited states. Nevertheless, as we shall see the obtained χ_0 matches with $\chi_{\rm VV}$ and $\Delta/k_{\rm B}$ matches with the estimated gap between the ground state and first excited state doublets from INS data.

Isothermal magnetization curves (M vs μ_0H) measured at $T = 0.4$, 0.6, 1, 1.8, 3, and 5 K are shown in Fig. 3(c). The magnetization at 0.4 K almost saturates in a low field of around 2 T, which is consistent with the low $\theta_{\rm CW}^{\rm LT}$ value. A slow increase of magnetization in higher fields can be attributed to the Van-Vleck susceptibility ($\chi_{\rm VV}$). From the linear fit of the curve in the high-field region ($\mu_0H \geqslant 5.5$ T), we obtained a slope of around $\chi_{\rm VV} \simeq 0.0125\ \mu_B/T = 0.007$ cm^3/mol, which was used in the low-T $\chi(T)$ analysis presented above. The fit is extrapolated down to zero field and from the y-axis intercept, we obtained the saturation magnetization $M_{\rm S} \simeq 1.24\ \mu_{\rm B}$, which points towards $J_{\rm eff} = 1/2$ ground state with $g \simeq 2.48$. This value of g is also in close agreement with the ESR results, which will be presented below.

Magnetic isotherms at slightly higher temperatures ($T > 1$ K) can be modeled by the following expression [37]:

$$M(H) = \chi_{\rm VV}H + N_{\rm A}g\mu_{\rm B}J_{\rm eff}B_{J_{\rm eff}}(x). \quad (3)$$

Here, $B_{J_{\rm eff}}(x)$ is the Brillouin function, which can be written as $B_{J_{\rm eff}}(x) = \frac{(2J_{\rm eff}+1)}{2J_{\rm eff}}\coth[\frac{(2J_{\rm eff}+1)}{2J_{\rm eff}}x] - \frac{1}{2J_{\rm eff}}\coth(\frac{x}{2J_{\rm eff}})$ and $x = g\mu_{\rm B}J_{\rm eff}H/k_{\rm B}T$ [38]. For this fit, we fixed $J_{\rm eff} = 1/2$, $\chi_{\rm VV} \simeq 0.007$ cm^3/mol, and $g \simeq 2.47$ (obtained from ESR). For high temperatures ($T = 1.8$, 3, and 5 K), Eq. (3) fits well to the isotherms while below 1 K, the fit deviates significantly from the experimental data, signaling the emergence of magnetic correlations. To illustrate this feature more clearly, we plotted the Van-Vleck corrected M (i.e., $M - M_{\rm VV}$) vs μ_0H scaled with respect to the temperature in Fig. 3(d). For $T \geqslant 1$ K, all the $M - M_{\rm VV}$ vs μ_0H/T curves collapse onto a single curve, reflecting the paramagnetic nature of the spins. However, for $T < 1$ K the curves show clear deviation from this pattern, demonstrating the development of magnetic correlations on a temperature scale comparable to the low $\theta_{\rm CW}^{\rm LT}$ value.

B. Specific heat

The temperature-dependent specific heat $C_{\rm p}(T)$ of NKNNO measured down to 0.4 K and in different applied fields is shown in Fig. 4. In a magnetic insulator, the total

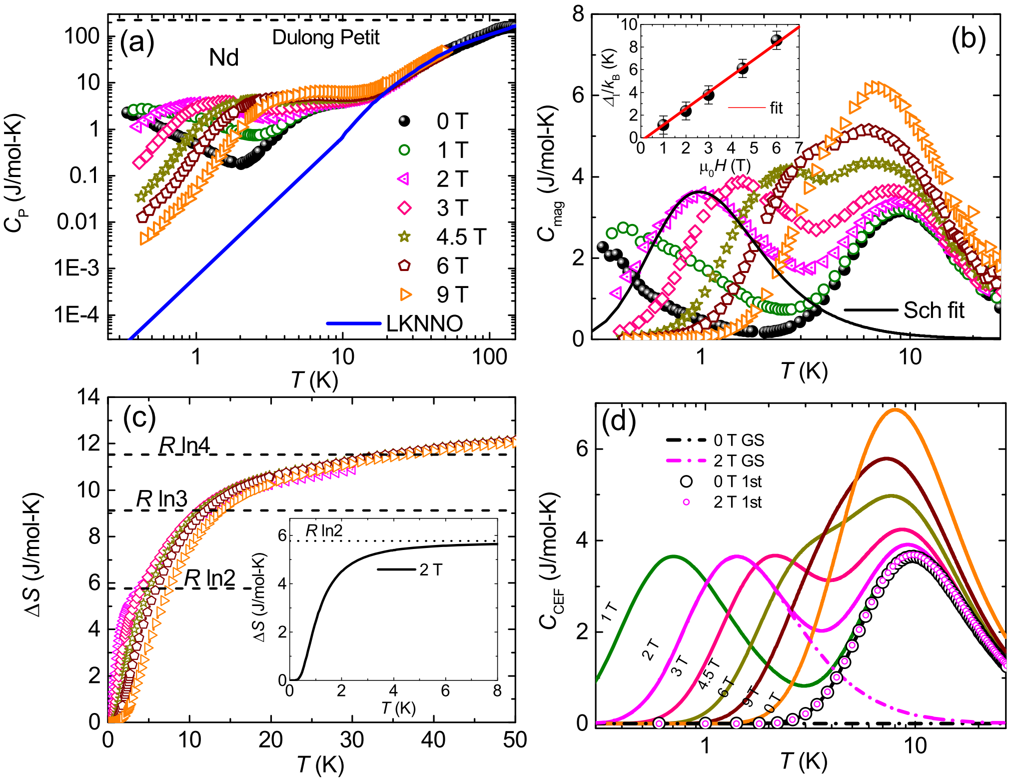

FIG. 4. (a) C_p vs T of NKNNO measured in different applied magnetic fields. The blue-solid line represents the phonon contribution (C_{ph}) of the nonmagnetic compound LKNNO. The horizontal-dashed line stands for the Dulong-Petit value $3nR$ (n is the number of atoms per formula unit). (b) C_{mag} vs T in different magnetic fields. The solid line is the Schottky fit using Eq. (4) to the 2 T data. (Inset) Δ_I vs H along with the linear fit. (c) Entropy change (ΔS) vs T in different magnetic fields. Inset: ΔS vs T associated with the broad maximum at T^{**} for the 2 T data. (d) Calculated C_{CEF} vs T in different magnetic fields, as discussed in the text. The solid lines represent C_{CEF} with contributions from the ground state and first excited state doublets in the CEF scheme. The dash-dotted lines and open circles separately show the contributions from ground-state excitations and excitations between the ground state and first excited states, respectively in zero field and $\mu_0 H = 2$ T.

specific heat $C_p(T)$ is the sum of the lattice contribution $[C_{ph}(T)]$, which dominates in the high-temperature region and the magnetic part $[C_{mag}(T)]$, which dominates in the low-temperature region. We estimated $C_{ph}(T)$ by measuring the zero-field specific heat of the non-magnetic isostructural compound LKNNO [see Fig. 4(a)] down to 2 K. The low-temperature specific heat data of LKNNO is fitted by βT^3 and further extrapolated down to 0.4 K. The estimated lattice specific heat of LKNNO was scaled with respect to NKNNO by taking the ratio of their atomic masses [39] and then subtracted from the total specific heat of NKNNO. The obtained $C_{mag}(T)$ at different fields is plotted in Fig. 4(b).

The zero-field C_{mag} shows a broad maximum at around $T^\star \sim 9$ K and an upturn at $T < 1$ K. The low-temperature upturn can be attributed to the buildup of short range magnetic correlations, since the value of θ_{CW}^{LT} is of the same order of magnitude. With increasing field, the position of the high-temperature maximum remains almost unchanged and another broad maximum ($T^{\star\star}$) appears at low temperature. The latter peak shifts to high temperatures with increasing field. Both peaks are also found to broaden with increasing field. In high magnetic fields ($\mu_0 H > 6$ T), the $T^\star$ and $T^{\star\star}$ peaks merge and form a single broad high-temperature peak. Similar behavior is reported for some Er^{3+} and Yb^{3+}-based compounds and ascribed to a multilevel Schottky effect due to the CEF levels and their splitting in applied fields [40–42]. As discussed later, the broad maximum at $T^{\star\star}$ corresponds to the transition between two Zeeman levels of the ground-state doublet while the peak at $T^\star$ represents the transitions between the ground state and first excited state doublets as well as among the excited state doublets [see Fig. 9(b) below].

The magnetic entropy $[\Delta S(T)]$ released at different fields, estimated by integrating C_{mag}/T over the entire temperature range is presented in Fig. 4(c). In zero field and 1 T, $\Delta S(T)$ could not be estimated reliably as our measurements down to 0.4 K could not reproduce the entire low-temperature anomaly. However, at $\mu_0 H = 2$ T where two broad maxima are distinctly visible, $\Delta S(T)$ features a plateau with $\Delta S \sim 5.7$ J mol^{-1} K^{-1} in the low-temperature regime before it attains a tendency of saturation to $\Delta S \sim Rln4 \sim 11.5$ J mol^{-1} K^{-1} (R is the universal gas constant) at high temperatures. Indeed, the value of $\Delta S \sim 5.7$ J mol^{-1} K^{-1} matches with $Rln2$, expected for a $J_{eff} = 1/2$ system. This further endorses that the ground state is governed by the lowest Kramers' doublet with $J_{eff} = 1/2$ [36]. The $\Delta S \sim 12$ J mol^{-1} K^{-1} value at 50 K is still smaller than the expected value for Nd^{3+} ($\sim Rln10 = 19.14$ J mol^{-1} K^{-1}) ion with $J = 9/2$.

In order to further confirm the $J_{eff} = 1/2$ ground state, the broad maximum at T^{**} in $C_{mag}(T)$ was fitted by the two-level

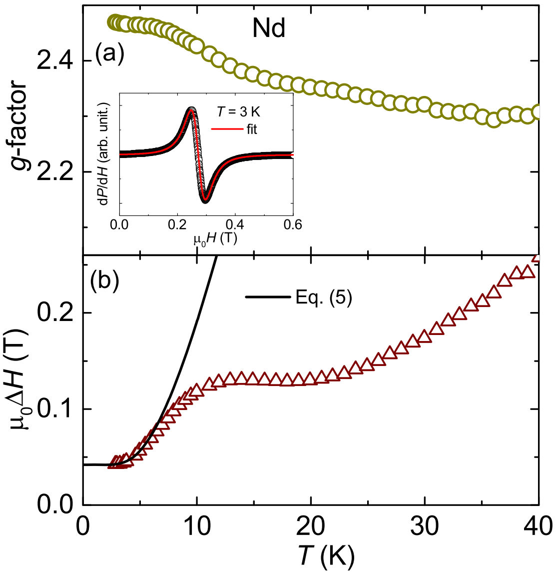

FIG. 5. (a) g factor as a function of temperature for NKNNO. (Inset) ESR spectra at $T = 3$ K. The solid line is a Lorentzian fit. (b) Temperature dependent ESR linewidth ($\mu_0\Delta H$). The solid line is the fit using Eq. (5).

Schottky function [38]

$$C_{\mathrm{Sch}}(T,H) = fR\left(\frac{\Delta_{\mathrm{I}}}{k_{\mathrm{B}}T}\right)^2 \frac{e^{\left(\frac{\Delta_{\mathrm{I}}}{k_{\mathrm{B}}T}\right)}}{\left[e^{\left(\frac{\Delta_{\mathrm{I}}}{k_{\mathrm{B}}T}\right)}+1\right]^2}. \tag{4}$$

Here, f is the molar fraction of free spins contributing to the Schottky anomaly and $\Delta_{\mathrm{I}}/k_{\mathrm{B}}$ is the energy gap between two Zeeman levels of the ground-state Kramers doublet. The fit of C_{mag} at 2 T in the temperature range 0.6–1.6 K yields $f \simeq 1$ and $\Delta_{\mathrm{I}}/k_{\mathrm{B}} \simeq 2.4$ K. We then extrapolated the fit from 0.4 to 30 K, as shown in Fig. 4(b). The calculated entropy corresponding to the maximum at T^{**} saturates to a value $\sim R\ln 2$ at around 6 K [see the inset of Fig. 4(c)], reflecting Kramers' doublet ground state with $J_{\mathrm{eff}} = 1/2$. The value $\Delta_{\mathrm{I}}/k_{\mathrm{B}}$ obtained in different fields is shown in the inset of Fig. 4(b). As expected, $\Delta_{\mathrm{I}}/k_{\mathrm{B}}$ varies linearly with field and a straight line fit ($\Delta_{\mathrm{I}} = \Delta_0 + g\mu_{\mathrm{B}}H$) [43] yields $g \simeq 2.3$, consistent with the ESR results. A fit using Eq. (4) to the second broad maximum at T^* results in no change in the gap ($\Delta_{\mathrm{II}} \sim 21$ K) value with field.

C. ESR

The results of ESR measurements on NKNNO are presented in Fig. 5. The inset of Fig. 5(a) illustrates a typical ESR spectrum at $T = 3$ K. We fitted the spectra at different temperatures using a powder-averaged Lorentzian line shape. The fit reproduces the spectral shape very well at $T = 3$ K, yielding an average low-temperature g-factor of $g \simeq 2.47$. As shown in Fig. 5(a), the g value decreases slowly with increasing temperature and attains a constant value of 2.32 above 30 K. Figure 5(b) presents the ESR linewidth as a function temperature. It depicts a broad maximum at ~10 K that matches with T^* observed in specific heat, mimicking the crystal field excitations.

Below the broad maximum, the relaxation (ΔH) can be fitted by [44]

$$\Delta H \propto \frac{1}{e^{\Delta^{\mathrm{esr}}/k_{\mathrm{B}}T} - 1}. \tag{5}$$

Here, $\Delta^{\mathrm{esr}}/k_{\mathrm{B}}$ represents the energy gap in the CEF scheme. This exponential behavior implies the spin-lattice relaxation process is dominated by an Orbach process due to the CEF [45]. Through SOC, this process involves a phonon absorption to and emission from a CEF energy level. The fit in the low-temperature regime (2.8–5 K) returns $\Delta^{\mathrm{esr}}/k_{\mathrm{B}} \simeq 22.2$ K, which is consistent with the energy gap (2.1 meV) between the ground and first excited doublets observed in the INS data.

D. Inelastic neutron scattering

Figure 6 presents the color plots of the INS spectra of NKNNO and LKNNO measured using neutrons of incident energy $E_{\mathrm{i}} = 40$ meV at temperatures $T = 6$ and 200 K and $E_{\mathrm{i}} = 14$ meV at $T = 6$ K [46]. For NKNNO, we observed a broad band of excitations around 20 meV, which are more pronounced at low temperature ($T = 6$ K) than at elevated temperatures and decrease in intensity with increasing Q, as we shall show below. Furthermore, no low-Q excitations are observed for the nonmagnetic analog compound LKNNO. These observations are consistent with a magnetic origin for the 20 meV excitation band in NKNNO. Given that the energy resolution for the chosen experimental setup is 0.9 meV, which is smaller than the width of the excitation band, we interpret it as arising from a group of closely spaced crystal field excitation, each of which is dispersionless, because CEF excitations are single-ion properties. In order to extract these high-energy CEF excitations from the background due to phonon scattering, we subtracted the INS spectra of nonmagnetic LKNNO in which the excitations are purely phononic, from the spectra of NKNNO. Figure 7 depicts the resulting phonon-subtracted INS spectra of NKNNO at $T = 6$ and 200 K. The intensity of the CEF excitations near 2 and 20 meV decreases with increasing Q $(= |\vec{Q}|)$, as expected because of the magnetic form-factor [$F(Q)$] in the neutron scattering cross section. We calculated $F^2(Q)$ for Nd^{3+} ion using the dipole approximation (see Appendix A for details on the magnetic cross section and the magnetic form factor) and compared with the experimental INS intensity in Fig. 8(a). The calculated intensity decreases monotonously with increasing Q and reproduces the experimental data very well at $T = 6$ K. The intensity of the CEF excitations furthermore diminishes with rising temperature due to thermal broadening and because of depopulation of the ground-state Kramers' doublet.

For a clear visualization of the CEF modes and to fit the INS data, we created a 2D plot of intensity versus energy transfer by integrating the phonon subtracted INS data in the wave vector $0 \leqslant Q \leqslant 3$ Å^{-1} regime, as shown in Figs. 7(c) and 7(d) for $T = 6$ K and 200 K, respectively. The observed strong signal at $\hbar\omega = 0$ meV corresponds to the quasielastic neutron scattering. In addition, we observed four CEF excitations for $T = 6$ K at around 2.3, 19.2, 20.9, and 22.6 meV

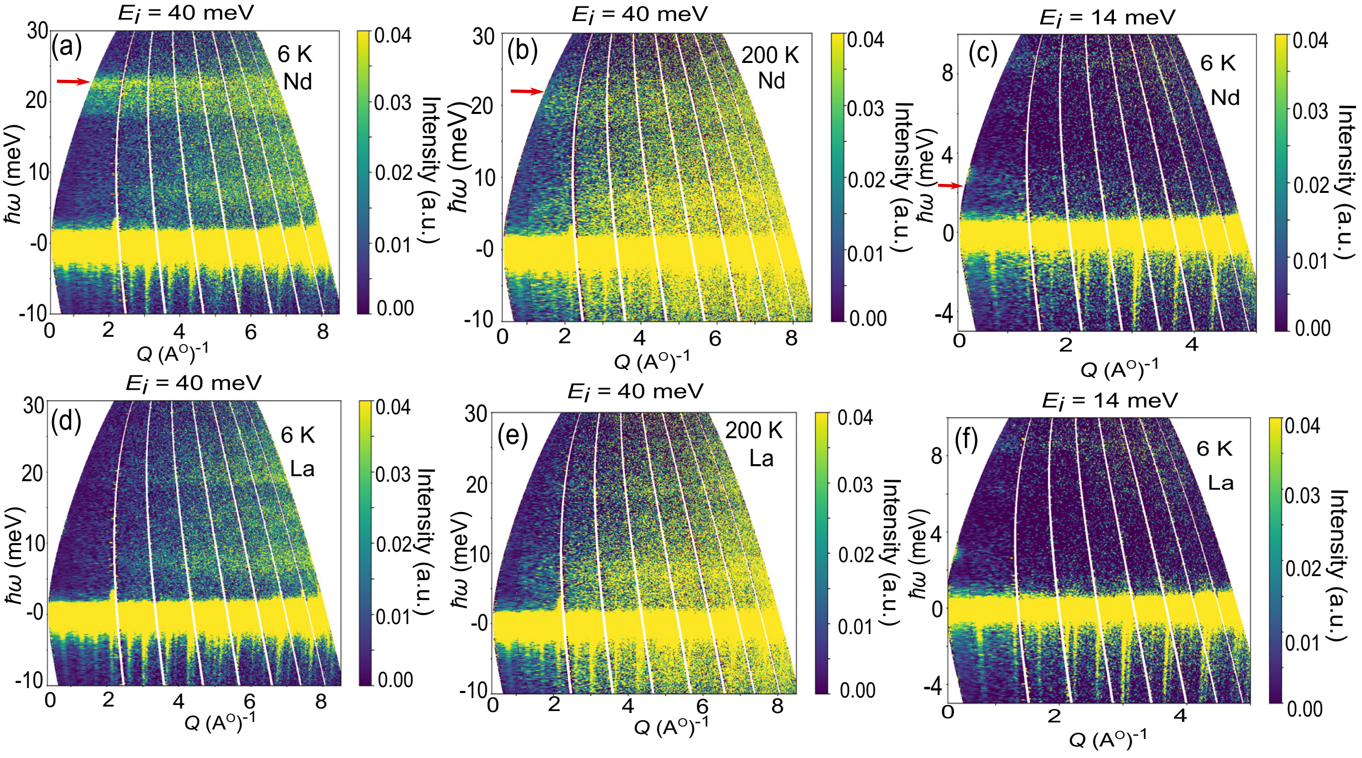

FIG. 6. Raw INS spectra $S(Q, \omega)$ of (a), (b) NKNNO and (d), (e) LKNNO (intensity as a function of energy and momentum transfers) at two different temperatures for $E_{\mathrm{i}} = 40$ meV. The red arrows indicate the high-energy CEF excitations in the NKNNO spectra. Raw INS spectra of (c) NKNNO and (f) LKNNO at $T = 6$ K for $E_i = 14$ meV. We note that for both these data sets, there is a feature at $Q \sim 0.37$ (Å)$^{-1}$ and $\hbar\omega \sim 3$ meV, which is ascribed to a spurious instrumental artefact. The red arrow marks the faint CEF excitations at around 2.1 meV, discussed in the text.

with the 2.3 meV excited Kramers doublet appearing as a weak but distinct shoulder on the dominant quasielastic signal [see inset of Fig. 7(c)]. There exists a weak low-energy mode in the spectra obtained with $E_i = 14$ meV for which the energy resolution is 0.3 meV [see Fig. 6(c)]. The inset of Fig. 7(c) shows the low-energy peak cleanly separated from the $\hbar\omega = 0$ peak. The momentum dependence of the low-energy excitations shown in Fig. 8(a) confirms its magnetic origin. In the low-temperature spectrum ($T = 6$ K), no peaks are observed near -20 meV in the negative energy transfer regions (reflecting transitions from excited state Kramers doublet to the ground-state doublet) at low temperatures. On the other hand, in the high-temperature ($T = 200$ K) spectrum, the increasing thermal population of excited CEF levels implies that such transitions become allowed and are observed as low-intensity peaks at negative energy transfers [47]. Figure 8(b) was produced using neutrons with higher incident energy $E_{\mathrm{i}} = 100$ meV and shows that at $T = 6$ K there are no additional high-energy CEF transitions for energy transfers up to $\hbar\omega = 65$ meV. Therefore, we used only the INS spectra corresponding to $E_{\mathrm{i}} = 40$ meV for the CEF analysis.

E. CEF analysis

The INS intensity versus energy transfer data can be analyzed using the CEF Hamiltonian. According to the Stevens convention, the CEF Hamiltonian can be written as [48]

$$\mathcal{H}_{\mathrm{CEF}} = \sum_{l,m} B_l^m \hat{O}_l^m. \tag{6}$$

Here, $\hat{O}_l^m$ are the Stevens operators [48,49], which are related to the angular momentum operators (see Appendix B). B_l^m are the multiplicative factors called CEF parameters, which are related to the electronic structure of the rare-earth materials (see Appendix B). Here, the even integer l varies from 0 to 6 for f electrons and the integer m ranges from $-l$ to l. In NKNNO, Nd^{3+} ion has a C_{4v} symmetric crystal field environment, which indicates that only five CEF parameters (B_2^0, B_4^0, B_6^0, B_4^4, and B_6^4) are nonzero [49]. Therefore, the CEF model Hamiltonian can be expressed as

$$\mathcal{H}_{\mathrm{CEF}} = B_2^0\hat{O}_2^0 + B_4^0\hat{O}_4^0 + B_4^4\hat{O}_4^4 + B_6^0\hat{O}_6^0 + B_6^4\hat{O}_6^4. \tag{7}$$

As presented in Figs. 7(c) and 7(d), we fitted the 6 K and 200 K data simultaneously using the above CEF model with the help of Mantid software [34,50]. For this fit, we used the starting CEF parameters of the point-charge model where we assumed that the surrounding ligands are electrostatic point charges [49]. The obtained best-fit CEF parameters that determine the correct CEF Hamiltonian of this system are tabulated in Table II.

Next, we diagonalized the Hamiltonian and obtained the CEF energy eigenvalues of the compound. The obtained energy eigenvalues are 0, 2.11, 19.22, 20.92, and 22.7 meV, corresponding to five doublets, as depicted in Fig. 9. The peaks observed in the INS data at $T = 6$ K [Fig. 7(c)] correspond to the transitions I, II, III, and IV, respectively between the ground state and excited states [51].

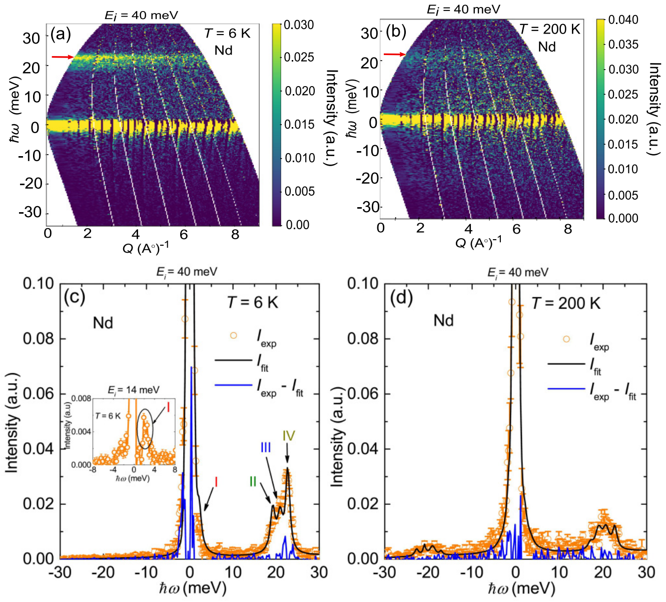

FIG. 7. INS spectra $S(Q,\omega)$ of NKNNO at (a) $T = 6$ K and (b) $T = 200$ K, after subtracting the phonon scattering contribution as discussed in the main text. The red arrow indicates the high-energy CEF excitations. The INS spectral intensity as a function of energy transfer at (c) $T = 6$ K and (d) $T = 200$ K, obtained by integrating intensity in the low wave vector $0 \leqslant Q \leqslant 3$ Å^{-1} regime. The arrows point to the CEF modes (I, II, III, and IV). Black solid line is the corresponding fit using the CEF Hamiltonian. Blue-solid line represents the difference between the observed and fitted intensities. Inset of (c): INS intensity vs energy transfer data at $T = 6$ K for $E_i = 14$ meV after subtracting the phonon contribution. The arrow marks the CEF excitations at around 2 meV.

From the CEF Hamiltonian [Eq. (7)], the wave functions corresponding to all the Kramers' doublets can be expressed as

$$|\psi_k, \pm\rangle = \sum_{m_J=-\frac{9}{2}}^{m_J=\frac{9}{2}} C_{m_J}^{k,\pm}\left|J = \frac{9}{2}, m_J\right\rangle. \tag{8}$$

Here, $C_{m_J}^{k,\pm}$ are the weighted coefficients of the eigenstates. The full list of energy eigenvalues and the corresponding coefficients ($C_{m_J}^{k,\pm}$) of different eigenstates for NKNNO are listed in Table III. The wave function of the ground-state doublet (lowest-energy doublet) is obtained to be

$$|\psi_0, \pm\rangle = \pm 0.749\left|\mp\frac{1}{2}\right\rangle \mp 0.045\left|\pm\frac{7}{2}\right\rangle \mp 0.661\left|\mp\frac{9}{2}\right\rangle. \tag{9}$$

TABLE II. Fitted CEF parameters for NKNNO.

B_l^m (meV)	Values
B_2^0	8.087×10^{-2}
B_4^0	-1.772×10^{-3}
B_4^4	-5.451×10^{-3}
B_6^0	-3.835×10^{-5}
B_6^4	1.766×10^{-3}

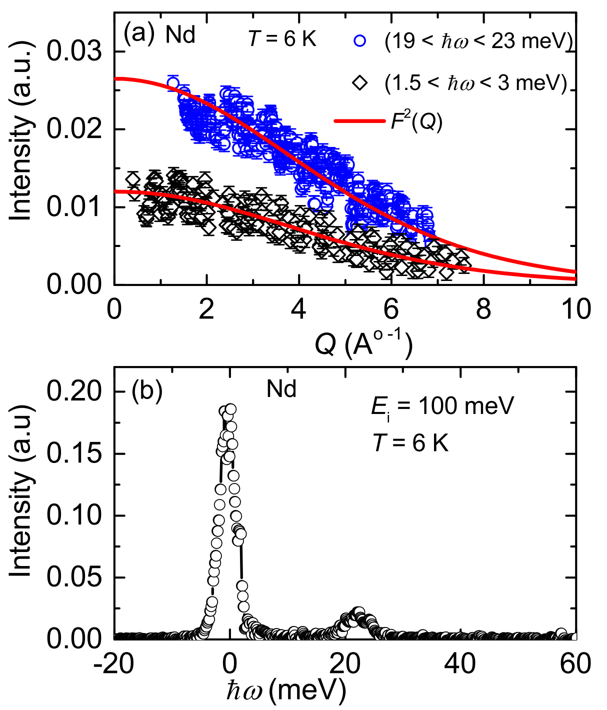

FIG. 8. (a) Q dependence of INS intensity at $T = 6$ K, obtained by integrating in the transfer energy range 19-23 meV and 1.5–3 meV for the $E_i = 40$ meV data. The red-solid lines are the square of magnetic form-factor [$F^2(Q)$] of Nd^{3+} ion. (b) The INS intensity versus energy transfer spectrum of NKNNO with $E_i = 100$ meV at $T = 6$ K, after subtracting the phonon part for the wave-vector range $0 \leqslant Q \leqslant 3$ Å^{-1}.

Similarly, one can obtain the wavefunctions of the higher-energy doublets by inserting the appropriate coefficients from Table III into Eq. (8).

In the absence of magnetic correlations, the thermodynamic properties at low temperatures are expected to be influenced significantly by the low-energy CEF excitations. In NKNNO, because of a small energy gap between the ground state and the first excited states, these CEF levels are expected to dominate the low-temperature specific heat as observed in NaYbSe$_2$ [42] and KErTe$_2$ [41]. To study the effect of CEF excitations on specific heat, we calculated single-ion specific heat [$C_{\mathrm{CEF}}(T)$] at different magnetic fields (see Appendix C) using the energy eigenvalues in Table II and taking into account the Zeeman splitting of the CEF levels [see Fig. 9(b)]. Here, we have taken $g \simeq 2.47$. The calculated results are presented in Fig. 4(d). In zero field, there is only one transition from ground-state doublet to the first excited state doublet, and the calculations yield a broad maximum in C_{CEF} at around ~9 K. The CEF contribution to the specific heat approaches zero below about 2.4 K in contrast to the low-temperature upturn observed in the experimental C_{mag}. This suggests that the low-temperature upturn in zero-field C_{mag} originates from spin-exchange interactions.

When the magnetic field is applied, the ground state and the first excited state doublets split further and become a four-level system. All the possible transitions between the energy levels are shown in Fig. 9(b). The calculated C_{CEF} results in two broad maxima reproducing our experimental $C_{\mathrm{mag}}(T)$. At

TABLE III. Energy eigenvalues and the coefficients ($C_{m_J}^{k,\pm}$) corresponding to different eigenstates of the CEF Hamiltonian for NKNNO.

E (meV)	$\|-\frac{9}{2}\rangle$	$\|-\frac{7}{2}\rangle$	$\|-\frac{5}{2}\rangle$	$\|-\frac{3}{2}\rangle$	$\|-\frac{1}{2}\rangle$	$\|\frac{1}{2}\rangle$	$\|\frac{3}{2}\rangle$	$\|\frac{5}{2}\rangle$	$\|\frac{7}{2}\rangle$	$\|\frac{9}{2}\rangle$
0.00	–0.661	0	0	0	0.749	0	0	0	–0.045	0
0.00	0	0.045	0	0	0	–0.749	0	0	0	0.661
2.11	0	0	0	–0.764	0	0	0	–0.644	0	0
2.11	0	0	–0.644	0	0	0	–0.764	0	0	0
19.22	0	0.973	0	0	0	–0.117	0	0	0	–0.1982
19.22	–0.1982	0	0	0	–0.117	0	0	0	0.973	0
20.92	0	0	–0.764	0	0	0	0.644	0	0	0
20.92	0	0	0	–0.644	0	0	0	0.764	0	0
22.70	0	–0.225	0	0	0	–0.652	0	0	0	–0.723
22.70	–0.723	0	0	0	-0.652	0	0	0	–0.225	0

$\mu_0 H = 1$ T, the low-temperature maximum at $T^{**} \sim 0.5$ K is caused by the transition between the Zeeman levels in the ground-state doublet. The high-temperature maximum at $T^{*} \sim 9$ K can be attributed to the superposition of transitions between the ground state and the first excited state doublets as well as the transitions among the split excited state doublets. With increasing field, the maximum at T^{**} moves towards high temperatures while the one at T^{*} remains temperature independent but with an increasing line broadening, consistent with the experimental $C_{\mathrm{mag}}(T)$ data. In Fig. 4(d), we have also separately shown the contributions from excitations of the Zeeman split ground-state doublet and superposition of excitations among the Zeeman split ground state and first excited state doublets at $\mu_0 H = 2$ T to highlight that they correspond to the low-T and high-T broad maxima, respectively. Please note that the remaining CEF energy levels (19.2, 20.9, and 22.7 meV) are much higher in energy than the ground state and first excited state. Therefore, the contributions from these higher CEF levels are negligible within our measured temperature range.

For a comparison with the experimental data, we made a 2D contour plot of $C_{\mathrm{CEF}}(T, H)$ and plotted T^{*} and T^{**} vs H in Fig. 10. The magnetic field variation of T^{*} and T^{**} obtained from the calculations match with that obtained from the experimental $C_{\mathrm{mag}}(T)$ data. A small difference in the values of T^{*} and T^{**} from the experiment and theory could be caused by the presence of a weak magnetic exchange interaction between the Nd^{3+} ions that is neglected in our calculations.

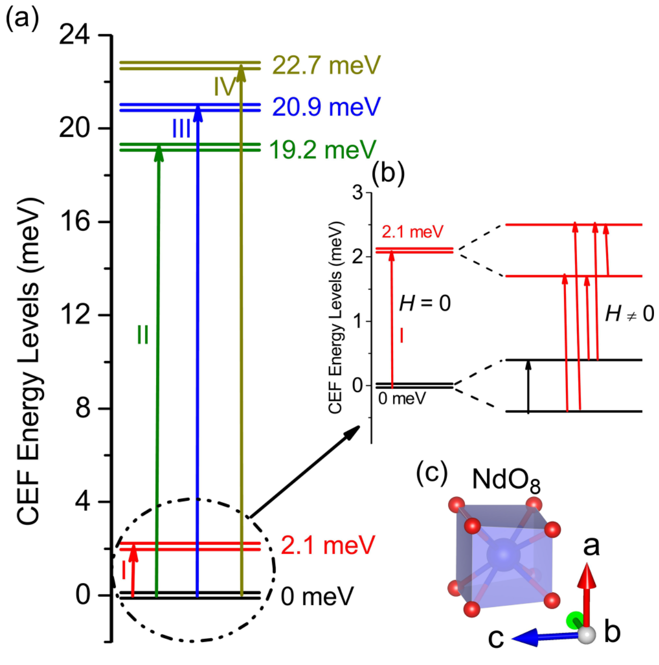

FIG. 9. (a) Schematic representation of CEF excitation energy levels (0, 2.11, 19.22, 20.92, and 22.7 meV) obtained from the zero-field INS data. The arrows indicate the CEF transitions between the states corresponding to the peaks observed in the INS data at $T = 6$ K. (b) Zeeman splitting of the ground and the first excited Kramers' doublets. (c) Distorted NdO_8 cube formed by Nd^{3+} ion that generates CEF.

IV. DISCUSSION

We studied the ground-state properties of an unexplored rare-earth-based FSL system NKNNO through thermodynamic and INS measurements. The low-T value of $\theta_{\mathrm{CW}}^{\mathrm{LT}} \simeq -0.6$ K indicates a weak AFM interaction between the

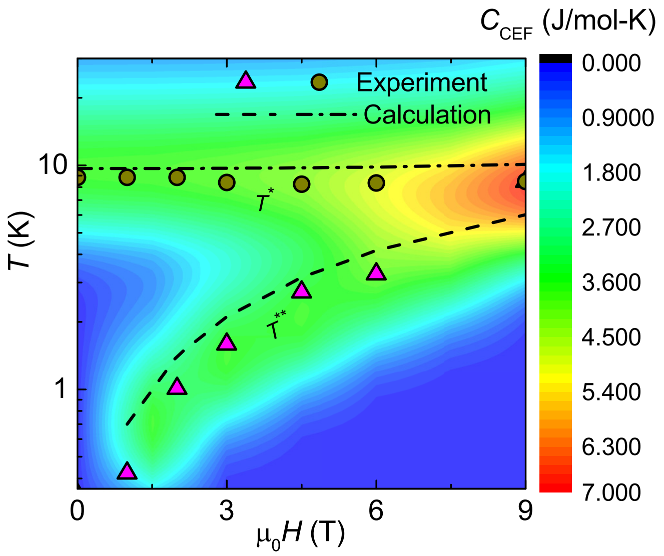

FIG. 10. 2D contour plot of C_{CEF} with field and temperature. On top of this plot, T^{*} and T^{**} obtained from the experimental C_{mag} (symbols) [from Fig. 4(b)] and calculated C_{CEF} (dashed line) [from Fig. 4(d)] are shown.

Nd^{3+} ions. The dipolar magnetic interaction of the system is calculated to be $E_{\mathrm{dip}} \simeq \frac{\mu_0 g^2 \mu_{\mathrm{B}}^2 J_{\mathrm{eff}}^2}{4\pi d^3} \simeq 0.015$ K [52]. Here, $d = a/\sqrt{2} \simeq 4.05$ Å is the distance between NN Nd^{3+} ions, μ_0 is the permeability of free space, $J_{\mathrm{eff}} = 1/2$, and $g \simeq 2.47$. This value of dipolar coupling is about one order of magnitude smaller than $\theta_{\mathrm{CW}}^{\mathrm{LT}}$, suggesting that the magnetic exchange interaction dominates over the dipole-dipole interaction. No magnetic LRO sets in down to 0.4 K possibly because of the magnetic frustration and/or two-dimensional geometry of the spin lattice. The magnetization and specific heat data indicate that the ground state is pseudospin-1/2 ($J_{\mathrm{eff}} = 1/2$). Typically, for compounds with $J_{\mathrm{eff}} = 1/2$ ground state, the dimensionless ratio should have a value $R \equiv (\frac{\mu_{\mathrm{eff}}}{\mu_{\mathrm{sat}}})^2 = 3$. This squared moment ratio for NKNNO in the low-T regime is estimated to be $R_{\mathrm{exp}} \simeq 3.06$, which confirms that the lowest Kramers' doublet with $J_{\mathrm{eff}} = 1/2$ is the ground state [53]. From the CEF energy diagram, the energy gap between the ground state and first excited state doublets is found to be about ~25 K (~2.1 meV). Hence, it is indeed expected that below this temperature scale, the lowest Kramers' doublet with $J_{\mathrm{eff}} = 1/2$ should be manifested as the ground state of the compound.

As discussed above, the wave functions [Eq. (9)] of the ground-state doublet are the linear combinations of $|\pm\frac{1}{2}\rangle$, $|\pm\frac{7}{2}\rangle$, and $|\pm\frac{9}{2}\rangle$ states. The weight factors of $|\pm\frac{1}{2}\rangle$ and $|\pm\frac{9}{2}\rangle$ are found to be larger compared to that of $|\pm\frac{7}{2}\rangle$. Thus, the obtained large coefficient of $|\pm\frac{1}{2}\rangle$ in the CEF ground-state wave function implies that the raising (J_+) and lowering (J_-) operators set a very high probability of quantum tunneling between these two states. At the same time, a significant value of the coefficient of $|\pm\frac{9}{2}\rangle$ also indicates the classical nature of the ground state. Nevertheless, the sizable contribution from $|\pm\frac{1}{2}\rangle$ to the ground-state doublet might facilitate strong quantum effects in NKNNO and hence QSL at low temperatures. Our findings are similar to that reported for the other rare-earth-based magnets (Na,K,Cs)Er(S,Se)$_2$ [16,54].

V. SUMMARY

We present the experimental study of an Nd^{3+}-based FSL compound NKNNO via magnetization, specific heat, ESR, and INS measurements. It shows the development of magnetic correlations below ~1 K in zero field though no magnetic LRO is detected down to 0.4 K, consistent with the low CW temperature obtained from the $\chi(T)$ analysis. Zero-field specific heat data manifest a single broad maximum at $T^* \simeq 9$ K because of CEF excitations and a low-temperature upturn, reminiscent of magnetic correlations. An external magnetic field suppresses the weak-magnetic correlations and produces two broad maxima in the low-temperature regime, mimicking the excitations among the Zeeman split low-energy CEF doublets. INS experiments reveal transitions between the CEF levels, enabling the fitting of CEF parameters to the energies and intensities of these modes. The ground-state doublet has a significant $J_z = \pm 1/2$ component in the wave function, which indicates the strong quantum effects in this compound at low temperatures. The small energy gap between the ground state and first excited state of the CEF levels favours Kramers' doublet with $J_{\mathrm{eff}} = 1/2$ ground state at low temperatures, consistent with the findings from magnetization and specific heat data. Finally, using the CEF energy eigenvalues obtained from INS and g value from ESR experiments we computed $C_{\mathrm{CEF}}(T)$ in different fields, which reproduce the positions of the broad maxima in experimental specific heat. This is a clear demonstration of the effect of CEF excitations in the low-temperature specific heat data. To determine whether NKNNO develops magnetic LRO or displays more exotic QSL or spin nematic behavior at $T = 0$, measurements at temperatures lower than 0.4 K are required.

ACKNOWLEDGMENTS

S.G. and R.N. would like to acknowledge SERB, India for financial support bearing sanction Grant No. CRG/2022/000997. S.G. was supported by the Prime Minister's Research Fellowship (PMRF) scheme and SERB (ITS), Government of India. N.B.C. was supported by the Danish National Committee for Research Infrastructure (NUFI) through the ESS-Lighthouse Q-MAT and by the Danish Agency for Science, Technology, and Innovation through the instrument center Danscatt. Experiments at the ISIS Neutron and Muon Source were supported by a beamtime allocation RB2310534 from the Science and Technology Facilities Council (STFC).

APPENDIX A

The intensity recorded in a neutron scattering experiment is simply the partial differential scattering cross section $\frac{d^2\sigma}{d\omega d\Omega}$ convolved with the instrumental resolution function. For a powder sample, the contribution from CEF level transitions from an initial state $|\psi_i\rangle$ of energy E_i^{CEF} to a final state $|\psi_f\rangle$ of energy E_f^{CEF} can be written as [47]

$$\frac{d^2\sigma}{d\omega d\Omega} = \frac{k_f}{k_i} S(Q, \omega). \tag{A1}$$

where $\mathbf{k}_i$ and $\mathbf{k}_f$ are the wave vectors of the incident and scattered neutrons and the dynamic structure factor is given by

$$S(Q, \omega) = CF^2(Q) e^{-2W(Q)} \sum_{\alpha = x,y,z} \sum_{i,f} p_i |\langle\psi_f|\hat{J}_\alpha|\psi_i\rangle|^2 \times \delta(\hbar\omega + E_i - E_f). \tag{A2}$$

Here, C is a numerical constant, and the transitions between the CEF levels are caused by angular momentum operators $\hat{J}_\alpha$ ($\alpha = x, y, z$) giving rise to peaks in the spectrum when the neutron energy transfer to the sample $E_i^n - E_f^n = \hbar\omega$ equals the difference between CEF levels $E_f - E_i$. The factor $p_i = e^{-\frac{E_i}{k_B T}} / \sum_i e^{-\frac{E_i}{k_B T}}$ reflects the thermal occupation probability for the initial CEF state. The factor $F(Q)$ is the magnetic form factor reflecting the spatial extent of the spin density. In the dipole approximation [47], one can write $F(Q) = \langle j_0(Q)\rangle + \frac{2-g_J}{g_J}\langle j_2(Q)\rangle = [\sum_i A_i e^{-a_i Q^2} + D] + \frac{2-g_J}{g_J}[\sum_i A_i' Q^2 e^{-a_i' Q^2} + D' Q^2]$, where, A_i, A_i', a_i, a_i', D, and D' are the magnetic form factor coefficients. These coefficients for Nd^{3+} ion are tabulated in Ref. [55]. Finally, $e^{-2W(Q)}$ is the Debye-Waller factor coming from the thermal motion of the magnetic ion. At low temperatures, the thermal motion of the ion is negligible. Therefore, one can neglect the Q dependence of the Debye-Waller factor at low temperatures [i.e., $e^{-2W(Q)} \simeq 1$].

APPENDIX B

Steven operators in Eq. (7) can be expressed in terms of angular momentum operators J_+, J_-, and J_z as [56]

$$\hat{O}_2^0 = \left[3J_z^2 - X\right],$$

$$\hat{O}_4^0 = \left[35J_z^4 - (30X - 25)J_z^2 + 3X^2 - 6X\right],$$

$$\hat{O}_4^4 = \tfrac{1}{2}[J_+^4 + J_-^4], \tag{B1}$$

$$\hat{O}_6^0 = \left[231J_z^6 - (315X - 735)J_z^4 \right. \tag{B2}$$

$$\left. + (105X^2 - 525X + 294)J_z^2 - 5X^3 + 40X^2 - 60X\right], \tag{B3}$$

$$\hat{O}_6^4 = \tfrac{1}{4}\left[(J_+^4 + J_-^4)(11J_z^2 - X - 38) + \right. \tag{B4}$$

$$\left. (11J_z^2 - X - 38)(J_+^4 + J_-^4)\right]. \tag{B5}$$

Here, $X = J(J+1)$.

According to the point charge model, the CEF parameters (B_l^m) in Eq. (7) can be written as [34,57]

$$B_l^m = \frac{4\pi}{2l+1} \times \frac{|e|^2}{4\pi\epsilon_0} \sum_i \frac{q_i}{r_i^{l+1}} a_0^l \langle r^l \rangle Z_l^m(\theta_i, \phi_i). \tag{B6}$$

where q_i is the charge of the ith point charge, r_i, θ_i, and ϕ_i are the relative polar coordinates of the ith point charge from the magnetic ion. a_0 is the Bohr radius and $\langle r^l \rangle$ is the lth order expectation value of the radial wave function of the magnetic ion.

APPENDIX C

Specific heat (C_{CEF}) for a N level system can be written as

$$C_{\text{CEF}}(N) = R\beta^2 \frac{1}{Z^2} \sum_{j>i}^{N} (E_j - E_i)^2 e^{-(E_i+E_j)\beta}, \tag{C1}$$

where R is the universal gas constant, $\beta = \frac{1}{k_B T}$, and $Z(=\sum_i e^{-\frac{E_i}{k_B T}})$ is the partition function. For NKNNO, in zero field, the ground-state doublet is separated from the first excited state doublet by an energy gap Δ (~2.11 meV). In the presence of a magnetic field, these doublets are split into four energy levels. Therefore, in the calculations shown in Fig. 4(d), we have taken $N = 4$.

---

[1] L. Savary and L. Balents, Quantum spin liquids: A review, Rep. Prog. Phys. **80**, 016502 (2017).

[2] L. Wang and A. W. Sandvik, Critical level crossings and gapless spin liquid in the square-lattice spin-1/2$J_1 - J_2$ Heisenberg antiferromagnet, Phys. Rev. Lett. **121**, 107202 (2018).

[3] N. Shannon, T. Momoi, and P. Sindzingre, Nematic order in square lattice frustrated ferromagnets, Phys. Rev. Lett. **96**, 027213 (2006).

[4] R. Nath, Y. Furukawa, F. Borsa, E. E. Kaul, M. Baenitz, C. Geibel, and D. C. Johnston, Single-crystal ^{31}P NMR studies of the frustrated square-lattice compound $Pb_2(VO)(PO_4)_2$, Phys. Rev. B **80**, 214430 (2009).

[5] R. Nath, A. A. Tsirlin, H. Rosner, and C. Geibel, Magnetic properties of $BaCdVO(PO_4)_2$: A strongly frustrated spin-$\frac{1}{2}$ square lattice close to the quantum critical regime, Phys. Rev. B **78**, 064422 (2008).

[6] S. Guchhait, D. V. Ambika, Q.-P. Ding, M. Uhlarz, Y. Furukawa, A. A. Tsirlin, and R. Nath, Deformed spin-$\frac{1}{2}$ square lattice in antiferromagnetic $NaZnVOPO_4(HPO_4)$, Phys. Rev. B **106**, 024426 (2022).

[7] P. Babkevich, V. M. Katukuri, B. Fåk, S. Rols, T. Fennell, D. Pajić, H. Tanaka, T. Pardini, R. R. P. Singh, A. Mitrushchenkov, O. V. Yazyev, and H. M. Rønnow, Magnetic excitations and electronic interactions in Sr_2CuTeO_6: A spin-1/2 square lattice Heisenberg antiferromagnet, Phys. Rev. Lett. **117**, 237203 (2016).

[8] M. Watanabe, N. Kurita, H. Tanaka, W. Ueno, K. Matsui, T. Goto, and M. Hagihala, Contrasting magnetic structures in $SrLaCuSbO_6$ and $SrLaCuNbO_6$: Spin-$\frac{1}{2}$ quasi-square-lattice $J_1 - J_2$ Heisenberg antiferromagnets, Phys. Rev. B **105**, 054414 (2022).

[9] A. A. Tsirlin, B. Schmidt, Y. Skourski, R. Nath, C. Geibel, and H. Rosner, Exploring the spin-$\frac{1}{2}$ frustrated square lattice model with high-field magnetization studies, Phys. Rev. B **80**, 132407 (2009).

[10] O. Mustonen, S. Vasala, K. P. Sadrollahi, E. Schmidt, C. Baines, H. C. Walker, I. Terasaki, F. J. Litterst, E. Baggio-Saitovitch, and M. Karppinen, Spin-liquid-like state in a spin-1/2 square-lattice antiferromagnet perovskite induced by d^{10}–d^0 cation mixing, Nat. Commun. **9**, 1085 (2018).

[11] A. A. Tsirlin and H. Rosner, Extension of the spin-$\frac{1}{2}$ frustrated square lattice model: The case of layered vanadium phosphates, Phys. Rev. B **79**, 214417 (2009).

[12] Y. Li, D. Adroja, P. K. Biswas, P. J. Baker, Q. Zhang, J. Liu, A. A. Tsirlin, P. Gegenwart, and Q. Zhang, Muon spin relaxation evidence for the U(1) quantum spin-liquid ground state in the triangular antiferromagnet $YbMgGaO_4$, Phys. Rev. Lett. **117**, 097201 (2016).

[13] J. G. Rau and M. J. P. Gingras, Magnitude of quantum effects in classical spin ices, Phys. Rev. B **92**, 144417 (2015).

[14] B. Tomasello, C. Castelnovo, R. Moessner, and J. Quintanilla, Single-ion anisotropy and magnetic field response in the spin-ice materials $Ho_2Ti_2O_7$ and $Dy_2Ti_2O_7$, Phys. Rev. B **92**, 155120 (2015).

[15] S. Petit, J. Robert, S. Guitteny, P. Bonville, C. Decorse, J. Ollivier, H. Mutka, M. J. P. Gingras, and I. Mirebeau, Order by disorder or energetic selection of the ground state in the XY pyrochlore antiferromagnet $Er_2Ti_2O_7$: An inelastic neutron scattering study, Phys. Rev. B **90**, 060410(R) (2014).

[16] S. Gao, F. Xiao, K. Kamazawa, K. Ikeuchi, D. Biner, K. W. Krämer, C. Rüegg, and T. H. Arima, Crystal electric field excitations in the quantum spin liquid candidate $NaErS_2$, Phys. Rev. B **102**, 024424 (2020).

[17] R. Sibille, N. Gauthier, H. Yan, M. C. Hatnean, J. Ollivier, B. Winn, U. Filges, G. Balakrishnan, M. Kenzelmann, N. Shannon, and T. Fennell, Experimental signatures of emergent quantum electrodynamics in $Pr_2Hf_2O_7$, Nat. Phys. **14**, 711 (2018).

[18] U. Arjun, K. Brinda, M. Padmanabhan, and R. Nath, Magnetic properties of layered rare-earth oxy-carbonates $Ln_2O_2CO_3$ (Ln = Nd, Sm, and Dy), Solid State Commun. **240**, 1 (2016).

[19] S. Nandi, Y. Jana, D. Swarnakar, J. Alam, P. Bag, and R. Nath, Magnetization process and specific heat properties of geometrically frustrated pyrochlores R_2FeSbO_7 (R^{3+} = Dy, Y) and spin-ice magnetic phase in Dy_2FeSbO_7, J. Alloys Compd. **714**, 318 (2017).

[20] Z. Ma, S. Zheng, Y. Chen, R. Xu, Z.-Y. Dong, J. Wang, H. Du, J. P. Embs, S. Li, Y. Li, Y. Zhang, M. Liu, R. Zhong, J.-M. Liu, and J. Wen, Possible gapless quantum spin liquid behavior in the triangular-lattice Ising antiferromagnet $PrMgAl_{11}O_{19}$, Phys. Rev. B **109**, 165143 (2024).

[21] K. Somesh, S. S. Islam, S. Mohanty, G. Simutis, Z. Guguchia, C. Wang, J. Sichelschmidt, M. Baenitz, and R. Nath, Absence of magnetic order and emergence of unconventional fluctuations in the $J_{\rm eff} = \frac{1}{2}$ triangular-lattice antiferromagnet $YbBO_3$, Phys. Rev. B **107**, 064421 (2023).

[22] A. Zorko, F. Bert, P. Mendels, K. Marty, and P. Bordet, Ground state of the easy-axis rare-earth kagome langasite $Pr_3Ga_5SiO_{14}$, Phys. Rev. Lett. **104**, 057202 (2010).

[23] V. Simonet, R. Ballou, J. Robert, B. Canals, F. Hippert, P. Bordet, P. Lejay, P. Fouquet, J. Ollivier, and D. Braithwaite, Hidden magnetic frustration by quantum relaxation in anisotropic Nd langasite, Phys. Rev. Lett. **100**, 237204 (2008).

[24] K. M. Ranjith, D. Dmytriieva, S. Khim, J. Sichelschmidt, S. Luther, D. Ehlers, H. Yasuoka, J. Wosnitza, A. A. Tsirlin, H. Kühne, and M. Baenitz, Field-induced instability of the quantum spin liquid ground state in the $J_{\rm eff} = \frac{1}{2}$ triangular-lattice compound $NaYbO_2$, Phys. Rev. B **99**, 180401(R) (2019).

[25] T. Fennell, M. Kenzelmann, B. Roessli, M. K. Haas, and R. J. Cava, Power-law spin correlations in the pyrochlore antiferromagnet $Tb_2Ti_2O_7$, Phys. Rev. Lett. **109**, 017201 (2012).

[26] J. Gaudet, A. M. Hallas, A. I. Kolesnikov, and B. D. Gaulin, Effect of chemical pressure on the crystal electric field states of erbium pyrochlore magnets, Phys. Rev. B **97**, 024415 (2018).

[27] Z. L. Dun, X. Li, R. S. Freitas, E. Arrighi, C. R. D. Cruz, M. Lee, E. S. Choi, H. B. Cao, H. J. Silverstein, C. R. Wiebe, J. G. Cheng, and H. D. Zhou, Antiferromagnetic order in the pyrochlores $R_2Ge_2O_7 (R = \text{Er, Yb})$, Phys. Rev. B **92**, 140407(R) (2015).

[28] K. Kimura, S. Nakatsuji, J.-J. Wen, C. Broholm, M. B. Stone, E. Nishibori, and H. Sawa, Quantum fluctuations in spin-ice-like $Pr_2Zr_2O_7$, Nat. Commun. **4**, 1934 (2013).

[29] E. Lhotel, S. Petit, S. Guitteny, O. Florea, M. C. Hatnean, C. Colin, E. Ressouche, M. R. Lees, and G. Balakrishnan, Fluctuations and all-in–all-out ordering in dipole-octupole $Nd_2Zr_2O_7$, Phys. Rev. Lett. **115**, 197202 (2015).

[30] U. Arjun, K. M. Ranjith, A. Jesche, F. Hirschberger, D. D. Sarma, and P. Gegenwart, Adiabatic demagnetization refrigeration to millikelvin temperatures with the distorted square lattice magnet $NaYbGeO_4$, Phys. Rev. B **108**, 224415 (2023).

[31] V. K. Singh, K. Nam, M. Barik, K. Boya, E. Kermarrec, P. Khuntia, K. H. Kim, S. Bhowal, and B. Koteswararao, Bi_2YbO_4Cl: A two-dimensional square-lattice compound with $J_{\rm eff} = \frac{1}{2}$ magnetic moments, Phys. Rev. B **109**, 075128 (2024).

[32] I. P. Roof, T.-C. Jagau, W. G. Zeier, M. D. Smith, and H.-C. zur Loye, Crystal growth of a new series of complex niobates, $LnKNaNbO_5$ (Ln = La, Pr, Nd, Sm, Eu, Gd, and Tb): Structural properties and photoluminescence, Chem. Mater. **21**, 1955 (2009).

[33] J. Rodríguez-Carvajal, Recent advances in magnetic structure determination by neutron powder diffraction, Phys. B: Condens. Matter **192**, 55 (1993).

[34] O. Arnold, J. Bilheux, J. Borreguero, A. Buts, S. Campbell, L. Chapon, M. Doucet, N. Draper, R. F. Leal, M. Gigg *et al.*, Mantid—Data analysis and visualization package for neutron scattering and μSR experiments, Nucl. Instrum. Methods Phys. Res. Sect. A **764**, 156 (2014).

[35] S. Mugiraneza and A. M. Hallas, Tutorial: a beginner's guide to interpreting magnetic susceptibility data with the Curie-Weiss law, Commun. Phys. **5**, 95 (2022).

[36] M. Pula, S. Sharma, J. Gautreau, S. K. P., A. Kanigel, M. D. Frontzek, T. N. Dolling, L. Clark, S. Dunsiger, A. Ghara, and G. M. Luke, Candidate for a quantum spin liquid ground state in the Shastry-Sutherland lattice material $Yb_2Be_2GeO_7$, Phys. Rev. B **110**, 014412 (2024).

[37] P. Biswal, S. Guchhait, S. Ghosh, S. N. Sarangi, D. Samal, D. Swain, M. Kumar, and R. Nath, Crystal structure and magnetic properties of the spin-$\frac{1}{2}$ frustrated two-leg ladder compounds $(C_4H_{14}N_2)Cu_2X_6 (X = \text{Cl and Br})$, Phys. Rev. B **108**, 134420 (2023).

[38] C. Kittel, *Introduction to Solid State Physics* (Wiley, Hoboken, NJ, 2004)

[39] M. Bouvier, P. Lethuillier, and D. Schmitt, Specific heat in some gadolinium compounds. I. Experimental, Phys. Rev. B **43**, 13137 (1991).

[40] J. Xing, L. D. Sanjeewa, J. Kim, W. R. Meier, A. F. May, Q. Zheng, R. Custelcean, G. R. Stewart, and A. S. Sefat, Synthesis, magnetization, and heat capacity of triangular lattice materials $NaErSe_2$ and $KErSe_2$, Phys. Rev. Mater. **3**, 114413 (2019).

[41] W. Liu, Z. Zhang, D. Yan, J. Li, Z. Zhang, J. Ji, F. Jin, Y. Shi, and Q. Zhang, Effects of the crystalline electric field in the $KErTe_2$ quantum spin liquid candidate, arXiv:2108.09693.

[42] K. M. Ranjith, S. Luther, T. Reimann, B. Schmidt, P. Schlender, J. Sichelschmidt, H. Yasuoka, A. M. Strydom, Y. Skourski, J. Wosnitza, H. Kühne, T. Doert, and M. Baenitz, Anisotropic field-induced ordering in the triangular-lattice quantum spin liquid $NaYbSe_2$, Phys. Rev. B **100**, 224417 (2019).

[43] S. Mohanty, S. S. Islam, N. Winterhalter-Stocker, A. Jesche, G. Simutis, C. Wang, Z. Guguchia, J. Sichelschmidt, M. Baenitz, A. A. Tsirlin, P. Gegenwart, and R. Nath, Disordered ground state in the spin-orbit coupled $J_{\rm eff} = \frac{1}{2}$ distorted honeycomb magnet $BiYbGeO_5$, Phys. Rev. B **108**, 134408 (2023).

[44] J. Sichelschmidt, P. Schlender, B. Schmidt, M. Baenitz, and T. Doert, Electron spin resonance on the spin-1/2

triangular magnet $NaYbS_2$, J. Phys.: Condens. Matter **31**, 205601 (2019).

[45] R. Orbach, Spin-lattice relaxation in rare-earth salts, Proc. R. Phys. Soc. A. **264**, 458 (1961).

[46] Data is available at STFC ISIS: https://doi.org/10.5286/ISIS.E.RB2310534.

[47] A. Boothroyd, *Principles of Neutron Scattering from Condensed Matter* (Oxford University Press, Oxford, 2020).

[48] K. W. H. Stevens, Matrix elements and operator equivalents connected with the magnetic properties of rare earth ions, Proc. Phys. Soc. Sec. A **65**, 209 (1952).

[49] M. Hutchings, *Point-Charge Calculations of Rnergy Levels of Magnetic Ions in Crystalline Electric Fields*, Solid State Physics Vol. 16 (Academic Press, Boca Raton, FL, 1964) p. 227.

[50] A. Furrer, J. Mesot, and T. Straessle, *Neutron Scattering in Condensed Matter Physics*, Series On Neutron Techniques And Applications (World Scientific, Singapore, 2009).

[51] R. Yamamoto, M. D. Le, D. T. Adroja, Y. Shimura, T. Takabatake, and T. Onimaru, Inelastic neutron scattering study of crystalline electric field excitations in the caged compounds NdT_2Zn_{20}(T = Co, Rh, and Ir), Phys. Rev. B **107**, 075114 (2023).

[52] J. Xiang, C. Su, N. Xi, Z. Fu, Z. Chen, H. Jin, Z. Chen, Z.-J. Mo, Y. Qi, J. Shen *et al.*, Dipolar spin liquid ending with quantum critical point in a Gd-based triangular magnet, arXiv:2301.03571.

[53] S. Guo, A. Ghasemi, C. L. Broholm, and R. J. Cava, Magnetism on ideal triangular lattices in $NaBaYb(BO_3)_2$, Phys. Rev. Mater. **3**, 094404 (2019).

[54] A. Scheie, V. O. Garlea, L. D. Sanjeewa, J. Xing, and A. S. Sefat, Crystal-field Hamiltonian and anisotropy in $KErSe_2$ and $CsErSe_2$, Phys. Rev. B **101**, 144432 (2020).

[55] E. Prince, *International Tables for Crystallography* (Springer Netherlands, Amsterdam, 2004).

[56] D. J. Newman and B. Ng, *Crystal Field Handbook* (Cambridge University Press, Cambridge, 2000).

[57] Y. Li, G. Chen, W. Tong, L. Pi, J. Liu, Z. Yang, X. Wang, and Q. Zhang, Rare-Earth triangular lattice spin liquid: A single-crystal study of $YbMgGaO_4$, Phys. Rev. Lett. **115**, 167203 (2015).

Correction: An author name was missing at publication. M. Aouane has been added as the sixth author.